SPACECRAFT TRANSFER TRAJECTORY DESIGN

EXPLOITING RESONANT ORBITS IN MULTI-BODY ENVIRONMENTS

A Dissertation

Submitted to the Faculty

of

Purdue University

by

Tatiana Mar Vaquero Escribano

In Partial Fulfillment of the

Requirements for the Degree

of

Doctor of Philosophy

August 2013

Purdue University

West Lafayette, Indiana

A papi, mami, y Migui.

To Matt.

ACKNOWLEDGMENTS

Y por fin salió el sol en esta ciudad eternamente nublada. Gracias no sólo por dejarme ir, sino por animarme a que me fuera. Hubiera sido imposible y no hubiera tenido sentido completar esta etapa sin el apoyo incondicional y el cariño que siempre me habéis mostrado. Es un orgullo y privilegio poder decir que soy vuestra hija y hermana. Y por ello, este logro es para vosotros, y para Cali.

Matt, we made it. I am enormously grateful for everything that you do for me and for giving up some of your goals so that I could pursue my own. I hope to be as supportive to you as you have been to me as you now pursue your goals.

Professor Howell, thank you for teaching me, both in and out of the classroom, everything that I know in this field. I am forever grateful for your support and guidance, and for the endless hours that you have spent revising my work. I would also like to thank the rest of my committee members, Professor DeLaurentis, Professor Crossley, and Professor Longuski, for providing valuable insight on this investigation.

I would like to acknowledge very important people in my life who not only encouraged me through these seemingly eternal years of graduate school, but made the journey enjoyable as well. *A mis abuelos, madrina, tíos, tías, primos y prima: Gracias por quererme y valorarme.* I am deeply grateful to my family-in-law, and especially to John and Teresa, for their encouragement through the good and the not-so-good times.

My colleagues and friends in the School of Languages and Cultures have been incredible sources of support and I have truly enjoyed our many, many non-technical conversations together. Of course and, for similar reasons, my friends in the Canary Islands must be properly thanked. They have always being 'there', even though we have not lived in the same city for years. *A Juanma y Liuva: Aunque nos veamos*

una vez al año, si eso, os aprecio mucho y agradezco vuestra amistad y confianza. Mantengo la esperanza de que algún día estemos más cerca.

I would like to express my gratitude to each member of our research group, past and present, for their friendship and for selflessly sharing their knowledge with me. I have learned, in some way or another, from each one of you and I am proud to be counted amongst all of you in this research group. I hope that our paths cross many times in the future.

Of course, this work could have not been completed without financial assistance. I would like to thank the School of Languages and Cultures, and especially Nicole Roger-Hogan, for their continuous support. This work was also partially supported by Zonta International through the Amelia Earhart Fellowship Program and by NASA Headquarters for the Program entitled "Research Opportunities in Space and Earth Science" under NASA Grant No. NNX13AH02G.

TABLE OF CONTENTS

LIST OF TABLES

LIST OF FIGURES

ABSTRACT

Vaquero Escribano, Tatiana Mar. Ph.D., Purdue University, August 2013. Spacecraft Transfer Trajectory Design Exploiting Resonant Orbits in Multi-Body Environments. Major Professor: Kathleen C. Howell.

Historically, resonant orbits have been employed in mission design for multiple planetary flyby trajectories and, more recently, as a source of long-term orbital stability. For instance, in support of a mission concept in NASA's Outer Planets Program, the Jupiter Europa Orbiter spacecraft is designed to encounter two different resonances with Europa during the 'endgame' phase, leading to Europa orbit insertion on the final pass. In 2011, the Interstellar Boundary Explorer spacecraft was inserted into a stable out-of-plane lunar-resonant orbit, the first of this type for a spacecraft in a long-term Earth orbit. However, resonant orbits have not yet been significantly explored as transfer mechanisms between non-resonant orbits in multi-body systems. This research effort focuses on incorporating resonant orbits into the design process to potentially enable the construction of more efficient or even novel transfer scenarios. Thus, the goals in this investigation are twofold: i) to expand the orbit architecture in multi-body environments by cataloging families of resonant orbits, and ii) to assess the role of such families in the design of transfer trajectories with specific patterns and itineraries. The benefits and advantages of employing resonant orbits in the design process are demonstrated through a variety of astrodynamics applications in several multi-body systems.

In the Earth-Moon system, locally optimal transfer trajectories from low Earth orbit to selected libration point orbits are designed by leveraging conic arcs and invariant manifolds associated with resonant orbits. Resonant manifolds in the Earth-Moon system offer trajectories that tour the entire space within reasonable time intervals, facilitating the design of libration point orbit tours as well as Earth-Moon cyclers. In

the Saturnian system, natural transitions between resonant and libration point orbits are sought and the problem of accessing Hyperion from orbits that are resonant with Titan is also examined. To add versatility to the proposed design method, a system translation technique enables the straightforward transition of solutions from the Earth-Moon system to any Sun-planet or planet-moon three-body system. The circular restricted three-body problem serves as a basis to quickly generate solutions that meet specific requirements, but candidate transfer trajectories are then transitioned to an ephemeris model for validation.

1. INTRODUCTION

Previous analyses concerning dynamical systems techniques and resonant orbits have demonstrated that the use of invariant manifolds and resonant flybys can enable previously unknown trajectory options and potentially reduce the propellant requirements. The conceptual trajectories that support interplanetary missions such as the Jupiter Icy Moons Orbiter (JIMO) [1] and the Jupiter Europa Orbiter (JEO) [2], are designed to exploit multiple gravity assists as well as low-thrust propulsion. The complexity of such mission scenarios and the environments comprised of multiple gravity fields suggest that dynamical systems techniques might offer important advantages. The JIMO spacecraft trajectory was initially designed to explore the icy moons of Jupiter, including Europa; Ganymede and Callisto were also flyby targets for the spacecraft. The Jupiter Europa Orbiter, a mission in NASA's Outer Planets Program, is planned to insert a spacecraft into orbit about Europa for determination of the presence or absence of a liquid ocean on the Jovian moon. Relevant to this investigation, the spacecraft encounters Europa in an 'endgame' phase. Different definitions exist for the endgame problem, but this phase typically includes the last several resonance transitions before the final approach to the desired moon. In the JEO endgame scenario, the first encounter is designed to insert the spacecraft into an orbit that is resonant with Europa and the second encounter shifts the spacecraft to a different resonance, leading to Europa Orbit Insertion (EOI) on the final pass. As a consequence, a number of recent investigations have explored the relationship between the invariant manifolds associated with unstable resonant orbits and the determination of their role in resonance transition.

Resonant orbits are applicable not only in flyby trajectory design; in fact, orbital resonance can be a source of long-term stability. In 2008, the Interstellar Boundary Explorer (IBEX) [3], the first spacecraft designed to collect data across the entire sky

about the heliosphere and its boundary, was launched into a high-altitude Earth orbit. However, due to the strong and repeated perturbations from the Moon's gravitational field, the nominal mission trajectory became unpredictable in the long term, that is, the time window of predictability was only 2.5 years into the future. Although this lack of long term predictability did not interfere with the planning efforts for the two-year nominal mission, it became impossible to estimate the ΔV required for long-term station-keeping. Thus, planning for an extended mission forced the execution of a set of three maneuvers to shift IBEX into a more predictable orbit while still meeting all the scientific requirements. In June 2011, IBEX was inserted into a remarkably stable out-of-plane lunar-resonant orbit; the IBEX resonant trajectory is the first of this type for a spacecraft in a long-term Earth orbit. However, the success of the IBEX trajectory has prompted consideration of this type of orbit for other applications. In April of 2013, NASA announced the selection of the Transiting Exoplanet Survey Satellite (TESS) [4], as part of NASA's Small Explorer Program. The space telescope is designed to search for extrasolar planets; it is scheduled for launch from Earth in 2017 and will be inserted directly into a long-term stable Earth orbit in resonance with the Moon.

Resonant orbits have not yet been extensively explored as transfer mechanisms between non-resonant orbits in multi-body systems, such as low-altitude orbits around primary bodies or libration point orbits. Therefore, the overarching goals in this research effort are twofold: (1) to expand the orbit architecture in multi-body environments by cataloging families of periodic resonant orbits, and (2) to assess the role of resonant orbits in the design of planar and three-dimensional transfer trajectories in such dynamical environments by exploiting resonant orbits and their associated invariant manifolds. Therefore, this investigation begins with the search, identification, and computation of resonant orbits in the circular restricted three-body problem (CR3BP). The determination of the orbits and their application is facilitated by Poincaré maps, which are successfully employed to examine the relationships between the invariant manifolds associated with resonant orbits. The intersections between

the invariant manifolds associated with these trajectories, as viewed in the Poincaré map, are then employed to search for potential resonance transitions and transfer trajectories with desired itineraries. The resulting transfer trajectories benefit from a reduced maneuver cost (ΔV) by shadowing manifold trajectories. In essence, the core of this investigation is an exploration of resonance conditions in multi-body environments by cataloging 2D and 3D n-periodic orbits in resonance with the smaller primary and by searching for transfers between *these* orbits and other orbits or locations of interest in the system via the application of dynamical systems theory and corrections strategies. A variety of applications in multiple n-body systems are introduced to highlight the benefit of incorporating resonant orbits into the trajectory design process and the usefulness of the proposed design technique.

1.1 Previous Contributions

Most of the dynamical systems techniques currently employed today actually appear in Poincaré's seminal work. In general terms, a dynamical systems approach involves an attempt to describe the evolution of a future state as it evolves from the current state; this description is either continuous via ordinary differential equations or discrete, using a map. In 1892, Poincaré predicted the existence of particular structures in a dynamical system, such as periodic orbits and invariant manifolds [5]. Dynamical chaos, one of the key concepts introduced by Poincaré, can be defined as the highly sensitive dependence of dynamical systems on initial conditions [5, 6]. In other words, small differences in initial conditions yield widely diverging results in chaotic systems and, as a result, long-term prediction is almost impossible. But, it is the existence of chaos in the restricted three-body problem that allows for transfers from an initial position to different destinations, perhaps quite distant, at very low cost. These concepts have been advanced by many researchers, including Birkhoff, Kolmogorov, Arnold, and Moser [7–10].

In the 1960's, the application of insight from the circular restricted three-body problem moved into the 'space age' when a mission to the Lagrange points was considered for NASA's Apollo program [11–13]. Since then, many of the structures that emerge in the CR3BP have been more actively exploited in trajectory design. Consequently, successful missions to the vicinity of the Lagrange points have since been launched, including the International Sun-Earth Explorer-3 (ISEE-3) [14], the Solar Heliospheric Observatory (SOHO) [15], the Advanced Composition Explorer (ACE) [16], and the Microwave Anisotropy Probe (MAP) [17]. Parallel to the development of these mission concepts, other researchers considered the possibility of applying dynamical systems techniques to the design of these type of trajectories. In fact, in the 1960's, Conley had investigated low energy transfer orbits to the Moon using dynamical system techniques [18]. However, the transfer orbits that Conley computed possessed a time-of-flight that was considered too long to be practical. Nevertheless, the foundation for future work was established, and other researchers rapidly recognized the significance of this design framework [19]. In the 1990's, the use of invariant manifolds in the design process to construct pathways between the Earth and the Sun-Earth libration points was finally applied in an actual trajectory: the trajectory supporting the Genesis mission [20–22]. Since then, these techniques have been increasingly applied in mission design [23–25].

The study of resonance, particularly within the context of flybys, has advanced significantly in the last decade, and dynamical systems techniques can now be applied to this problem. The application of gravity flyby techniques to mission design also has a long history, first introduced by Minovitch [26, 27] and others at the Jet Propulsion Laboratory (JPL). In nearly all flyby trajectories involving one or multiple planets, some form of resonance is involved. One advantage of resonant flybys in spacecraft applications is the construction of trajectories with much lower maneuver costs. This efficient result is based on the exchange in momentum between the spacecraft and the planetary body during the flyby. A recent example, one that reflects the use of resonance during planet or moon encounters is the Jupiter Europa Orbiter trajectory,

which incorporates two different resonances with Europa before capture around the Jovian moon [28]. The concept of resonance also dictates the natural motion of celestial bodies. In fact, orbital resonances play a decisive role in the long term dynamical behavior and, in some cases, even in the physical evolution of the planets, their natural satellites, and other small bodies in the planetary system [29]. One of the most significant examples of natural resonance in the solar system is comets in resonance with planetary orbits. The Jupiter family of comets, such as Gehrels 3, Oterma, and Helin-Roman-Crockett, are known to frequently transition between 3:2 and 2:3 resonances, sometimes including temporary captures by Jupiter. As a result, many researchers have attempted to explain this phenomenon [22, 30–33].

Any application of the natural "resonance hopping" phenomenon to the transfer design problem requires a fundamental understanding of the connection between resonances. The relationship between planar stable and unstable orbits in resonance with Europa has been previously explored. Anderson and Lo examine various techniques in considering low-energy trajectory design for missions to Europa, as well as the Europa Orbiter (EO) spacecraft. In their investigations, Lo and Anderson first use Poincaré sections to search for unstable resonant orbits in support of the Europa Orbiter trajectory concept [34–36]. The invariant manifolds from these unstable resonant orbits reflect the resonance transitions of the actual EO trajectory. The trajectory clearly exploits the invariant manifolds associated with periodic orbits. (Note, however, that the original EO trajectory was designed without the use of manifolds [37].) Anderson also introduces a flyby design that exploits heteroclinic and homoclinic connections associated with resonant orbits in the Jupiter-Europa system [38]. Extending the work of Lo and Anderson, some of these techniques are applied to the Saturn-Titan system with emphasis on three-dimensional resonant orbits [39]. More specifically, Vaquero and Howell focus on the analysis and design of trajectories that transition between interior and exterior resonant orbits as well as between libration point orbits in the Saturn-Titan system [40]. As an application of resonance in the Saturnian system, Vaquero and Howell introduce the design of a preliminary transfer trajectory to

access the orbit of Hyperion, a moon of Saturn in resonance with Titan, by exclusively exploiting the invariant manifolds associated with periodic resonant orbits.

Resonance conditions in the Earth-Moon neighborhood have been previously investigated as well. Parker and Lo explore the use of planar unstable resonant orbits and their associated invariant manifolds to investigate mission scenarios near the Earth involving periodic flybys of the Moon [41]. Many other researchers have studied the exploitation of the invariant manifolds associated with Lyapunov and halo orbits to access the vicinity of the Moon from a low Earth orbit [42–44]. The exploration of the Earth-Moon space, however, remains open and new trajectory design options may arise by gaining a better understanding of the dynamical structure in this regime. In contrast to other systems, some significant factors influence the behavior in the Earth-Moon region including the presence of only a single major natural satellite, i.e., the Moon. Additionally, the mass parameter, μ, is two and three orders of magnitude larger in the Earth-Moon system than in the Saturnian and Jovian systems. As a result, the impact of the Moon's gravity on the spacecraft path is much larger, also influencing the stability of certain types of periodic orbits. Potentially, these very characteristics also enable expanded trajectory design options and novel mission scenarios.

1.2 Dissertation Overview

This investigation is organized as follows:

- Chapter 2: The n-body problem is described, and the necessary background regarding the formulation of the circular restricted three-body problem is developed. This chapter includes the derivation of the differential equations and the integrals of the motion, equilibrium solutions, the state transition matrix, and a series of numerical techniques that are employed in the computation of periodic solutions and transfer trajectories in the CR3BP. The computation of families of orbits is enabled through the use of single-parameter and pseudo-

arclength continuation methods. The required background in equilibrium point and orbital stability is also developed and stability-energy plots that represent orbital characteristics associated with families of periodic orbits are introduced. The goals in this investigation are achieved through the exploitation of dynamical systems theory and, thus, a background in invariant manifold theory is first introduced followed by the definition of the concept of Poincaré maps and the technique used in their computation. Appropriate coordinate frame transformations are derived.

- Chapter 3: A comprehensive analysis of periodic orbits in multi-body environments is developed. Such families of periodic orbits include planar and three-dimensional libration point orbits as well as families of resonant orbits. A variety of numerical examples of such periodic solutions are included and discussed in detail. Families of planar and three-dimensional resonant orbits in multi-body systems are a focus in this investigation and, thus, these families are evaluated in the Earth-Moon system and in the ephemeris model.

- Chapter 4: The construction of reduced-cost transfer trajectories with desired itineraries is one of the two major objectives in this investigation. The theory and techniques employed in the transfer design capability that enables the construction of such trajectories are detailed in this chapter. Basic numerical examples of invariant manifolds associated with libration point orbits and Poincaré maps are offered to illustrate the use of dynamical systems techniques in this investigation. Finally, a general description of the proposed end-to-end transfer design process is detailed step-by-step in this chapter.

- Chapter 5: The concept of unstable resonant orbits and invariant manifolds as well as their applicability to preliminary trajectory design is further demonstrated through a variety of applications in multi-body trajectory design. Applications of resonant orbits are introduced in two three-body systems, i.e., the Earth-Moon and Saturn-Titan systems. Numerous examples of 2D and 3D

natural transfers as well as transfers that include maneuvers are presented in each dynamical regime. A direct optimization technique is developed to further reduce the propellant requirement when incorporating maneuvers. The three-body model serves as a basis to quickly generate solutions that meet specific requirements. Candidate transfer trajectories are then transitioned to a higher-fidelity model that includes solar gravitational effects to validate the solutions generated in the 3B model and to demonstrate the existence of resonant conditions in the full ephemeris model. Preliminary transfer cost and time-of-flight analyses are provided to illustrate the benefits of incorporating intermediate resonant arcs into the trajectory design process. Finally, to add versatility to the proposed transfer design capability, a system translation technique is introduced to allow transfer trajectories in a given three-body system to be straightforwardly translated to other systems.

- Chapter 6: The final chapter includes a summary of the contributions of this investigation, along with recommendations to further investigate the problem.

2. SYSTEM MODELS AND NUMERICAL METHODS

The exploration of any problem involving resonances typically defines a resonance initially within the context of the two-body problem and conics. This investigation, however, is focused on resonance conditions in a higher-fidelity environment, that is, involving multiple gravitational fields. Thus, the circular restricted three-body problem serves as the basis for the majority of this analysis. As a background that facilitates an understanding of the problem, the general n-body problem is first introduced and then the framework, assumptions, and full formulation of the circular restricted three-body problem are detailed for this application. A general description of basic differential corrections algorithms along with orbit continuation schemes are also developed, that provide a foundation for the majority of the trajectory design applications demonstrated in this investigation. Dynamical systems techniques play a major role in this analysis and, therefore, a general background on invariant manifold theory and Poincaré mapping techniques are included as well. Coordinate frame transformations are also summarized for clarity and completeness.

2.1 The General n-Body Problem

Frequently, the ultimate goal in an investigation represented in terms of the n-body problem is a prediction of the motion of n celestial bodies given only their present position and velocity. The n-body model, frequently formulated as an ephemeris model, is fundamental in the analysis of trajectories that support actual missions since it is higher-fidelity and allows for the incorporation of perturbations and additional gravitational forces that exist in the true dynamical environment. Non-gravitational forces can also be accommodated, in general, but are not included in this investigation. A diagram to define notation in the n-body problem appears in Figure 2.1.

The $\hat{X}, \hat{Y}, \hat{Z}$ system of coordinates denotes an inertial reference frame; point O identifies the origin, overbars indicate vectors, and carats represent unit vectors. The directional components of any vectors are identified with arrows and subscripts in the figure. The gravitational bodies in the system are labeled P_i, P_j, P_q, where P_i represents the body of interest, i.e., the spacecraft, P_j describes all other gravitational bodies, and P_q is the central body. The vector $\bar{r}_{qj}$ then describes the position of each perturbing body, P_j, with respect to the central body, P_q. Suitable approximations for the relative locations of the celestial bodies are obtained directly from the NASA Jet Propulsion Laboratory (JPL) DE405 planetary ephemeris data file [45]. Then, the position vector of each perturbing body relative to the body of interest, i.e., $\bar{r}_{ij}$, is directly obtained using the relationship,

$$\bar{r}_{ij} = \bar{r}_{qj} - \bar{r}_{qi} \tag{2.1}$$

Both position vectors, $\bar{r}_{qj}$ and $\bar{r}_{qi}$, are known within this context and, therefore, $\bar{r}_{ij}$ is also known from equation (2.1), at least to the degree of accuracy available from the observational ephemeris data.

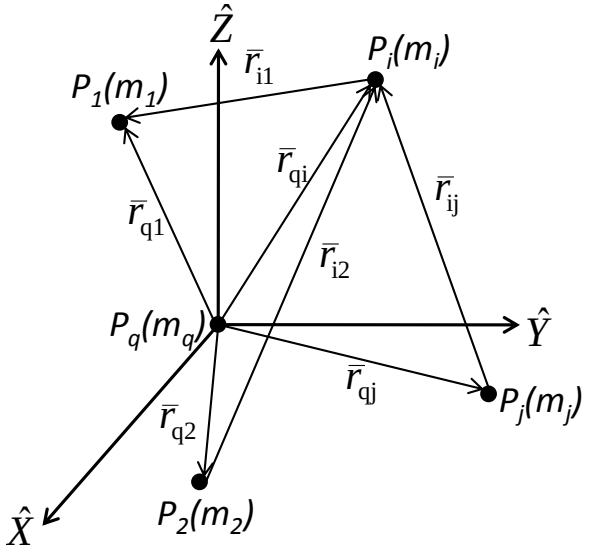

Figure 2.1. Definitions in the n-Body Problem

The mutual gravity between the n point masses is assumed to be the only force acting within the system. Then, from Newton's Second Law, the equations of motion are derived assuming that the masses in the system are constant and all derivatives are evaluated relative to an inertial observer. The resulting vector equation of motion for a particle P_i under the gravitational influence of n other particles is written,

$$m_i \frac{d^2 \bar{r}_i}{dt^2} = -G \sum_{\substack{j=1 \\ j \neq i}}^{n} \frac{m_i m_j}{r_{ji}^3} \bar{r}_{ji} \tag{2.2}$$

where G is the universal gravitational constant and m_i and m_j represent the mass of the particle of interest and the masses of the other bodies that gravitationally influence the motion of $P_i(m_i)$, respectively. The vectors $\bar{r}_i$ and $\bar{r}_j$ describe the position of particles $P_i(m_i)$ and $P_j(m_j)$ relative to an inertially fixed base point. In equation (2.2), however, the number of dependent variables, that is, the scalar components of the position and velocity of P_i, $(\bar{r}_i, \dot{\bar{r}}_i)$, is greater than the number of first-order equations. Ultimately, six scalar, first-order differential equations are required to model the degrees of freedom for *each* particle in an n-body system, that is, a total of $6n$ nonlinear and coupled differential equations for a system of n particles. From fundamental concepts in mechanics, only 10 integrals of motion are known to exist in this problem and the general n-body problem is not solvable analytically. Thus, an alternative relative formulation is more successful, i.e., expressing the position of the body of interest, $P_i(m_i)$, relative to the central body, $P_q(m_q)$. In the relative n-body problem, such a relative vector equation of motion is written,

$$\frac{d^2 \bar{r}_{qi}}{dt^2} + G \frac{(m_i + m_q)}{r_{qi}^3} \bar{r}_{qi} = G \sum_{\substack{j=1 \\ j \neq i,q}}^{n} m_j \left(\frac{\bar{r}_{ij}}{r_{ji}^3} - \frac{\bar{r}_{qj}}{r_{qj}^3} \right) \tag{2.3}$$

The terms on the right represent the perturbation due to additional gravitational fields, or particles, on the motion of both P_q and P_i. In the two-body problem, all the perturbing terms are removed and a closed-form analytical solution is available. However, this analytical result no longer exists if even one more body is added to the system. But, the dynamical system of equations in equation (2.3) can be numerically

simulated. If approximations for the motion of all particles P_j as well as the central body P_q are available, propagations for the motion of particle P_i can proceed. Given an acceptable set of initial conditions, the result is indeed an approximation for the motion of P_i but sufficiently accurate for many applications. However, appropriate initial conditions can be extremely nontrivial to produce.

2.2 The Circular Restricted Three-Body Problem (CR3BP)

Ultimately, trajectory designs for spacecraft applications require a capability to produce quality state vectors to initiate the design process. An understanding of the dynamical foundations of the behavior is critical, but the complexities of the n-body problem preclude a general solution. A simpler model that retains some of the fundamental structures is a key component in developing design strategies. Limiting the number of particles reduces the complexity of the governing differential equations and numerous insights generally emerge. Thus, the three-body problem is very useful. For three gravitational sources, equation (2.3) reduces to the form,

$$m_3 \frac{d^2 \bar{r}_3}{dt^2} = -G \frac{m_3 m_1}{r_{13}^3} \bar{r}_{13} - G \frac{m_3 m_2}{r_{23}^3} \bar{r}_{23} \tag{2.4}$$

where m_3 is the infinitesimally small mass of the third particle of interest P_3, and the masses m_1 and m_2 comprise a 'primary system'. But, solving equation (2.4) analytically requires the time history for the location of the primaries, that is, $\bar{r}_1(t)$ and $\bar{r}_2(t)$. Such information is not available (without approximation) since P_1 and P_2 are influenced by the motion of P_3 and its instantaneous position $\bar{r}_3(t)$. Recall that the simultaneous solution for all three position vectors requires 18 integrals, but only 10 are available. In the two-body problem, reformulating the problem in terms of relative motion is significant and yields an analytical solution, so the same strategy is employed for $n = 3$. Consider the motion of P_3 with respect to P_1,

$$\frac{d^2 \bar{r}_{13}}{dt^2} + G \frac{(m_3 + m_1)}{r_{13}^3} \bar{r}_{13} = G m_2 \left(\frac{\bar{r}_{32}}{r_{23}^3} - \frac{\bar{r}_{12}}{r_{12}^3} \right) \tag{2.5}$$

and the motion of P_3 with respect to P_2,

$$\frac{d^2\bar{r}_{23}}{dt^2} + G\frac{(m_3 + m_2)}{r_{23}^3}\bar{r}_{23} = Gm_1\left(\frac{\bar{r}_{31}}{r_{13}^3} - \frac{\bar{r}_{21}}{r_{12}^3}\right) \tag{2.6}$$

This relative formulation results in two second-order vector differential equations for $\bar{r}_{13}$ and $\bar{r}_{23}$. A total of 12 constants are required and only 10 are available. Even though the relative-equation formulation reduces the number of equations that are necessary to completely model the system, a general closed-form analytical solution still does not exist. Further simplification is warranted to gain insight into the behavior of the system.

2.2.1 Assumptions

Three additional assumptions are critical to further decrease the complexity of the problem. All the assumptions are key in describing the motion of the primary system, i.e., P_1 and P_2. These assumptions are summarized as follows:

1. The mass of the third particle, P_3, is assumed to be infinitesimally small relative to the masses of primary particles P_1 and P_2, that is, $m_3 \ll m_1, m_2$, and, thus, m_3 does not influence the motion of m_1 and m_2. This mass relationship is reasonable when m_3 represents a comet, spacecraft, or moon moving under the influence of the planets and/or the Sun.

2. If m_3 does not influence the motion of m_1 and m_2, then m_1 and m_2 represent an isolated two-body system. The solution in such a system is known to be a conic section. For many applications of interest, the solution is a closed conic. The masses m_1 and m_2 comprise the primary system; m_1 is arbitrarily selected as the larger primary. The center of mass is located at the barycenter on the line joining the primaries.

3. If the path in the relative two-body primary system is closed, it can be described as an ellipse. To further restrict the motion, it is assumed that P_1 and P_2 move

on circular orbits. This conic motion of the primaries is planar. However, the motion of P_3 is not constrained and the third particle is free to move in all three spatial dimensions.

Given these assumptions, the problem is reformulated as demonstrated in Figure (2.2). From this relative formulation, the vector equation of motion for P_3 is written,

$$m_3 \frac{d^2 \bar{r}_3}{dt^2} = -G\frac{m_3 m_1}{r_{13}^3}\bar{r}_{13} - G\frac{m_3 m_2}{r_{23}^3}\bar{r}_{23} \tag{2.7}$$

The position vectors in equation (2.7) are then defined in Figure 2.2.

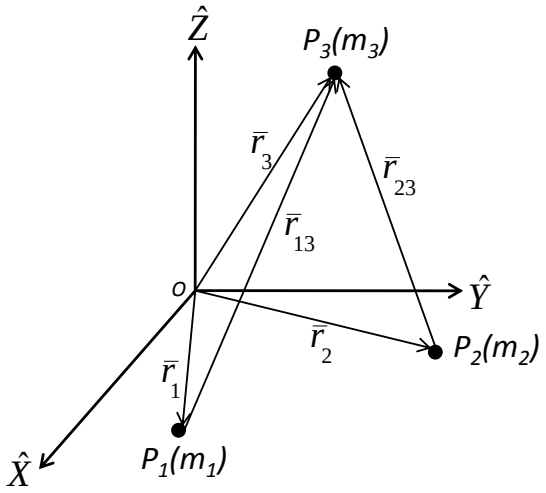

Figure 2.2. Formulation of the Three-Body Problem

2.2.2 Characteristic Quantities and Nondimensionalization

Further insight into this complex problem is gained by nondimensonalizing the parametric quantities in equation (2.7). The characteristic length, l^*, is defined as the distance between the primaries. The characteristic mass, m^*, represents the sum

of the masses of the two primaries, and the orbital period of the system primaries in their relative motion is defined as the characteristic time, t^*. In summary,

$$l^* = \|\bar{r}_1\| + \|\bar{r}_2\| \tag{2.8}$$

$$m^* = m_1 + m_2 \tag{2.9}$$

$$t^* = \left(\frac{l^{*3}}{\widetilde{G}m^*}\right)^{\frac{1}{2}} \tag{2.10}$$

$$\widetilde{G} = \frac{Gl^{*3}}{m^* t^{*2}} = 1 \tag{2.11}$$

$$N = \left(\frac{\widetilde{G}m^*}{l^{*3}}\right)^{\frac{1}{2}} \tag{2.12}$$

where G is the universal gravitational constant and N is the conic definition of the dimensional mean motion corresponding to the motion of the primaries. The mean motion is nondimensionalized to the value n^* such that,

$$n^* = Nt^* = 1 \tag{2.13}$$

and time, the independent variable in the differential equations, is nondimensionalized such that,

$$\tau = \frac{t}{t^*} \tag{2.14}$$

In addition to the characteristic quantities, the mass fraction μ is associated with the two system primaries P_1 and P_2 and is defined as,

$$\mu = \frac{m_2}{m_1 + m_2} = \frac{m_2}{m^*} \tag{2.15}$$

where P_2 is arbitrarily defined as the smaller primary such that $m_2 < m_1$. This mass ratio is often used to parameterize the ensuing motion.

2.2.3 Differential Equations of Motion

The differential equations that govern the motion of P_3 are applicable to a wide variety of systems in a nondimensional form. Equation (2.7) can be simplified with the

aid of the characteristic quantities. In addition, a formulation relative to a rotating observer adds great insight and further applications. This rotating frame facilitates the identification of fixed equilibrium points corresponding to particular solutions in the CR3BP, which serve as the starting point for the determination of periodic orbits.

Two coordinate frames are significant in the formulation of the CR3BP; an inertial and a rotating reference frame. To define the rotating frame, first recall the inertial frame, I, that is defined in Figure 2.1. The origin of the inertial frame is also fixed at B, the system barycenter. Then, an additional reference frame, R, rotates but is also centered at B such that the x-axis of the rotating frame is always parallel to the line connecting P_1 to P_2, and directed from the larger towards the smaller primary. Let $\hat{x}$ represent a unit vector in this direction. Since P_1 and P_2 move on conic paths, their mutual plane of motion remains fixed. This fixed plane is defined as the common $\hat{X}\hat{Y}$- and $\hat{x}\hat{y}$-plane. The z-axis of the rotating frame, i.e., $\hat{z}$, is parallel to the orbital angular momentum vector associated with the motion of the system; thus $\hat{z}$ and $\hat{Z}$ are parallel. Then, $\hat{y}$ completes the right-handed vector basis. The angle θ denotes the orientation of the rotating frame with respect to the inertial frame. The dimensional rate of change of θ, i.e., $\frac{d\theta}{dt}$, is the angular velocity of the primary system, which is constant for circular orbits of the primaries and equal to the mean motion, N.

Once the rotating frame is defined, the derivation of the equations of motion is straightforward. The positions of P_1, P_2, and P_3 with respect to the barycenter are defined by the vectors $\bar{D}_1$, $\bar{D}_2$, and $\bar{P}$, respectively. The position of P_3 relative to P_1 is $\bar{D}$ and that of P_3 relative to P_2 is $\bar{R}$. Let the position vector $\bar{P}$ be defined in terms of the scalar components,

$$\bar{P} = x_d\hat{x} + y_d\hat{y} + z_d\hat{z} \tag{2.16}$$

where x_d, y_d, z_d are dimensional scalar quantities measured relative to the rotating frame. With these vector definitions, the nondimensional distances $\bar{r}$, $\bar{d}$, and $\bar{\rho}$ are written,

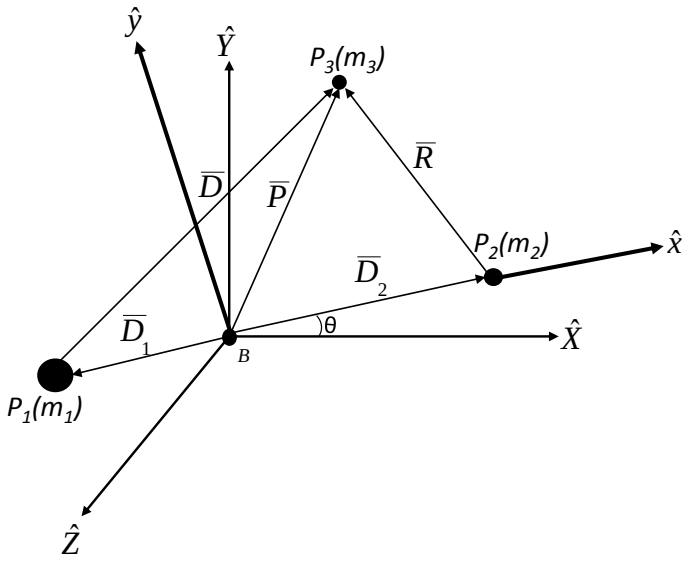

Figure 2.3. Formulation of the CR3BP Relative to a Rotating Reference Frame

$$\bar{r} = \frac{\bar{R}}{l^*} = (x - 1 + \mu)\,\hat{x} + y\hat{y} + z\hat{z} \tag{2.17}$$

$$\bar{d} = \frac{\bar{D}}{l^*} = (x + \mu)\,\hat{x} + y\hat{y} + z\hat{z} \tag{2.18}$$

$$\bar{\rho} = \frac{\bar{P}}{l^*} = x\hat{x} + y\hat{y} + z\hat{z} \tag{2.19}$$

where $l^* = \left\|\bar{D}_1\right\| + \left\|\bar{D}_2\right\|$ and x, y, z are nondimensional quantities measured relative to the rotating frame. The specific quantities defined in Figure 2.3 and equations (2.16)-(2.19) are substituted into equation (2.7). The result is a vector, second-order differential equation for the motion of m_3 under the gravitational influence of larger masses m_1 and m_2,

$$\bar{\rho}'' = -(1 - \mu)\frac{\bar{d}}{d^3} - \mu\frac{\bar{r}}{r^3} \tag{2.20}$$

where the primes indicate derivatives with respect to nondimensional time, τ, relative to an inertial reference frame centered on the barycenter of the system. It is desirable to express equation (2.20) in terms of the Cartesian coordinates and the rotating

reference frame. Expressions for $\bar{\rho}'$ and $\bar{\rho}''$ are derived from the Basic Kinematic Equation, BKE, that is,

$$\bar{\rho}' = \frac{{}^{I}d\bar{\rho}}{d\tau} = \frac{{}^{R}d\bar{\rho}}{d\tau} + {}^{I}\bar{\omega}^{R} \times \bar{\rho} \tag{2.21}$$

$$\bar{\rho}'' = \frac{{}^{I}d^2\bar{\rho}}{d\tau^2} = \frac{{}^{R}d^2\bar{\rho}}{d\tau^2} + 2{}^{I}\bar{\omega}^{R} \times \frac{{}^{R}d\bar{\rho}}{d\tau} + {}^{I}\bar{\omega}^{R} \times \left({}^{I}\bar{\omega}^{R} \times \bar{\rho}\right) \tag{2.22}$$

where ${}^{I}\bar{\omega}^{R} = n^*\hat{z}$ is the nondimensional angular velocity of the rotating reference frame with respect to the inertial frame. The term $\frac{{}^{R}d\bar{\rho}}{d\tau}$ represents the change in the position vector as viewed from the rotating frame. The kinematic expressions for the velocity and acceleration relative to an observer in frame R are,

$$\dot{\bar{\rho}} = \frac{{}^{R}d\bar{\rho}}{d\tau} = \dot{x}\hat{x} + \dot{y}\hat{y} + \dot{z}\hat{z} \tag{2.23}$$

$$\ddot{\bar{\rho}} = \frac{{}^{R}d^2\bar{\rho}}{d\tau^2} = \ddot{x}\hat{x} + \ddot{y}\hat{y} + \ddot{z}\hat{z} \tag{2.24}$$

where the dots indicate a derivative with respect to the nondimensional time, τ, and relative to the rotating reference frame. Substituting equation (2.24) into equation (2.22) results in the following kinematic expansion,

$$\bar{\rho}'' = \left(\ddot{x} - 2n^*\dot{y} - n^{*2}x\right)\hat{x} + \left(\ddot{y} + 2n^*\dot{x} - n^{*2}y\right)\hat{y} + \ddot{z}\hat{z} \tag{2.25}$$

The kinematic expression for the acceleration in equation (2.25) is substituted into the left side of equation (2.20). The resulting vector equation of motion (EOM) reduces to the well known scalar, second-order differential equations in the CR3BP,

$$\ddot{x} - 2n^*\dot{y} - n^{*2}x = -\frac{(1-\mu)(x+\mu)}{d^3} - \frac{\mu}{r^3}(x - 1 + \mu) \tag{2.26}$$

$$\ddot{y} + 2n^*\dot{x} - n^{*2}y = -\frac{(1-\mu)}{d^3}y - \frac{\mu}{r^3}y \tag{2.27}$$

$$\ddot{z} = -\frac{(1-\mu)}{d^3}z - \frac{\mu}{r^3}z \tag{2.28}$$

where the magnitudes of $\bar{d}$ and $\bar{r}$ are evaluated as,

$$d = \sqrt{(x+\mu)^2 + y^2 + z^2} \tag{2.29}$$

$$r = \sqrt{(x-1+\mu)^2 + y^2 + z^2} \tag{2.30}$$

These differential equations govern the motion of P_3 under the gravitational influence of the primary bodies; the result is viewed by a rotating observer. All simulations in the CR3BP result from the numerical integration of these nondimensional equations of motion.

2.2.4 Integral of Motion

The differential equations of motion in equations (2.26)-(2.28) can be further simplified by defining a pseudo-potential function. The scalar pseudo-potential U^* is defined as,

$$U^* = \frac{1-\mu}{d} + \frac{\mu}{r} + \frac{1}{2}n^{*2}(x^2+y^2) \tag{2.31}$$

The differential equations of motion in equations (2.26)-(2.28) is rewritten in terms of the pseudo-potential function and appear in the following form,

$$\ddot{x} - 2n^*\dot{y} = \frac{\partial U^*}{\partial x} \tag{2.32}$$

$$\ddot{y} + 2n^*\dot{x} = \frac{\partial U^*}{\partial y} \tag{2.33}$$

$$\ddot{z} = \frac{\partial U^*}{\partial z} \tag{2.34}$$

These equations and equations (2.26)-(2.28) are equivalent.

The form of the equations in (2.32)-(2.34) does admit an integral. It is possible to produce the integral of the motion in the CR3BP by operating on equations (2.32)-(2.34). Using a dot product between the differential equations and the rotating velocity vector, $\dot{\bar{\rho}} = \dot{x}\hat{x} + \dot{y}\hat{y} + \dot{z}\hat{z}$, the resulting scalar equations are summed to yield,

$$\dot{x}\ddot{x} + \dot{y}\ddot{y} + \dot{z}\ddot{z} = \frac{dU^*}{d\tau} \tag{2.35}$$

The scalar relationship in equation (2.35) is directly integrated over nondimensional time, τ, to produce the well known Jacobian integral, or Jacobi constant, C,

$$\frac{1}{2}\left(\dot{x}^2 + \dot{y}^2 + \dot{z}^2\right) = U^* - \frac{C}{2} \tag{2.36}$$

The constant of integration is defined as $-\frac{C}{2}$ for convenience such that the integral of motion can be more easily expressed in the form,

$$V^2 = 2U^* - C \tag{2.37}$$

where the speed relative to the rotating frame is denoted V. Thus, one integral of motion exists, but one constant is not sufficient for a closed-form solution. However, the lack of an analytical solution does not prevent a numerical analysis.

2.2.5 Equilibrium Solutions

For a coupled, nonlinear set of differential equations, the behavior of the system is typically first investigated via equilibrium solutions. Equilibrium solutions are sought by examination of the system equations when the first and second derivatives are equal to zero. In equations (2.32)-(2.34), if $\dot{\bar{\rho}}$ and $\ddot{\bar{\rho}}$ are zero, it is implied that the velocity and acceleration relative to the rotating frame are zero. Thus, if P_3 possesses no initial velocity or acceleration with respect to the rotating frame, P_3 theoretically maintains the given position indefinitely, relative to the rotating frame. Thus, from equations (2.32)-(2.34) these equilibrium locations, denoted Lagrange points or libration points, are determined by evaluating the gradient of the pseudo-potential function when the value is equal to zero,

$$\frac{\partial U^*}{\partial x} = \frac{\partial U^*}{\partial y} = \frac{\partial U^*}{\partial z} = 0 \tag{2.38}$$

where U^* is the pseudo-potential function from equation (2.31).

The locations of these five equilibrium points, as viewed in the rotating frame, are indicated in Figure 2.4. They are denoted by the symbol L_i, $i = 1, ..., 5$. By convention, the equilibrium point to the left of the smaller primary is labeled L_1; L_2 is located to the right of the smaller primary, and L_3 is the furthest point on the x-axis on the far side of the larger primary. The equilateral point with a positive y-component is labeled L_4; the final libration point with a negative y-component is L_5. All five

equilibrium points are located in the plane of motion of the primaries, that is, $z = 0$. Three of the five, the collinear points, lie along the x-axis, and the remaining two, the equilateral points, form equilateral triangles with the primaries. The distances γ_1, γ_2, γ_3 locate the equilibrium points relative to the primaries. Effectively, at these equilibrium locations, the gravitational and centrifugal forces in the system cancel.

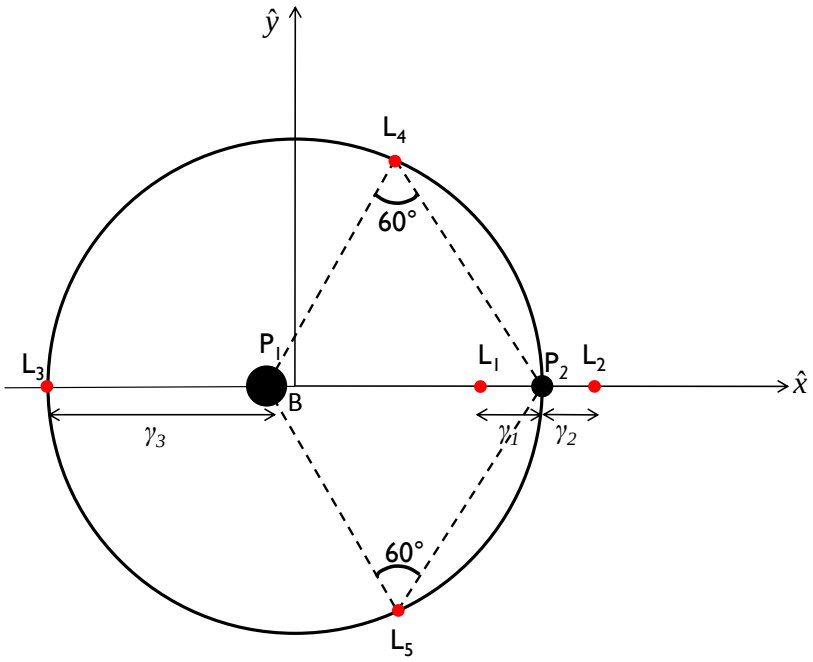

Figure 2.4. Relative Location of the Lagrange Points, L_i, in the CR3BP

The locations of the collinear points are computed from equation (2.31) by expanding the partial expression $\frac{\partial U^*}{\partial x} = 0$ and solving for the three distinct x-axis crossings that correspond to the locations of L_1, L_2, and L_3. The specific values for γ_1, γ_2, and γ_3 are determined from fifth-order polynomials, which are derived by substituting the (x,y,z) coordinates of L_1, L_2, and L_3 [39]. The locations of the equilateral points L_4 and L_5 are computed with a similar approach, that is, $\frac{\partial U^*}{\partial x} = \frac{\partial U^*}{\partial y} = 0$. The terms in this expression is algebraically manipulated to solve for d and r, leading to unit values in both cases. Hence, with $r = 1$ and $d = 1$ and the distance between the primaries normalized to one, that is, $d_1 + d_2 = 1$, it is straightforward to deduce that

L_4 and L_5 are located at the vertices of two equilateral triangles with the primaries. The distance from the equilibrium point to one of the primaries is the same as the distance between the two primaries. Thus, the angle between the line connecting the point to the primary and the line connecting the two primaries is equal to 60 degrees. Given this geometry, it is apparent that the coordinates corresponding to the equilateral points are $x = \frac{1}{2} - \mu$, $y = \pm\frac{\sqrt{3}}{2}$ and $z = 0$.

2.2.6 Zero Velocity Surfaces and Curves

The new equilibrium solutions and the existence of the Jacobi constant lead to two more important concepts: zero relative velocity and the zero velocity surfaces. Reconsider the Jacobian integral, equation (2.37). If the relative velocity V is zero and the full expression for the pseudo-potential function U^* from equation (2.31) is inserted, then the relationship appears in the following form,

$$x^2 + y^2 + \frac{2}{d}(1-\mu) + \frac{2}{r}\mu = C \tag{2.39}$$

Recall that C is always positive since x^2 and y^2 are always positive and $\frac{2(1-\mu)}{d} > 0$, $\frac{2\mu}{r} > 0$ as well because d and r are distances and $0 < \mu < 1$. For reference, the values of the Jacobi constant at each libration point in the Earth-Moon system are summarized in Table 2.1 and labeled C_{L_1}, C_{L_2}, C_{L_3}, C_{L_4}, and C_{L_5}.

Table 2.1 Jacobi Constant Values Corresponding to the Lagrange Points in the Earth-Moon System

C_{L_1}	C_{L_2}	C_{L_3}	C_{L_4}	C_{L_5}
3.188340	3.172160	3.012147	2.987997	2.987997

For a given value of C, an infinite number of x, y, and z combinations satisfy equation (2.39). Together, the solutions define a surface in three-dimensional space. Hence, equation (2.39) represents the equation for a surface of zero velocity. A contour of the surface in a given plane yields a curve, and is typically labeled a zero

velocity curve. These zero velocity curves were first applied by Hill to a special case of the restricted three body problem, known as the Hill's problem [46]. For a given value of μ, the surface and, thus, the contour, will change by varying the value of C. These zero velocity surfaces delineate two types of regions: a region where motion is physically possible and a "forbidden" region, or region of exclusion, where motion is physically impossible. The expression for Jacobi constant in equation (2.37) suggests possible restrictions on the allowed positions of P_3. When $C > 2U^*$, the velocity, V, is imaginary. The position states, x, y, and z, are therefore constrained such that $2U^* \geq C$, and the regions where V is imaginary are accordingly denoted "forbidden". Without a maneuver that alters the velocity state and, thus, the value of Jacobi constant, the zero velocity surfaces constrain the motion throughout any time evolution.

2.3 The State Transition Matrix

In the circular restricted three-body problem, one specific objective is the exploration of different types of solutions to the nonlinear differential equations as well as the dynamical behavior in the vicinity of these solutions. Periodic orbits in the vicinity of the libration points represent one specific type of solution that is a particular focus in this analysis. To compute periodic orbits, the equations are typically linearized relative to a reference solution and a variable sensitivity matrix $\Phi(\tau, \tau_0)$ is required to determine many of the periodic orbits of interest. The sensitivity matrix is, in fact, very useful beyond just periodic orbits, e.g., in targeting and stability analysis as well. This matrix $\Phi(\tau, \tau_0)$, denoted the State Transition Matrix (STM), is associated with the variational equations relative to any general reference arc that satisfies the nonlinear differential equations in the CR3BP.

To produce a trajectory with a set of desired characteristics, the initial propagation of a baseline arc is essential. The diagram in Figure 2.5 illustrates a reference trajectory arc, $\bar{x}(\tau) = [\bar{r}(\tau), \bar{v}(\tau)]$, as well as a perturbed path relative to the refer-

ence, $\bar{x}_d(\tau) = [\bar{r}_d(\tau), \bar{v}_d(\tau)] = \bar{x}(\tau) + \delta\bar{x}(\tau)$. The six-dimensional state vectors $\bar{x}_d(\tau)$ and $\bar{x}(\tau)$ are comprised of position and velocity states. The vectors $\bar{r}(\tau_i), \bar{v}(\tau_i)$ represent the three-dimensional position and velocity states at time τ_i along the reference trajectory. The vector $\bar{r}_d(\tau_i)$ denotes the position state along the perturbed path. This state, i.e., $\bar{r}_d(\tau_i)$, might represent some desired position; the initial state on the reference can be modified to deliver the vehicle to $\bar{r}_d$. At any time τ_i, $\delta\bar{x}(\tau_i)$ is the six-element variational vector representing the perturbed state relative to the reference.

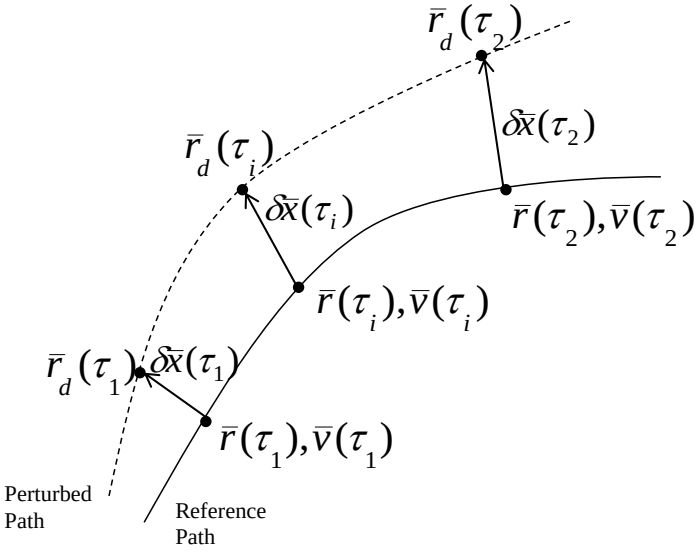

Figure 2.5. Perturbed Path Relative to the Reference Trajectory Arc

To develop the set of variational equations, begin with the state space representation of the nonlinear equations of motion in the CR3BP. The first-order form of the nonlinear system of differential equations is generally represented as,

$$\dot{\bar{x}} = \bar{f}(\bar{x}, \tau) \tag{2.40}$$

The desired solution nearby the reference, i.e., $\bar{x}_d(\tau)$, can be represented in terms of a Taylor series expansion relative to the reference. By retaining only the linear terms, the first-order variations relative to the reference are defined. This expansion results

in a linear equation expressed in terms of the variations in the state, $\delta\bar{x}(\tau)$, of the form,

$$\delta\dot{\bar{x}}(\tau) = A(\tau)\delta\bar{x}(\tau) \tag{2.41}$$

where $A(\tau)$ is the Jacobian matrix and $\delta\bar{x}(\tau) = [\delta x \quad \delta y \quad \delta z \quad \delta\dot{x} \quad \delta\dot{y} \quad \delta\dot{z}]^T$. Equation (2.41) can be expanded in matrix form as,

$$\begin{bmatrix} \delta\dot{x} \\ \delta\dot{y} \\ \delta\dot{z} \\ \delta\ddot{x} \\ \delta\ddot{y} \\ \delta\ddot{z} \end{bmatrix} = \begin{bmatrix} 0 & 0 & 0 & 1 & 0 & 0 \\ 0 & 0 & 0 & 0 & 1 & 0 \\ 0 & 0 & 0 & 0 & 0 & 1 \\ U^*_{xx} & U^*_{xy} & U^*_{xz} & 0 & 2 & 0 \\ U^*_{yx} & U^*_{yy} & U^*_{yz} & -2 & 0 & 0 \\ U^*_{zx} & U^*_{zy} & U^*_{zz} & 0 & 0 & 0 \end{bmatrix} \begin{bmatrix} \delta x \\ \delta y \\ \delta z \\ \delta\dot{x} \\ \delta\dot{y} \\ \delta\dot{z} \end{bmatrix} \tag{2.42}$$

The lower left block of the Jacobian matrix involves the second partial derivatives of the pseudo-potential function, U^*, from equation (2.31). The partials are evaluated individually as,

$$U^*_{xx} = \frac{\partial^2 U^*}{\partial x^2} = 1 - \frac{(1-\mu)}{d^3} + \frac{3(1-\mu)(x+\mu)^2}{d^5} - \frac{\mu}{r^3} + \frac{3\mu(x-1+\mu)^2}{r^5} \tag{2.43}$$

$$U^*_{yy} = \frac{\partial^2 U^*}{\partial y^2} = 1 - \frac{(1-\mu)}{d^3} + \frac{3(1-\mu)y^2}{d^5} - \frac{\mu}{r^3} + \frac{3\mu y^2}{r^5} \tag{2.44}$$

$$U^*_{zz} = \frac{\partial^2 U^*}{\partial z^2} = -\frac{(1-\mu)}{d^3} + \frac{3(1-\mu)z^2}{d^5} - \frac{\mu}{r^3} + \frac{3\mu z^2}{r^5} \tag{2.45}$$

$$U^*_{xy} = \frac{\partial^2 U^*}{\partial x \partial y} = U^*_{yx} = \frac{3(1-\mu)(x+\mu)y}{d^5} + \frac{3\mu(x-1+\mu)y}{r^5} \tag{2.46}$$

$$U^*_{xz} = \frac{\partial^2 U^*}{\partial x \partial z} = U^*_{zx} = \frac{3(1-\mu)(x+\mu)z}{d^5} + \frac{3\mu(x-1+\mu)z}{r^5} \tag{2.47}$$

$$U^*_{yz} = \frac{\partial^2 U^*}{\partial y \partial z} = U^*_{zy} = \frac{3(1-\mu)zy}{d^5} + \frac{3\mu zy}{r^5} \tag{2.48}$$

where d and r are defined in equations (2.29)-(2.30). So, the general solution to equation (2.41) is of the form,

$$\delta\bar{x}(\tau) = \Phi(\tau, \tau_0)\delta\bar{x}_0 \tag{2.49}$$

where $\Phi(\tau, \tau_0)$ is the STM and $\delta\bar{x}_0$ is the six-element initial deviation from a given initial state $\bar{x}_0$ that is associated with the reference. Neither the matrix $A(\tau)$ nor $\Phi(\tau, \tau_0)$ is constant, in general, although $A(\tau)$ is constant for variations relative to a constant reference solution such as the equilibrium points. The evolution of the matrix $\Phi(\tau, \tau_0)$ is governed by the matrix differential equation,

$$\dot{\Phi}(\tau, \tau_0) = A(\tau)\Phi(\tau, \tau_0) \tag{2.50}$$

which represents 36 scalar differential equations since $\Phi(\tau, \tau_0)$ is a 6×6 matrix. Including the integration of the six scalar differential equations for the state vector $\bar{x}$, simulation in the CR3BP involves the numerical integration of a total of 42 differential equations. At the initial time, the matrix $\Phi(\tau, \tau_0)$ is equal to the 6×6 identity matrix.

The elements of the STM contain valuable information about the sensitivities of the final state to variations in the initial state. That is, the partial derivatives in the STM reflect the change in a final scalar state element due to a change in the corresponding initial state element, that is,

$$\begin{bmatrix} \delta x_f \\ \delta y_f \\ \delta z_f \\ \delta \dot{x}_f \\ \delta \dot{y}_f \\ \delta \dot{z}_f \end{bmatrix} = \begin{bmatrix} \frac{\partial x}{\partial x_0} & \frac{\partial x}{\partial y_0} & \frac{\partial x}{\partial z_0} & \frac{\partial x}{\partial \dot{x}_0} & \frac{\partial x}{\partial \dot{y}_0} & \frac{\partial x}{\partial \dot{z}_0} \\ \frac{\partial y}{\partial x_0} & \frac{\partial y}{\partial y_0} & \frac{\partial y}{\partial z_0} & \frac{\partial y}{\partial \dot{x}_0} & \frac{\partial y}{\partial \dot{y}_0} & \frac{\partial y}{\partial \dot{z}_0} \\ \frac{\partial z}{\partial x_0} & \frac{\partial z}{\partial y_0} & \frac{\partial z}{\partial z_0} & \frac{\partial z}{\partial \dot{x}_0} & \frac{\partial z}{\partial \dot{y}_0} & \frac{\partial z}{\partial \dot{z}_0} \\ \frac{\partial \dot{x}}{\partial x_0} & \frac{\partial \dot{x}}{\partial y_0} & \frac{\partial \dot{x}}{\partial z_0} & \frac{\partial \dot{x}}{\partial \dot{x}_0} & \frac{\partial \dot{x}}{\partial \dot{y}_0} & \frac{\partial \dot{x}}{\partial \dot{z}_0} \\ \frac{\partial \dot{y}}{\partial x_0} & \frac{\partial \dot{y}}{\partial y_0} & \frac{\partial \dot{y}}{\partial z_0} & \frac{\partial \dot{y}}{\partial \dot{x}_0} & \frac{\partial \dot{y}}{\partial \dot{y}_0} & \frac{\partial \dot{y}}{\partial \dot{z}_0} \\ \frac{\partial \dot{z}}{\partial x_0} & \frac{\partial \dot{z}}{\partial y_0} & \frac{\partial \dot{z}}{\partial z_0} & \frac{\partial \dot{x}}{\partial \dot{x}_0} & \frac{\partial \dot{z}}{\partial \dot{y}_0} & \frac{\partial \dot{z}}{\partial \dot{z}_0} \end{bmatrix} \begin{bmatrix} \delta x_0 \\ \delta y_0 \\ \delta z_0 \\ \delta \dot{x}_0 \\ \delta \dot{y}_0 \\ \delta \dot{z}_0 \end{bmatrix} \tag{2.51}$$

This matrix is an effective linear predictor of the sensitivity of the final state to variations in the initial state, or in the state vector at an earlier time. The use of the STM is fundamental in any targeting scheme, including the design of transfer trajectories, the computation of periodic orbits, and any assessment of stability.

2.4 Differential Corrections Schemes

The existence of periodic motion in the CR3BP is well-known, and identifying periodic orbits in the vicinity of the libration points is extremely useful, offering valuable insight concerning the behavior in these regions. The computation of this periodic motion in the nonlinear system involves the use of a multi-dimensional version of a Newton-Raphson differential corrections process or "shooting method". In this investigation, single and multiple shooting algorithms are implemented to generate periodic orbits and solve a variety of other types of trajectory design problems as well. The formulation and implementation of such differential corrections algorithms are initially detailed in this section.

2.4.1 General Variable-Time Single Shooting Method

With the availability of the appropriate mathematical model, that is, the equations of motion and the differential equations governing the state transition matrix, numerical simulation from a given initial state to any future time is straightforward to accomplish. The STM associated with any arbitrary trajectory arc aids in the prediction of the appropriate adjustments in the initial state to shift the final state to a desired set of values at the end point. Since the differential equations are nonlinear and a solution for $\delta\bar{x}(\tau_i)$ is based upon a linear expansion, the variation $\delta\bar{x}(\tau_i)$ is an approximation. Generally, the closer the perturbed state to the reference, the more accurate the approximation. If the variations are sufficiently small, the approximation can be employed, with the aid of the appropriate differential corrections process, to adjust the initial state such that the path evolves and reaches some desired state downstream.

A basic and simple differential corrections procedure is a simple or single shooting algorithm. It is termed "single shooting" because only a single numerically integrated trajectory arc is involved. Many single shooting problems can be formulated, but a common, straightforward example in the CR3BP, one that clearly illustrates the

single shooting method, is the computation of a periodic orbit symmetric across the xz-plane. To be periodic, an orbit must repeat for greater than one period. Frequently, periodic orbits possess a plane of symmetry. Assuming that the derivative is continuous and there are no singularities, the trajectory intersects the symmetry plane perpendicularly. Thus, symmetry properties are exploited in the corrections scheme, that is, only half of the orbit is investigated and the integration is generally initiated using a point in the plane of symmetry. In the CR3BP, the xz-plane is a plane of symmetry. Thus, to construct a periodic orbit that is symmetric across the xz-plane, the initial conditions are defined in terms of a state vector of the form $\bar{x}_0 = [x_0 \;\; 0 \;\; z_0 \;\; 0 \;\; \dot{y}_0 \;\; 0]^T$. At the desired final endpoint, the state vector is written in the same form, that is, $\bar{x}_f = [x_f \;\; 0 \;\; z_f \;\; 0 \;\; \dot{y}_f \;\; 0]^T$. Thus, only six quantities are necessary to completely define the problem, i.e., $x_0,\ z_0,\ \dot{y}_0,\ x_f,\ z_f,\ \dot{y}_f$, plus τ_f, the time when the path re-crosses the plane perpendicularly, equal to one half of the orbit period. The number of unknowns is further reduced to four, that is $x_0,\ z_0,\ \dot{y}_0$, and τ_f, by enforcing a stopping condition at the xz-plane crossing, i.e., $y_f = 0$. The final state, $\bar{x}_f$, is a function of the initial state and the time interval τ_f. The impact of a change in the initial conditions ($x_0,\ y_0,\ z_0,\ \dot{x}_0,\ \dot{y}_0,\ \dot{z}_0$) on the final states at τ_f is typically investigated via the linear variational equations, written in vector form as,

$$\delta\bar{x} = \Phi(\tau_f, 0)\delta\bar{x}_0 + \dot{\bar{x}}|_{\tau_f}\delta\tau_f \tag{2.52}$$

or expressed in matrix form as,

$$\begin{bmatrix} \delta x \\ \delta y \\ \delta z \\ \delta\dot{x} \\ \delta\dot{y} \\ \delta\dot{z} \end{bmatrix}_{\tau_f} = \begin{bmatrix} \phi_{11} & \phi_{12} & \phi_{13} & \phi_{14} & \phi_{15} & \phi_{16} \\ \phi_{21} & \phi_{22} & \phi_{23} & \phi_{24} & \phi_{25} & \phi_{26} \\ \phi_{31} & \phi_{32} & \phi_{33} & \phi_{34} & \phi_{35} & \phi_{36} \\ \phi_{41} & \phi_{42} & \phi_{43} & \phi_{44} & \phi_{45} & \phi_{46} \\ \phi_{51} & \phi_{52} & \phi_{53} & \phi_{54} & \phi_{55} & \phi_{56} \\ \phi_{61} & \phi_{62} & \phi_{63} & \phi_{64} & \phi_{65} & \phi_{66} \end{bmatrix}_{\tau_f} \begin{bmatrix} \delta x_0 \\ \delta y_0 \\ \delta z_0 \\ \delta\dot{x}_0 \\ \delta\dot{y}_0 \\ \delta\dot{z}_0 \end{bmatrix} + \begin{bmatrix} \dot{x} \\ \dot{y} \\ \dot{z} \\ \ddot{x} \\ \dot{y} \\ \dot{z} \end{bmatrix}_{\tau_f} (\delta\tau_f) \tag{2.53}$$

where the subscript τ_f indicates that the corresponding quantities are evaluated at the final time. The matrix equation (2.53) is reduced to simplify the problem. Recall

that the initial state is integrated until $y_f = 0$, i.e., the "stopping condition", and the corresponding time is defined as τ_f. The desired final value for y is specified as zero, so $\delta y_f = 0$. Since a perpendicular crossing of the xz-plane is enforced, the final desired values for $\dot{x}$ and $\dot{z}$ are zero, that is, $\dot{x}_f = \dot{z}_f = 0$, and consequently $\delta\dot{x}_f = \delta\dot{z}_f = 0$ after convergence. However, these values are not zero until the iterative process is complete and the algorithm converges to the desired final values (to within some acceptable tolerance). To achieve these desired values, the changes in $\dot{x}$ and $\dot{z}$ in equation (2.53) are specified such that $\delta\dot{x}_f = -\dot{x}_f$ and $\delta\dot{z}_f = -\dot{z}_f$, respectively. Equations for δy_f, $\delta\dot{x}_f$, and $\delta\dot{z}_f$ are then employed to solve for the unknown variables, that is, the changes in the initial states, δx_0, δz_0, and $\delta\dot{y}_0$ to target a perpendicular crossing; the goal of this iterative process is an improvement in the initial guess for the originating state by correcting the values for $x_0, z_0, \dot{y}_0$. Recall that the initial state possesses the form $[x_0\ 0\ z_0\ 0\ \dot{y}_0\ 0]^T$, thus, $\delta y_0 = \delta\dot{x}_0 = \delta\dot{z}_0 = 0$. Substituting these values into matrix equation (2.53) results in a set of three equations in the four unknowns $\delta x_0, \delta z_0, \delta\dot{y}_0, \delta\tau_f$. The option employed in this analysis to solve this system of equations involves reducing the number of unknowns to three by arbitrarily selecting one initial condition and constraining it to be fixed throughout the simulation. For example, since an infinite number of periodic solutions exist, select x_0 and fix the value throughout the integration, such that $\delta x_0 = 0$. The system of equations is reduced to three equations in three unknowns,

$$\begin{bmatrix} \delta y \\ \delta\dot{x} \\ \delta\dot{z} \end{bmatrix}_{\tau_f} = \begin{bmatrix} \phi_{23} & \phi_{25} & \dot{y}_f \\ \phi_{43} & \phi_{45} & \ddot{x}_f \\ \phi_{63} & \phi_{65} & \ddot{z}_f \end{bmatrix} \begin{bmatrix} \delta z_0 \\ \delta\dot{y}_0 \\ \delta\tau_f \end{bmatrix} \tag{2.54}$$

Thus, the matrix in equation (2.54) is square and is inverted to solve for $\delta z_0, \delta\dot{y}_0$, and $\delta\tau_f$. The system is then integrated with the updated initial conditions. Since this is a linear corrections process for a nonlinear problem, the algorithm is iterative. This procedure is repeated until the values for $\dot{x}$ and $\dot{z}$ are zero to within a specified tolerance. The problem is further reduced, to a 2x2 matrix inversion, by exploiting the information concerning the variation in the period, $\delta\tau_f$ [39]. After this iteration

process is complete, a perpendicular crossing is assumed and a periodic orbit in the CR3BP is determined. Independent of the option to compute either a periodic orbit or a trajectory arc with some desired end-state constraints, the basis for the targeting algorithm is the same: a multi-dimensional Newton-Raphson method that generally converges to a solution within three to four iterations.

2.4.2 General Variable-Time Multiple Shooting Method

In this analysis, the simple, yet robust, single shooting algorithm is exploited to generate periodic orbits that are symmetric across the xz-plane. However, many periodic solutions exist in the CR3BP that do not possess a plane of symmetry. Additionally, convergence issues may arise if the integration times along the arcs are too long. Consider a transfer path from low Earth orbit to the Moon as an illustrative example of a relatively long numerical propagation. As the variations are propagated, the linear approximation loses accuracy, so the sensitivities associated with the extended numerically integrated trajectory segments increase substantially. An alternative formulation is necessary to target these type of solutions.

In a multiple shooting algorithm, the trajectory is discretized into a series of "patch points" and multiple integrated segments are employed to satisfy the trajectory constraints. Consequently, the sensitivities associated with a longer numerical propagation are reduced by integrating over smaller segments. Another advantage of the multiple shooting scheme over the single shooter is the ability to apply path constraints at initial, final, and intermediate patch points, generally allowing more control over the entire trajectory. In this investigation, a multiple (or parallel) shooting scheme is exploited to produce asymmetric periodic orbits and continuous multi-body transfer trajectories with different itineraries and patterns. The general scheme appears in Figure 2.6 with the representation of an initial guess in Figure 2.6(a) and a converged solution in Figure 2.6(b). Note that the initial path, represented via a series of intermediate arcs, is discontinuous in position and velocity. The goal is to

employ the corrections algorithm to enforce continuity in all seven states, that is, position, velocity, and time.

Many different formulations exist to implement a multiple shooting process. In this investigation, a straightforward free variables and constraints implementation is selected [47, 48]. This approach employs a single vector update within each iteration and a single scalar criteria for convergence. It is not the only, nor even the best, implementation for all applications. But, the method is quite robust and performs well for all of the demonstrations and examples in this investigation. Consider a free variable vector $\bar{X}$ comprised of a n number of state vectors and $n-1$ integration times, i.e., $\bar{X} = [\bar{x}_1 \quad ... \quad \bar{x}_n \quad \tau_1 \quad ... \, \tau_{n-1}]^T$. To ensure that the trajectory possesses some desired characteristics, the free variable vector is subject to m scalar constraint equations satisfying $\bar{F}(\bar{X}) = [\bar{x}_2^\tau - \bar{x}_2 \quad .. \quad \bar{x}_n^\tau - \bar{x}_n]^T = \bar{0}$, where the vectors $\bar{x}_n^\tau$ are the final integrated states along each trajectory arc after any propagation step. To construct a smooth, continuous path, the discontinuities represented in $\bar{F}(\bar{X})$ must be removed.

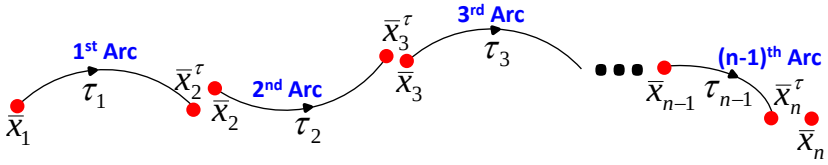

(a) Initial Guess

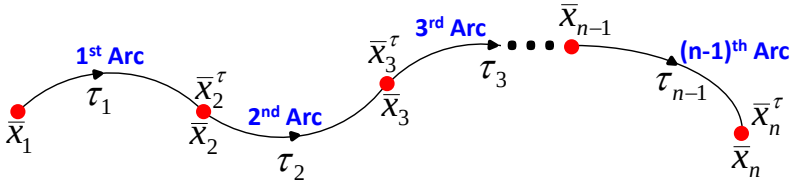

(b) Continuous Trajectory

Figure 2.6. Schematic of a Multiple Shooting Algorithm

In the resonance transition analysis, likely quantities to be constrained include position and velocity, although other quantities such as end-point constraints, e.g.,

distances or angles, can also be incorporated. Given this problem formulation, the goal is the numerical computation of a solution $\bar{X}^*$ that satisfies the constraint equations, that is, $\bar{F}(\bar{X}^*) = \bar{0}$, within a specified tolerance. Satisfying these vector constraints produces a natural trajectory that is continuous in position and velocity to some desired tolerance. Through this iterative process, the design vector $\bar{X}$ is updated using the Jacobian matrix, that is, $D\bar{F}(\bar{X})$, which requires partial derivatives relating the variations in the constraints to the changes in the free variables. For the general variable-time, multiple shooting algorithm, the Jacobian matrix is formed by,

$$D\bar{F}(\bar{X}) = \frac{\partial \bar{F}(\bar{X})}{\partial \bar{X}} = \begin{bmatrix} \frac{\partial \bar{x}_2^t}{\partial \bar{x}_1} & -\frac{\partial \bar{x}_2}{\partial \bar{x}_2} & & \frac{\partial \bar{x}_2^t}{\partial t_1} & & \\ & \ddots & \ddots & & \ddots & \\ & & \frac{\partial \bar{x}_n^t}{\partial \bar{x}_{n-1}} & -\frac{\partial \bar{x}_n}{\partial \bar{x}_n} & & \frac{\partial \bar{x}_n^t}{\partial t_{n-1}} \end{bmatrix} \tag{2.55}$$

which can be rewritten in terms of the elements of the various state transition matrices, identity matrices, and time derivatives, $\dot{\bar{x}}_i^t$, i.e,

$$D\bar{F}(\bar{X}) = \frac{\partial \bar{F}(\bar{X})}{\partial \bar{X}} = \begin{bmatrix} \Phi(t_2, t_1) & -I_{6\times 6} & & \dot{\bar{x}}_2^t & & \\ & \ddots & \ddots & & \ddots & \\ & & \Phi(t_n, t_{n-1}) & -I_{6\times 6} & & \dot{\bar{x}}_n^t \end{bmatrix} \tag{2.56}$$

Along each arc, the partials of the end states with respect to the initial states are, in fact, simply the elements of the state transition matrix. The time derivatives are evaluated at the final state along each integrated arc. If the number of free variables equals the number of constraints, a unique solution is obtained via a simple multivariable Newton's Method,

$$\bar{X}^{j+1} = \bar{X}^j - D\bar{F}(\bar{X}^j)^{-1}\bar{F}(\bar{X}^j) \tag{2.57}$$

where $\bar{X}^j$ and $\bar{X}^{j+1}$ represent the current and updated iterations of the design vector, respectively. If more free variables exist than constraints, infinitely many solutions exist. The selection of a single solution among all possible solutions requires the

specification of some selection criteria. In this analysis, a solution $\bar{X}^*$ is obtained by employing an iterative first-order minimum-norm update equation,

$$\bar{X}^{j+1} = \bar{X}^j - D\bar{F}(\bar{X}^j)^T[D\bar{F}(\bar{X}^j) \cdot D\bar{F}(\bar{X}^j)^T]^{-1}\bar{F}(\bar{X}^j) \tag{2.58}$$

A minimum-norm solution is selected because the difference between one iteration and the next is minimized to ensure that the converged solution remains close to the initial guess and, therefore, retains most of the characteristics of the initial guess. This implementation of a multiple shooting scheme represents a powerful and versatile design capability that can be applied to compute *any* periodic orbit as well as to design a wide variety of multi-body transfer trajectories.

Application: Targeting Asymmetric Planar and Three-Dimensional Periodic Orbits with Multiple Shooting

Basic differential corrections algorithms allow for the computation of a wide variety of periodic orbits and trajectories in the CR3BP. For instance, families of periodic planar Lyapunov as well as three-dimensional halo orbits are efficiently generated using a single shooting strategy and a continuation scheme. However, more complex periodic orbits, such as planar and three-dimensional asymmetric resonant and libration point orbits require the use of a more general corrections scheme that does not rely on periodicity or symmetry assumptions. A variety of corrections schemes are available to compute these trajectories, but a multiple shooting scheme with periodicity constraints is employed in this investigation. To illustrate the general method of free variables and constraints as employed in the computation of complex trajectories, consider a planar periodic orbit in the vicinity of L_4. Note that the general description of this algorithm applies to the computation of any 2D and 3D periodic orbit. Even though $z = \dot{z} = 0$ for the selected representative planar periodic orbit near L_4, the targeting algorithm is generalized to accept all six-dimensional states corresponding to 3D periodic orbits.

Initially, a linear guess for the initial states along the path seeds the multiple shooting algorithm to produce a period orbit in the nonlinear system. The analytical solution from the linear problem, near L_4 in this example, is then discretized into four segments – although any number of segments can be selected – equally spaced in time as indicated in the schematic in Figure 2.7,

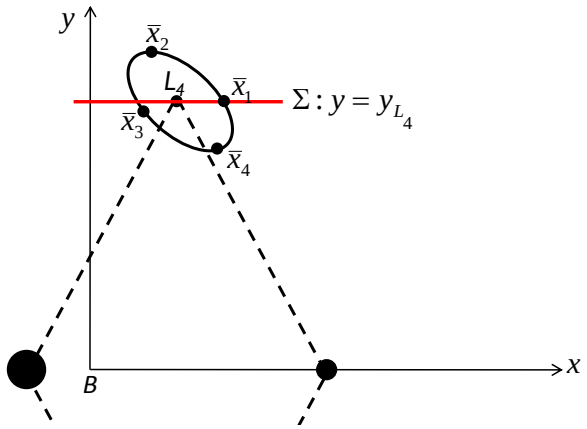

Figure 2.7. Schematic of a Linear Analytical Solution in the Vicinity of L_4

where $\bar{x}_1 = [x_1\ y_1\ z_1\ \dot{x}_1\ \dot{y}_1\ \dot{z}_1]^T$, $\bar{x}_2 = [x_2\ y_2\ z_2\ \dot{x}_2\ \dot{y}_2\ \dot{z}_2]^T$, $\bar{x}_3 = [x_3\ y_3\ z_3\ \dot{x}_3\ \dot{y}_3\ \dot{z}_3]^T$, and $\bar{x}_4 = [x_4\ y_4\ z_4\ \dot{x}_4\ \dot{y}_4\ \dot{z}_4]^T$ are directly computed from the linear approximation and the integration time between $\bar{x}_i$ and $\bar{x}_{i+1}$ is $\frac{T}{4}$. In general, the plane of symmetry serves as the 'stopping' criteria in the calculation of symmetric periodic orbits. Likewise, a geometric line, labeled Σ in Figure 2.7, facilitates the computation of asymmetric orbits. As illustrated in Figure 2.7, the 'hyperplane' Σ is selected such that it cuts through the entire family. In this example, the hyperplane is a line at $y = y_{L_4}$ and extends across all x values. The initial state, $\bar{x}_1$, must be selected to be on the hyperplane, i.e., the constraint $y - y_{L_4} = 0$ is enforced. Consequently, the selected initial conditions from the linear analysis must initially satisfy this constraint. Then, the free variable vector, $\bar{X}$, is defined by all the discrete state vectors and the period T,

$$\bar{X} = \begin{bmatrix} \bar{x}_1 \\ \bar{x}_2 \\ \bar{x}_3 \\ \bar{x}_4 \\ T \end{bmatrix} \tag{2.59}$$

resulting in a total of 25 free scalar variables. The constraint vector, $\bar{F}(\bar{X})$, is constructed based upon the requirement for continuity in position and velocity, periodicity constraints, and one additional constraint to ensure that the initial state corresponding to the periodic orbit is on the reference hyperplane, Σ,

$$\bar{F}(\bar{X}) = \begin{bmatrix} \bar{x}_2(\bar{x}_1, \frac{T}{4}) - \bar{x}_2 \\ \bar{x}_3(\bar{x}_2, \frac{T}{4}) - \bar{x}_3 \\ \bar{x}_4(\bar{x}_3, \frac{T}{4}) - \bar{x}_4 \\ x_4(\bar{x}_4, \frac{T}{4}) - x_1 \\ y_4(\bar{x}_4, \frac{T}{4}) - y_1 \\ z_4(\bar{x}_4, \frac{T}{4}) - z_1 \\ \dot{x}_4(\bar{x}_4, \frac{T}{4}) - \dot{x}_1 \\ \dot{z}_4(\bar{z}_4, \frac{T}{4}) - \dot{z}_1 \\ y_1 - y_{L_4} \end{bmatrix} = \bar{0} \tag{2.60}$$

where $\bar{x}_{i+1}(\bar{x}_i, \frac{T}{4})$ is the final integrated state vector along each segment, which is represented in Figure 2.6 using shortened notation as $\bar{x}_{i+1}^{\tau}$. Note that it is sufficient to enforce periodicity in only five states, that is, the integrated selected five states along the last segment must be equal to the initial selected five states along the first segment. Any five states can be selected to enforce periodicity. In this analysis, $\dot{y}$ is generally not included in the periodicity constraints, but any other state can be excluded. The period along the orbit, or the total integration time T, is a free variable and, thus, the integration time along each segment is equal to $\frac{T}{4}$, resulting in a total of 24 constraints. Because there are more variables than constraints, the problem can be solved iteratively using the minimum-norm update equation in equation (2.58). A

variety of periodic orbits in the vicinity of the equilateral points are calculated using this corrections scheme and illustrated in Chapter 3.

2.4.3 Trajectory Continuation Schemes

For many applications in astrodynamics, it is often desirable to identify a group or family of related periodic orbits rather than a single trajectory. A continuation method is employed to generate a family of orbits or solutions. Each member of a family possesses characteristics in common and can be distinguished through a particular problem parameter, P. In a family of orbits, then, 'continuation' is a technique used to compute multiple trajectories by determining each orbit using equation (2.54) and a corrections process [49]. In the simplest continuation process, each new member is initially seeded for computation by using the initial states from the previous successfully converged solution and a new value of the parameter. Once periodicity is achieved and the first orbit is computed, the value of the constraining parameter is modified and the process repeats to determine additional orbits in the family.

Single-Parameter Continuation

A commonly employed single-parameter continuation scheme involves stepping along a physical parameter such as Jacobi constant or one of the Cartesian coordinates that specify the initial position, such that $P = C$ or x_i. To compute a family of solutions, the continuation algorithm steps through increasing or decreasing values of the selected constraining parameter. For example, if the scalar x-component is selected as the stepping parameter and $\Delta x(\tau_0)$ is defined as a fixed step in the x-direction where $x(\tau_0)$ is the fixed quantity in the determination of each orbit, then, the initial guess for the initial state corresponding to the next orbit in the family is obtained by adding the fixed step $\Delta x(\tau_0)$ to the x-component of $\bar{x}_1(\tau_0)$, that is, $\bar{x}_2(\tau_0) = [x_1 + \Delta x(\tau_0) \;\; y_1 \;\; z_1 \;\; \dot{x}_1 \;\; \dot{y}_1 \;\; \dot{z}_1]$. The differential corrections process is applied to obtain the correct initial state for this second periodic orbit in the family, and the

process is continued to generate additional orbits in the family. Other commonly used constraining parameters in a physical, single-parameter continuation scheme include energy or time-of-flight.

Pseudo-Arclength Continuation

A special type of single-parameter continuation is the pseudo-arclength continuation method. This approach is based on the selection of a specific continuation parameter that may not be a physical quantity. Rather, the parameter is constructed to follow the evolution of the family of orbits that may not be a predetermined direction in configuration space. Implementing this continuation method involves stepping along the parameter values by fixing this parameter with an additional constraint [47, 50, 51]. In this analysis, a pseudo-arclength continuation strategy is straightforwardly incorporated into a multiple shooting algorithm with periodicity constraints to facilitate the computation of families of asymmetric periodic orbits in the restricted three-body problem.

Recall that, in a given application, $\bar{X}^*$ is defined as a vector of free variables that essentially represents a solution, or orbit, in a family. In this single-parameter continuation method, an initial guess for a new orbit in the family, $\bar{X}^0_{i+1}$, is calculated from a previously converged member in the family, $\bar{X}^*_i$. Both $\bar{X}^*_i$ and $\bar{X}^0_{i+1}$ represent free variable vectors and $\bar{X}^*_i$ satisfies the constraint vector $\bar{F}\left(\bar{X}^*_i\right) = \bar{0}$. Rather than stepping in a physical direction, in a pseudo-arclength continuation scheme a scalar step of size Δk is defined in a direction tangent to the family. Recall that there are generally more free variables than constraints in the computation of a 3D periodic orbit via a multiple shooting algorithm, since it is only necessary to enforce five periodicity constraints. However, with the addition of the pseudo-arclength constraint, the Jacobian matrix becomes a square matrix. As a consequence, a prediction for a nearby solution, $\bar{X}^0_{i+1}$, is generated and a unique solution, $\bar{X}^*_i$, for the next orbit exists from the update equation. The prediction exists in the nullspace of the Jaco-

bian matrix $D\bar{F}(\bar{X}_i^*)$; a unit vector tangent to the family at $\bar{X}_i^*$ is obtained from the null vector, $\Delta\bar{X}_i^*$, of the Jacobian matrix. Then, given a scalar step-size Δk, a linear prediction for a nearby solution is constructed as follows,

$$\bar{X}_{i+1}^0 = \bar{X}_i^* + \Delta k \cdot \Delta\bar{X}_i^* \tag{2.61}$$

An additional scalar constraint is added to the constraint vector, $\bar{F}(\bar{X})$, resulting in an augmented constraint vector, $\bar{G}(\bar{X}_{i+1})$, defined as,

$$\bar{G}(\bar{X}_{i+1}) = \begin{bmatrix} \bar{F}(\bar{X}_{i+1}) \\ (\bar{X}_{i+1}^0 - \bar{X}_i^*)^T \Delta\bar{X}_i^* - \Delta k \end{bmatrix} \tag{2.62}$$

Since the number of free variables is equal to the number of constraints and the updated Jacobian matrix is a square matrix, a solution is efficiently obtained using the update equation,

$$\bar{X}_{i+1}^{j+1} = \bar{X}_{i+1}^j - [D\bar{G}(\bar{X}_{i+1}^j)]^{-1}\bar{G}(\bar{X}_{i+1}^j) \tag{2.63}$$

The updated free-variable vector typically requires iteration to meet the constraints to an acceptable tolerance. The entire algorithm is then reapplied iteratively to further continue the family of solutions. In general, the pseudo-arclength continuation approach tends to be more robust than other single-parameter continuation methods as a unique family of solutions is guaranteed and no *a priori* knowledge regarding the evolution of the family is required.

2.5 Stability Analysis

For many astrodynamics applications, the stability of any periodic orbit is frequently critical in assessing its suitability. For instance, unstable orbits are sought in the design of transfer trajectories, whereas stable trajectories are frequently the focus in the design of long-term stable spacecraft orbits where little station-keeping is required to maintain the spacecraft near the reference path. In the CR3BP, the sta-

bility associated with a particular constant or periodic solution is determined through the examination of the state transition matrix.

2.5.1 Stability of the Constant Equilibrium Solutions

The stability of the five equilibrium points, i.e., constant solutions, are investigated by using the variational equations and the state transition matrix. The specific developments and definitions used in this section closely follow the discussion in *Theory of Orbits: The Restricted Problem of Three Bodies*, by Szebehely [46]. The nonlinear system of differential equations in equations (2.32)-(2.34) are linearized relative to the equilibrium solutions yielding a set of linear variational equations that are employed to assess the stability of the equilibrium points, and, thus, gain insight into the nature of the motion in the vicinity of the libration points. Stability can be discussed from many different perspectives. But, in a general sense, stability is always defined in terms of a reference solution. If a disturbance from the reference path yields behavior that remains in the small neighborhood of an equilibrium point, then the reference solution is considered stable. However, there are also other types of stability, such as Poisson stability, as well as Laplace or Hill stability. The stability criteria employed in this investigation to assess the equilibrium points is Lyapunov stability, and this approach is only valid if the reference solution is constant. For computation, Lyapunov stability is based on the characteristics of the eigenvalues determined from the characteristic equation associated with matrix A, which is indeed constant for the equilibrium points and is derived from the variational equations relative to L_i and appears in general form in equation (2.41). (In the case of periodic orbits, where the Jacobian matrix is not constant but periodic, the following Lyapunov analysis is not valid and further stability concepts must be introduced.)

The initial conditions near a reference solution, $\bar{x}_{eq}(\tau)$, is represented in terms of a variation $\delta\bar{x}$, that is, $\bar{x}(\tau) = \bar{x}_{eq}(\tau) + \delta\bar{x}(\tau)$. Recall that equation (2.41) represents the linearized system about some reference solution $\bar{x}_{eq}(\tau)$. If the reference solution

is a fixed point such as $\bar{x}_{eq}(\tau) = \bar{x}_{eq}$, that is, an equilibrium solution of the system, then the Jacobian matrix $A(\tau) = A$ is constant and the variational equation appears in the form,

$$\delta\dot{\bar{x}}(\tau) = A\delta\bar{x}(\tau) \tag{2.64}$$

In such a case, the general solution to equation (2.64) is,

$$\delta\bar{x}(\tau) = e^{A(t-t_0)}\delta\bar{x}(\tau_0) \tag{2.65}$$

which can also be expanded and written in the form,

$$\delta\bar{x}(\tau) = \sum_{j=1}^{n} c_j e^{\lambda_j(t-t_0)}\bar{v}_j \tag{2.66}$$

where the coefficients c_j are determined from the initial conditions, and λ_j and $\bar{v}_j$ represent the eigenvalues and eigenvectors associated with matrix A. The stability of the equilibrium points is determined from the characteristics of the eigenvalues λ_j that are computed from the constant matrix based on the following criteria:

- *Complex eigenvalues.* If *all* the eigenvalues possess negative real parts, then the equilibrium point is asymptotically stable. If some of the eigenvalues possess positive real parts, then the equilibrium point is unstable. This criteria is valid for multiple roots.

- *Pure imaginary eigenvalues.* If *all* the eigenvalues are imaginary, generally, the motion is oscillatory and the solution is defined as stable, but not asymptotically stable. However, if there are multiple roots, the solution contains mixed (periodic and secular) terms, and thus, is unstable.

- *Real eigenvalues.* If *any* of the eigenvalues are positive real integers, the reference solution is unstable. If the roots are all negative real integers, the solution is stable. This criteria holds for multiple roots.

The eigenvalues associated with the collinear points possess real and imaginary parts. At least one eigenvalue includes a positive real part and, thus, L_1, L_2, and L_3 are unstable. Yet, it is desirable to investigate the motion in the vicinity of these equilibrium points. With the appropriate selection of the initial conditions, the divergent motion can be suppressed in the linear system, resulting in an ellipse about the libration point with semi-major and semi-minor axes parallel to the y-axis and x-axis, respectively. Because of the instability, however, these ellipses are not periodic in the real system, and the motion will quickly diverge if propagated in the nonlinear EOMs. Nonetheless, a periodic solution in the nonlinear system is straightforwardly determined with a numerical corrections process.

2.5.2 Stability of Periodic Orbits

Unlike the equilibrium points, a periodic orbit is not a constant solution. Nevertheless, the stability of each planar, periodic orbit can be assessed by investigating the eigenvalues of the corresponding monodromy matrix. The monodromy matrix is defined as the state transition matrix evaluated after precisely one orbital revolution. The eigenvalues of the monodromy matrix are examined as the family evolves by calculating them for each periodic orbit in the family. The eigenvalues possess exactly the same value irregardless of the point along the orbit at which they are computed. As stated in Lyapunov's Theorem [52], the eigenvalues of the monodromy matrix are also known to appear in reciprocal pairs:

Theorem 2.5.2.1 (Lyapunov's Theorem) *If λ_j is an eigenvalue of the monodromy matrix $\Phi(\tau_0 + T, \tau_0)$ of a t-invariant system, then λ_j^{-1} is also an eigenvalue of $\Phi(\tau_0 + T, \tau_0)$, with the same structure of elementary divisors.*

In the CR3BP, the second-order system possesses three degrees of freedom and, thus, the monodromy matrix is defined in terms of six eigenvalues. For a periodic orbit to exist in the CR3BP, a minimum pair of eigenvalues must be equal to one because of the reciprocal nature of the eigenvalues. The monodromy matrix is a real matrix,

so its eigenvalues are real or, if complex, appear in complex conjugate pairs on the unit circle. To assess the stability of a periodic orbit, it is necessary to investigate the characteristics of these eigenvalues associated with the monodromy matrix with a focus on the non-unity eigenvalues. A periodic orbit is defined as:

- unstable if $|\lambda| > 1$, i.e., the magnitude of the eigenvector goes to infinity as time goes to infinity,
- stable if $|\lambda| < 1$, i.e., the magnitude of the eigenvector approaches zero as time goes to infinity.

If the magnitude of the eigenvector does not change, i.e., $|\lambda| = 1$, the eigenvalue corresponds to the center subspace [53]. When representing these eigenvalues, the unstable λ, λ_u, are located outside the unit circle; the stable λ, λ_s, are located within the unit circle, and the unity eigenvalues are on the unit circle. Representing the eigenvalues on the complex plane offers little insight concerning the natural behavior of the periodic orbit. Thus, the stability index is introduced as an alternative design parameter to better represent the stability characteristics associated with a given periodic orbit and leverage the fact that the eigenvalues occur in reciprocal pairs. The stability index, ν, is defined as,

$$\nu = \frac{1}{2}\left(\lambda + \frac{1}{\lambda}\right) \tag{2.67}$$

where λ is the eigenvalue of the monodromy matrix that possesses the largest modulus [13, 48, 54]. If the stability index is less than or equal to one, that is, $|\nu| \leq 1$, then, the periodic orbit is considered to be marginally stable, in which case the corresponding eigenvalues do not yield stable and unstable invariant manifolds. For application purposes, the periodic orbits possessing this type of stability index do not allow for transfers shadowing invariant manifolds to and from the orbit. Similarly, if $|\nu| \geq 1$, the periodic orbit includes an eigenvalue with magnitude greater than one, and its associated stable and unstable invariant manifolds can be computed [13, 55]. Moreover, the size of the stability index determines how fast the invariant manifolds approach

or depart the orbit, that is, the larger the size of ν, the faster the manifolds approach or depart the orbit. This information is useful in transfer design. Conversely, a small stability index reflects very slow departures and is related to low station-keeping requirements. Thus, this parameter offers valuable information concerning the periodic orbit of interest and is employed to determine transfer opportunities to and from the given orbit as well as other dynamic characteristics relevant to mission design.

2.6 Invariant Manifolds

The role of the invariant manifolds is also significant in building a framework to model the dynamical environment in the CR3BP and, thus, knowledge of any manifold structure improves the efficiency of the trajectory design process in this regime. The use of invariant manifolds in the design of transfer trajectories with specific patterns and itineraries for different values of the mass fraction, μ, is the main focus of this effort. Therefore, a general background concerning the phase space near periodic orbits in the CR3BP is key and a necessary component for the understanding of resonant orbits and their associated manifolds. In addition to this basic theoretical background in invariant manifold theory, a method for the numerical computation of the unstable and stable manifolds is also detailed.

2.6.1 Invariant Manifolds for Fixed Points

The geometrical theory of dynamical systems is based on the phase portrait associated with solutions to a nonlinear set of differential equations. Equilibrium points and periodic orbits are two types of solutions in the CR3BP that yield a very interesting structure in terms of the phase space. The geometry of the phase space is investigated by considering these particular solutions to nonlinear differential equations and the structure associated with the local flow. The following background information follows directly from the discussion in Parker and Chua [56], Guckenheimer

and Holmes [57], as well as Perko [58] on continuous and discrete time autonomous systems.

The phase portrait near the equilibrium points, L_i, is determined from the variational equations relative to L_i and the associated stability is determined from the characteristics of the eigenvalues λ_j that are computed from the constant matrix A. Recall that if the real part of the eigenvalue is negative for all λ_j, then sufficiently small perturbations tend to zero as time approaches infinity, and $\bar{x}_{eq}$ is defined as asymptotically stable. If the real part of the eigenvalue is positive for any λ_j, then a perturbation grows with time, and $\bar{x}_{eq}$ is denoted as unstable. If $\bar{x}_{eq}$ possesses eigenvalues λ_i and λ_j such that the associated real parts are both positive and negative, then $\bar{x}_{eq}$ is non-stable. A non-stable equilibrium point is a saddle point, which is consistent with an examination of the collinear points L_1, L_2, and L_3; a stable or unstable equilibrium point with no complex eigenvalues is labeled a node, and an equilibrium point is hyperbolic if all eigenvalues possess non-zero real parts. Let the Jacobian matrix for the system described by equation (2.64) possess n_s eigenvalues with positive real parts, n_u eigenvalues with negative real parts, and n_c eigenvalues with zero real parts. The eigenvectors associated with these eigenvalues are linearly independent, thus, they span $\Re^n$. The n-dimensional space $\Re^n$ is generally represented in terms of three fundamental subspaces: the stable subspace E^s, the unstable subspace E^u, and the center subspace E^c. These are the invariant subspaces associated with the linear variational equations in equation (2.64). Subscripts s, u, c reflect the dimension of each subspace such that $\text{rank}(A) = n_s + n_u + n_c$. A solution initially in a specific subspace remains in that subspace for all time, leading to the definitions of the local stable and unstable manifolds. Given the equilibrium solution, $\bar{x}_{eq}$, the Stable Manifold Theorem (Guckenheimer and Holmes [57]) states that if all eigenvalues, λ_j, associated with the constant Jacobian matrix possess non-zero real parts, then $\bar{x}_{eq}$ is a hyperbolic equilibrium point, and does not possess a center manifold. Local stable and unstable invariant manifolds, W^s_{loc} and W^u_{loc}, are related to the invariant subspaces E^s and E^u associated with the linear system. The term

"invariant" simply indicates that a point on the manifold will remain on the manifold as time progresses [57]:

Theorem 2.6.1.1 (Stable Manifold Theorem) *Suppose the nonlinear system of differential equations in first-order form* $\dot{\bar{x}}(\tau) = \bar{f}(\bar{x}(\tau))$ *possesses a hyperbolic equilibrium point* $\bar{x}_{eq}$*. Then there exist local stable and unstable manifolds* $W^s_{loc}(\bar{x}_{eq})$*,* $W^u_{loc}(\bar{x}_{eq})$*, of the same dimension* n_s*,* n_u*, as those of the eigenspaces* E^s*,* E^u*, of the linearized system in equation* (2.64)*, and tangent to* E^s *and* E^u *at* $\bar{x}_{eq}$*. These local stable and unstable manifolds,* $W^s_{loc}(\bar{x}_{eq})$*,* $W^u_{loc}(\bar{x}_{eq})$*, are as smooth as function* $\bar{f}$*.*

Let $\bar{x}_{eq}$ be the equilibrium point of a two-dimensional first-order system with eigenvalues λ_s and λ_u, as well as eigenvectors $\bar{v}_s$ and $\bar{v}_u$, that span the subspaces E^s and E^u. Hence, $\bar{v}_s$ and $\bar{v}_u$ form a basis in $\Re^2$. The diagram in Figure 2.8 illustrates the flow to and from $\bar{x}_{eq}$, which is governed by the corresponding eigenstructure, that is, the figure is a representation of a planar projection of the stable and unstable manifolds at $\bar{x}_{eq}$. For this particular example, the stable and unstable eigenvector subspaces are each comprised of one eigenvector, that is, $E_s = \bar{v}_s$, and $E_u = \bar{v}_u$. The local branch of the invariant manifold $W^{s^+}_{loc}$ is represented by $+\bar{v}_s$, and $W^{s^-}_{loc}$ corresponds to $-\bar{v}_s$. Similarly, $W^{u^+}_{loc}$ is defined by $\bar{v}_u$, and $W^{u^-}_{loc}$ corresponds to $-\bar{v}_u$. In other words, the local stable and unstable manifolds are parallel to the stable and unstable eigenvectors. The local invariant manifolds W^s_{loc} and W^u_{loc} possess nonlinear global analogs W^s and W^u that can be approximated by propagating the flow backwards in time along W^s_{loc} and forward in time along W^u_{loc}, respectively.

If $\bar{x}_{eq}$ is a non-hyperbolic equilibrium point, that is, n_s, n_u, and n_c are all non-zero, the structure of the local flow is governed by the Center Manifold Theorem for Flows, as stated by Guckenheimer and Holmes [57]:

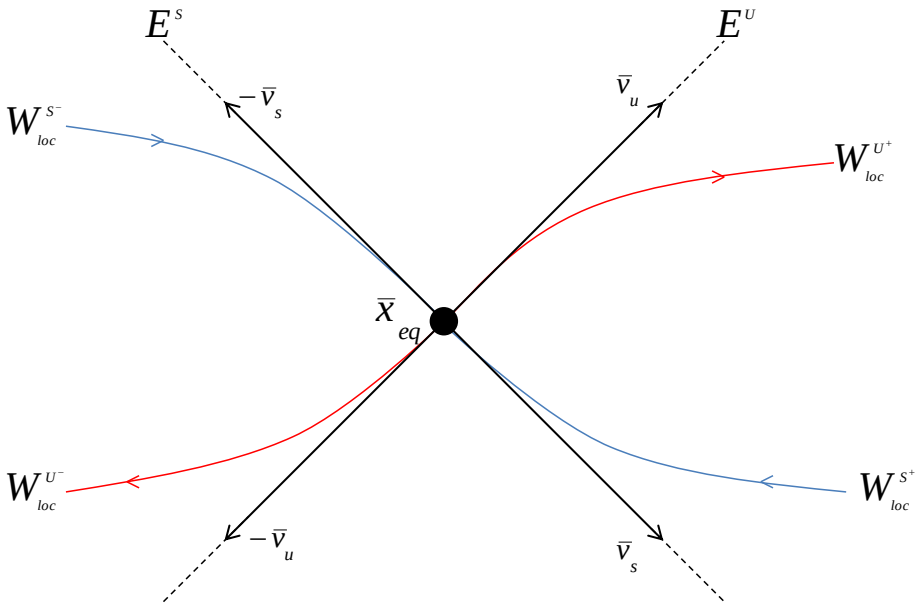

Figure 2.8. Representation of the Stable and Unstable Manifolds Associated with an Equilibrium Point

Theorem 2.6.1.2 (Center Manifold Theorem for Flows) *Let $\bar{f}$ be a vector field on $\Re^n$ vanishing at the origin $\bar{f}(\bar{x}_{eq}) = \bar{0}$ and $A = D\bar{f}(\bar{x}_{eq})$. The spectrum of* A *is divided into three parts n_s,n_c, and n_u with*

$$Re[\lambda] < 0; \lambda \in n_s \tag{2.68}$$

$$Re[\lambda] = 0; \lambda \in n_c \tag{2.69}$$

$$Re[\lambda] > 0; \lambda \in n_u \tag{2.70}$$

Let the generalized eigenspaces be E^s, E^c, and E^u, respectively. Then, there exist stable and unstable invariant manifolds W^u and W^s tangent to the E^u and E^s at $\bar{x}_{eq}$, and a center manifold at W^c tangent to the center subspace E^c at $\bar{x}_{eq}$. The manifolds W^u, W^s, and W^c are all invariant for the flow $\bar{f}$. The stable and unstable manifolds are unique, but W^c need not be.

The existence of a center manifold implies that the structure of the flow near the equilibrium point, possessing at least one zero eigenvalue, is more diverse than an

equilibrium point with no center subspace. The solutions initially in the center manifold neither grow nor decay over time, relative to $\bar{x}_{eq}$. Periodic orbits such as Lyapunov orbits as well as quasi-periodic trajectories, for example, near-vertical, out-of-plane orbits, are examples of types of motion that might exist in the center subspace near the equilibrium point, $\bar{x}_{eq}$.

Manifold structures have been studied by many researchers, and their application to trajectory design in multi-body regimes has been demonstrated. In fact, transfers between different three-body systems are a new focus for potential mission scenarios [59], in which the exploitation of the invariant manifolds associated with these orbits plays a crucial role.

2.6.2 Invariant Manifolds for Periodic Orbits

Calculating stable and unstable manifolds associated with periodic orbits is more complex than the underlying structure for equilibrium points. Although a periodic orbit is a solution of the nonlinear differential equations, the associated variational equation in equation (2.41) yields a Jacobian matrix that is not constant. However, it is possible to discretize the continuous time system to form a map. Various types of maps are useful, but Poincaré maps are most applicable for interpretation of the phase space in this problem. Poincaré maps reduce the dimensionality of the problem and are a valuable tool in the study of a periodic orbit and the natural flow in its vicinity. The concept for the construction of a Poincaré map is illustrated in Figure 2.9. To construct this map, a surface Σ that is transverse to the flow, is defined at a particular point along the flow. In Figure 2.9, a periodic orbit, defined in terms of the state $\bar{x}$ and labeled Γ, is initiated in the plane Σ and returns to intersect the plane after exactly one period. Note that the hyperplane Σ may be higher-dimensional and is not necessarily defined in physical space. Nevertheless, a truly periodic orbit returns to exactly the same point on the plane after each revolution. Such a point is denoted a 'fixed point', labeled in the map as $\bar{x}^*$. Then, for any point $\bar{x} \in \Sigma$ sufficiently close

to the fixed point, $\bar{x}^*$, a propagation of the nonlinear differential equations through $\bar{x}$, intersects the plane Σ again at the first return point $P(\bar{x})$, generally near the original fixed point.

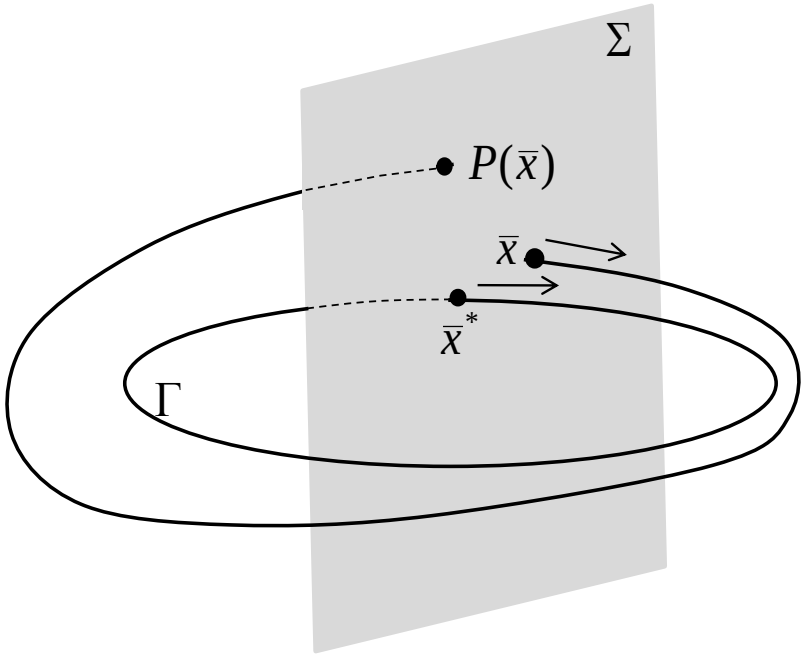

Figure 2.9. The Poincaré Map

Because Poincaré maps preserve most of the properties of periodic and quasi-periodic trajectories from the original system, they are also used as a powerful tool for stability analysis od periodic and quasi-periodic orbits. The stability of a periodic orbit from the original system is closely related to the stability of the fixed point of the associated Poincaré map. Thus, Poincaré maps offer evidence of stability and manifold representations. Consider an initial state, close to the fixed point, propagated to subsequent crossings of the plane. The orbit is defined as unstable if subsequent returns to the map diverge from the original fixed point and the orbit is considered stable if the recurring crossings of the map approach the original point. If there is no detectable pattern, then the orbit is labeled chaotic. The fixed points along a periodic orbit are used to compute the corresponding stable and unstable

manifolds. Each of the fixed points is an (*n-1*)-dimensional representation of the periodic orbit in $\Re^n$. Therefore, the stable, unstable, and center subspaces possess the dimensions of n_s, n_u, and n_c. The dimension of the unstable and stable manifolds of a periodic orbit is stated in the Stable Manifold Theorem for Periodic Orbits [58]:

Theorem 2.6.2.1 (Stable Manifold Theorem for Periodic Orbits) *Let an open subset of* $\Re^n$ *contain a periodic orbit* $\Gamma : \bar{x} = \gamma(\tau)$ *of period T. Let* ϕ_t *be the flow and* $\gamma(\tau) = \phi_\tau(\bar{x}^*)$. *If k characteristic exponents of* $\gamma(\tau)$ *have a negative real part where* $0 \leq K \leq n-1$ *and* $n-K-1$ *of them have a positive real part, then there is a* $\delta > 0$ *such that the stable manifold of* Γ,

$$S(\Gamma) = \bar{x} \in N_\delta(\Gamma) | d(\phi_\tau(\bar{x}), \Gamma) \to 0 \text{ as } \tau \to \infty \text{ and } \phi_\tau(\bar{x}) \in N_\delta(\Gamma) \text{ for all } \tau \geq 0$$

is a (K+1)-dimensional, differentiable manifold which is positively invariant under the flow ϕ_τ, *and the unstable manifold* Γ,

$$U(\Gamma) = \bar{x} \in N_\delta(\Gamma) | d(\phi_\tau(\bar{x}), \Gamma) \to 0 \text{ as } \tau \to -\infty \text{ and } \phi_\tau(\bar{x}) \in N_\delta(\Gamma) \text{ for all } \tau \leq 0$$

is an (n-K)-dimensional, differentiable manifold which is negatively invariant under the flow ϕ_τ. *Furthermore, the stable and unstable manifolds of* Γ *intersect transversally in* Γ.

The stable manifold associated with the periodic orbit Γ, that is, $W^s(\Gamma)$, possesses a dimension $n_s + 1$, and the unstable manifold associated with the periodic orbit, i.e., $W^u(\Gamma)$, has dimension $n_u + 1$. Hence, the dimensions of $W^s(\Gamma)$ and $W^u(\Gamma)$ are always one degree higher than E^s and E^u, respectively. Recall the monodromy matrix, first introduced in connection with orbital stability, and Lyapunov's Theorem 2.5.2.1. For stable and unstable manifolds of a periodic orbit to exist, the monodromy matrix must possess at least one stable and one unstable eigenvalue. However, not all the members in a given family of periodic orbits in the CR3BP possess a stable and unstable eigenvalue. Therefore, it is convenient to develop a method to identify which members in the family do possess stable and unstable eigenvalues, and thus, stable and unstable manifolds. The stability index, ν, defined in equation (2.67),

is associated with each member in a family of periodic orbits and provides useful information regarding the existence of stable and unstable manifolds.

2.6.3 Numerical Computation of Invariant Manifolds

The invariant manifolds corresponding to a periodic orbit can be calculated using the eigenvector corresponding to an eigenvalue of magnitude greater than one in the direction of the local unstable manifold, and the eigenvector corresponding to an eigenvalue less than one in the direction of the local stable manifold. That is, $W_{loc}^{u^+}$ departs the fixed point along the positive direction of $\bar{v}_u$, and $W_{loc}^{u^-}$ departs $\bar{x}^*$ along the negative direction consistent with $\bar{v}_u$. Similarly, $W_{loc}^{s^+}$ approaches the fixed point on the periodic orbit along $+\bar{v}_s$, and $W_{loc}^{s^-}$ approaches the fixed point from the direction of $-\bar{v}_s$.

The computation of the invariant manifolds requires the propagation of an initial state close to the fixed point in the direction of the desired eigenvector. The algorithm to compute these trajectories is defined as follows: $\bar{x}_{u^+}$ is defined as a point on the local unstable manifold and along the positive direction, $W_{loc}^{u^+}$. Then, integrating forward and backward from point $\bar{x}_{u^+}$ yields W^{u^+}. Calculating a half manifold involves locating a point on $W_{loc}^{u^+}$, and integrating from this point. To locate a point locally near $\bar{x}^*$, $W_{loc}^{u^+}$ is approximated to first order by the unstable eigenvector $\bar{v}_u$, i.e., by choosing a point close to $\bar{x}^*$ that lies on $\bar{v}_u$, that is,

$$\bar{x}_{u^\pm} = \bar{x}^* \pm l \cdot \bar{v}_u \tag{2.71}$$

In equation (2.71), l is the offset in the direction of the unstable eigenvector, and its value is of critical importance. If l is too large, the computed value for $\bar{x}_{u^\pm}$ is not a good approximation; if l is too small, the trajectory spends too long near the fixed point and the integration error accumulates with little progress along the path. There are various ways of selecting the appropriate value of l. One option that has proven

useful for conceptual insight is to define the components of the unstable eigenvector, $\bar{v}_u = [x_u \; y_u \; z_u \; \dot{x}_u \; \dot{y}_u \; \dot{z}_u]^T$, and define $\bar{v}^{W_u}$ such that,

$$\bar{v}^{W_u} = \frac{\bar{v}_u}{[x_u^2 + y_u^2 + z_u^2]^{\frac{1}{2}}} \tag{2.72}$$

$$\bar{x}_{u^\pm} = \bar{x}^* \pm \tilde{d} \cdot \bar{v}^{W_u} \tag{2.73}$$

In equation (2.73), the value $\tilde{d}$ is selected by interpreting it as a distance relative to the fixed point. Similarly, the positive and negative branches of the local stable manifold can be computed in a similar way by defining the components of the stable eigenvector, $\bar{v}_s = [x_s \; y_s \; z_s \; \dot{x}_s \; \dot{y}_s \; \dot{z}_s]^T$, and defining $\bar{v}^{W_s}$ such that,

$$\bar{v}^{W_s} = \frac{\bar{v}_s}{[x_s^2 + y_s^2 + z_s^2]^{\frac{1}{2}}} \tag{2.74}$$

$$\bar{x}_{s^\pm} = \bar{x}^* \pm \tilde{d} \cdot \bar{v}^{W_s} \tag{2.75}$$

where the symbol $\pm$ represents $\bar{x}_{s^+}$ for the half-manifold in the positive direction along the stable eigenvector and $\bar{x}_{s^-}$ for the half-manifold associated with a direction opposite to the stable eigenvector.

2.7 Poincaré Maps

Maps have been used extensively in the last few decades, especially to add insight and expose dynamical structure in complex systems. Due to Henri Poincaré (1899), many systems of differential equations can be represented in terms of maps by reducing the study of a continuous time system to the study of an associated discrete time system. Poincaré first utilized this concept in his studies of the CR3BP; now, virtually any discrete time system that is associated with a set of ordinary differential equations is labeled a "Poincaré map". This technique offers three main advantages: reduction of dimension, global dynamics, and conceptual clarity. The construction of a Poincaré map eliminates at least one variable in the problem, resulting in the

analysis of a lower-dimensional system. In lower-dimensional problems, numerically computed Poincaré maps deliver an insightful display of the global dynamics of a system, highlighting the existence of periodic, quasi-periodic and chaotic behavior.

For the planar CR3BP in $\Re^4$, the surface of section, or hyperplane Σ, is typically specified by fixing one of the coordinates, frequently $y = 0$, producing a surface in $\Re^3$. The three-dimensional surface is projected onto a plane by specification of another parameter. For example, to generate a two-dimensional Poincaré section, a value for the Jacobi constant can be specified and a grid of initial conditions for x and $\dot{x}$ are selected and integrated forward in time. Then, with C, x and $\dot{x}$ initially defined, as well as $y = 0$, the corresponding initial values for $\dot{y}$ can be calculated from the expression for the Jacobi constant in equation (2.37), that is,

$$\dot{y} = \pm\sqrt{x^2 + y^2 + \frac{2(1-\mu)}{d} + \frac{2\mu}{r} - \dot{x}^2 - C} \tag{2.76}$$

where d and r are calculated from equations (2.29)-(2.30). Note that in the planar problem, $z = \dot{z} = 0$. Therefore, all six states are recovered from each return to the map. Alternatively, an initial range of values for $\dot{y}$ can be defined and the corresponding values for $\dot{x}$ can be calculated from equation (2.37). A variety of quantities can be computed and employed to represent each crossing on the Poincaré map. Common quantities used to plot the intersections in this investigation are $x - \dot{x}$ and $y - \dot{x}$, although a wide range of dynamical quantities are also considered, such as Delaunay variables [31], L and $\bar{g}$, and apse locations [60].

Hénon produced maps in the 1960's for application to the restricted three-body problem [61]. For relatively high values of the Jacobi constant, the orbits possess Hill stability and, if C is sufficiently high, the perturbations are weak and most orbits are periodic or quasi-periodic. An orbit is Hill stable when the Jacobi constant is larger than the value of Jacobi constant at the equilibrium point L_2; the L_1 and L_2 gateways are both closed and no escape from the region about P_2 can occur. In contrast, if $C < C_{L_2}$, the gateway and consequently the zero velocity curve is open and escape is possible [62]. There are common structures that are easily identified

from Hénon maps; "chain of islands" structures can appear as well as "dusty" or chaotic regions, where subsequent returns do not form any patterns. When islands are apparent, the center of each island contains a point that intersects the surface of section repeatedly. These centers correspond to stable, periodic orbits. Each crossing that forms a chain of islands corresponds to a single quasi-periodic trajectory. Thus, each stable periodic orbit is surrounded by many chains of islands corresponding to quasi-periodic orbits. The other phenomena that occurs between chains of islands is the formation of "dusty" regions or zones of chaos, where continuity is broken and the regions between curves are filled with unordered crossings. For a given system, as the energy level varies, the surface of section changes in character, and one particular structure may become more predominant than another. Hénon considered systems where the orbits are no longer Hill stable. In such systems, there remain quasi-periodic motions corresponding to closed curves or to chains of islands, but almost all motions outside the largest closed curves lead to an escape of the small mass to infinity. However, closed curves of islands demonstrate the possibility of bounded motion even below the limit of Hill stability.

As an introductory example to explore the information available in Poincaré sections, consider the Hénon map in Figure 2.10. The original plots and a more extended discussion on surfaces of section is offered by Hénon [61]. The section in Figure 2.10 is a section constructed in the planar CR3BP for $\mu = 0.5$. In this system, the mass of the larger primary is the same as the mass of the smaller primary, that is, $m_1 = m_2$. This μ value might represent a binary star system comprised of two stars orbiting their center of mass. The section is defined such that $C = 4.5$, $y = 0$ and $\dot{y} > 0$. A range of values for x_0 and $\dot{x}_0$ are selected and sufficient returns to the hyperplane are used to yield curves that indicate quasi-periodic orbits. Note that $\dot{x}$, represented along the y-axis, is labeled V_x on the map. Maps are labeled 'one-sided' if only the negative or positive returns to the map are considered and 'two-sided' if crossings from both directions are plotted. The map on Figure 2.10 is a one-sided map.

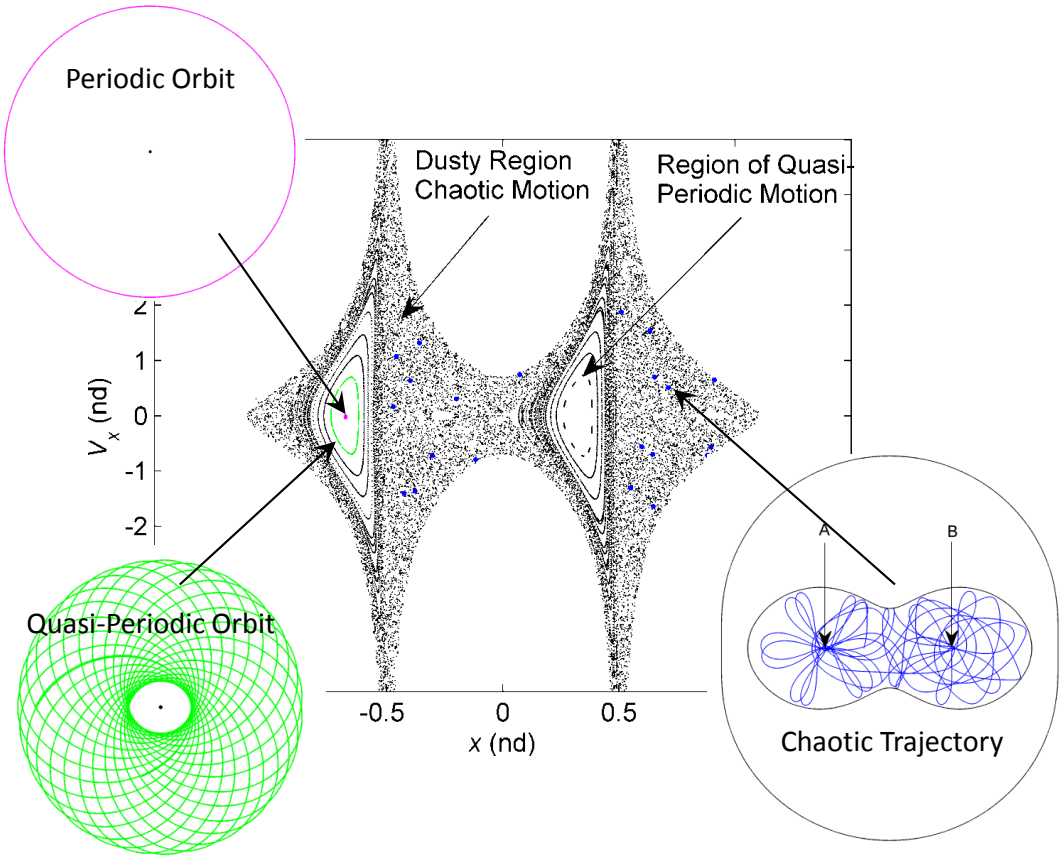

Figure 2.10. Sample Dynamical Structures Identified on a Poincaré Map for $\mu = 0.5$ and $C = 4.5$

Each crossing in a map that forms a chain of islands corresponds to a single quasi-periodic trajectory. As an illustrative example, the crossings corresponding to a quasi-periodic orbit are plotted in green and the associated quasi-periodic is represented in green. The center crossing plotted in magenta is the center of one of the chain of islands; this intersection corresponds to the periodic orbit that appears in magenta. Recall that this trajectory appears as a single point in the map, and each stable periodic orbit is surrounded by many chains of islands corresponding to quasi-periodic orbits. To illustrate the chaotic behavior in the 'dusty' region, a chaotic trajectory is plotted in blue. For reference, the first 20 crossings with the hyperplane

are plotted as blue dots. Note that the dots representing each crossing are enlarged to aid in visualization.

2.8 Coordinate Frame Transformations: Rotating to/from Inertial Frame

Coordinate frame transformations are often necessary to compute and view trajectories in multi-body regimes. Although visualizing trajectories in the rotating frame offers very useful information, it is also desirable to view these trajectories from the perspective of the inertial reference frame. For instance, the calculation of a resonant orbit in the circular restricted three-body model requires the initial computation of the resonance in the two-body model viewed in an inertial reference frame. Transformation between inertial and rotating coordinates is facilitated with the appropriate direction cosine matrix [63]. Recall that the angle θ is defined as the orientation angle of the rotating frame R $(\hat{x} - \hat{y} - \hat{z})$ with respect to the inertial frame I $(\hat{X} - \hat{Y} - \hat{Z})$ such that $\theta = 0^{\circ}$ when the two sets of unit vectors are aligned. The orientation angle changes at a constant rate in the circular restricted three-body model, that is, $\dot{\theta}$=constant. The position vector $\bar{\rho}$ with respect to the barycenter is expressed in terms of either the rotational or the inertial unit vectors, which are related by the direction cosine matrix, ${}^{I}C^{R}$, that is,

$$\begin{bmatrix} \hat{X} \\ \hat{Y} \\ \hat{Z} \end{bmatrix} = {}^{I}C^{R}(\tau) \begin{bmatrix} \hat{x} \\ \hat{y} \\ \hat{z} \end{bmatrix} \tag{2.77}$$

This direction cosine matrix reflects a simple rotation about the z-axis, which is common to both frames. Since the angle θ varies at a constant rate, the matrix ${}^{I}C^{R}$ is an explicit function of the nondimensional time, τ. Hence, $\theta = n^{*}(\tau - \tau_0)$, where τ_0 is the initial time and the nondimensional mean motion, n^{*}, is equal to one by definition. Thus, the direction cosine matrix can be expressed directly in terms of the nondimensional time as,

$$ {}^{I}C^{R}(\tau) = \begin{bmatrix} cos(\tau-\tau_0) & -sin(\tau-\tau_0) & 0 \\ sin(\tau-\tau_0) & cos(\tau-\tau_0) & 0 \\ 0 & 0 & 1 \end{bmatrix} \tag{2.78} $$

Note that the direction cosine matrix in equation (2.78) can be inverted to obtain the inverse transformation, i.e., from rotational to inertial coordinates.

The availability of the position and the velocity vectors in terms of rotational and inertial coordinates is very useful. However, such a transformation also involves the use of the basic kinematic equation from equation (2.21). The nondimensional position and velocity vectors expressed in terms of inertial and rotating coordinates are, respectively,

$$ \bar{\rho}_{in} = X_{in}\hat{X} + Y_{in}\hat{Y} + Z_{in}\hat{Z} \tag{2.79} $$

$$ \bar{\rho}'_{in} = X'_{in}\hat{X} + Y'_{in}\hat{Y} + Z'_{in}\hat{Z} \tag{2.80} $$

$$ \bar{\rho}_{rot} = x\hat{x} + y\hat{y} + z\hat{z} \tag{2.81} $$

$$ \bar{\rho}'_{rot} = (\dot{x} - n^*y)\,\hat{x} + (\dot{y} + n^*x)\,\hat{y} + \dot{z}\hat{z} \tag{2.82} $$

leading to the position and velocity transformation. Then, the transformation from rotating to inertial coordinates appears as a 6×6 block matrix, that is,

$$ \begin{bmatrix} X_{in} \\ Y_{in} \\ Z_{in} \\ X'_{in} \\ Y'_{in} \\ Z'_{in} \end{bmatrix} = \begin{bmatrix} {}^{I}C^{R}(\tau) & 0_{3\times3} \\ {}^{I}\dot{C}^{R}(\tau) & {}^{I}C^{R}(\tau) \end{bmatrix} \begin{bmatrix} x \\ y \\ z \\ \dot{x} \\ \dot{y} \\ \dot{z} \end{bmatrix} \tag{2.83} $$

where the submatrix $0_{3\times3}$ is the 3×3 zero matrix, the submatrix ${}^{I}C^{R}(\tau)$ is represented in equation (2.78), and the submatrix $\dot{C}(\tau)$ is defined as,

$$ \dot{C}(\tau) = \begin{bmatrix} -sin(\tau-\tau_0) & -cos(\tau-\tau_0) & 0 \\ cos(\tau-\tau_0) & -sin(\tau-\tau_0) & 0 \\ 0 & 0 & 0 \end{bmatrix} \tag{2.84} $$

Then, the expression in equation (2.84) relating the velocities can be combined with the expression relating positions in equation (2.78) to create a 6×6 transformation matrix that transforms a six-dimensional state with respect to an observer in the rotating frame R and expressed in terms of rotating coordinates, i.e., $\bar{x} = [x \;\; y \;\; z \;\; \dot{x} \;\; \dot{y} \;\; \dot{z}]^T$, to an inertial state expressed in inertial coordinates, i.e., $\bar{x} = [X_{in} \;\; Y_{in} \;\; Z_{in} \;\; \dot{X}_{in} \;\; \dot{Y}_{in} \;\; \dot{Z}_{in}]^T$, in a single step. The inverse of this block matrix leads to the inverse transformation, that is, to transform inertial states to rotating states.

Given the necessary background regarding the formulation of the circular restricted three-body problem, the derivation of the differential equations, and the development of a series of numerical techniques that facilitate the computation of periodic solutions and transfer trajectories in multi-body environments, a comprehensive analysis of families of periodic orbits in multi-body environments is presented followed by a variety of astrodynamics applications that demonstrate the applicability of resonant orbits and invariant manifolds to preliminary trajectory design.

3. PERIODIC SOLUTIONS AND RESONANT FAMILIES

There are an infinite number of periodic solutions in the circular restricted three-body problem, as noted by Poincaré in 1892. These periodic orbits are generally collected into families of solutions that share a set of orbital characteristics. Although a wide variety of families of periodic orbits have been extensively investigated, many of the solutions remain unknown. Families of Lyapunov and halo orbits are common examples of periodic motion in the vicinity of the libration points in multi-body systems. Their applicability to mission design has also been demonstrated and it is now well-accepted that these orbit are fundamental structures for mission design applications. Other families of periodic orbits have also been studied by many researchers including P_2-centered orbits, such as distant retrograde, distant prograde, and low prograde orbits. Families of periodic resonant orbits, which are the core of this investigation, can also be cataloged in the CR3BP, and similar to libration point orbits, families of resonant orbits can prove very useful in the construction of a trajectory that satisfies all mission design requirements. However, to assess the role of periodic orbits in trajectory design, these families of periodic orbits must be generated and their orbital characteristics evaluated. In this chapter, common planar and three-dimensional libration point orbits, distant retrograde orbits, and resonant orbits are calculated, categorized into families, and investigated in terms of energy and stability characteristics.

3.1 Planar Periodic Libration Point Orbits in the CR3BP

In general, families of periodic orbits near the libration points are calculated in the nonlinear system from an initial guess originating in the linear system. In this investigation, families of planar, symmetric periodic orbits near the collinear libra-

tion points L_1, L_2, and L_3 are straightforwardly calculated using a single shooting corrections algorithm wrapped in a single-parameter continuation scheme. Likewise, more complex planar, asymmetric periodic orbits in the vicinity of the equilateral libration points L_4 and L_5 are generated using a multiple shooting algorithm and a pseudo-arclength continuation strategy.

3.1.1 Families of Orbits

While an infinite number of planar and non-planar periodic orbits exist near all five libration points in the CR3BP, perhaps the most simple and well-known type of planar periodic motion near the collinear libration points is a Lyapunov orbit. A Lyapunov orbit is a periodic orbit in the plane of motion of the primaries, that is, a planar orbit in the xy-plane that is symmetric across the x-axis. In this investigation, Lyapunov orbits are determined numerically using a variable-time single shooting algorithm that exploits the associated symmetry properties to simplify the corrections process. Even though each Lyapunov orbit is uniquely characterized by the parameter A_y, that is, the maximum y-excursion as measured from the x-axis, it is often desirable to identify a group of related periodic orbits rather than a single trajectory. A single-parameter continuation method is employed to generate a family of periodic orbits. For these particular families, the constraining parameter in the continuation scheme is selected to be the value of Jacobi constant. Lyapunov orbits are known to exist in different three-body systems; sample trajectories in the vicinity of L_1 (green), L_2 (blue), and L_3 (magenta) in the Earth-Moon system are illustrated in Figure 3.1. Only a small subset of trajectories is represented in Figure 3.1, but there are an infinite number of periodic orbits in each family. For reference, in the Earth-Moon system, the mass fraction is equal to a value of $\mu = 0.01215057$, the distance between L_1 and the Moon is computed as 58,017.33 km, and the distance between L_3 and the Earth is 391,004.72 km. Note that both the Earth and the Moon are sized to the correct scale in Figure 3.1. For completeness, Table 3.1 includes the non-zero initial conditions

and the corresponding values of the Jacobi constant associated with the smallest and largest y-amplitude members that are plotted in each of the three families of planar, periodic orbits in the vicinity of the collinear points as represented in Figure 3.1. The position and velocity components in Table 3.1 are given in dimensional units, i.e., km and km/s, respectively, and are measured with respect to the Earth-Moon barycenter. Recall that these orbits are all planar, i.e., $z = \dot{z} = 0$, and because of symmetry properties, $y_0 = \dot{x}_0 = 0$.

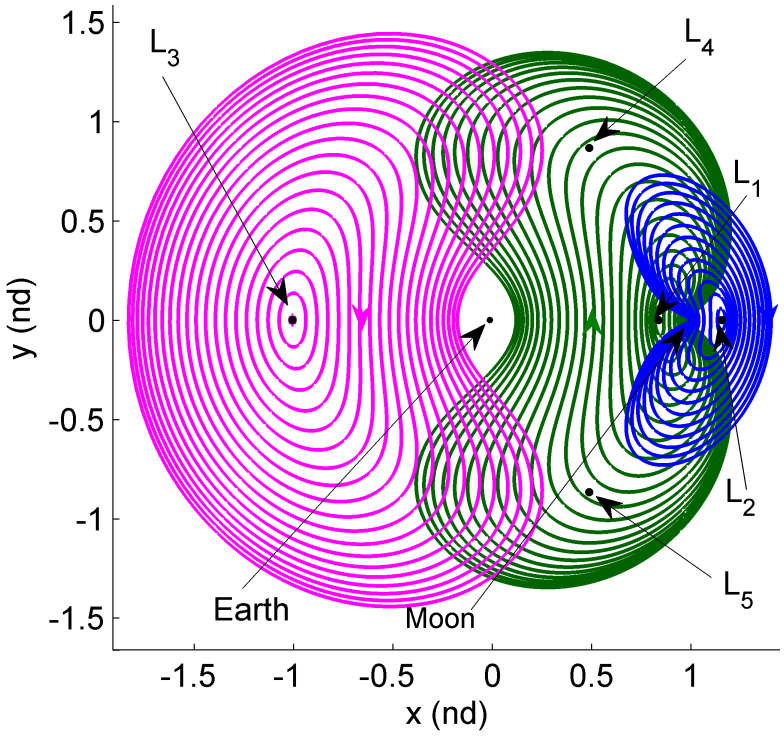

Figure 3.1. Planar Periodic Orbits near L_1 (Green), L_2 (Blue), and L_3 (Magenta) in the Earth-Moon System

Families of periodic orbits also exist in the vicinity of the equilateral points L_4 and L_5 for all values of μ. Examples of short and long period planar solutions have been computed by numerous researchers [55, 64]. To obtain short and long period analytical solutions, the equations of motion are linearized relative to L_4 and L_5. The solutions to the appropriate linear system of equations in the vicinity of the equilateral points are elliptical in shape [46]. These linear orbits are then employed as initial

Table 3.1 Initial Conditions and Jacobi Constant Values Corresponding to the Smallest and Largest Lyapunov Orbits that Appear in Figure 3.1

Lyapunov orbit	x (km)	$\dot{y}$ (km/sec)	Period (days)	C
Smallest L_1	3.230816×10^5	-0.029831	11.69886	3.187639
Largest L_1	3.780436×10^5	-2.563588	30.55283	2.232253
Smallest L_2	4.511119×10^5	-0.107852	14.72479	3.163271
Largest L_2	5.443804×10^5	-0.762761	33.94186	2.891267
Smallest L_3	-3.816471×10^5	-0.025391	27.00326	3.011988
Largest L_3	-6.109020×10^4	-3.469237	27.15708	2.041567

guesses that seed the corrections algorithm to produce short and long period orbits in the nonlinear system. Unlike Lyapunov orbits, these short and long period orbits are not symmetric across the xz-plane. Therefore, symmetry properties can no longer be exploited to generate these orbits. A variety of corrections schemes are typically used to compute sample periodic orbits around L_4 and L_5, but a multiple shooting scheme with periodicity constraints is employed in this investigation. Once an asymmetric periodic orbit near the equilateral points is calculated in the nonlinear system, a continuation method is employed to 'grow' a family. Recall that continuation can be accomplished by selecting a constraining parameter, modifying the value of this parameter, and repeating the corrections process to determine a subsequent orbit. The families of Lyapunov orbits as illustrated in Figure 3.1 are generated constraining the value of the Jacobi constant, although fixing the x-component of the initial state is also a commonly used constraining parameter in the continuation process. Alternatively, if no *a priori* information regarding the direction of growth is available, a family can be expanded employing pseudo-arclength continuation, which involves stepping through a certain parameter on the reference plane by fixing this parameter with an additional constraint. For instance, the sample short and long period orbits

near L_4 and L_5 that are plotted in Figure 3.2 are generated via a pseudo-arclength continuation method; L_4 short and long period orbits are plotted in blue and L_5 short and long period orbits appear in green. For reference, Table 3.2 includes the non-zero initial conditions and corresponding values of the Jacobi constant associated with the smallest and largest members that are plotted in each of the four families of periodic orbits in the vicinity of the equilateral points.

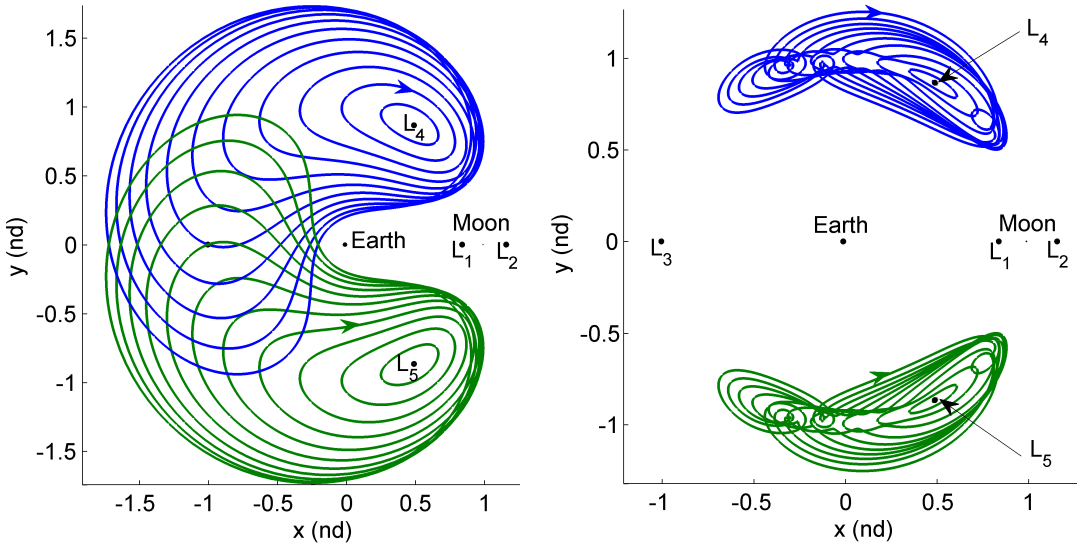

(a) Sample L_4 and L_5 Short Period Orbits (b) Sample L_4 and L_5 Long Period Orbits

Figure 3.2. Representative Orbits in Families of Short and Long Period Orbits near L_4 (Blue) and L_5 (Green) in the Earth-Moon System

3.1.2 Initial State, Stability, and Energy Representations

In this analysis, the first step in the transfer trajectory design process requires the selection of the departure and arrival orbits, as well as the intermediate orbit(s) that generate the appropriate arcs to serve as the transfer mechanism(s). Viewing each available family of periodic orbits solely in position space, that is, as represented in Figure 3.1, does not facilitate the selection process as minimal insight into the orbital characteristics or the relationship to other families of periodic orbits is offered

Table 3.2 Initial Conditions and Jacobi Constant Values Corresponding to the Smallest and Largest Short and Long Period Orbits that Appear in Figure 3.2

	Smallest Short	Largest Short	Smallest Long	Largest Long
x (km)	1.875293×10^5	1.875293×10^5	1.875293×10^5	1.875293×10^5
y (km)	3.325958×10^5	1.173108×10^5	3.343088×10^5	2.193537×10^5
$\dot{x}$ (km/sec)	-0.001282	-1.267916	0.004396	-0.437537
$\dot{y}$ (km/sec)	0.000514	-0.429798	-0.002365	0.208535
Period (days)	28.58520	27.30586	91.49739	113.695
C	2.987996	2.037918	2.988003	2.975903

from such a representation. Rather, it is desirable to display relevant information regarding a group of planar families of periodic orbits in a condensed 2D plot. Such orbital properties include initial states, energy or Jacobi constant values, and stability indices for each member that is numerically constructed in a family. The parameters associated with several families are then displayed on a 2D graph to offer a composite-view of the orbits as well as the relationship that may exist between specific members.

With the appropriate choice of parameters, relevant information about each periodic orbit can be insightfully represented on a 2D figure, labeled in this analysis as a $\nu - C$ plot, a stability and energy plot. Initial states and energy levels are represented along the x-axis and y-axis, respectively. Consider a planar, symmetric, periodic orbit with initial state $\bar{x}_0 = [x_0 \quad 0 \quad 0 \quad 0 \quad \dot{y}_0 \quad 0]^T$. If the scalar position coordinate x_0 is represented on the x-axis and the corresponding value of Jacobi constant is plotted on the y-axis, then the remaining non-zero initial state, i.e., $\dot{y}_0$, is directly obtained from the expression for the integral of the motion. Therefore, a point on the $\nu - C$ plot describes the complete 6D initial state and corresponding energy level for the selected planar, symmetric, periodic orbit. Then, a combination of qualitative parameters aid in the representation of the in-plane and out-of-plane stability indices.

Recall that a periodic orbit in the CR3BP possesses six eigenvalues; two λ's have values that are equal to one because of periodicity. In the planar case, the remaining two pairs are associated with the in-plane and out-of-plane motion, respectively. The corresponding in-plane and out-of-plane stability indices, ν_{2D} and ν_{3D}, are calculated from the eigenvalues associated with the planar and three-dimensional motion using equation (2.67). Color is employed to represent ν_{2D} values and the length of an arrow reflects the ν_{3D} values. For example, the absence of an arrow indicates that the orbit is stable; conversely, a longer arrow represents an orbit with a larger magnitude of the unstable index ν_{3D}. Similarly, variations in color along a color bar indicate shifts in the in-plane stability. Each particular family of periodic orbits is then identified on the graph by a specific marker; for example, circles represent members in family a, squares illustrate family b, etc. The diagram in Figure 3.3 illustrates the basic construction of a stability-energy plot. The colored dot with the attached arrow in Figure 3.3 represents orbital characteristics of a single periodic orbit, i.e., C as a function of x_0. Then, a set of dots with attached arrows represents the members in a family.

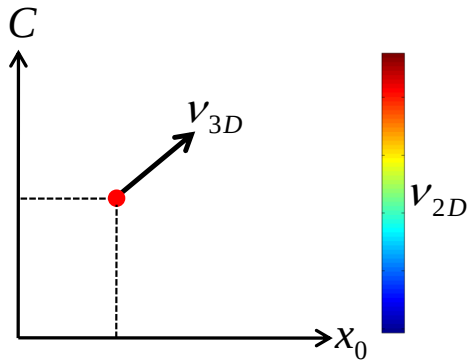

Figure 3.3. Diagram of a $\nu - C$ Plot: Initial State, Stability, and Energy Representation for Families of Periodic Orbits

Stability-energy plots are very useful in providing information 'at a glance' concerning a selected family of orbits. Information summarized for three planar families is illustrated in Figure 3.4, i.e., the stability and energy properties associated with mem-

bers in the families of Lyapunov orbits in the vicinity of L_1, L_2, and L_3, respectively; members in the L_1 Lyapunov family are represented by a circle, a square identifies L_2 Lyapunov members, and a triangle represents members in the L_3 Lyapunov family. For better visualization, zoomed-views of the L_1 and L_2 families appear on the right. It is observed that the family of L_1 Lyapunov orbits possesses larger values of both the in-plane and out-of-plane stability indices, as represented by the longer arrows and larger variation in colors. The family of L_3 Lyapunov orbits, however, is considerably more stable than the families near L_1 and L_2, as expected.

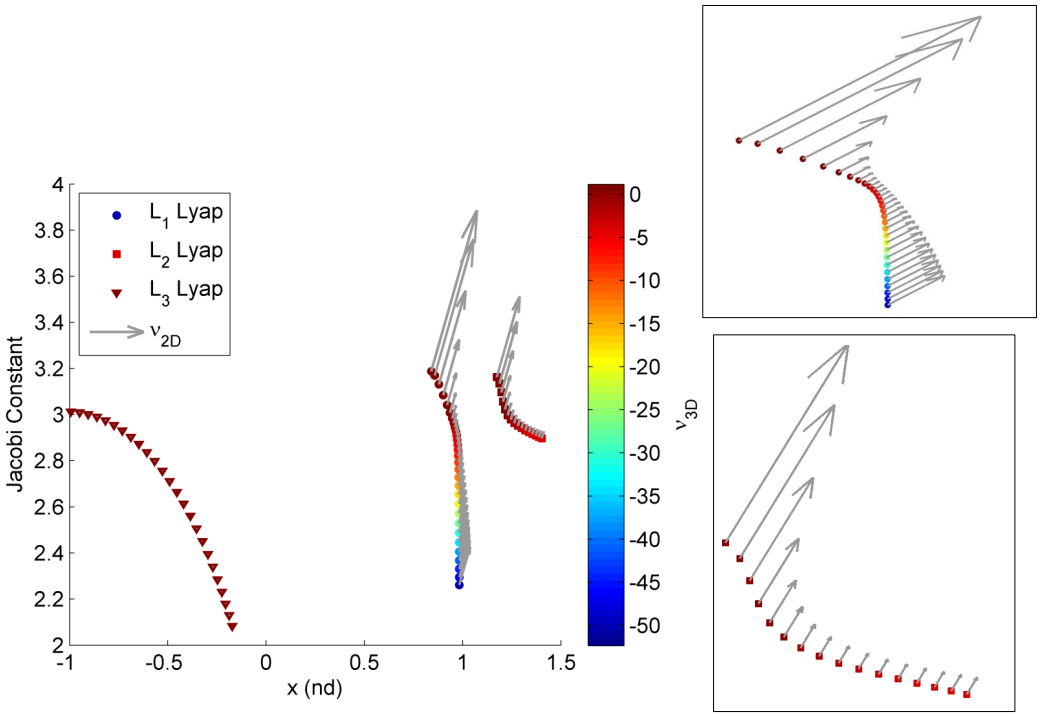

Figure 3.4. Initial State, Stability, and Energy Representation of L_1, L_2, and L_3 Families of Lyapunov Orbits in the Earth-Moon System; Boxed-Plots Represent Zoomed-Views of L_1 and L_2 Families of Lyapunov Orbits

Transfer and bifurcation information can also be discerned from the stability-energy plot. A natural transfer (no maneuvers required) between two periodic orbits, also known as heteroclinic connection, may exist if the departure and arrival periodic

orbits are unstable and possess the same value of Jacobi constant [41]. For example, given the instability associated with the L_1 and L_2 Lyapunov families (represented by the length of an arrow), a free transfer can be constructed between an L_1 and L_2 Lyapunov orbits at the same energy level. These stability-energy representation also supplies insightful information regarding bifurcations and the existence of new families of periodic orbits. A bifurcation may result in the formation of a new family of periodic orbits [54, 65]. In this analysis, bifurcations to 3D families of periodic orbits are quite useful. Changes in the out-of-plane stability index along a family are easily tracked to identify potential bifurcations. In particular, as the stability index passes through the values $\nu_{3D} = \pm 1$, the eigenvalues transition between the unit circle and the real axis, which indicates the location of a possible bifurcation.

The stability-energy plots in Figure 3.5 and Figure 3.6 represent the initial state and relevant orbital characteristics associated with the families of short and long period orbits near L_4 and L_5 as illustrated in Figure 3.2, respectively. Both families of L_4 and L_5 short period orbits are linearly stable, whereas a subset of long period orbits are clearly unstable in the figure.

The selection of the initial, final, and intermediate orbits employed in a transfer design process is then facilitated by combining different families on a single stability-energy graph.

3.2 Planar Periodic Distant Retrograde and Prograde Orbits in the CR3BP

The existence of symmetric, periodic motion in the CR3BP is not limited to the regions in the vicinity of the libration points. In fact, prograde and retrograde periodic orbits exist in the CR3BP near the smaller primary, P_2, and have been examined by numerous researchers [41,66,67]. Distant prograde and retrograde orbits about the smaller primary are initially generated in the Hill's problem, but can be transitioned to the restricted three-body problem with the aid of a corrections scheme.

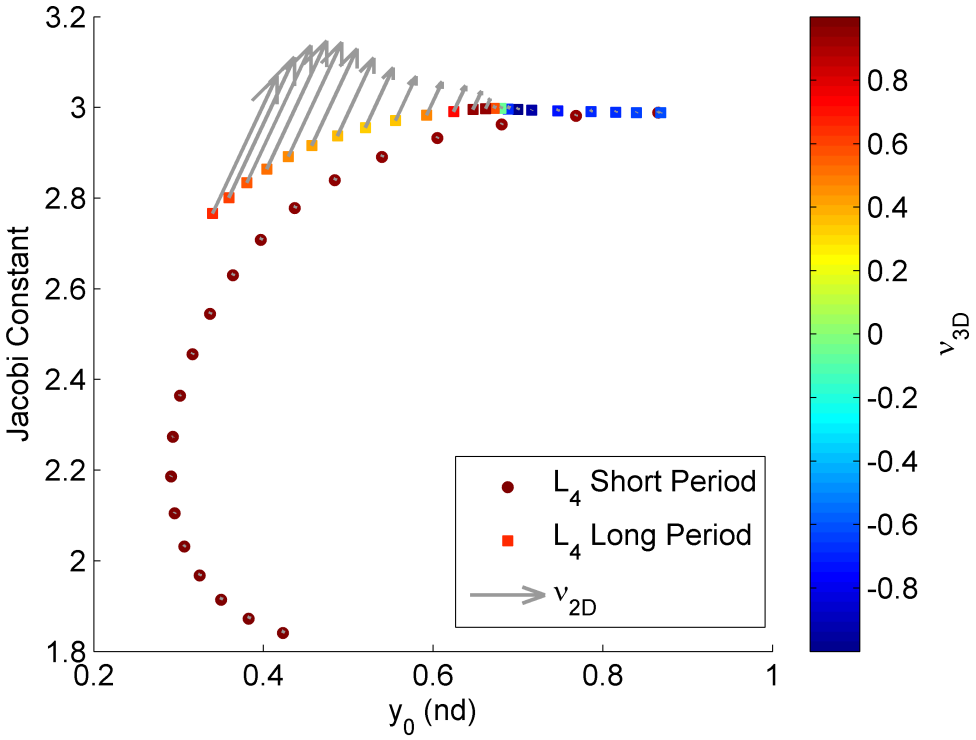

Figure 3.5. Initial State, Stability, and Energy Representation of Families of Short and Long Period Orbits Near L_4 in the Earth-Moon System

In this analysis, families of planar, symmetric P_2-centered orbits are straightforwardly calculated in various three-body systems using a single shooting corrections algorithm.

3.2.1 Families of Orbits

Well-known families of P_2-centered orbits include distant retrograde orbits, commonly labeled DROs, distant prograde orbits, or DPOs, and low prograde orbits, labeled LoPOs in this investigation to distinguish them from libration point orbits (LPOs). Representative members in families of P_2-centered orbits in the Earth-Moon system appear in Figure 3.7; DROs are plotted in purple (Figures 3.7(a)-3.7(b)), LoPOs appear in teal (Figure 3.7(c)), and DPOs are orange (Figures 3.7(d)-3.7(e)). The family of distant retrograde orbits extends to the vicinity of the larger primary, i.e.,

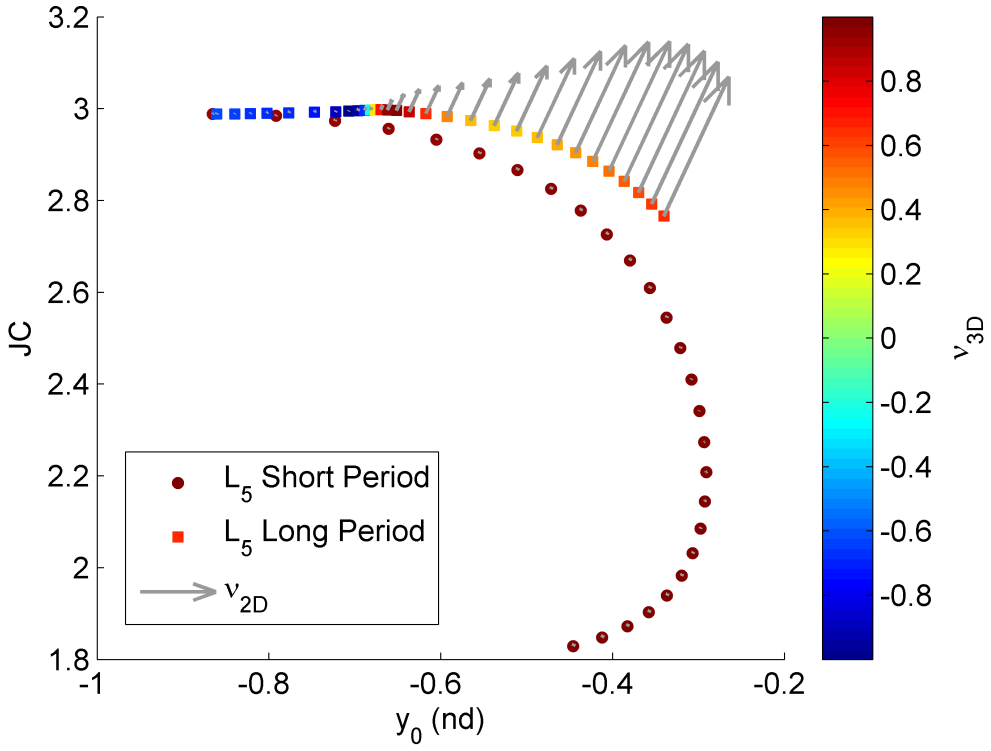

Figure 3.6. Initial State, Stability, and Energy Representation of Families of Short and Long Period Orbits Near L_5 in the Earth-Moon System

the Earth, and the direction of motion is retrograde as viewed from the rotating reference frame. Conversely, the direction of motion along low prograde orbits is direct as viewed from the rotating frame, but unlike DROs, LoPOs remain in the vicinity of the smaller primary. Distant prograde orbits about P_2 include orbits that are nearly symmetrical in comparison to smaller DROs but, as the family grows, DPOs loop around the smaller primary including two close flybys of P_2 and eventually impacting the surface. Similar to Lyapunov orbits, distant prograde and retrograde orbits are symmetric across the x-axis and, given the appropriate initial conditions, are straightforwardly computed via a variable-time single shooting corrections method. For completeness, Table 3.3 includes the non-zero initial conditions and corresponding values of the Jacobi constant associated with the smallest and largest members in each of the three families of P_2-centered periodic orbits plotted in Figure 3.7.

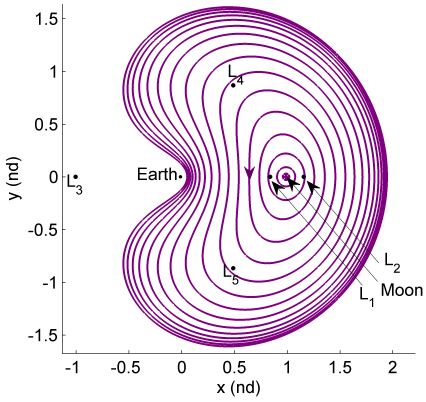

(a) Distant Retrograde Orbits

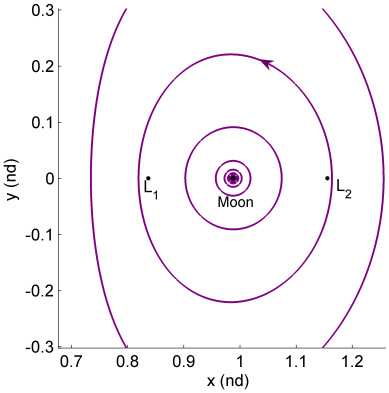

(b) Zoomed-View Near P_2

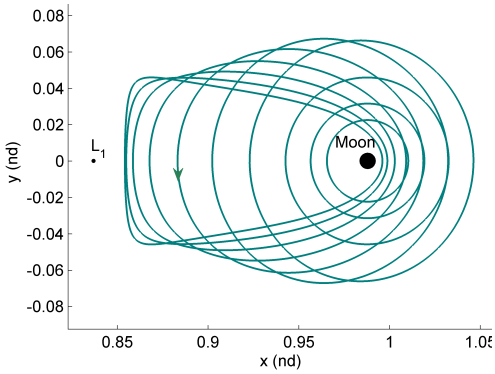

(c) Low Prograde Orbits

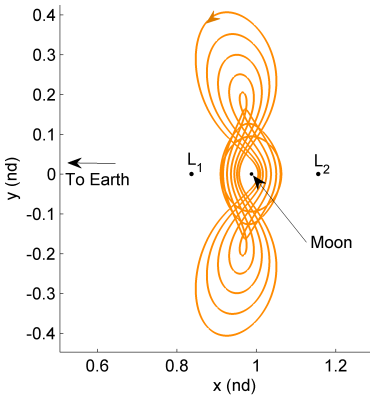

(d) Distant Prograde Orbits

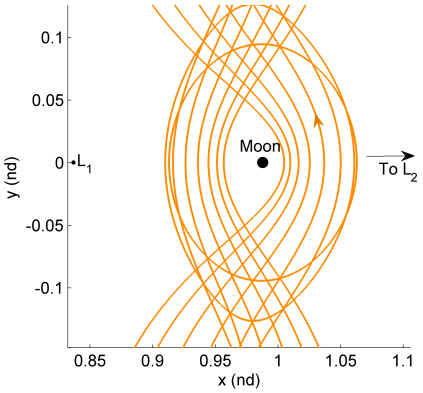

(e) Zoomed-View Near P_2

Figure 3.7. Representative Orbits in Families of P_2 Centered Orbits: Distant Retrograde Orbits in a) and b), Low Prograde Orbits in c), and Distant Prograde Orbits in d) and e) in the Earth-Moon System Plotted in the Rotating Reference Frame

Table 3.3 Initial Conditions and Jacobi Constant Values Corresponding to the Smallest and Largest Orbits that Appear in Figure 3.7

Periodic Orbit	x (km)	$\dot{y}$ (km/sec)	Period (days)	C
Smallest DRO	3.772718×10^5	1.419054	0.125953	4.834447
Largest DRO	2.017355×10^4	5.506869	27.36475	1.707646
Smallest LoPO	3.883351×10^5	0.732860	0.857669	3.526827
Largest LoPO	3.826977×10^5	1.749746	11.00989	3.181978
Smallest DPO	$4.085966\text{e}\times10^5$	0.372318	7.908883	3.159087
Largest DPO	3.849971×10^5	1.353889	31.47199	2.979179

3.2.2 Initial State, Stability, and Energy Representation

A stability-energy plot is constructed to represent the initial states, Jacobi constant values, and stability properties associated with the families of P_2-centered orbits that appear in Figure 3.7. Distant retrograde orbits are represented with a circle, low prograde orbits are identified by squares, and triangles represent members along the family of distant prograde orbits. Recall that each marker is colored according to the value of the out-of-plane stability index. For better visualization, zoomed-views of the regions in the vicinity of the Moon are provided in the $\nu - C$ plot in Figure 3.8. The boxed image in the lower left corresponds to the family of low prograde orbits and the boxed plot in the lower right represents the family of distant prograde orbits. Note that distant prograde orbits are unstable, whereas only a small subset of the family of low prograde orbits is unstable, as indicated by the color and the length of the arrows in Figure 3.8. Conversely, distant retrograde orbits are mostly stable, as indicated by the absence of arrows in the figure.

Bifurcation information is also clearly discerned from the stability-energy plot in Figure 3.8. That is, the variation in color along the family of DROs, represented by dots in Figure 3.8, suggests the location of a possible bifurcation to a 3D family of distant retrograde orbits. As illustrated in Figure 3.8, the out-of-plane stability index

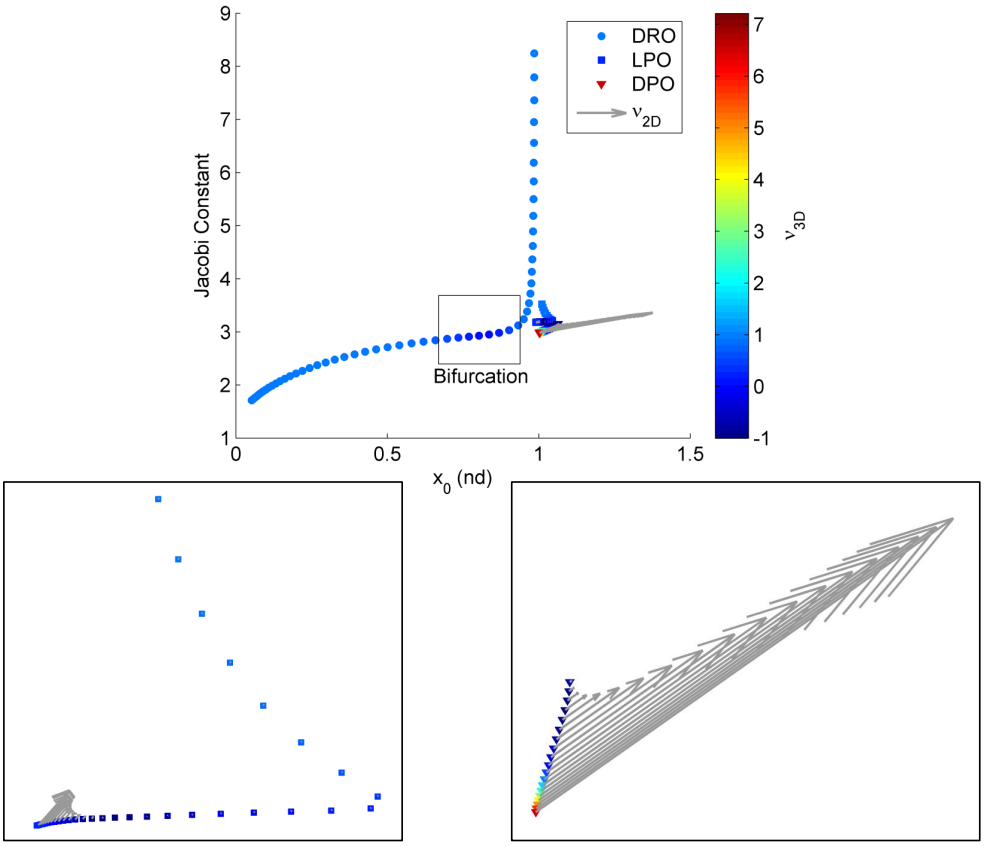

Figure 3.8. Initial State, Stability, and Energy Representation of Families of Distant Retrograde Orbits, Distant Prograde Orbits, and Low Prograde Orbits in the Earth-Moon System; Boxed-Plots Represent Zoomed-Views of Families of Distant Prograde Orbits and Low Prograde Orbits

varies from $\nu_{3D} = 1$ to $\nu_{3D} = -1$, as represented by the change in color from cyan to blue to cyan. This change in stability indicates that the eigenvalues transition between the unit circle and the real axis, highlighting the location of a bifurcation and, thus, the presence of a family of 3D distant retrograde orbits.

3.3 Application of Stability-Energy Plots: 2D Periodic Orbit Chains between Libration Point Orbits and Distant Retrograde Orbits

Stability-energy plots offer a composite view of multi-body orbits possessing a variety of characteristics. Providing access to a large assortment of orbit types within one representation offers a unique design perspective. In other words, representing different families of periodic orbits on a single ν-C plot enables exploration of the relationships between the various orbit families as well as discovery of solutions not explicitly made available otherwise. Recall that a natural transfer between two periodic orbits, i.e., a transfer trajectory that requires no maneuvers to transition from one orbit to another, also known as heteroclinic connection, may exist if the departure and arrival periodic orbits are unstable and possess the same value of Jacobi constant [68]. Such two periodic orbits are easily identified on a ν-C plot by selecting two points on the graph that possess the same value of y (corresponding to the same value of Jacobi constant) and an arrow of some length. Recall that the length of the arrow in a ν-C plot qualitatively represents the in-plane stability index, ν_{2D}, and, likewise, the absence of an arrow indicates that the orbit is stable. Color is then used to represent out-of-plane stability index values. Given the instability associated with the L_1 and L_2 Lyapunov families, a cost-free transfer can be constructed between an L_1 and L_2 Lyapunov orbits at the same energy level. This type of transfer, or heteroclinic connection, is well-known to exist between L_1 and L_2 Lyapunov orbits [68, 69]. However, if a family of distant prograde orbits is also added to the stability-energy plot representing L_1 and L_2 Lyapunov orbits, new insight is gained on the relationship between the three families of periodic orbits. Consider the ν-C plot in Figure 3.9. The family of L_1 and L_2 Lyapunov orbits are represented by squares and triangles, respectively; the family of DPOs appears in the center, between the L_1 and L_2 Lyapunov families, represented by circles. Recall that the family of DPOs appears plotted in configuration space in Figures 3.7(d)-3.7(e) and the L_1 and L_2 Lyapunov families are plotted in Figure 3.1. The region on the graph highlighted by the box indicates the

availability of potential cost-free transfers, that is, a region where sets of three orbits that are unstable and possess the same value of Jacobi constant are found.

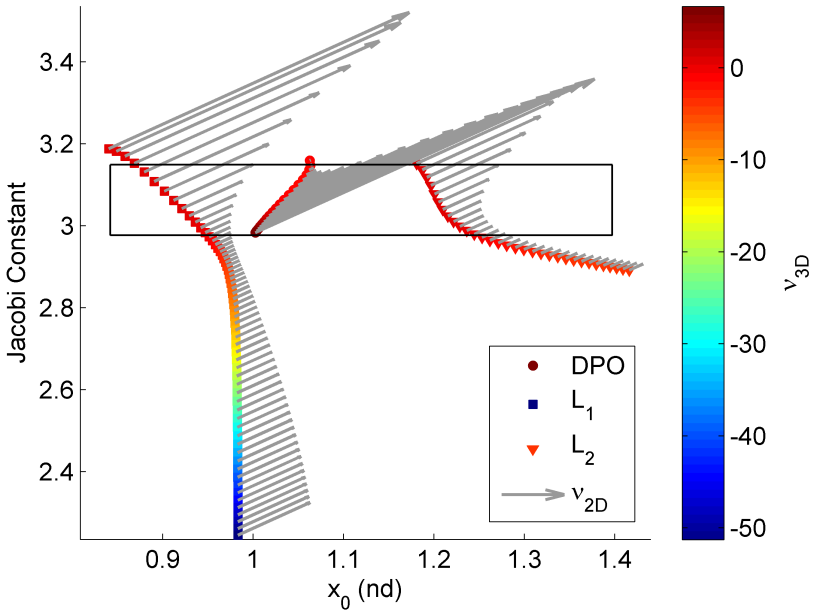

Figure 3.9. Initial State, Stability, and Energy Representation of Families of Distant Retrograde Orbits, L_1 and L_2 Lyapunov Orbits in the Earth-Moon System; Boxed-Region Represents an Energy Range for Potential Cost-Free Transfers between the Three Families

The composite view of the three families of periodic orbits in Figure 3.9 suggests a possible connection between orbit structures. Consider the two sets of unstable periodic orbits, including a DPO and an L_1 and an L_2 Lyapunov orbit, at $C = 3.05$ and $C = 3.12$ plotted in Figure 3.10. A cost-free transfer between the two Lyapunov orbits near L_1 and L_2 at each energy level is calculated from the intersection of the unstable manifold associated with the L_1 Lyapunov orbit and the stable manifold associated with the L_2 Lyapunov orbit. The resulting heteroclinic connections for each of the selected values of Jacobi constant appear in Figure 3.11. For reference, the three periodic orbits, i.e., the libration point orbits and the distant prograde orbit, are also plotted in gray. The unstable manifold trajectory that departs the L_1 Lyapunov orbit appears in magenta and the stable manifold trajectory that approaches the L_2

Lyapunov orbit is plotted in blue. This type of 'direct' heteroclinic connection (< 1 rev) are common and well-known to exist between planar libration point orbits [69]. However, the merged views of the L_1-L_2 heteroclinic connection and the distant prograde orbit reveal an association between the two orbit structures at each energy level. In this composite view, it is apparent that the heteroclinic connection inherits characteristics associated with the nearby DPO for for values of Jacobi constant.

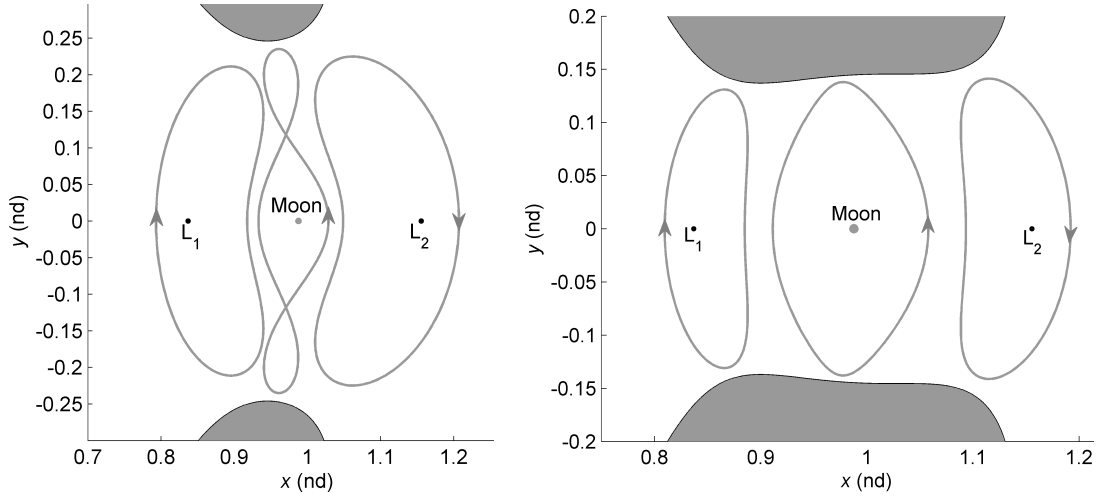

(a) $C = 3.05$ (b) $C = 3.12$

Figure 3.10. Distant Prograde Orbits and L_1 and L_2 Lyapunov Orbits at Different Energy Levels in the Earth-Moon System

The selected distant prograde orbits for $C = 3.05$ and $C = 3.12$ are unstable and, therefore, possess stable and unstable manifold trajectories that asymptotically approach and depart the orbit. Exploiting these manifold structures, a pair of heteroclinic connections is also located from a Poincaré section that connect the L_1 Lyapunov orbit to the DPO, represented by the magenta and green arcs in Figure 3.12, and the DPO to the L_2 Lyapunov orbit, illustrated by the red and blue arcs. The resemblance between the connections in Figure 3.11 and Figure 3.12 suggests a strong relationship between these orbit structures. Note also the similarity between the heteroclinic connections in Figure 3.11(b) and Figure 3.12(b) and the L_2 to L_1 connection employed for the P1 spacecraft in the ARTEMIS mission [70].

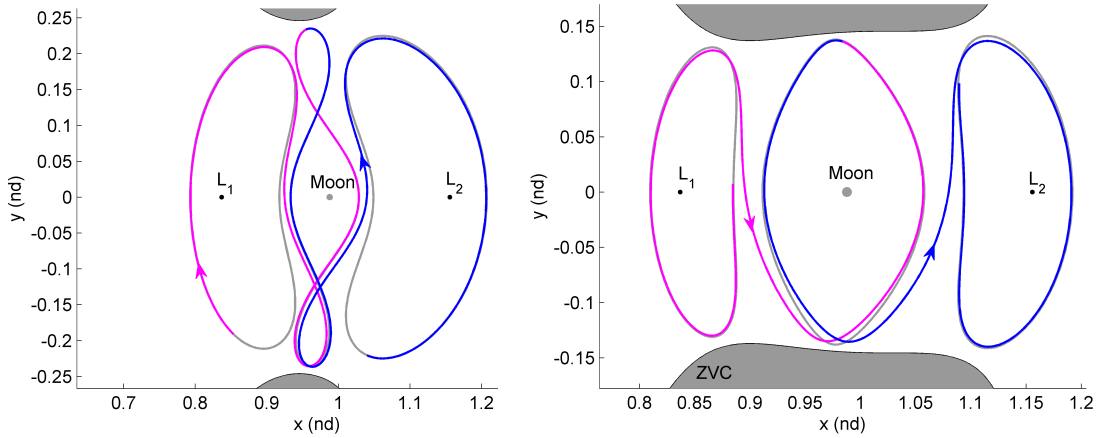

(a) $C = 3.05$ (b) $C = 3.12$

Figure 3.11. Heteroclinic Connections between L_1 and L_2 Lyapunov Orbits in the Earth-Moon System for $C = 3.05$ and $C = 3.12$

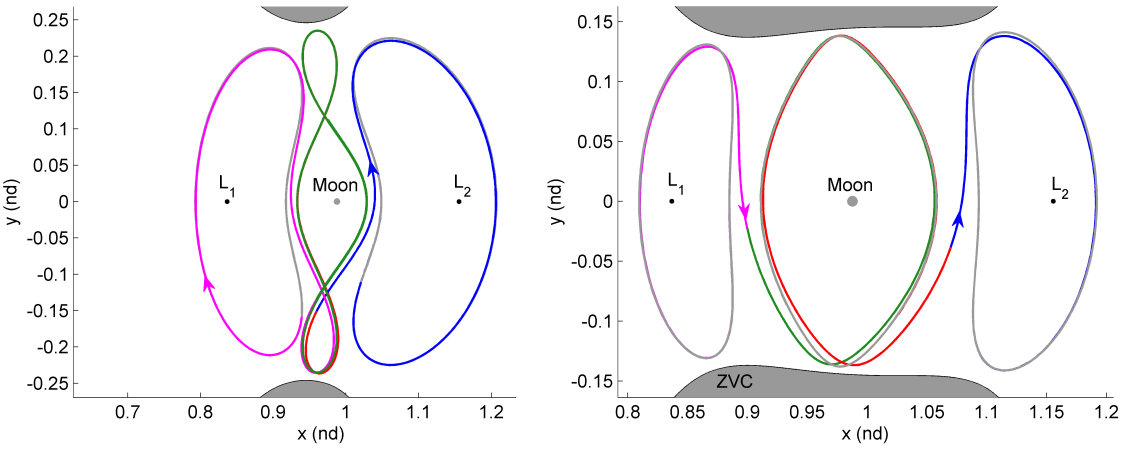

(a) $C = 3.05$ (b) $C = 3.12$

Figure 3.12. Heteroclinic Chains connecting an L_1 Lyapunov to a DPO, and the DPO to an L_2 Lyapunov Orbit in the Earth-Moon System for $C = 3.05$ and $C = 3.12$

Poincaré maps are a valuable tool in the exploration of the role of distant prograde orbits in facilitating connections between nearby Lyapunov orbits. For an appropriately selected Poincaré section, each of the connections depicted in Figures 3.11-3.12 is represented as an intersection of stable and unstable manifold crossings on the map.

The Poincaré map that appears in Figure 3.13 is constructed by defining the surface of section at $x = 1 - \mu$, i.e., the the x-location of the Moon, and displaying crossings of the (i) unstable manifold associated with the L_1 Lyapunov orbit (magenta), (ii) stable manifold associated with the L_2 Lyapunov orbit (blue), (iii) stable manifold associated with the distant prograde orbit (green), and (iv) unstable manifold associated with the distant prograde orbit (red), each for the energy level $C = 3.12$. A similar Poincaré map can be generated for $C = 3.05$. An intersection between the magenta and blue contours, as viewed on the Poincaré map, indicate the existence of a heteroclinic connection between the L_1 and L_2 Lyapunov orbits. Similarly, overlap between the magenta and green (red and blue) contours reveals the existence of connections between the L_1 Lyapunov and DPO (DPO and L_2 Lyapunov). The close proximity of the three intersections of the manifolds on the map suggest a strong relationship between the L_1-L_2 heteroclinic connection and the L_1-DPO-L_2 heteroclinic chain at the given energy level. To further demonstrate this relationship, a second map, corresponding to the value of Jacobi constant $C = 3.172$, for which the distant prograde orbit is stable and no longer possesses invariant manifolds, is generated and plotted in Figure 3.13(b). Thus, only the crossings of the unstable (magenta) and stable (blue) manifold associated with the L_1 and L_2 Lyapunov orbits at $C = 3.172$ appear. At this particular energy level, the magenta and blue contours do not intersect, as viewed on the Poincaré map, indicating that a heteroclinic connection of the characteristics represented in Figure 3.11 does not exist between the Lyapunov orbits. Because the DPO is stable, it is suspected that the L_1-L_2 heteroclinic connection will not appear on the map at $C = 3.172$.

Interestingly, it appears as though the existence of heteroclinic connections between L_1 and L_2 Lyapunov orbits that possess characteristics of the nearby distant prograde orbit, i.e., a natural transfer between LPOs that shadows an intermediate DPO, appears to be strongly related to the existence of invariant manifolds associated with the distant prograde orbits. This potential connection between orbit structures is clearly

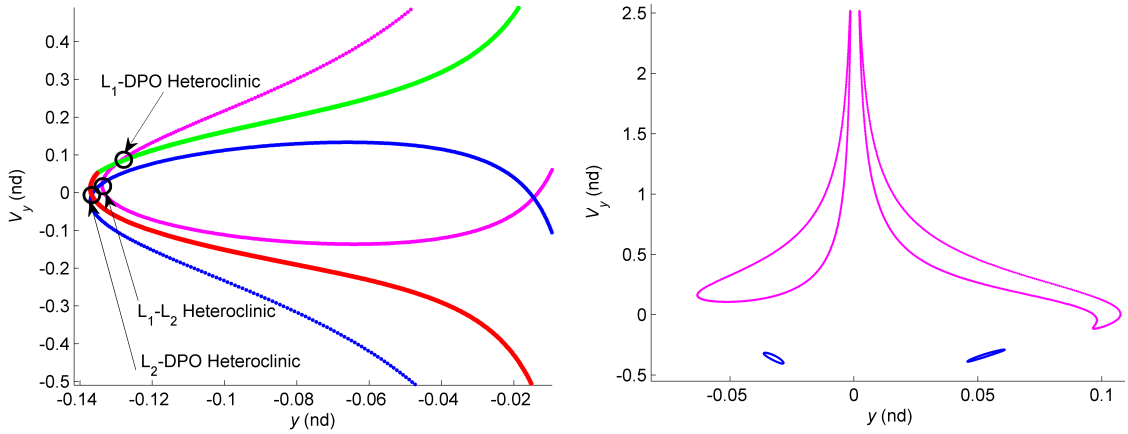

(a) $C = 3.12$ (b) $C = 3.172$

Figure 3.13. Poincaré Maps Highlighting the Existence ($C = 3.12$) and Non-Existence ($C = 3.172$) of a Heteroclinic Connection between L_1 and L_2 Lyapunov Orbits

highlighted by the stability-energy plot in Figure 3.9, demonstrating the usefulness of this type of representation.

3.4 Three-Dimensional Periodic Libration Point Orbits in the CR3BP

The existence of periodic motion in the vicinity of the collinear libration points is not limited to the xy-plane. In fact, a variety of 3D libration point orbits are known to exist and are easily generated using either a single or multiple shooting corrections scheme. One of the most common examples of three-dimensional, periodic orbits near the collinear libration points are 'halo' orbits. These orbits were first introduced for astrodynamics applications by Robert Farquhar in his Ph.D. dissertation in 1968 [71]. Numerous other researchers have subsequently investigated these orbits and they have served as the basis for spacecraft trajectories in a number of successful missions [13, 20, 21].

Three-dimensional halo trajectories are symmetric across the xz-plane. Halo orbits bifurcate from the family of Lyapunov orbits, that is, a common orbit exists

in both the planar, periodic Lyapunov family as well as the halo family of three-dimensional periodic orbits. The two families intersect at this one single orbit, i.e., the bifurcating orbit. A change in stability, as reflected in the eigenvalues of the monodromy matrix, indicates the presence of a bifurcating orbit. Recall that the stability properties change whenever the eigenvalues depart from or arrive at the unit circle in the complex plane.

A strategy that is an extension of the single shooting scheme used to compute planar, periodic Lyapunov orbits, is employed to determine three-dimensional, periodic halo orbits. Once the bifurcating Lyapunov orbit is identified, a corrections process with continuation is employed to compute a three-dimensional halo orbit. In the corrections process to compute a 3D, periodic orbit, the out-of-plane component, z, is fixed at a specific value. The value of z at the initiation of the corrections process is also employed as the continuation parameter. The initial state that produces the bifurcating orbit is perturbed by a small distance Δz in the z-direction and used as the initial guess to compute the out-of-plane halo orbit. Then, the appropriate variations in the initial state yield a three-dimensional, periodic halo orbit. Each halo orbit is uniquely characterized by the orbit's maximum z-excursion measured relative to the xy-plane, i.e., the A_z parameter. As in the case of the planar periodic orbits, once a halo orbit is calculated, it is desirable to generate a family of orbits with the same characteristics. A corrections scheme with continuation is employed to generate a family of halo orbits. In this analysis, to compute the next orbit in the family from the previous one, a fixed step is initiated in the z-direction and the corrections process is repeated at each step to yield a new three-dimensional halo orbit. The form of the mathematical model for the CR3BP lends itself to two types of analytical symmetry: time-invariance symmetry and xy-plane symmetry [72]. That is, if the independent variable, time (τ), is transformed to $t = -\tau$, it is clear that, if $[x \;\; y \;\; z \;\; \dot{x} \;\; \dot{y} \;\; \dot{z}]^T$ satisfies the EOMs for $\Delta\tau > 0$, then $[x \;\; -y \;\; z \;\; -\dot{x} \;\; \dot{y} \;\; -\dot{z}]^T$ satisfies the EOMs for $\Delta\tau < 0$. Two families also exist such that, if $[x \;\; y \;\; z \;\; \dot{x} \;\; \dot{y} \;\; \dot{z}]^T$ satisfies the equations of motion, then so does $[x \;\; y \;\; -z \;\; \dot{x} \;\; \dot{y} \;\; -\dot{z}]^T$. Thus, due to the xy-plane symmetry property,

each of these out-of-plane orbits is associated with a mirror image trajectory across the xy-plane. The 'northern' halo orbits extend in the positive z-direction and the 'southern' halo family expands along the negative z-direction. Representative members of families of northern halo orbits in the vicinity of the collinear libration points appear in Figure 3.14 for the Earth-Moon system. For further reference, Table 3.4 includes the non-zero initial conditions, period, and value of Jacobi constant for the smallest and largest members of each of the halo families represented in Figure 3.14. Note that the largest halo orbit plotted in these figures is not the termination of the family; it is simply the last orbit computed in the continuation process. Recall that, at a crossing of the xz-plane, $y = \dot{x} = \dot{z} = 0$ due to periodicity.

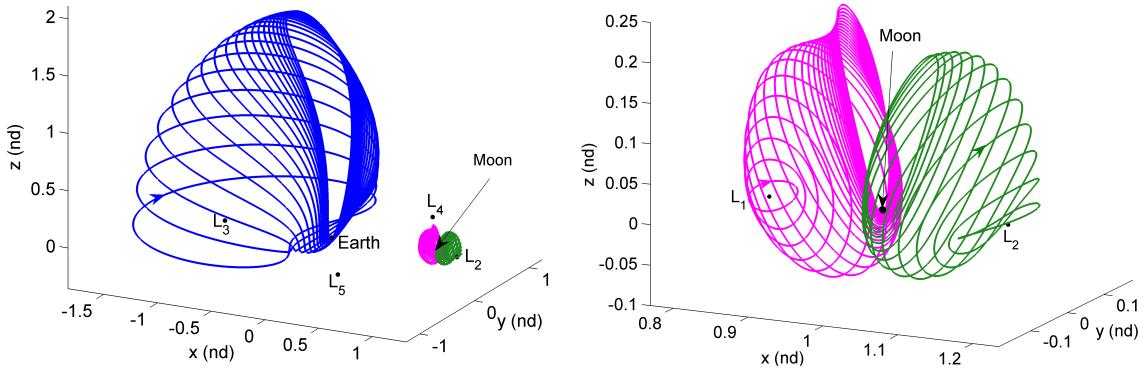

(a) L_1, L_2, and L_3 Halo Families (b) Zoomed-View of L_1 and L_2 Halo Families

Figure 3.14. Three-Dimensional, Periodic, Halo Orbits in the vicinity of L_1, L_2, and L_3 in the Earth-Moon System Plotted in the Rotating Reference Frame

Families of Lyapunov orbits include additional bifurcating orbits to other three-dimensional, periodic orbits in the vicinity of the collinear libration points, i.e., axial and vertical orbits [48, 55]. These families of planar and three-dimensional periodic orbits have been investigated by numerous researchers in the last three decades, and extensive literature is available on these orbits and their computation. It is also well known that these orbits exist for all values of the mass fraction μ and are now employed in a wide variety of applications in mission design.

Table 3.4 Non-Zero Initial Conditions and Jacobi Constant Values of the Smallest and Largest Halo Orbits plotted in Figure 3.14

Halo orbit	x (km)	z (km)	$\dot{y}$ (km/sec)	Period (days)	C
Smallest L_1	3.165079×10^5	4.911168×10^3	0.132168	11.916236	3.172951
Largest L_1	3.588093×10^5	9.538669×10^4	0.092217	8.370736	2.979821
Smallest L_2	4.538545×10^5	5.698212×10^3	-0.160975	14.824071	3.151156
Largest L_2	4.145036×10^5	7.777207×10^4	-0.200804	10.045596	3.015391
Smallest L_3	-6.518874×10^5	2.380426×10^4	1.310270	27.093310	2.422084
Largest L_3	-1.439092×10^5	7.338609×10^5	0.286495	26.596884	1.089065

Three-dimensional, asymmetric, periodic orbits also exist in the vicinity of the equilateral libration points. Examples of periodic motion near L_4 and L_5 are vertical and axial orbits and are generated employing a multiple shooting algorithm with periodicity constraints wrapped in a pseudo-arclength continuation scheme similar to the process that targets short and long period orbits. Families of planar and out-of-plane libration point orbits are not independent; in fact, the mapping of one family leads to another. The dependencies between families have also been addressed by numerous researchers [55]. For instance, planar orbits near L_4 and L_5 share a bifurcating orbit with the family of Lyapunov orbits around L_3; L_4 axial orbits bifurcate from the near-rectilinear L_1 halo orbits, and the L_4 axial family terminates with an L_4 vertical orbit. That is, the most vertical member of the axial family that appears in Figure 3.15(b) is the bifurcating orbit to the family of vertical orbits that appear in Figure 3.15(a). For better visualization, the bifurcating orbit is plotted in black in Figure 3.15(b). Thus, this terminating orbit serves as a basis for computing the L_4 vertical family. The corresponding L_4 and L_5 vertical and axial families can be obtained by reflecting the L_4 orbit families across the xz-plane. Representative L_4 and L_5 vertical and axial orbits are plotted in Figure 3.15.

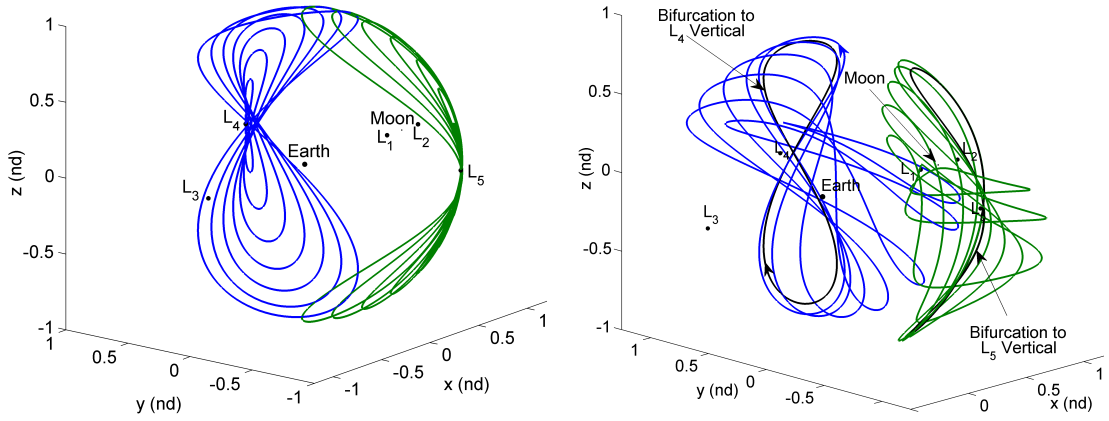

(a) L_4 and L_5 Vertical Families

(b) L_4 and L_5 Axial Families

Figure 3.15. Three-Dimensional, Periodic, Vertical and Axial Orbits in the vicinity of L_4 and L_5 in the Earth-Moon System

Three-dimensional periodic libration point orbits in the Sun-Earth and Earth-Moon systems have been considered for a wide variety of mission design applications, ranging from solar observations [15] to lunar south pole coverage [73]. More recently, P_2-centered orbits, such as distant retrograde orbits, have been proposed as quarantine, or 'storage', orbits in asteroid retrieval mission concepts [74]. However, one of the objectives in this investigation is to expand the orbit architecture in planet-moon systems by incorporating families of resonant orbits and assessing their applicability to trajectory design. Therefore, some background in resonant orbits is necessary, from their more familiar definition in the two-body model to their computation in the CR3BP and higher-fidelity models.

3.5 Resonant Orbits

Resonant orbits in multi-body regimes are the main focus of this investigation. A resonance exists when there is a simple integer relationship between frequencies or periods [75]. Resonances occur under different conditions, such as mean motion resonance, Laplace resonance, secular resonance, and Kozai resonance. However, the

focus of this investigation is orbit-orbit resonance, when the periods involved represent the orbits of two or more bodies. Consider two bodies of arbitrary mass, denoted as A and B and consider the relationship that may exist between the periods of their motion. An orbit-orbit resonance is defined by the ratio p:q, where p indicates the period of motion for body B and q represents the period of motion for body A in resonance with body B. These 'periods' p and q can be rotational and orbital periods of a single body, as in the case of spin-orbit coupling (the orbital period of the Moon is equal to its rotational period), or the orbital periods of two or more bodies, as in the case of orbit-orbit coupling (Neptune and Pluto are in a 3:2 resonance.) In addition to the resonances involving their orbital periods, some of the planets in the solar system are also involved in long-term or secular resonances associated with the precession of the planetary orbits in space [75].

Orbit-orbit resonance does not occur only in Sun-planet systems. Many of the moons in the Saturn and Jupiter systems are in resonance. For example, three of the satellites in the Jupiter system possess orbital periods that are related by an integer ratio. Io is in a 2:1 resonance with Europa, but Europa is also in a 2:1 resonance with Ganymede. These three satellites together move in a configuration labeled as a Laplace resonance. In a Laplace resonance, three or more orbiting bodies possess a simple integer ratio between their orbital periods. In this case, Ganymede, Europa, and Io are in a 1:2:4 orbital resonance. The Saturn system has the widest variety of resonant phenomena. Mimas and Tethys share a 4:2 orbit-orbit resonance, Enceladus and Dione share a 2:1 orbit-orbit resonance and Titan and Hyperion share a 4:3 orbit-orbit resonance. Moreover, almost all the gaps between Saturn's rings can be explained by resonant effects.

3.5.1 Planar Resonant Orbits in the Two-Body Model

In the two-body problem, there are three types of conic sections: ellipses, parabolas, and hyperbolas. Parabolic and hyperbolic trajectories escape the vicinity of the

attractive center, and therefore, are not of interest in the discussion of resonant trajectories, which, by definition, repeat a given configuration. Elliptical orbits, however, are closed and periodic relative to the inertial frame. Circular orbits are a special case of elliptical orbits, and are considered as such. To investigate conic resonance, consider two bodies, A and B, in orbit about a primary body. The primary represents a planet or the Sun; thus, body A is a 'massless' second planet or moon. Body B then models a spacecraft, moon, or asteroid, of much smaller mass than the primary body. Body B is defined to be in orbital resonance with the massless body A when it completes exactly p orbits about the primary in the same time that is required for body A to complete q orbits. For convenience, the primary body is subsequently selected to be a planet, body A is defined as a moon associated with the primary planet, and body B represents a spacecraft. In this definition of orbital resonance, p and q are positive integers, and by convention, p is associated with body B, that is, the spacecraft, and q reflects the period of body A, that is, the moon about the planet. For example, a spacecraft in a 1:2 resonance with Europa completes one revolution around Jupiter in the same time that Europa completes two periods. In an orbit-orbit resonance, the spacecraft and the moon possess periods of revolution that are a simple integer ratio. Assume that the spacecraft and the moon possess orbital periods T_p and T_q respectively, such that ratio between periods is,

$$\frac{p}{q} = \frac{n_p}{n_q} = \frac{\frac{1}{T_p}}{\frac{1}{T_q}} = \frac{T_q}{T_p} \tag{3.1}$$

The mean motion n_i corresponding to body i, is a function of the mass of the planet and the semi-major axis of the orbit, i.e.,

$$n_i = \sqrt{\frac{Gm_1}{a_i^3}} \tag{3.2}$$

where Gm_1 is the gravitational parameter of the planet in this two-body model. The orbital period T_i is proportional to the inverse of the mean motion, n_i. The most straightforward approach to generate a planar resonant orbit in the two-body model is selection of the set of initial conditions at periapsis or apoapsis. In the two-body

problem, periapsis is defined as the point along an elliptical trajectory that is closest to the primary gravitational source, and apoapsis is the point of greatest separation from the attracting center. The six-element initial state vector required to compute a resonant orbit has the form $\bar{q}_0 = [x_0 \quad y_0 \quad z_0 \quad \dot{x}_0 \quad \dot{y}_0 \quad \dot{z}_0]^T$. For a planar resonant orbit $z_0 = \dot{z}_0 = 0$. If the set of initial conditions is selected at an apse location, then $y_0 = 0$, and the initial velocity is entirely in the y-direction, that is, $\dot{x}_0 = 0$. Hence, the initial state reduces to the form $\bar{q}_0 = [x_0 \quad 0 \quad 0 \quad 0 \quad \dot{y}_0 \quad 0]^T$, where x_0 and $\dot{y}_0$ are the initial position along the x-axis and the velocity is completely in the y-direction, respectively. The initial state is expressed in terms of inertial coordinates and can be computed from the expressions for the selected orbital elements, that is,

$$a = \left[\mu_{2B}\left(\frac{P}{2\pi}\right)^2\right]^{\frac{1}{3}} \tag{3.3}$$

$$r = \frac{p}{1 + ecos\theta^*} \tag{3.4}$$

$$p = a(1 - e^2) \tag{3.5}$$

$$V_{in} = \sqrt{2\mu_{2B}\left(\frac{1}{r} - \frac{1}{2a}\right)} \tag{3.6}$$

where p is the semilatus rectum, V_{in} the inertial velocity in the y-direction. The angle θ^* is the true anomaly, that is, the angle that defines the position of the particle along the conic trajectory. At periapsis, $\theta^* = 0°$; at apoapsis $\theta^* = 180°$. In equation (3.3), μ_{2B} is the gravitational parameter in the two-body problem, defined as $\mu_{2B} = Gm_A$, where m_A is the mass of the primary. To initiate a search for resonant orbits, the orbital eccentricity, e, is arbitrarily selected such that, initially, the spacecraft radius at periapsis, r_p, lies between the two primaries, that is, the planet and the moon. For a resonant orbit, let the period, P, be equal to the period of the spacecraft, therefore, it is also a function of the resonant ratio $p{:}q$ and the period of the moon, that is,

$$P = P_{s/c} = \left(\frac{q}{p}\right) P_{moon} \tag{3.7}$$

where $P_{s/c}$ is the period of the spacecraft and P_{moon} is the period of the moon in resonance with the spacecraft. Once the initial state is defined, it is possible to compute the resonant trajectory of interest in the inertial reference frame employing the analytical solution available. However, valuable insight is obtained from a view of this resonant trajectory in a rotating frame. The three axes corresponding to a rotating frame in the two-body model are defined such that the planet and its moon remain stationary along the x-axis, the z-axis is parallel to the orbital angular momentum vector, and the y-axis completes the right-handed triad. With this definition of the rotating frame, the initial state can be transformed from inertial to rotating coordinates using the transformation in equation (2.83).

To illustrate orbital resonance within the context of a two-body model, consider the 1:2 resonant orbit in Figure 3.16. This resonant orbit is computed in the two-body Earth system, where the Moon is temporarily assumed to be massless and orbiting the Earth in a circular orbit ($e = 0$) with a radius equal to the lunar semi-major axis, $a = 384,400$ km. The pericenter of the spacecraft elliptical orbit is selected such that it intersects the Moon's orbit when the spacecraft is at periapsis, r_p. The corresponding initial values for position and velocity are calculated from equations (3.3)-(3.6) using the specified values for a and e. The inertial and rotating views of the 1:2 resonant trajectory in the two-body model are illustrated in Figure 3.16. Recall that in this p:q resonance, the spacecraft completes one revolution around the Earth in the exact same time interval that is required for the Moon to complete two revolutions. In the inertial view, the Moon's trajectory around the Earth is plotted in magenta, and the spacecraft resonant trajectory appears in green.

Resonant orbits viewed from the perspective of the rotating frame offer valuable insight since this view illustrates the relationship between resonance and the frequency of conjunctions [75], in this case, with the Moon. A conjunction occurs when the planet, the moon, and the spacecraft are aligned. Note the relative positions of the Earth, the Moon, and the spacecraft at $t = 0$ in Figure 3.16. In this example, the Earth and the Moon are aligned with the spacecraft at periapsis. A special feature

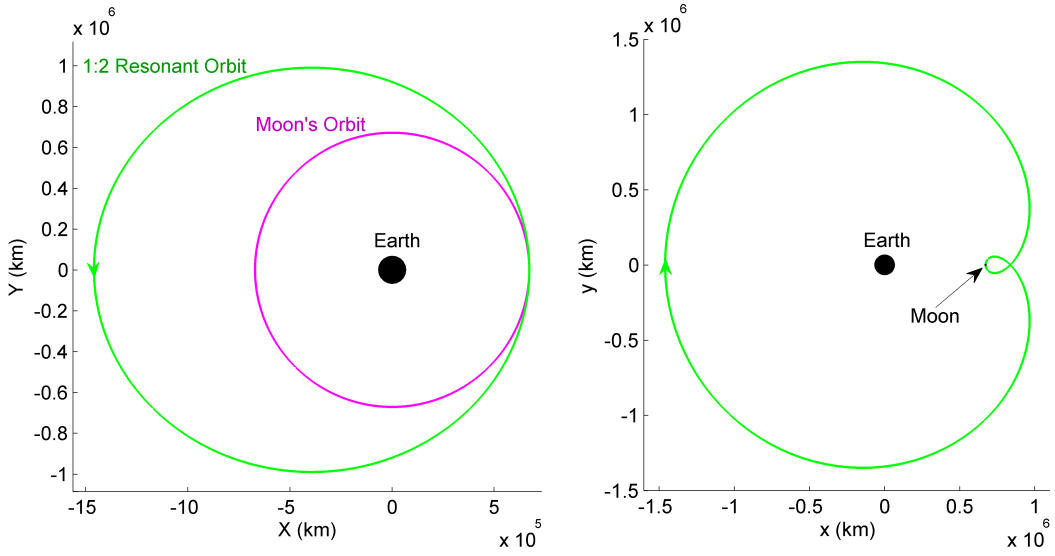

(a) Inertial View (b) Rotating View

Figure 3.16. Inertial and Rotating Views of a Spacecraft Earth Orbit in a 1:2 Resonance with the Moon

of resonant orbits, and one that occurs only in the rotating frame, is the formation of "loops", which indicate the passage of the spacecraft through an apse location. Thus, the number of loops in a resonant trajectory determines p in a p:q resonance. Resonant orbits are categorized based on the p:q ratio. Exterior resonant orbits have a p:q ratio such that $p<q$, while in an interior resonance, the ratio p:q is such that $p>q$.

3.5.2 Planar Resonant Orbits in the CR3BP

The determination of orbital resonance conditions in the CR3BP is more complex than the analysis in terms of conic orbits. In the restricted three-body model, the p:q resonant ratio is not precisely equal to the ratio of the orbital periods corresponding to the bodies in resonance. In a multi-body problem, with the gravity of two or more bodies incorporated in the model, the time to complete a revolution is not even constant. Instead, for a p:q resonance in the circular restricted three-body problem,

the spacecraft completes p orbits around the primary in *approximately* the same time required for the moon to complete q revolutions; thus, the ratio of the orbital periods is not rational, but rather an approximate rational fraction. However, resonant orbits in the CR3BP are still closed, periodic trajectories as observed in the rotating reference frame.

Adding a third gravity field to the two-body model adds perturbations to the trajectory, generally resulting in a orbit that is not closed or periodic. Hence, a strategy is required to compute closed, periodic, resonant orbits in the CR3BP. A targeting scheme, similar to one employed to compute planar, periodic orbits in the vicinity of the Lagrange points, can be applied to the computation of periodic resonant orbits. A reasonably accurate starting estimate for the initial state is generated from the two-body model, but with the state transformed to the rotating reference frame. This starting vector seeds the corrections scheme to target a perpendicular crossing of the x-axis in a nonlinear propagation. Two-dimensional resonant orbits, like Lyapunov orbits, are symmetric across the xz-plane; thus, it is sufficient to investigate only half of the resonant path, and then use symmetry to compute the second half of the orbit. For implementation of the corrections procedure, note that, for most resonant orbits, additional non-perpendicular crossings of the x-axis are likely to occur. The numerical integration process is forced to terminate only at the desired perpendicular crossing, i.e., one half the resonant orbit. There are several ways to construct the algorithm. One method consists of incorporating the period as the stopping condition for the corrections algorithm; that is, if the period of the desired resonant orbit is known, the algorithm can be forced to stop at a time approximately equal to one-half of the period of the resonant orbit. Alternatively, restricting the location of the x-axis crossing is also effective. Once a single, periodic, resonant orbit is determined in the CR3BP, it is possible to generate multiple resonant orbits with the same characteristics, that is, a family of p:q resonant orbits, by employing a continuation method in the corrections scheme. The same strategy is employed to generate almost any family of interior and exterior resonant orbits. Virtually, any p:q resonant ratio exists and

the corresponding resonant orbit can be computed within the context of the CR3BP. Representative members from a selection of planar families of symmetric p:q resonant orbits in the Earth-Moon system are plotted in Figure 3.17. For reference, the corrected non-zero initial state, period, and value of Jacobi constant associated with the orbit in the resonant family that is highlighted in black in Figure 3.17 are listed in Table 3.5. Recall that the periodic orbits in Figure 3.17 are planar and symmetric, i.e., $y_0 = z_0 = \dot{x}_0 = \dot{z}_0$.

Table 3.5 Initial Conditions and Jacobi Constant Values Corresponding to Highlighted p:q Resonant Orbits in Figure 3.17

Resonant Orbit	x (km)	$\dot{y}$ (km/sec)	Period (days)	C
1:1	6.183349×10^4	3.134709	27.275025	2.113788
1:2	6.137113×10^4	3.207443	54.503233	1.753856
1:3	1.518035×10^6	-3.883575	81.705406	1.734273
1:4	1.839938×10^6	-4.756000	109.07019	1.780249
2:1	5.583800×10^4	3.231936	27.285047	2.650281
2:2	6.183349×10^4	3.134709	27.275025	2.113788
2:3	1.852180×10^5	1.366602	80.764832	2.500500
2:4	6.137113×10^4	3.207443	54.503233	1.753856
3:1	7.878624×10^3	7.795142	27.285691	2.656044
3:2	1.545850×10^5	1.490095	54.549560	2.856750
3:3	6.183349×10^4	3.134709	27.275025	2.113788
3:4	2.195762×10^5	1.094060	107.28509	2.631025
4:1	1.045610×10^5	1.870956	27.280582	3.725914
4:2	5.583800×10^4	3.231936	27.285047	2.650281
4:3	5.340899×10^5	-1.049612	81.502603	2.351093
4:4	6.183349×10^4	3.134709	27.275025	2.113788

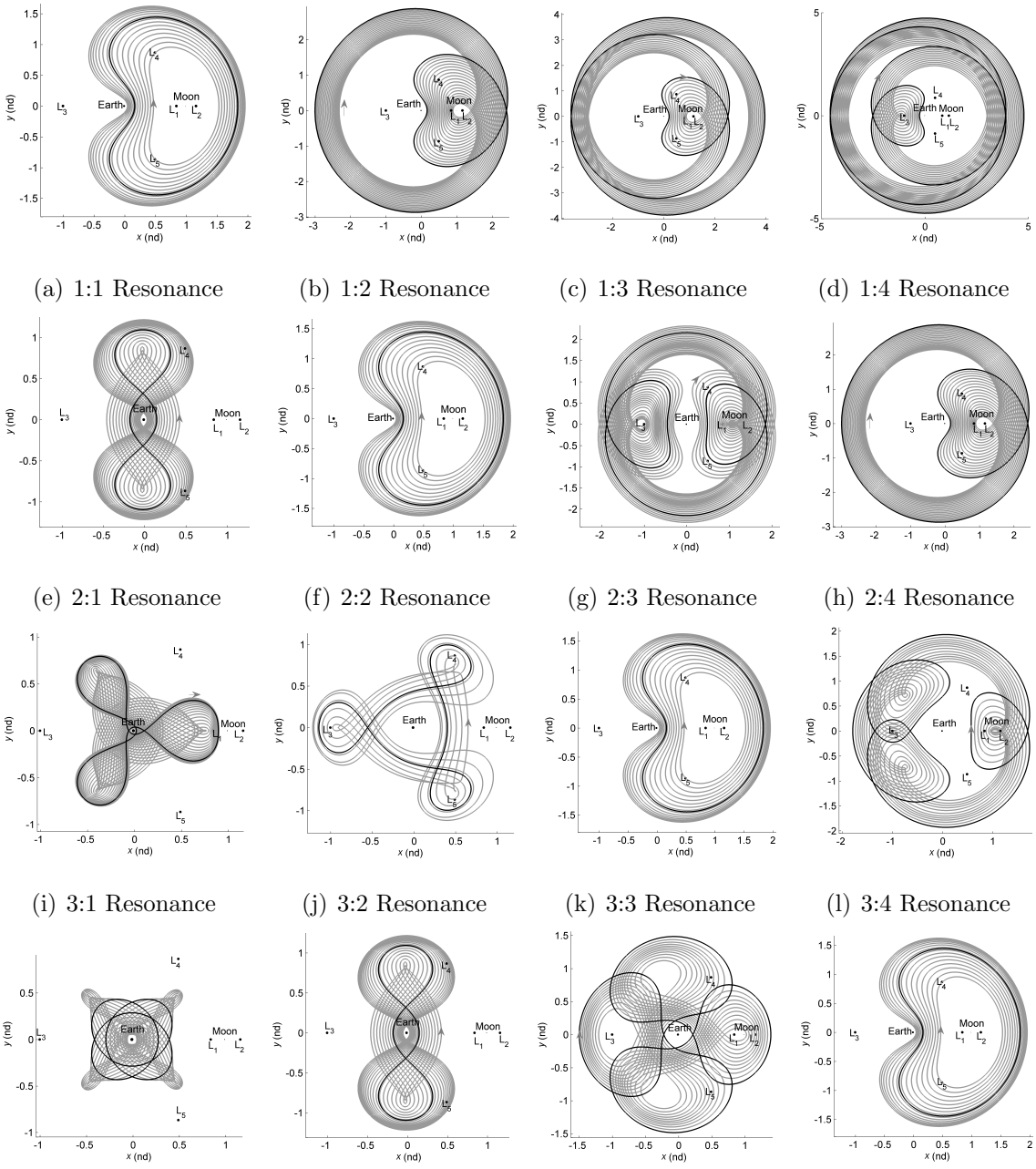

(a) 1:1 Resonance (b) 1:2 Resonance (c) 1:3 Resonance (d) 1:4 Resonance

(e) 2:1 Resonance (f) 2:2 Resonance (g) 2:3 Resonance (h) 2:4 Resonance

(i) 3:1 Resonance (j) 3:2 Resonance (k) 3:3 Resonance (l) 3:4 Resonance

(m) 4:1 Resonance (n) 4:2 Resonance (o) 4:3 Resonance (p) 4:4 Resonance

Figure 3.17. Representative Members in 2D Families of p:q Resonant Orbits in the Earth-Moon System Plotted in the Rotating Reference Frame

3.5.3 Three-Dimensional Resonant Orbits in the CR3BP

Similar to families of planar Lyapunov orbits, families of 2D resonant orbits also include bifurcating orbits to three-dimensional, periodic resonant orbits. These bifurcating orbits can be identified by examining the eigenvalues of the monodromy matrix corresponding to each orbit in the family. Recall that the presence of a bifurcating orbit is indicated by a change in stability, as reflected in the eigenvalues of the monodromy matrix. Once the bifurcating orbit is identified, it is possible to target these out-of-plane families by employing an algorithm based on the same scheme used to compute halo orbits from a bifurcating Lyapunov orbit. First, the resonant orbit that bifurcates to a different family of orbits is isolated by examining the eigenvalues of the monodromy matrix computed for each orbit in the planar family, and identifying a change in the characteristics of these eigenvalues. The bifurcating orbit is then slightly perturbed in the z-direction and the resulting state seeds the corrections scheme to target a three-dimensional, symmetric resonant orbit. As in the case of planar resonant orbits, additional non-perpendicular crossings may occur along these families of 3D resonant orbits. Thus, the corrections algorithm targets a perpendicular crossing. Representative members from a selection of planar (gray) and 3D (blue) families of symmetric p:q resonant orbits in the Earth-Moon system are plotted in Figure 3.18. Note that two bifurcating orbits exist in the planar family of 2:3 resonant orbits. Thus, two out-of-plane families of 2:3 resonant orbits are constructed and representative members are illustrated in Figure 3.18(e) and Figure 3.18(f).

The families of three-dimensional orbits illustrated in Figure 3.18 represent out-of-plane resonant orbits, symmetric across the xz-plane, and are computed similarly to halo orbits, that is, by adding a small perturbation in the initial z-component. The initial state associated with any of these symmetric 3D resonant orbits has the form $\bar{x}_0 = [x_0 \;\; 0 \;\; z_0 \;\; 0 \;\; \dot{y}_0 \;\; 0]$. However, asymmetric 3D resonant orbits also exist and can be computed employing a variable-time multiple shooting corrections scheme with periodicity constraints. These 3D asymmetric resonant orbits are analogous to

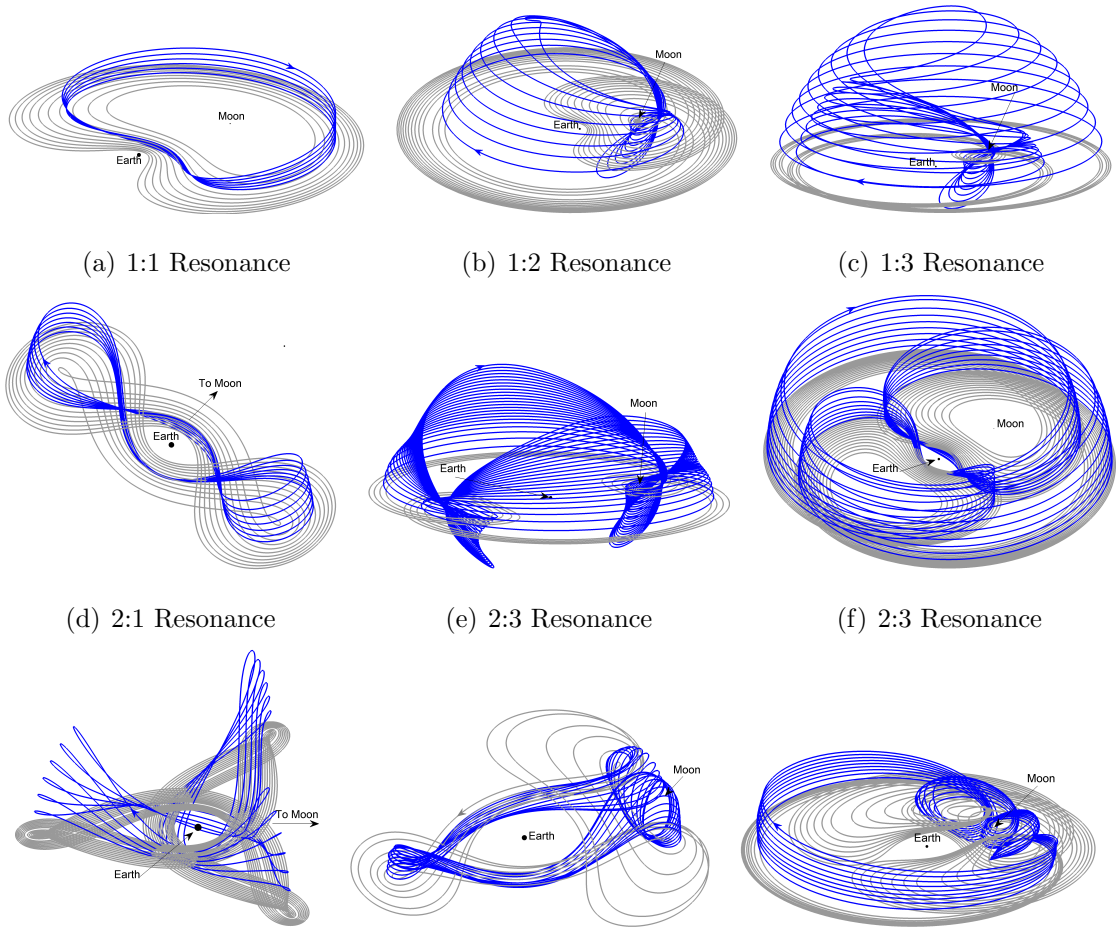

(a) 1:1 Resonance (b) 1:2 Resonance (c) 1:3 Resonance

(d) 2:1 Resonance (e) 2:3 Resonance (f) 2:3 Resonance

(g) 3:1 Resonance (h) 3:2 Resonance (i) 3:4 Resonance

Figure 3.18. Sample Orbits in 2D and 3D Families of p:q Resonant Orbits in the Earth-Moon System

3D axial libration point orbits and are thus termed 'axial' resonant orbits. Axial resonant orbits are calculated by slightly perturbing the bifurcating orbit in the $\dot{z}$-direction. The resulting initial state of the form $\bar{x}_0 = [x_0 \;\; 0 \;\; 0 \;\; 0 \;\; \dot{y}_0 \;\; \dot{z}_0]$ seeds the corrections scheme to target a 3D asymmetric resonant orbit by enforcing continuity in position and velocity throughout the entire path as well as periodicity between the initial and final states. Representative members from a selection of 3D families of p:q axial resonant orbits in the Earth-Moon system are plotted in blue in Figure 3.19. For reference, selected planar orbits are plotted in gray.

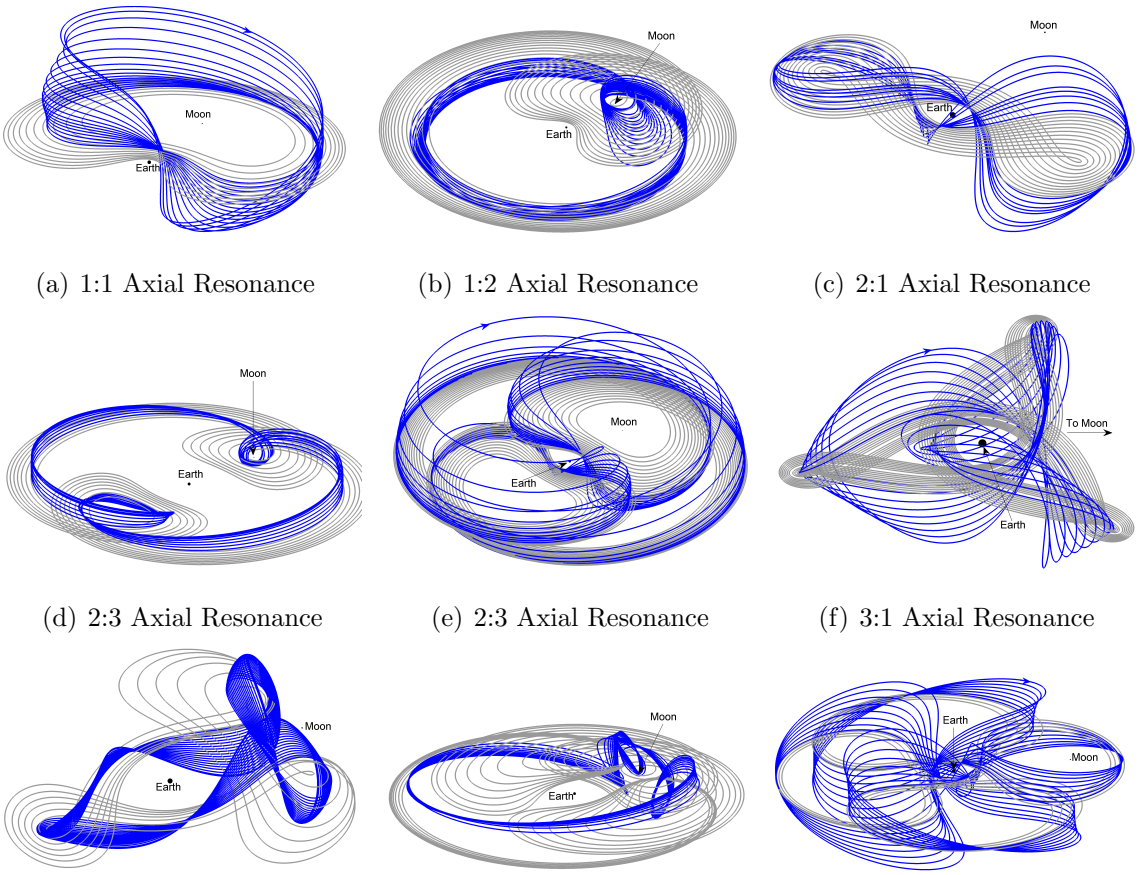

(a) 1:1 Axial Resonance (b) 1:2 Axial Resonance (c) 2:1 Axial Resonance

(d) 2:3 Axial Resonance (e) 2:3 Axial Resonance (f) 3:1 Axial Resonance

(g) 3:2 Axial Resonance (h) 3:4 Axial Resonance (i) 4:3 Axial Resonance

Figure 3.19. Sample Orbits in 2D (Gray) and 3D (Blue) Families of Axial Resonant Orbits in the Earth-Moon System

3.5.4 Three-Dimensional Resonant Orbits in the Ephemeris Model

The restricted three-body model serves as a powerful tool to generate preliminary transfer trajectories in this analysis as it allows periodic orbits and invariant manifolds to be directly leveraged. However, to assess the impact of a higher-fidelity dynamical model, the CR3BP resonant orbits are transitioned to a dynamical model that incorporates n-body dynamics and planetary ephemerides. Note that periodic orbits in the CR3BP exist as quasi-periodic trajectories in a higher-fidelity model. To transition a resonant orbit to an ephemeris model, begin with the converged solution in the CR3BP. The orbit is first discretized into a series of patch points; each patch

point is comprised of the time and the 6D state vector at a selected point along the trajectory. The series of patch points along the reference orbit in the CR3BP are then *stacked* to construct an orbit with a desired number of revolutions in the ephemeris model. Note that certain interior resonant trajectories that pass near the primaries are more sensitive and, thus, require a larger number of patch points for convergence. Using the appropriate transformations and an initial Julian date, each patch point is transformed into an Earth-centered, inertial Earth J2000 coordinate frame and the n-body relative equations of motion detailed in Section 2.1 are implemented within a multiple shooting algorithm that yields the desired continuous trajectory in position and velocity in the ephemeris model. To illustrate this transition process, a representative member from each resonant family is selected and using the trajectory in the CR3BP as the initial guess, the orbit is numerically generated in an Earth-Moon-Sun point mass dynamical model incorporating the JPL DE405 ephemerides for the locations of the relevant bodies. The resulting 3D quasi-periodic resonant orbits, plotted in purple, appear in Figure 3.20. For better visualization, only the planar projection is illustrated. Note that the period of these orbits and, thus, the resonant ratio, is preserved when transitioned to the ephemeris model.

A particular class of resonant orbits in the Earth-Moon system has already proven quite useful in trajectory design for a specific mission scenario. The IBEX spacecraft is currently located in a long-term stable Earth orbit in resonance with the Moon's orbit. The selection of this particular orbit for the extended IBEX mission was based primarily on three factors: minimization of the radiation dose, improvement of science collection and avoidance of long eclipses [76]. Based on this criteria, the spacecraft was recently maneuvered from its nominal trajectory into this new stable orbit in a 3:1 resonance with the Moon. The extended orbit for the IBEX spacecraft resembles one of the 3D orbits plotted in Figure 3.18(g). This type of resonant orbit, along with other lunar resonant orbits, are likely useful for many types of mission trajectories, including weather and space science applications [77]. Note that, although the resonant families illustrated in Figures 3.17-3.20 are Earth-Moon

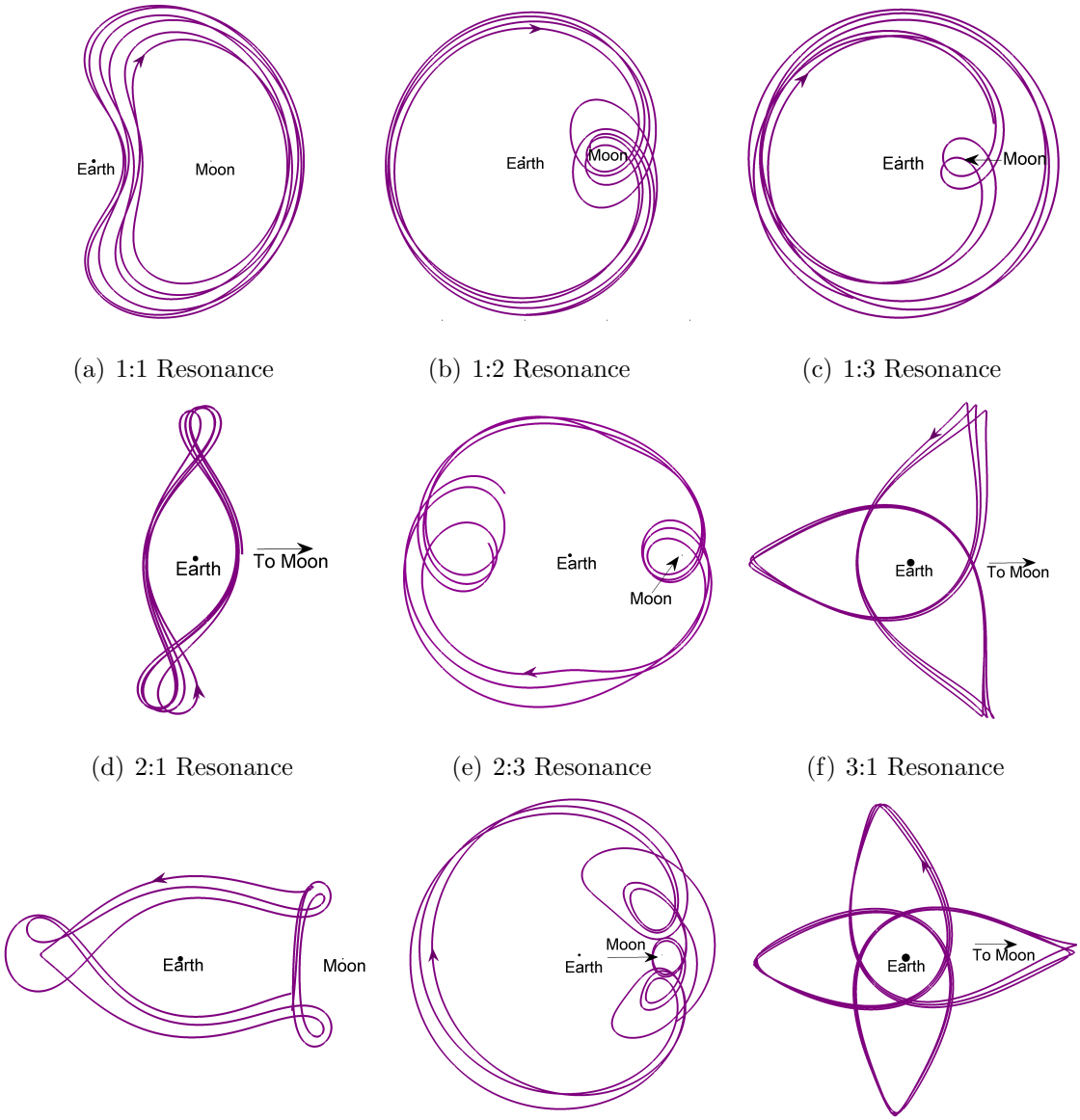

(a) 1:1 Resonance (b) 1:2 Resonance (c) 1:3 Resonance

(d) 2:1 Resonance (e) 2:3 Resonance (f) 3:1 Resonance

(g) 3:2 Resonance (h) 3:4 Resonance (i) 4:1 Resonance

Figure 3.20. xy-Views of Representative 3D Resonant Orbits in the Ephemeris Model

periodic orbits, similar families of 3D resonant orbits are straightforwardly computed for different values of the mass fraction μ [39, 40, 78]. For instance, a family of planar 3:4 resonant orbits similar to the family that appears in Figure 3.18(i) is the focus of the Europa Orbiter end-game scenario [34]. Thus, resonant orbits are not only

of interest from a dynamical analysis perspective but also for applications to meet current mission design requirements.

4. APPLICATIONS OF RESONANT ORBITS TO TRAJECTORY DESIGN

A goal in this investigation is the incorporation of resonant orbits into a transfer trajectory design process to enable the construction of cost efficient, and potentially novel, transfer paths between selected orbits. The proposed trajectory design capability relies on the exploitation of invariant manifolds as the main transfer mechanisms and Poincaré maps to aid in the visualization of these manifold trajectories. In this chapter, a general description of the transfer design strategy is summarized. The role of resonant orbits in the design of planar and three-dimensional transfer trajectories with specific itineraries in multi-body systems is then assessed through a variety of astrodynamics applications.

4.1 Basic Design Strategy: Invariant Manifolds and Poincaré Maps

A priori knowledge of any manifold structure improves the efficiency of the trajectory design process in multi-body regimes. Invariant manifold arcs with specific patterns for different values of the mass fraction, μ, are sought in this investigation to facilitate the design of transfer trajectories with desired itineraries. The invariant manifolds associated with libration point orbits near L_1 and L_2 possess very well-defined dynamical structures. The stable and unstable trajectories form 'tubes' of incoming and outgoing trajectories to and from the periodic orbit, respectively. Recall the family of planar L_1 Lyapunov orbits in Figure 3.1. As a representative example of the natural manifold flow, the global invariant manifolds corresponding to the smallest Lyapunov orbit in the figure from the L_1 family are computed and plotted in Figure 4.1. The magenta (W^{u-}) and red (W^{u+}) trajectories correspond to trajectories comprising the unstable manifold calculated from the negative and

positive directions along the unstable eigenvector, respectively; the blue (W^{s-}) and green (W^{s+}) arcs reflect the trajectories along the stable manifold, computed from the negative and positive directions along the stable eigenvector, respectively. As illustrated in Figure 4.1, a subset of manifold trajectories, W^{u-} and W^{s-} travel to the vicinity of the Earth, and the other subset, W^{u+} and W^{s+}, flow towards the Moon. To better indentify the manifold structure, it is desirable to compute the trajectories from multiple fixed points along the orbit. For illustration purposes, a total of 40 (evenly-spaced in time) fixed points are selected along the periodic orbit near L_1 and the propagation time to construct both the stable and the unstable manifold is equal to 21.7 days. An offset value $\tilde{d}$ equal to 30 km is a reasonable choice for periodic orbits in the Earth-Moon system.

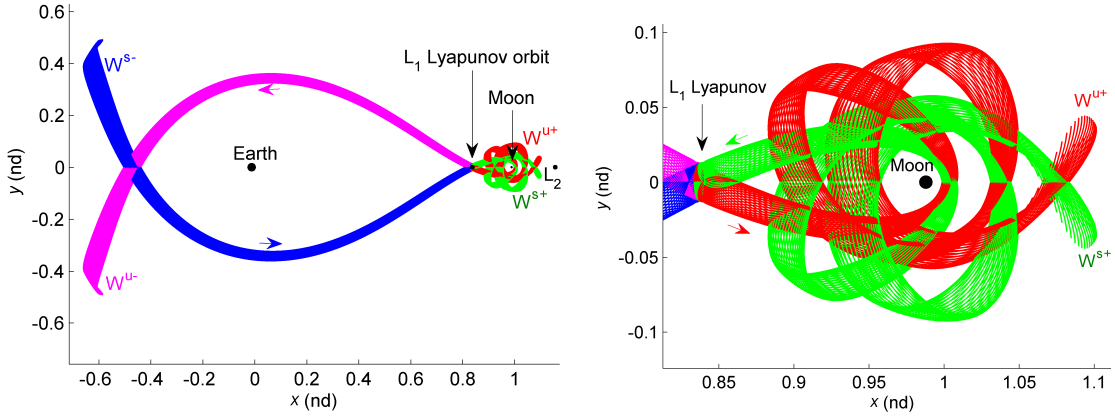

(a) Stable and Unstable Manifolds

(b) Zoomed-View Near the Moon

Figure 4.1. Global Stable and Unstable Manifolds Associated with a Lyapunov Orbit in the Vicinity of L_1 in the Earth-Moon System at a Given Energy Level

In contrast to the invariant manifolds associated with libration point orbits, the trajectories along the invariant manifolds corresponding to resonant orbits possess their own distinctive behavior. However, the arcs are tangled, so plotting these paths in position space does not offer any clear insight. Thus, it is necessary to incorporate a technique that offers a different representation of these manifold trajectories. Maps

that identify, and potentially isolate, the manifold trajectories aid in visualization and offer clues concerning the relationships between these manifolds and other structures in the phase space. To illustrate this behavior, consider the 1:2 unstable resonant orbit in the Earth-Moon system plotted in Figure 4.2(a). A representation of the invariant manifolds emanating from the 1:2 resonant orbit appears in configuration space in Figure 4.2(b). The trajectories on the stable manifold are plotted in blue and the trajectories on the unstable manifold are represented in magenta. Unlike the stable and unstable manifolds associated with libration point orbits, the manifolds associated with resonant orbits do not form tube-like structures when propagated forward and backward in time. It is apparent that these trajectories travel between the interior and exterior regions, but it is almost impossible to distinguish any particular trajectory from an x-y position representation. To better visualize the natural flow associated with resonant orbits, a Poincaré map is constructed.

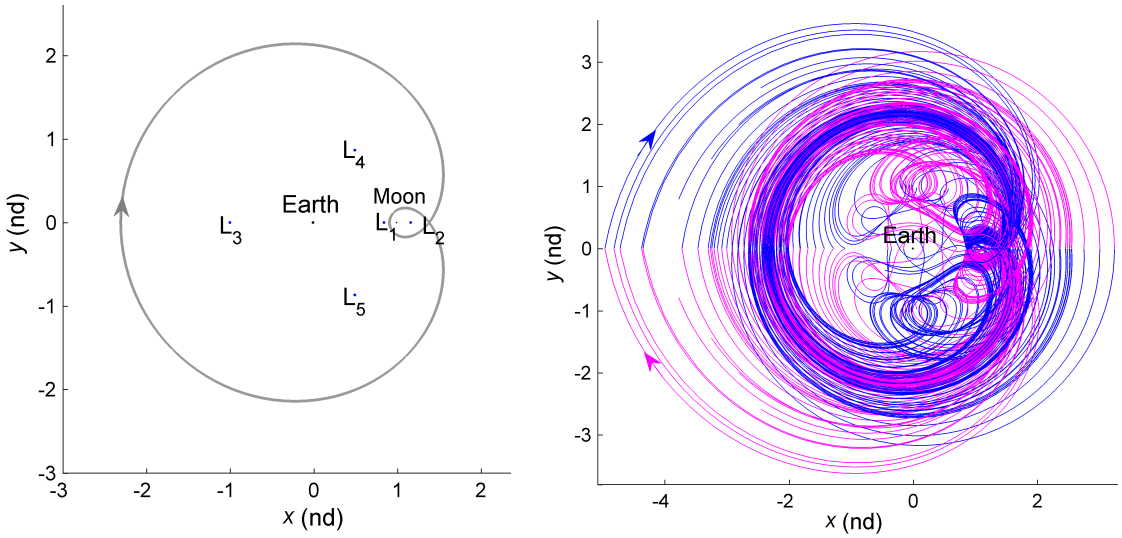

(a) 1:2 Resonant Orbit

(b) Stable and Unstable Manifolds

Figure 4.2. Position Representation of the Invariant Manifolds Associated with a 1:2 Unstable Resonant Orbit in the Earth-Moon System

The hyperplane Σ that defines the surface of section is placed to intersect the unstable orbit of interest; in this example, Σ is located such that $y = 0$. Then, the manifold trajectories originating at each fixed point along the unstable resonant orbit are integrated backward and forward in time to compute the global stable and unstable manifolds, and the returns to the map of each manifold trajectory are recorded and plotted using a combination of position and velocity states, i.e., $x - \dot{x}$. The resulting maps appear in Figure 4.3. Each dot represents a return to the map; the blue dots correspond to returns of the stable manifold arcs and the magenta dots represent crossings of the unstable manifold trajectories. For better visualization, the surface of section is split into two smaller sections; subsection (a) on the negative x-axis, illustrated in Figure 4.3(a), and subsection (b) near the smaller primary on the positive x-axis, illustrated in Figure 4.3(b). For reference, the two fixed points associated with the 1:2 resonant orbit appear on the maps as larger black dots.

Although the relationship between the manifolds representing the 1:2 resonant orbit is not initially apparent, the manifold structure is visually more apparent in a surface of section. In particular, the intersection of the manifold 'lines' on the map are key to the design of natural transfers between resonant orbits. In the planar problem, an intersection on the map implies an intersection in phase space, resulting in a natural transfer between two or more unstable periodic orbits with no maneuvers. Additionally, maps also aid in the computation of transfer trajectories that include maneuvers when a natural connection is not available. In such cases, an estimate for the size of the maneuver that is required to connect the arcs can also be discerned from the map, allowing for the examination of potential regions where the required ΔV may be smaller.

4.2 Arc Blending Scheme: End-to-End Transfer Design Process

The availability of low-cost transfer trajectories is enabled through the exploitation of the invariant manifolds. Given the complexity of resonant manifold structures

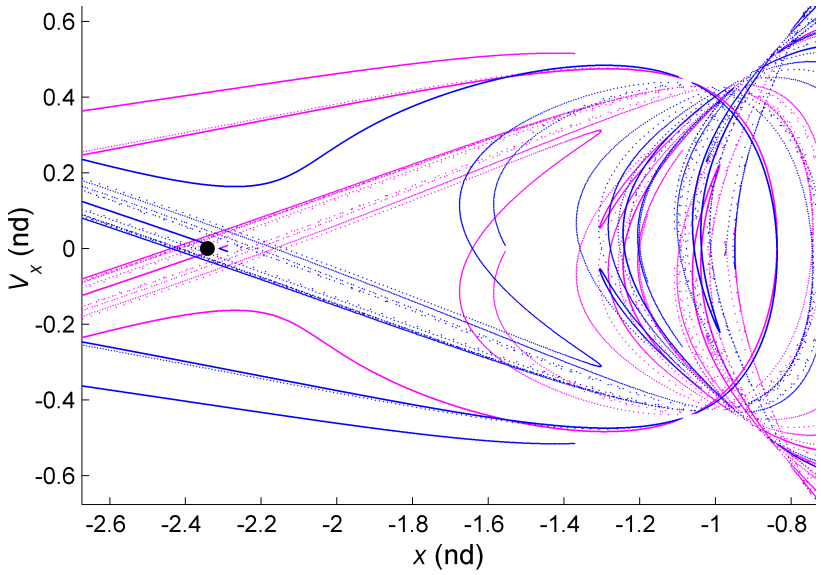

(a) Poincaré Map ($x < 0$)

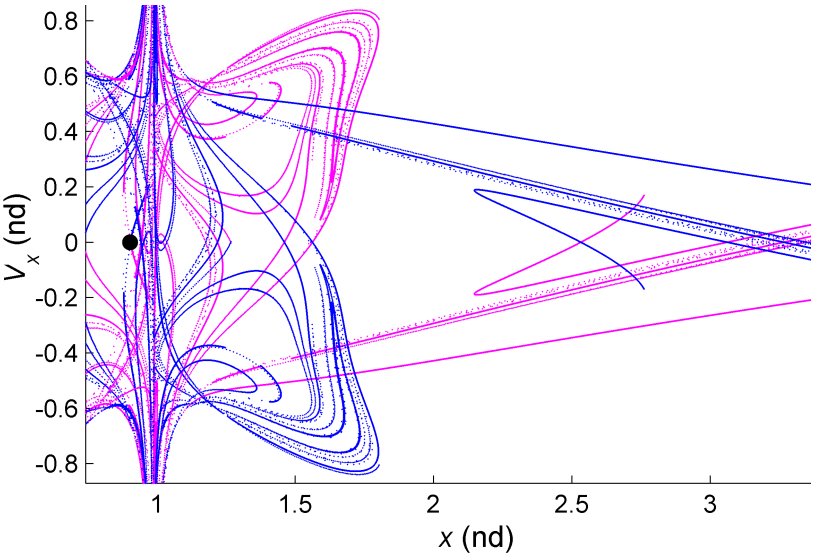

(b) Poincaré Map ($x > 0$)

Figure 4.3. Position-Velocity Representation of the Invariant Manifolds Associated with a 1:2 Unstable Resonant Orbit on a Surface of Section Defined at $y = 0$

in phase space, an alternative visualization technique is sought to reveal the flow in the vicinity of periodic orbits. From the maps, intermediate arcs are identified and

employed as initial guesses for the construction of transfer trajectories. Such intermediate arcs may be associated with resonant or non-resonant orbits, depending on the application and type of transfer trajectory to be constructed. Once the arcs are obtained from the Poincaré maps, a robust and versatile corrections process is implemented to remove the discontinuities that exist in position and/or velocity between the connecting arcs. The result is a continuous trajectory that may be natural or include maneuvers if a cost-free option is not available. In most trajectory design scenarios, a natural, maneuver-free end-to-end trajectory may not be available. In such scenarios, a local optimization algorithm is also employed with the objective of reducing the associated transfer cost to a minimum. Once a continuous, end-to-end transfer trajectory is constructed exploiting the invariant manifolds associated with resonant orbits, constrained minimization is applied via a Sequential Quadratic Programming (SQP) optimization algorithm to further decrease the maneuver cost to a local minimum. The steps involved in the transfer design process are generally defined as follows:

- *Step 1.* Select and construct the initial and final orbits that serve as the starting and ending locations on the transfer path. Such orbits include, but are not limited to, resonant orbits, libration point orbits, distant periodic orbits, and two-body orbits, such as low and geostationary Earth orbits. The stability associated with these orbits is not a decision factor in the selection process, as intermediate maneuvers are incorporated throughout the transfer path to correct for velocity discontinuities when necessary. Note, however, that the availability of stable and unstable manifolds emanating from the initial and/or final orbits significantly reduces the cost of transfer.

- *Step 2.* Select the unstable periodic orbits that serve as transfer mechanisms, or connectors, between the initial and final orbits. Resonant orbits are the focus of this investigation and, thus, most of the design examples exclusively exploit resonant orbits as the connecting arcs, but the selection of these intermediate

orbits is certainly not limited to resonant orbits. The corrections algorithm is generalized to admit any periodic orbit and any intermediate arc.

- *Step 3.* Generate a number of stable and unstable manifold trajectories associated with the selected intermediate orbit(s) by stepping off selected fixed points in the direction of the stable and unstable eigenvectors.

- *Step 4.* Define the appropriate surface(s) of section, e.g., $y = 0$, to represent position-velocity maps $(x - \dot{x})$, or $\bar{r} \cdot \dot{\bar{r}} = 0$ to construct an apse map, where $\bar{r}$ is defined as the radial distance between the spacecraft and a primary and $\dot{\bar{r}}$ is the speed of the spacecraft relative to the rotating frame. After numerically integrating the stable and unstable manifold trajectories, record and plot the returns of each trajectory to the surface(s) of section.

- *Step 5.* From the appropriate map, identify potential transitions for each transfer phase and obtain the corresponding intermediate arcs, i.e., integrate the six states associated with the selected return to the map in forward time to produce the stable manifold trajectory and in backward time to generate the unstable manifold arc. Recall that feasible connecting arcs are located near the intersections of stable and unstable manifold lines on the maps.

- *Step 6.* Decompose the initial and final periodic orbits as well as the selected intermediate arcs into smaller segments. With the aid of a multiple shooting corrections algorithm, blend the subarcs into a trajectory that is continuous in position, allowing for intermediate ΔV maneuvers, if desired, at specified patch points. Additional design constraints, such as maximum ΔV or time-of-flight, can be simultaneously applied to maintain the cost and the TOF values within desired bounds.

- *Step 7.* Post-processing options include (i) the application of direct optimization techniques to the constructed point solution to produce a locally optimal trajectory, and (ii) the validation of the solutions initially generated in the three-body

model by transitioning the transfer path to a higher-fidelity model that includes planetary ephemerides and solar gravitational effects.

- *Step 8.* To add versatility to the proposed design method, an additional system translation technique can be applied to allow transfer trajectories in a given three-body system to be quickly translated to other systems, i.e., sample transfers are quickly generated in a Sun-planet or planet-moon system directly from a transfer initially calculated the Earth-Moon system.

In summary, identification of the unstable resonant orbits, recognition of the resonance transitions, computation of suitable trajectory arcs, and blending of the arcs into a variable trajectory that yields a complete design is the overarching goal. A variety of transfer design scenarios in multi-body systems are considered in this investigation. The design process varies depending on the design case, but, generally, steps 1-8 allow the computation of trajectories with desired patterns and itineraries, which may be natural or include maneuvers.

4.3 Resonance Transition in the Saturnian System

The resonance transition problem in a multi-body gravitational environment has been approached from different angles by a number of researchers [31–33, 79]. The motivation for the results presented in this section, however, is the previous work regarding the analysis of the invariant manifolds emanating from resonant orbits involved in the Jupiter Europa Orbiter end-game scenario encounters [28, 34–36, 39]. One obvious extension to the analysis in the Jovian regime is the application to other multi-body systems, such as the Saturn-Titan system. A major difference between the Saturn-Titan system and the Jupiter-Europa system is the presence of only a single major moon, i.e., Titan. The mass parameter, μ, is an order of magnitude larger in the Saturn-Titan system such that the effect of Titan's gravity on the spacecraft is much larger than the effect of Europa in the Jupiter-Europa system. This difference in μ also affects the stability of certain orbits in the Saturn-Titan system; unstable resonant

orbits are highly sensitive to small perturbations, potentially delivering useful transfer scenarios. In contrast, stable resonant orbits can also be a source of long term stability and are well suited for the design of long term stable spacecraft orbits.

A transfer design process that blends manifold arcs associated with unstable resonant orbits is employed to produce continuous paths that transition between interior and exterior resonances in the Saturn-Titan system at a specific energy level. Natural, cost-free transfers between resonant and libration point orbits are computed with the aid of Poincaré maps and invariant manifolds. To further illustrate the application of dynamical systems theory, a periodic orbit that cycles indefinitely between two resonances is also detailed. As an illustrative example of exploiting the natural dynamics of resonant orbits to construct low-ΔV transfers, the problem of accessing Hyperion from an orbit resonant with Titan is explored. To demonstrate that the transfers use near-minimum propellant by shadowing the invariant manifolds associated with unstable resonant orbits, an optimization algorithm is applied to generate a locally optimal transfer trajectory from the resonant orbit of interest to Hyperion's orbit, which is then compared to the manifold transfer.

4.3.1 Planar Natural Transfers: Resonant Transfers and Chains

Unstable resonant orbits in the Saturn-Titan system serve as the focus in the following examples and Poincaré maps are constructed to display the associated stable and unstable manifolds. Once potential resonance transitions are identified from the maps, a multiple shooting scheme is employed to blend the periodic orbits and the manifolds arcs into a continuous, ΔV-free path.

Design of Planar Transfers

Consider the exterior 3:4 orbit that is in resonance with Titan illustrated in Figure 4.4. The non-zero initial state, the Jacobi constant value, and the unstable eigenvalue associated with this planar resonant orbit are listed in Table 4.1. The

invariant manifolds associated with this 3:4 resonant trajectory are computed using an offset value of 30 km and a total of 100,000 fixed points evenly spaced in time along the orbit. The trajectories along the stable manifold are propagated backwards in time for 50 non-dimensional time units, equivalent to 126.8 days. Similarly, the trajectories along the unstable manifold are integrated forward in time for the same interval. To illustrate other dynamical structures at this particular energy level, the returns of the invariant manifolds to the map are plotted against a background map that includes some of these structures. The set of initial conditions used to generate the background surface of section is selected to be in the vicinity of the resonant orbit. Recall that the bounds for this planar problem are defined with $y = 0$ and $z_0 = \dot{z}_0 = 0$; the corresponding value of $\pm\dot{y}_0$ is calculated from the expression for Jacobi constant. In propagating the initial conditions, long integration times are necessary to produce sufficient crossings to yield a dense and well-defined map. For this particular example, an integration time of approximately 7 years is employed to generate the background map plotted in gray in Figure 4.5. The related quantities in the plot are position and velocity, that is, x and $\dot{x}$ (labeled V_x) on the map. For reference, the regions (a) and (b) along the x-axis that are used as initial conditions for the maps are noted in Figure 4.4. The stable and unstable manifolds (labeled $W^s_{p:q}$ and $W^u_{p:q}$) are plotted in blue and magenta, respectively.

Potential resonant transitions can be identified and exploited from the Poincaré map that includes the invariant manifolds and the background map. From the map in Figure 4.5, it is apparent that these manifolds travel extensively to different regions of the map, i.e., the returns of the manifolds to the map are not confined to a small region. Different areas of the map are potentially associated with other unstable resonant orbits, therefore, promoting possible natural resonance transitions. Thus, it is desirable to further examine the relationship between the 3:4 resonance and other structures. The 'crossings' of the stable and unstable manifolds on the map near $\dot{x} = 0$ are of special interest as these intersections may reveal potential locations of unstable periodic solutions. Recall that the objective is to transition between

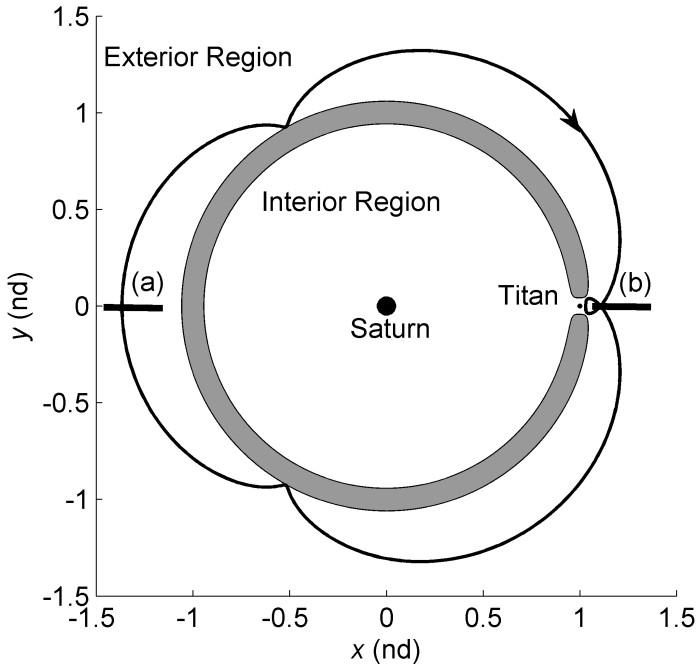

Figure 4.4. A Planar, Periodic 3:4 Resonant Orbit in the Saturn-Titan Three-Body System ($C = 3.01000$). Bold Black Lines (a) and (b) Indicate Initial Condition Regions for the Maps in Figure 4.5

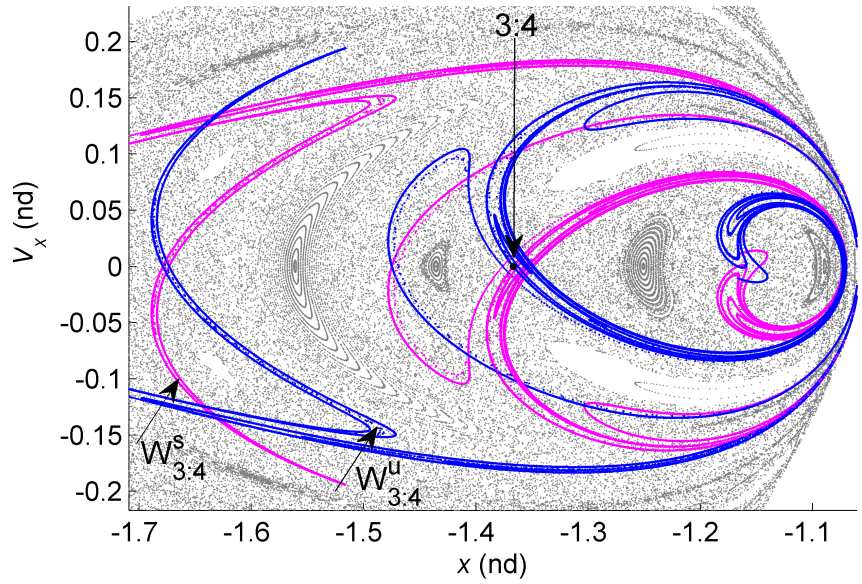

(a) $x < 0$

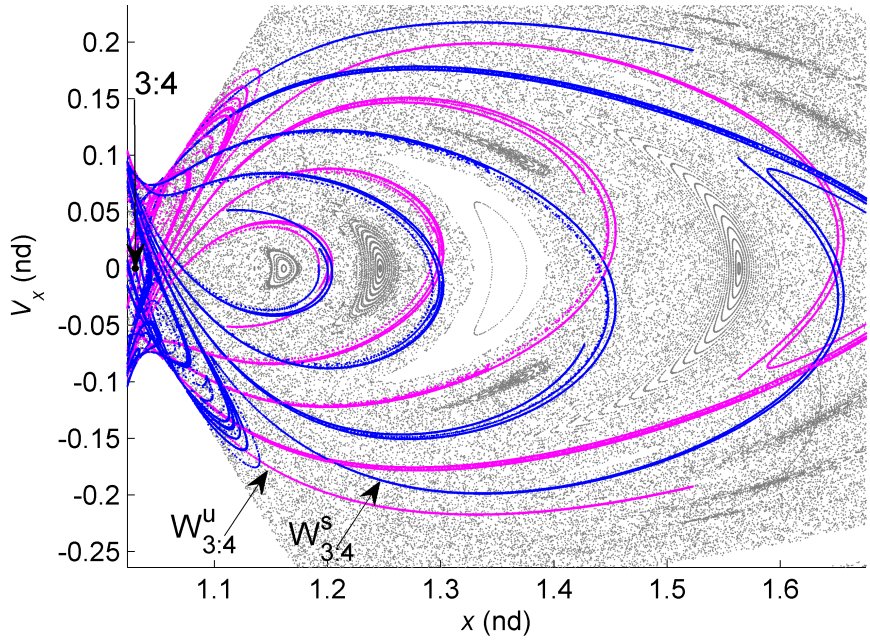

(b) $x > 0$

Figure 4.5. Poincaré Section Illustrating the Invariant Manifolds Associated with the 3:4 Resonant Orbit Zoomed to Focus on Regions (a) and (b) from Figure 4.4. Stable Manifolds Plotted in Blue and Unstable Manifolds Plotted in Magenta

two or more unstable periodic orbits at no cost by exploiting invariant manifolds. If the arrival orbit is selected *a priori*, then the corresponding fixed points can be plotted on the map and a connection between manifolds trajectories is sought directly from the map. However, more options may be available if all the crossings of the returns to the map are thoroughly investigated. Assuming a periodic orbit exists near a particular intersection on the map, an approximation for the initial state of the form $[x_0 \quad 0 \quad 0 \quad 0 \quad \dot{y}_0 \quad 0]$ can be easily recovered from the manifold returns. Recall that the corresponding value for $\dot{y}_0$ is calculated from the expression for Jacobi constant. Then, a simple technique based on two-body approximations can be applied to estimate the period of the unstable orbit from the eccentricity and semi-major axis values that are instantaneously computed from the equations for the angular momentum and the semilatus rectum [39]. The estimated period and state from the map are subsequently incorporated as the initial guess in the corrections algorithm to compute the corresponding unstable periodic orbit in the CR3BP. Although a variety of exterior and interior resonant orbits are sought following this procedure, the resulting trajectory can also be non-resonant. Once the unstable orbits are identified on the surface of section, it is necessary to compute their invariant manifolds to confirm that a transition is possible between these trajectories and the initial 3:4 resonant orbit. Due to the natural dynamics of the system, if a connection is identified, it is expected that the orbits expose similar manifold structures. The integration times that are required to compute the invariant manifolds vary from orbit to orbit. Of course, the manifolds for orbits that are more unstable depart or approach the orbit faster than the manifolds associated with orbits possessing a smaller stability index.

For illustration purposes, consider an interior orbit resonant with Titan as well as the Lyapunov orbits near L_1 and L_2 at the specified energy level. These three orbits are plotted in Figures 4.6(a)-4.6(b). The corresponding orbital periods, unstable eigenvalues, and initial states are listed in Table 4.1. The interior resonant orbit in Figure 4.6(a) is computed from an initial guess obtained from the Poincaré map

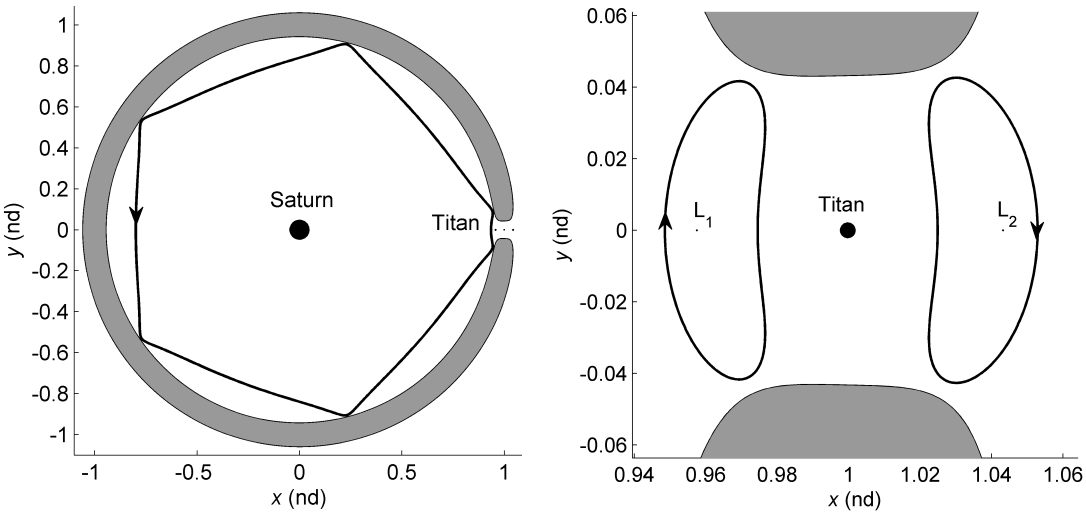

(a) A 6:5 Resonant Orbit

(b) L_1 and L_2 Lyapunov Orbits

Figure 4.6. Periodic Orbits at $C = 3.010000$ in the Saturn-Titan Three-Body System

Table 4.1 Initial State, Period, and Unstable Eigenvalue for Selected Periodic Orbits ($C = 3.010000$)

Periodic Orbits	x (km)	$\dot{y}$ (km/s)	T (days)	λ_u
3:4 resonant orbit	1.25869×10^6	0.477301	66.3312	2,129.81
6:5 resonant orbit	1.14214×10^6	0.545759	71.2638	191.641
L_1 Lyapunov orbit	1.15897×10^6	0.447315	8.2829	1,004.72
L_2 Lyapunov orbit	1.25231×10^6	0.549329	79.7260	892.850

associated with the 3:4 unstable resonant orbit in Figure 4.5. This periodic orbit, together with the L_1 and L_2 Lyapunov orbits, possess manifold structures that are very similar to those of the 3:4 resonant orbit. Thus, natural transitions between these orbits are identified from the maps and calculated exploiting stable and unstable manifolds.

A transfer process that employs a combination of stable and unstable manifold arcs is designed to yield a continuous trajectory that transitions between the periodic

orbits of interest. Once the connecting arcs are identified from the Poincaré map, they are linked to the periodic orbits as a complete path that is then decomposed into smaller subarcs. A multiple-shooting algorithm blends these subarcs into a single continuous trajectory, enforcing continuity in position and velocity at each subarc interface. The resulting trajectory serves as a natural, ΔV-free connection between resonant orbits. Note, however, that as long as there exists a relationship between the invariant manifolds associated with different periodic orbits, virtually any connection can be accommodated using this technique, demonstrating its versatility and robustness. A selection of trajectory design scenarios illustrates the usefulness of this process.

Scenario A: 3:4 Resonance $\rightarrow$ L_2 Lyapunov $\rightarrow$ L_1 Lyapunov $\rightarrow$ Titan Impact. The spacecraft in this first design scenario is originally orbiting about Saturn in a 3:4 periodic orbit resonant with Titan. After completing one full cycle in this orbit, a transition occurs and the path merges into an unstable manifold arc that departs the 3:4 resonant orbit and approaches the L_2 Lyapunov orbit at the specified energy level. This manifold arc is defined with a duration of 39.7 days. Arriving at the L_2 libration point orbit, one revolution is completed and the path merges into a stable manifold arc associated with the L_1 Lyapunov orbit, thus, approaching the L_1 libration point orbit in 12.4 days. After a full revolution in the L_1 libration point orbit, the path transitions onto an unstable manifold arc associated with this L_1 Lyapunov orbit for 2.47 days that eventually results in a Titan impact. After corrections, the resulting trajectory, as plotted in Figures 4.7(a) and 4.7(b), is continuous in position and velocity, with the desired Jacobi constant value of $C = 3.010000$.

Scenario B: 3:4 Resonance $\rightarrow$ 6:5 Resonance $\rightarrow$ L_1 Lyapunov $\rightarrow$ Titan Capture. In this second design scenario, the spacecraft follows a different manifold arc associated with the L_1 Lyapunov orbit that does not result in a direct impact

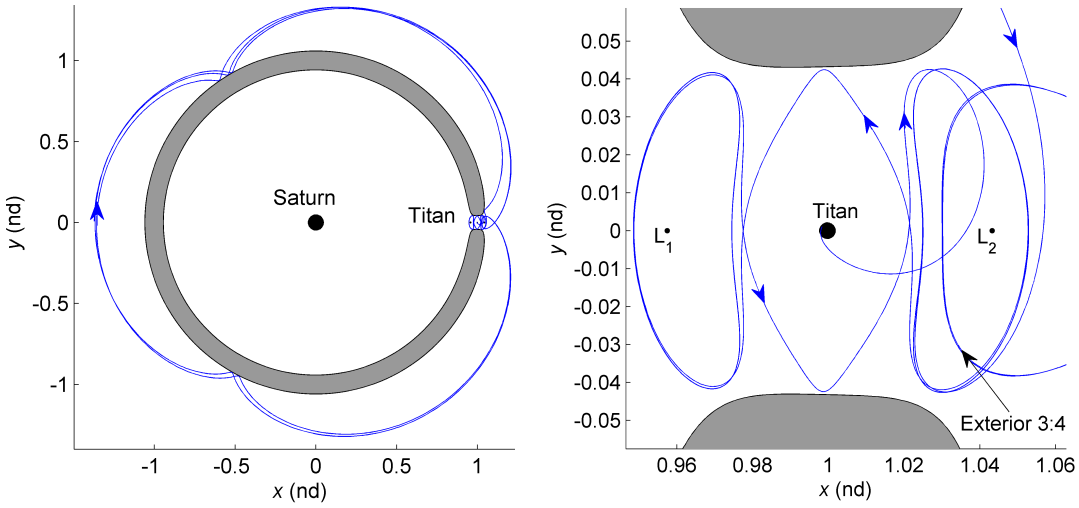

(a) Transfer Trajectory

(b) Zoom-in View of the Titan Region

Figure 4.7. Transfer Design - Scenario A: 3:4 Resonance $\rightarrow$ L_2 Lyapunov $\rightarrow$ L_1 Lyapunov $\rightarrow$ Titan Impact

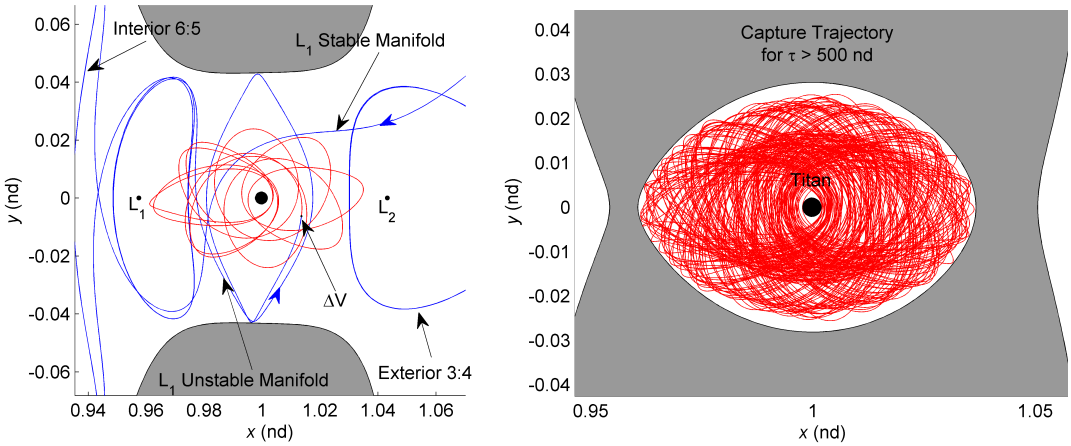

(a) Transfer Trajectory

(b) Capture Orbit Around Titan

Figure 4.8. Transfer Design - Scenario B: 3:4 Exterior Resonance → 6:5 Interior Resonance → L_1 Lyapunov → Titan Capture

with Titan but subsequently surrounds Titan and remains in the moon vicinity. At a specified point along this manifold arc, a maneuver is implemented to decrease the energy level and close the zero velocity curve and, thus, renders a capture orbit around Titan. The maneuver occurs in a specific location such that the resulting capture trajectory maintains a specified minimum distance from Titan's surface. The magnitude of this ΔV is 123.672 m/s and the maneuver is entirely in the $\dot{y}$-direction. The resulting transfer trajectory appears in Figure 4.8(a) and the maneuver location is indicated with a black dot. The trajectory in Figure 4.8(b) is a plot of the capture trajectory integrated for 3.476 years. The energy level post-maneuver is $C = 3.015860$ and, thus, in this dynamical model, the spacecraft remains in orbit around Titan unless another force is introduced (e.g., a second maneuver) to again shift the energy level. Note that this maneuver is not optimal; it is simply applied for illustration.

Transfer design scenarios A and B are presented as illustrative examples, but other natural transitions with different itineraries are also available for different energy

levels in the Saturn-Titan system and can be calculated following the same design process [40].

Design of Planar Periodic Resonant Chains

Poincaré maps are also a powerful tool in the search and identification of other type of trajectories. Recall that in the planar case, an intersection in the map is an intersection in phase space. That is, an intersection of the stable and unstable manifolds associated with one particular unstable periodic orbit on the Poincaré section – generated for a particular value of Jacobi constant – is a point that approaches the resonant orbit when numerically integrated into the future as well as into the past. Such a trajectory is termed a homoclinic connection. Similarly, a heteroclinic connection is calculated from the intersection of the stable manifolds associated with the departure orbit and the unstable manifolds associated with the arrival orbit. Then, the intersection of these manifold trajectories is a point that departs one orbit when numerically integrated into the future and approaches a different orbit when numerically integrated into the past. For convenience, consider two unstable resonant orbits with resonant ratios a:b and c:d. A homoclinic connection is defined such that $W^u_{a:b} \subset W^s_{a:b}$, or $W^u_{c:d} \subset W^s_{c:d}$; similarly, a heteroclinic connection between the two resonant orbits is defined such that $W^u_{a:b} \subset W^s_{c:d}$, or $W^u_{c:d} \subset W^s_{a:b}$ for the reverse motion. Note, however, that these types of natural connections are certainly not limited to resonant orbits and *may* exist between any set of unstable periodic orbits [31].

As an application of dynamical systems theory, consider a homoclinic connection that asymptotically departs and approaches the 3:4 resonant orbit plotted in Figure 4.4. Once the stable and unstable manifold arcs that result in a homoclinic connection are identified from the map and numerically calculated, it is possible, in some instances, to further correct the homoclinic trajectory into a new periodic orbit by enforcing the appropriate periodicity constraints. In fact, Lo and Parker demonstrate that unstable periodic orbits can be chained together using their invariant

manifolds to produce new periodic orbits, termed "chains," which strongly resemble their generating orbits [68]. These chains are similar to the homoclinic cycles previously described, i.e., a homoclinic connection with a desired itinerary corrected for periodicity and, thus, one that cycles indefinitely between specific regions in space.

To illustrate the concept of these 2D periodic resonant chains, consider a homoclinic connection that departs and approaches the 3:4 resonant orbit when propagated forward and backward in time. A particular subset of the manifolds from the 3:4 resonance travel to the interior region, shadowing the 6:5 resonant orbit. To highlight the relationship between the two unstable resonant orbits, the intersection on the Poincaré map for the homoclinic connection is selected to be *near* the fixed point corresponding to the 6:5 resonant orbit, as illustrated in Figure 4.9. The path that results from propagating this intersection point on the map forward and backward in time naturally follows both resonant orbits, that is, the interior 6:5 and the exterior 3:4 resonant orbits. The initial state is obtained from the Poincaré map in Figure 4.9(b) and is integrated forward and backward in time until the path reaches the 3:4 resonant orbit. To produce a resonant chain, or a cycle between resonances, it is necessary to numerically correct this path via a single shooting scheme to obtain a periodic orbit that shadows the invariant manifolds associated with the two resonant orbits. The resulting trajectory is plotted in Figure 4.10(a) and its periodicity is represented by the two perpendicular crossings.

Consistent with previous periodic orbits, it is possible to generate a family of resonant chains using a continuation scheme, although the size of these families is dependent on the relationship between their associated invariant manifolds. Note that each member represented in a family of periodic orbits possesses a different value of Jacobi constant. The family of periodic resonant chains plotted in Figures 4.11(a)-4.11(b) is generated exploiting the invariant manifolds associated with a member of the 3:4 resonant family at each particular energy level. Recall that the appropriate manifold arcs are selected from the intersection on the map near the 6:5 resonant orbit and are subsequently corrected in a numerical scheme to obtain a periodic

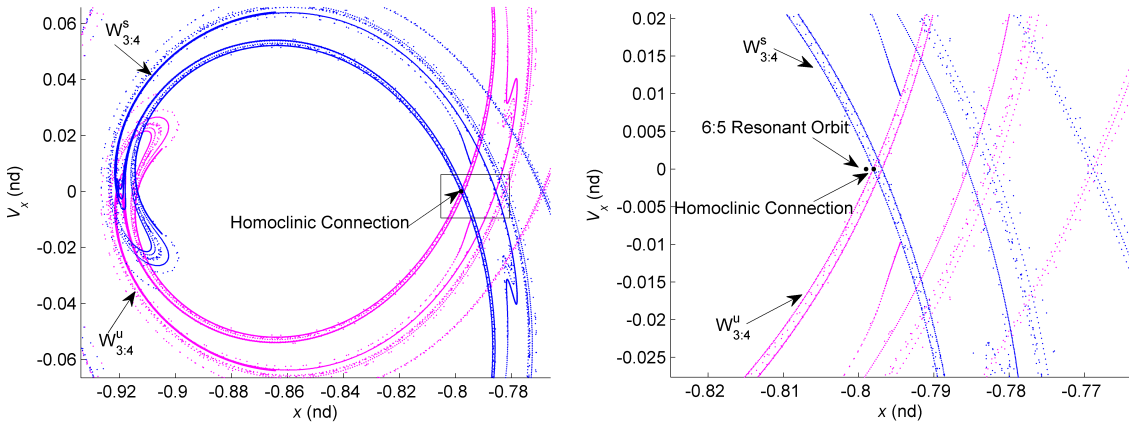

(a) $C = 3.01$ (b) Zoomed View of Boxed Region

Figure 4.9. Poincaré Maps Displaying the Invariant Manifolds Associated with a 3:4 Resonance at $C = 3.01$ in the Saturn-Titan Three-Body Model

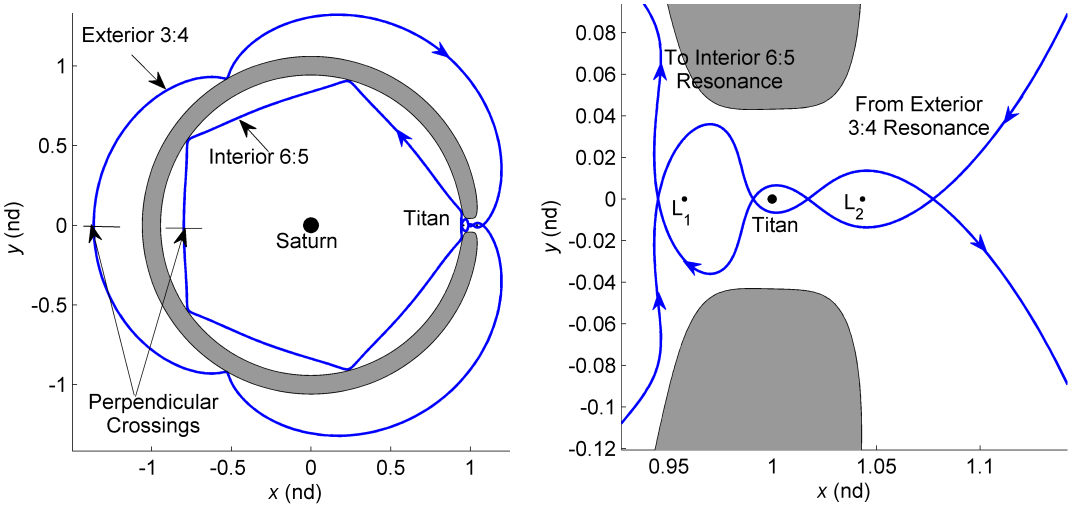

(a) Periodic Resonant Chain (b) Zoomed View of Region Near Titan

Figure 4.10. Periodic Chain Connection Between Interior and Exterior Resonant Orbits

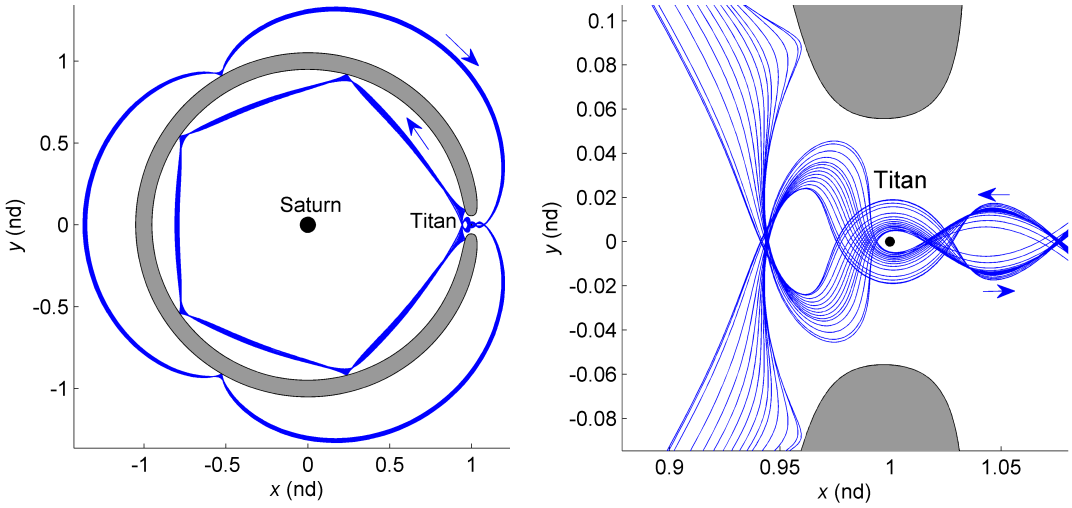

(a) Family of Homoclinic-Type Resonant Orbits

(b) Zoom-in View of the Titan Region

Figure 4.11. Representative Orbits in a Family of Periodic Homoclinic-Type Resonant Orbits

trajectory that cycles between the two resonances. The intersection on the map occurs at a different location in position and velocity on the map for each value of Jacobi constant, that is, as the energy changes, the manifolds "shift" in space as does the location of the intersection representing the homoclinic trajectory. Thus, the existence of the family of periodic resonant chains is limited to the existence of a connection between manifolds. For a given energy level, if the stable and unstable manifolds associated with the 3:4 resonant orbit do not intersect in the vicinity of the 6:5 resonance, it is not possible to generate the desired homoclinic periodic orbit. This phenomenon is illustrated in Figures 4.12(a)-4.12(c). The gap between the stable and the unstable manifolds in Figure 4.12(c) indicates that there is no intersection between that particular set of manifolds at $C < 3.01400$. Thus, it is suspected that this family of periodic resonant chains ends for a value of Jacobi constant $C < 3.01400$.

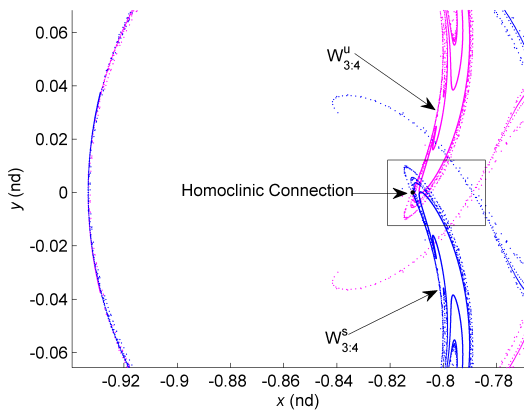

(a) $C = 3.013231$

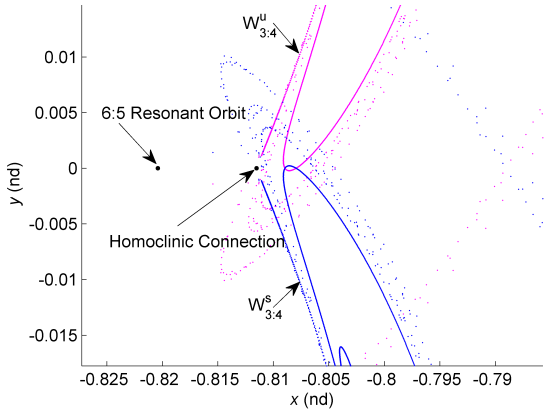

(b) Zoomed View of Boxed Region

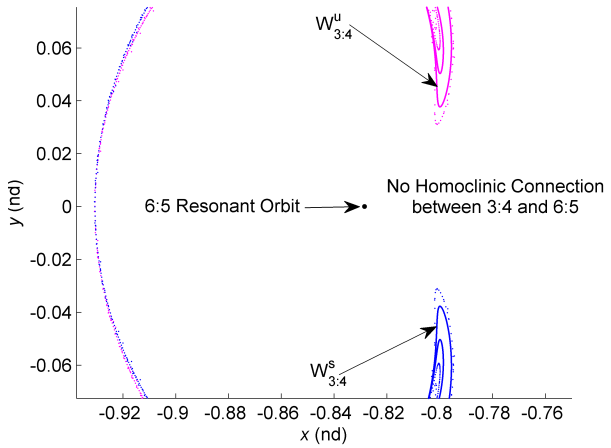

(c) $C = 3.014000$

Figure 4.12. Poincaré Maps Displaying the Invariant Manifolds Associated with Two 3:4 Resonances at Different Energy Levels

4.3.2 Planar ΔV-Transfers: Accessing the Orbit of Hyperion

The problem of accessing Hyperion is investigated by exploiting the natural dynamics of planar resonant orbits. Hyperion is characterized by its irregular shape, its chaotic rotation, its fairly eccentric orbit and, perhaps most notable here, for its proximity to Titan [80]. Hyperion is known to be in a 3:4 resonance with Titan, that is, Hyperion completes three revolutions around Saturn in the time Titan completes four.

To investigate the accessibility of Hyperion from an orbit around Saturn, it is first necessary to approximate Hyperion's ephemeris orbit to a 3:4 resonant orbit in the CR3BP. The development of a model for Hyperion within the context of the CR3BP requires information on the moon, period, location, orientation, and Jacobi constant. The ephemeris data for Hyperion's trajectory is obtained over the course of 20 years, from 01/01/2000 to 01/01/2020, using the Horizons database [81] and representative information appears in Figure 4.13. The approximate value of the Jacobi constant for the ephemeris data ranges from $C = 3.02500$ to $C = 2.99500$, as illustrated in Figure 4.13(b). The corresponding average value, $C = 3.00937$, denoted C_{Hyp}, is selected for this investigation, which corresponds to Hyperion's orbit in approximately August 2019. This value is highlighted by a red line in Figure 4.13(b). The ephemeris data is viewed in a rotating frame and plotted in Figure 4.13(a). The shape of the 3:4 resonance is apparent from the observational data. Then, a subset of this ephemeris data is used in a numerical corrections scheme that reconverges the ephemeris trajectory in the CR3B model. The converged 3:4 resonant orbit appears in Figure 4.13(c).

Hyperion's 3:4 resonant orbit, as modeled in the CR3BP, is a linearly stable orbit, i.e., the eigenvalues associated with the monodromy matrix are all complex. Even though this result is not surprising, there is no natural flow to and from the orbit that can be exploited to construct continuous transfer paths that approach the orbit. A maneuver is required to access or depart the orbit and, hence, the term 'non-natural'

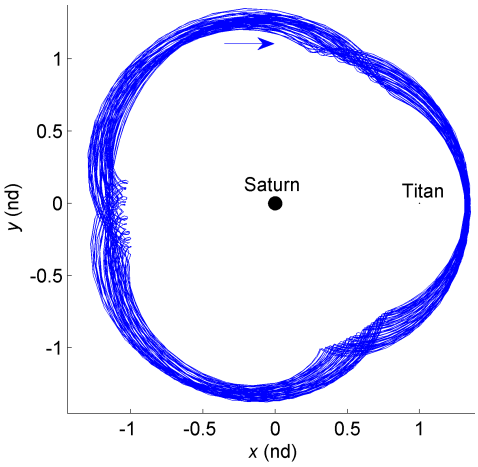

(a) Ephemeris Trajectory

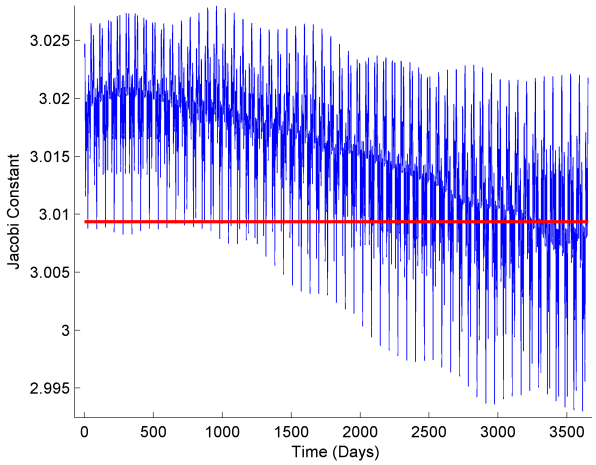

(b) Variation in C Over 20 years

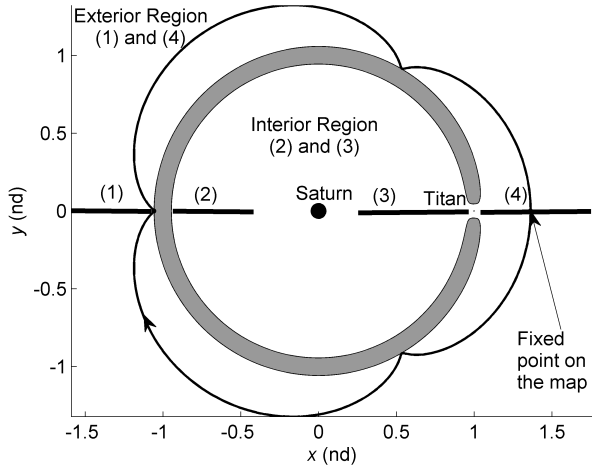

(c) CR3BP Trajectory - $C \simeq 3.009368$

Figure 4.13. Hyperion's Orbit in the Ephemeris and CR3B Models

transfer. However, the use of invariant manifolds to access the vicinity of this orbit may offer viable trajectory concepts. Transfers to this orbit from different departure orbits are explored, and the associated costs to insert into this orbit are demonstrated.

Consider the corresponding L_1 and L_2 Lyapunov orbits at $C = C_{Hyp}$. The invariant manifolds associated with the L_1 orbit are displayed on a surface of section plotted against a background that highlights other dynamical structures, i.e., regions of periodic, quasi-periodic, and chaotic motion at this particular energy level in Figures 4.14-4.15. The maps in Figure 4.14 correspond to the regions highlighted in Figure 4.13(c) on the negative x-axis near periapsis, that is, the regions on the x-axis labeled (1) and (2). The maps in Figure 4.15 correspond to the regions (3) and (4) on the positive x-axis in the vicinity of Titan. Recall that all four surfaces of section are located at $y = 0$ and the maps represent the intersections of the manifolds and other dynamical structures plotted in x and $\dot{x}$. These maps are employed to identify other stable and unstable resonant orbits that could serve as potential departure orbits to efficiently reach the 3:4 orbit of Hyperion. The identification of stable resonant orbits is facilitated by the background map, which highlights regions of periodic and quasi-periodic motion. That is, each chain of islands is evaluated and stable resonant orbits are identified at the center. Unstable resonant orbits, however, are located in regions of chaotic motion. The intersections of the stable and unstable manifolds associated with the selected libration point orbit at C_{Hyp} as viewed on the Poincaré maps aid in the identification of unstable resonant structures that may be used in the design of transfer trajectories to Hyperion. The identified stable resonant orbits at the center of a region of quasi-periodic behavior are labeled on the maps. As illustrative examples, consider two unstable periodic orbits in resonance with Titan: a 3:5 exterior resonance and a 5:4 interior resonance. One of the fixed points associated with the 5:4 unstable resonant orbit is labeled in Figure 4.14(b). Two of the crossings of the 3:5 unstable resonant orbit with the map appear in Figure 4.14(a) as black dots. Note that this particular resonant orbit pierces the surface of section seven times but only two are perpendicular crossings. Therefore, five of the seven fixed points are

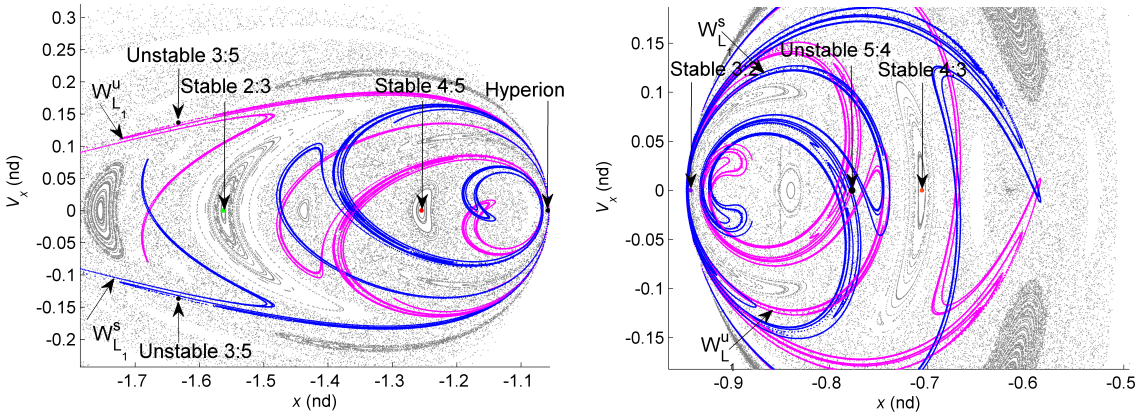

(a) Exterior Region, $x < 0$

(b) Interior Region, $x < 0$

Figure 4.14. Poincaré Section Illustrating the Invariant Manifolds Associated with an L_1 Lyapunov Orbit at $C = C_{Hyp}$; Maps that Correspond to Crossings (1) and (2) in Figure 4.13(c)

not located along the $\dot{x} = 0$ axis. Two transfers to Hyperion's 3:4 resonant orbit are produced for illustration, but other scenarios are available. Transfer trajectory A departs from the 5:4 interior resonance and transfer trajectory B originates at the 3:5 exterior resonance. The design approach to construct these transfer trajectories is similar to that followed to generate previous natural transitions. The manifold arcs from the unstable resonant orbits are employed to depart the orbits and approach the vicinity of Hyperion's orbit, where a maneuver is introduced to insert onto the stable orbit.

Transfer Trajectory A: The continuous transfer illustrated in Figure 4.16 departs from an initial interior 5:4 resonant orbit along an unstable manifold arc that merges with a stable manifold arc associated with the L_2 Lyapunov orbit, approaching the orbit after 41.5 days. After one revolution in the L_2 Lyapunov, the path departs the Titan region on an unstable manifold arc that eventually approaches the vicinity of Hyperion's orbit, actually near L_3. The time-of-flight along this manifold arc is 105.5 days. At the point indicated in Figure 4.16(b),

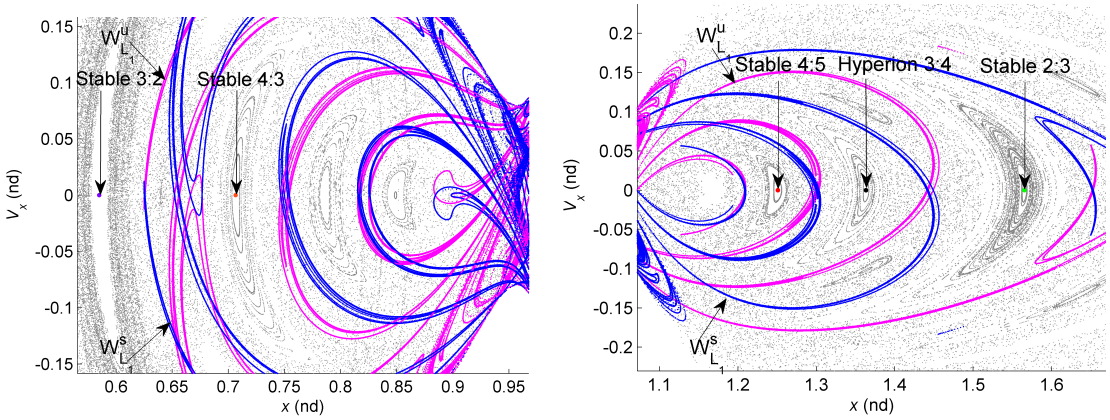

(a) Interior Region, $x > 0$

(b) Exterior Region, $x > 0$

Figure 4.15. Poincaré Section Illustrating the Invariant Manifolds Associated with an L_1 Lyapunov Orbit at $C = C_{Hyp}$; Maps that Correspond to Crossings (3) and (4) in Figure 4.13(c)

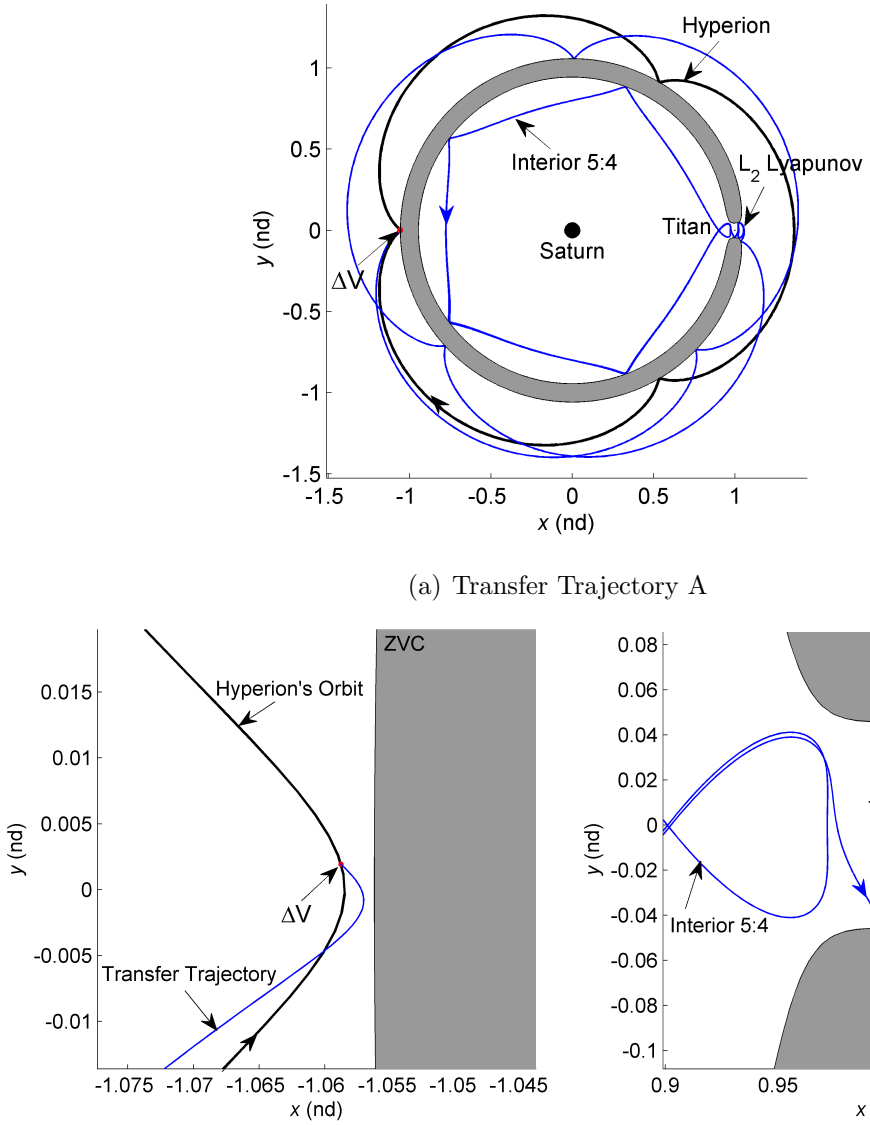

(a) Transfer Trajectory A

(b) Zoomed View of Maneuver Location

(c) Zoomed View Near Titan

Figure 4.16. Transfer Trajectory to Hyperion Departing from an Interior 5:4 Resonant Trajectory

which corresponds to an intersecting point in position, a sub-optimal maneuver of 61.90 m/s yields insertion into Hyperion's orbit.

The insertion location represented in Figure 4.16(b) is not the only point of access to Hyperion's orbit. Two particular locations along Hyperion's orbit are considered for insertion: one near periapsis ($x < 0$) and another near apoapsis ($x > 0$) of the

stable 3:4 resonant orbit, but alternative locations may be available. Two different maps, illustrated in Figure 4.17, are generated at these particular locations to represent the relationship between the manifold transfer trajectory and Hyperion's orbit. The unstable manifolds (magenta) associated with the L_2 Lyapunov orbit appear on the maps plotted against a background map (gray). The transfer trajectory and Hyperion's two fixed points are labeled as black and red dots on the maps, respectively. It is straightforward to compute the required ΔV at insertion from the map by using a combination of position and velocity to plot these crossings. As illustrated in Figures 4.17(a)-4.17(b), the insertion cost is lower near periapsis, that is, $\Delta V_{peri} = 61.90$ m/s. The unstable manifold trajectories pass closer to Hyperion's orbit near periapsis. This relationship is better illustrated in Figure 4.17(a); the intersections of the transfer trajectory and Hyperion's orbit are closer in x and $\dot{x}$ that those in Figure 4.17(b), resulting in a smaller insertion maneuver. A maneuver $\Delta V_{apo} = 343.00$ m/s is required to insert into Hyperion's orbit near apoapsis. In this situation, Poincaré maps help illustrate qualitatively the cost of insertion into a stable orbit. One interesting feature of these maps as opposed to the maps illustrated in Figures 4.14-4.15 is the lack of symmetry across the plane $\dot{x} = 0$. The surface of section is specified at the y-coordinate value of the apse points, i.e., $y_{r_p} = 0.01640$ near periapsis and $y_{r_a} = -0.1781$ near apoapsis, so the regions of quasi-periodic motion are no longer symmetric across the plane $\dot{x} = 0$, although all the features associated with quasi-periodicity and periodicity are still preserved.

Transfer Trajectory B: The transfer trajectory that appears in Figure 4.18 is designed to depart along an unstable manifold from an initial exterior 3:5 resonant orbit. The unstable manifold approaches the vicinity of Hyperion's orbit after 105.5 days, again in the vicinity of L_3, even though the L_3 point is unavailable due to the zero velocity curves. Note that this transfer trajectory does not enter the P_1 nor P_2 region and does not exploit any of the libration point orbits or the associated invariant manifolds considered in previous transfer designs. At the point indicated in Figure 4.18(b), a sub-optimal maneuver of 163.2 m/s is added

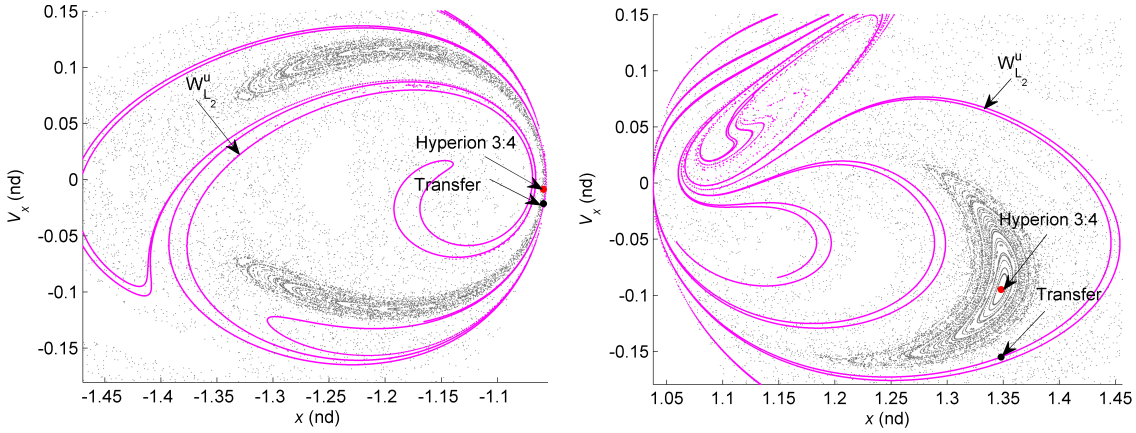

(a) Map near Periapsis

(b) Map near Apoapsis

Figure 4.17. Transfer Trajectory A to Hyperion from Interior 5:4 Resonant Orbit Represented on a Poincaré Map Along with the Unstable Manifolds Associated with an L_2 Lyapunov Orbit at $C = C_{Hyp}$

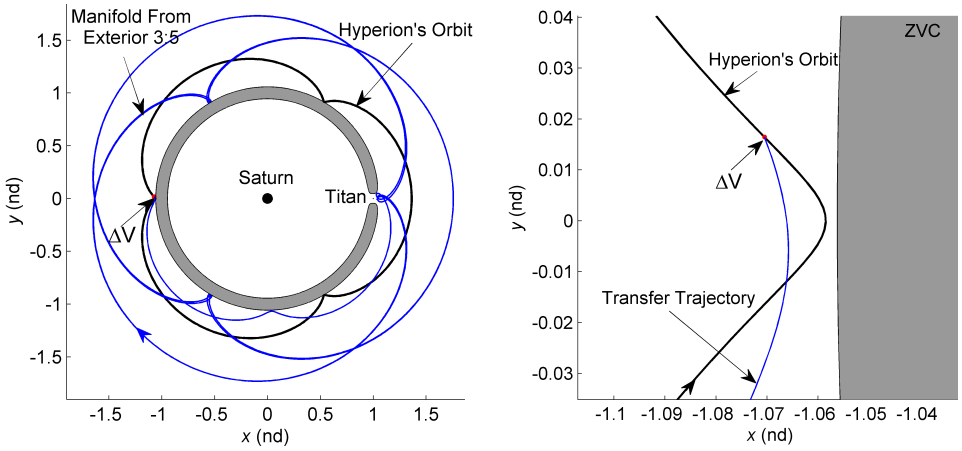

(a) Rotating Frame View

(b) Maneuver Location

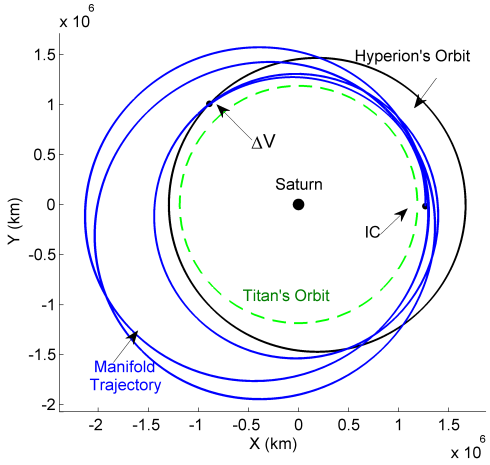

(c) Inertial Frame View

Figure 4.18. Transfer Trajectory B to Hyperion's Orbit from Exterior 3:5 Resonant Trajectory

to insert into Hyperion's orbit. The continuous transfer trajectory, as viewed in the rotating reference frame, is illustrated in Figure 4.18(a). For completeness, the transfer trajectory is plotted in the inertial frame in Figure 4.18(c).

Design of a Locally Optimal Transfer Trajectory to Hyperion's Orbit

Both illustrative transfer trajectories A and B to Hyperion's orbit may be sub-optimal trajectories. They are constructed by linking stable and unstable manifold arcs associated with resonant and Lyapunov orbits, and thus, benefit from a reduced cost. However, it is possible to locally optimize these trajectories. As an illustrative example, transfer trajectory B to Hyperion from an initial exterior 3:5 resonant orbit with Titan is considered for optimization. The resulting trajectory is then compared with the manifold, sub-optimal transfer trajectory B plotted in Figure 4.18.

In the optimization process, a single, locally optimal transfer trajectory is identified by 1) specifying the desired departure and arrival orbits, and 2) modifying the initial state of the spacecraft as well as the time-of-flight. In this particular case, the departure orbit is the exterior 3:5 resonant orbit and the arrival orbit is Hyperion's 3:4 stable resonant orbit as modeled in the CR3BP. The location on both the departure and arrival orbits is variable, that is, the initial and final position states on the transfer trajectory are not fixed but are constrained to be along the departure and arrival orbits of interest. This is achieved by allowing the integration times along the orbits to be variables and by formulating the initial and final position states as equality constraints. An additional equality constraint is also added to ensure that the magnitude of the initial maneuver does not alter the energy level, i.e., the value of C is fixed at $C = C_{Hyp}$. Recall that the 3:5 exterior resonant orbit also possesses the same value of Jacobi constant, i.e., $C_{3:5} = C_{Hyp}$. An inequality constraint is specified to enforce positive time-of-flight, that is, $\text{TOF}_i > 0$. The decision variables are the initial position and initial velocity associated with the transfer arc and the integration times, that is, $\bar{X} = [x_0\ y_0\ z_0\ \dot{x}_0\ \dot{y}_0\ \dot{z}_0\ \text{TOF}_1\ \text{TOF}_2\ \text{TOF}_3]$. The first and third integration times specify the departure and arrival locations on the 3:5 resonant orbit and on Hyperion's orbit, respectively. The intermediate integration time corresponds to the time-of-flight along the transfer arc that connects the initial and final orbits of interest. The objective function returns the magnitude of the minimum

initial and final maneuvers required to depart the 3:5 resonant orbit and to insert into the moon's stable orbit, that is, $J(\bar{X}) = \Delta V_0 + \Delta V_f$. A number of optimization algorithms can potentially be used to solve the problem. One common and efficient constrained nonlinear programming algorithm available is Sequential Quadratic Programming (SQP). MATLAB's `fmincon` function is the optimization routine employed in this analysis. The SQP routine is a quasi-Newton direct method of minimizing a continuous constrained nonlinear objective function by solving a simpler quadratic programming sub-problem [82]. The locally optimal design that results in a transfer trajectory from the 3:5 resonant orbit to Hyperion's orbit is $\bar{X}^* = [1.04145\ 0\ \ 0\ \ -0.000001\ \ 0.078162\ \ 0\ \ 1.07044\times10^{-6}\ \ 204.011\ \ 33.2508]$, where the position and velocity states are expressed in non-dimensional units and the time-of-flight in days. In the optimization process, numerical gradients are used and all constraints are met within the specified non-default tolerances ($\texttt{TolX} = \texttt{TolCon} = \texttt{TolFun} = 1\times10^{-12}$). An `exitflag` value of 1 is achieved, which indicates that first optimality conditions are satisfied. The magnitude of the minimum initial maneuver required to depart the 3:5 resonant orbit and target Hyperion's orbit is $\Delta V_0 = 7.1112$ mm/s and the time-of-flight is 204.011 days. The magnitude of the insertion maneuver is $\Delta V_f = 156.101$ m/s. The resulting optimal transfer trajectory as well as the non-optimal transfer trajectory B are plotted in Figure 4.19 for comparison.

The relationship between the optimal transfer trajectory and the manifold transfer is apparent in Figure 4.19. In fact, the locally optimal trajectory appears to shadow an unstable manifold trajectory associated with the 3:5 resonant orbit. To illustrate this relationship, the returns of the optimal transfer to a surface of section defined at $y = 0$ are labeled and plotted in Figure 4.20 together with the crossings of the stable (blue) and unstable (magenta) manifolds associated with the 3:5 resonant orbit. For better visualization, Figures 4.20(b)-4.20(d) offer zoomed views of the crossing regions on the map. The Poincaré maps demonstrate that the locally optimal transfer trajectory is indeed a manifold arc. The initial maneuver required to depart the unstable 3:5 resonant orbit is of the order of mm/s, which is comparable to the actual

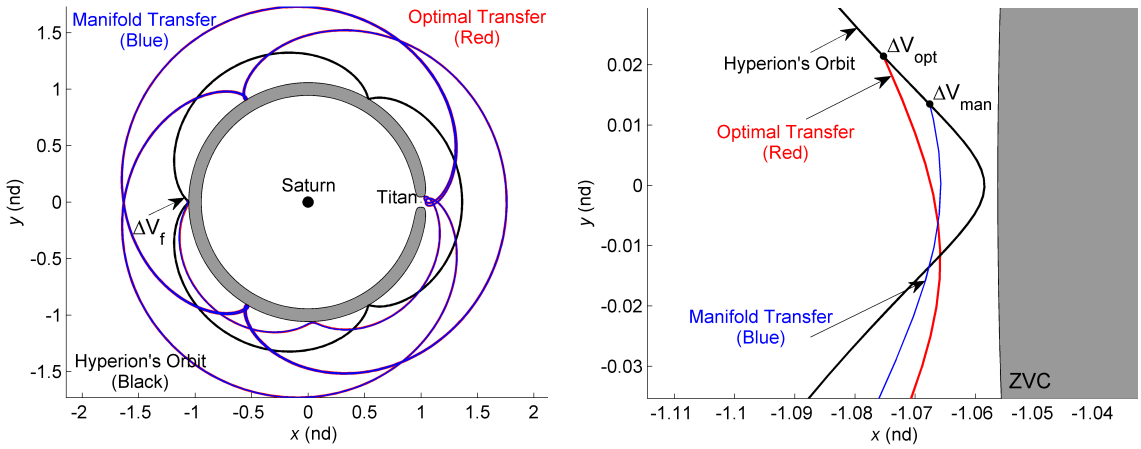

(a) Manifold and Optimal Transfers

(b) Insertion Region near Periapsis

Figure 4.19. Locally Optimal Transfer (Red) and Manifold Transfer Trajectory B (Blue) to Hyperion's 3:4 Resonant Orbit

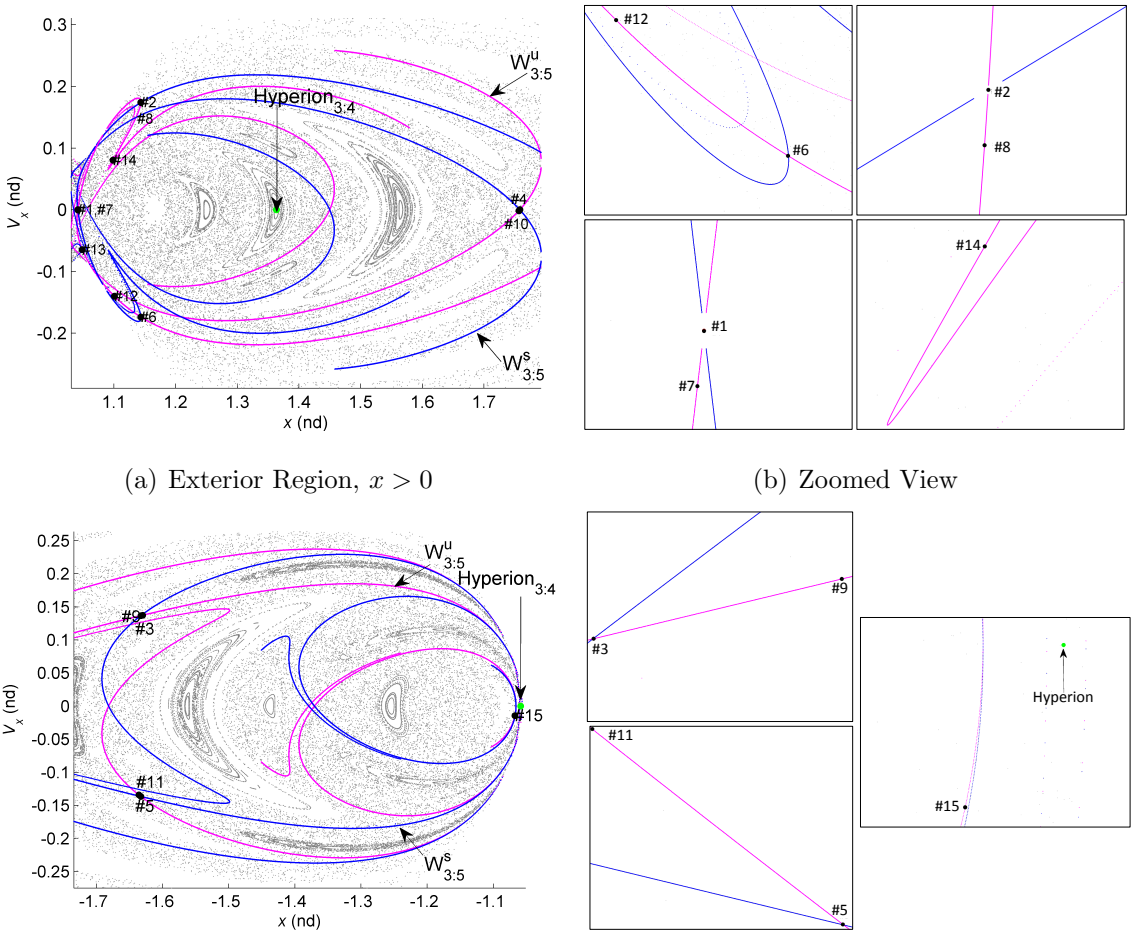

(a) Exterior Region, $x > 0$

(b) Zoomed View

(c) Exterior Region, $x < 0$

(d) Zoomed View

Figure 4.20. Optimal Transfer Trajectory to Hyperion Displayed on a Poincaré Map with the Invariant Manifolds Associated with the 3:5 Resonant Orbit

cost associated with stepping onto an unstable manifold trajectory. However, the optimization algorithm results in a slightly different manifold trajectory than the one selected to construct transfer trajectory B. As represented in Figure 4.19(b), the arrival location of the optimal trajectory is slightly different, resulting in a only slightly lower cost of insertion into Hyperion's orbit.

The same general local optimization algorithm can be employed to reduce the time-of-flight along the transfer arc. To do so, transfer trajectory B is employed as an

initial guess, but the transfer time-of-flight is formulated as an inequality constraint, that is, $\mathrm{TOF}_2 \leq \mathrm{t}_{max}$. In other words, the goal is still to minimize the magnitude of the sum of the initial and final maneuvers, but with an upper limit on TOF. As an illustrative example, if the transfer time-of-flight is to be reduced by 50%, i.e., $t_{max} =$ 102 days, the algorithm results in a locally optimal transfer trajectory that appears to be a shorter, more direct unstable manifold trajectory. The initial manuever is slightly higher, that is, $\Delta V_0 = 30.706$ cm/s, and the maneuver required to insert into Hyperion's orbit is approximately 35 m/s larger, that is, $\Delta V_f = 191.189$ m/s. In comparison, the time-of-flight is reduced by approximately 50% while the total transfer cost is increased by 18%. The resulting shorter optimal transfer trajectory as well as the non-optimal transfer trajectory B are plotted in Figure 4.21.

In essence, the very small ΔV_0 required to depart the unstable 3:5 resonant orbit and target Hyperion's orbit is employed to place the spacecraft on an unstable manifold trajectory associated with the 3:5 resonant orbit. As a result, the total cost of departure and insertion (ΔV_T) is minimized and by allowing the departure and arrival locations to vary on the orbits, the algorithm converges on a more suitable manifold trajectory. Therefore, for this particular case, the most affordable way to travel from the specified location on the 3:5 resonant orbit to the arrival location on Hyperion's orbit is to coast along an unstable manifold trajectory.

Exploration and exploitation of Poincaré sections for application to trajectory design in astrodynamics has emerged only recently, but offers great insight, as illustrated by the design examples included in this section. Poincaré sections are also particularly effective in locating and computing stable and unstable resonant orbits and the display of the manifold structures associated with unstable periodic orbits is also facilitated by these maps. The Saturn-Titan regime is explored by searching for transfers between planar resonant and Lyapunov orbits. However, the design space is large and the exploration options remain open.

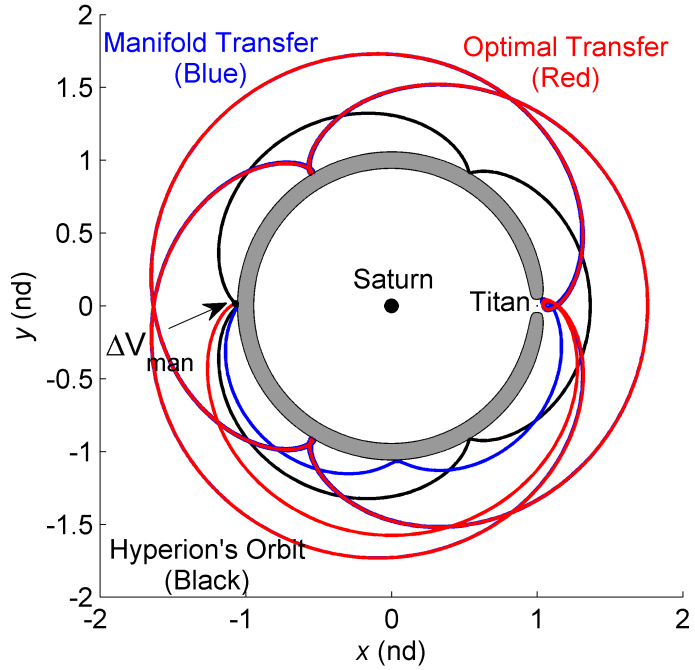

(a) Manifold and Optimal Short-TOF Transfers

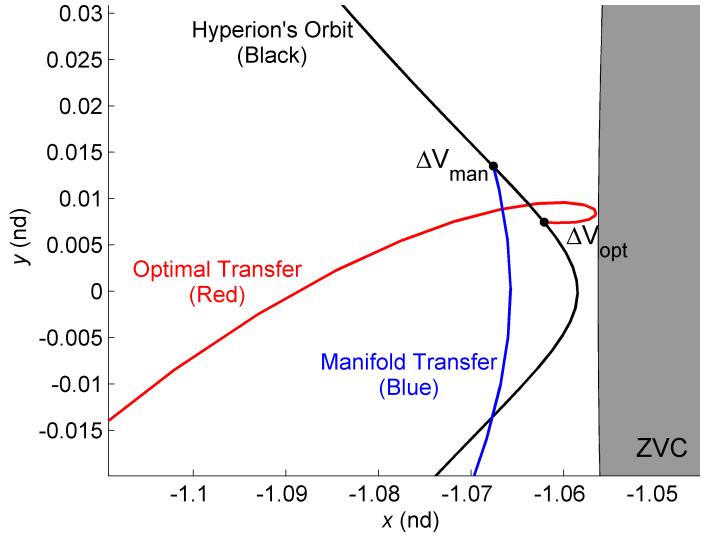

(b) Zoomed-View of Insertion Region

Figure 4.21. Locally Optimal Transfer (shorter TOF) and Manifold Transfer Trajectory B to Hyperion's 3:4 Resonant Orbit

4.4 Resonance Transition in the Earth-Moon System

The region of space in the Earth-Moon neighborhood has been extensively investigated. Resonant orbits have also been a focus in such investigations. For instance, Parker and Lo explore the use of unstable resonant orbits and their associated invariant manifolds to investigate mission scenarios near Earth involving periodic flybys of the Moon [41]. In this investigation, an extension of some of these analyses and a better understanding of the dynamical structure in this regime is sought. Some significant factors influence the behavior in the Earth-Moon region including the presence of only a single major natural satellite, i.e., the Moon. Additionally, the mass parameter is larger in the Earth-Moon system ($\mu \approx 0.0122$) than in the Saturn-Titan ($\mu \approx 2.3658 \times 10^{-4}$) and Jupiter-Europa ($\mu \approx 2.5266 \times 10^{-5}$) systems; as a result, the effect of the Moon's gravity on the spacecraft is *much* larger, also affecting the stability of certain periodic orbits. Potentially, these very characteristics enable expanded trajectory design options and mission scenarios.

4.4.1 Planar Natural Transfers: Resonant Homoclinic and Heteroclinic Connections

Similar relationships to those found between planar resonant orbits in the Saturn-Titan and Jupiter-Europa system also exist in the Earth-Moon system. In this analysis of the natural dynamics associated with resonant orbits in the Earth-Moon regime, natural connections between 2D resonant orbits are examined. As an illustrative example of the existence of natural transfer trajectories between these type of orbits, consider the planar families of 1:2 and 2:3 resonant orbits plotted in Figures 3.17(b)-3.17(g). In particular, consider a member in each family, plotted in Figures 4.22(a)-4.22(b).

The invariant manifolds associated with these periodic orbits, in resonance with the Moon, are computed using an offset value of 30 km and a total of 10,000 fixed points evenly spaced in time along the orbits. The trajectories along the stable

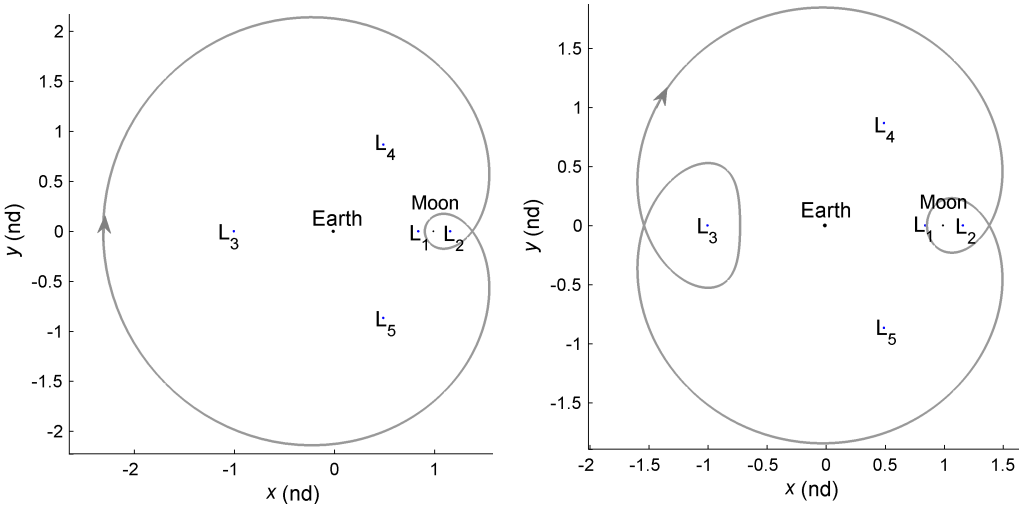

(a) 1:2 Resonance

(b) 2:3 Resonance

Figure 4.22. Two-Dimensional 1:2 and 2:3 Resonant Orbits in the Earth-Moon System (Moon Enlarged x2)

manifold tube are propagated backwards in time for 40 non-dimensional time units, equivalent to 174 days. Similarly, the trajectories along the unstable manifold tube are integrated forward in time for the same interval. For a wider view of the invariant manifolds and their relationship to other dynamical structures, it is necessary to plot them against a background that includes some of these structures. The set of initial conditions used to generate this surface of section is selected to be in the vicinity of the periapsis of the resonant orbits of interest. An integration time of approximately 7 years is employed to generate the one-sided background maps in Figures 4.23(a)-4.23(b). The quantities used in plotting are position and velocity, that is, x and $\dot{x}$, labeled V_x on the map.

Recall that an intersection in the Poincaré map is an intersection in phase space. If the intersection corresponds to a stable and an unstable manifold associated with the *same* periodic orbit, then a homoclinic connection can be calculated. Conversely, a heteroclinic trajectory can be computed from the intersection between an unstable (departure orbit) and a stable (arrival orbit) manifold. As illustrated on the one-sided surfaces of section plotted in Figures 4.23(a)-4.23(b), multiple homoclinic and

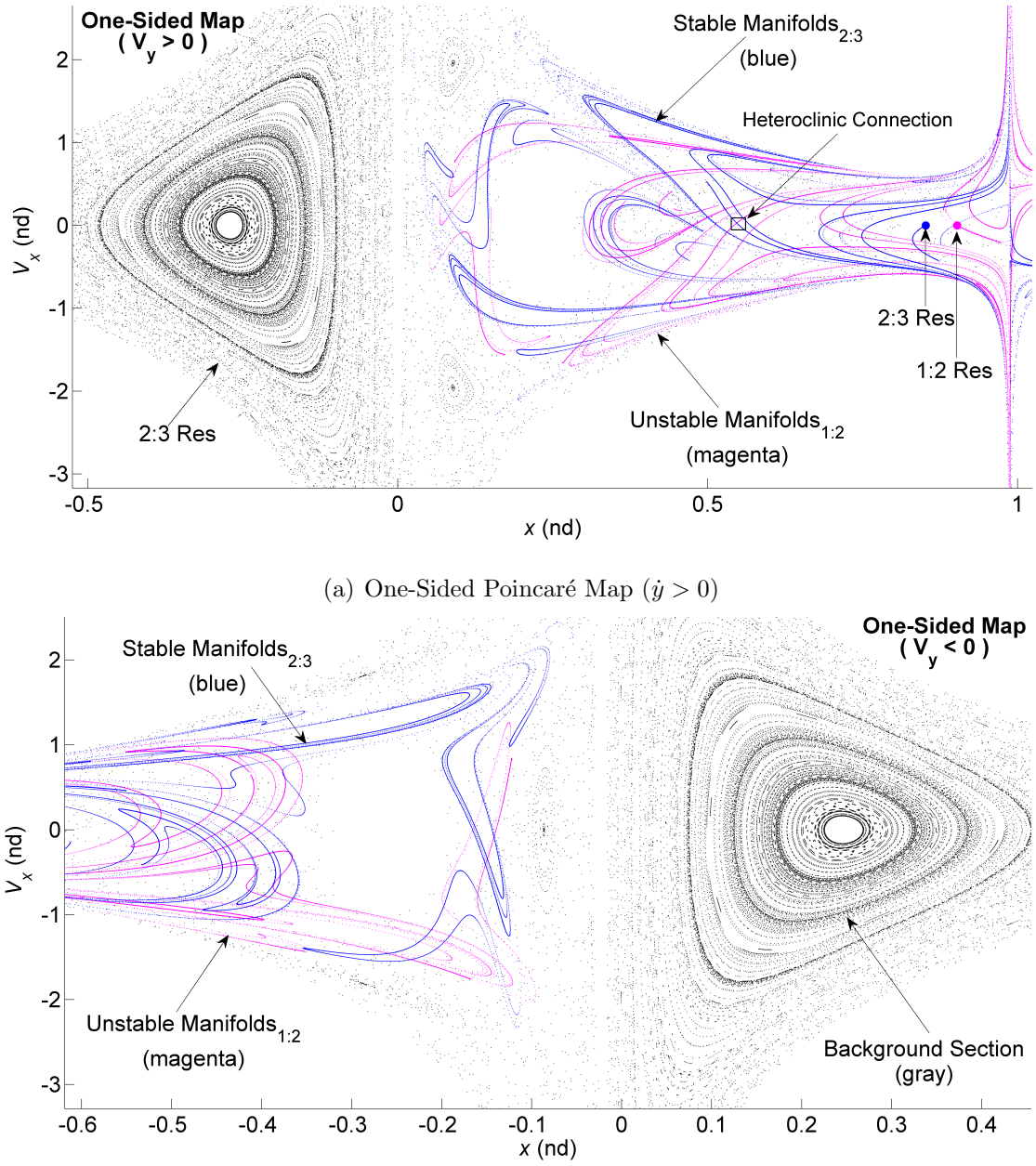

(a) One-Sided Poincaré Map ($\dot{y} > 0$)

(b) One-Sided Poincaré Map ($\dot{y} < 0$)

Figure 4.23. Surface of Section Illustrating the Stable (Blue) and Unstable (Magenta) Manifolds Associated with the 2:3 and 1:2 Resonant Orbits Plotted in Figures 4.22(a)-4.22(b)

heteroclinic trajectories exist between the 1:2 and 2:3 resonant orbits at the selected energy level, i.e., $C = 2.8284$. Three connections are detailed in this analysis as il-

lustrative examples; a heteroclinic connection and two homoclinic trajectories exist between each resonant orbit of interest. The heteroclinic connection is computed from an intersection of the unstable manifold associated with the 1:2 resonant orbit and the stable manifold associated with the 2:3 resonant orbit. The actual intersection in phase space is labeled on the map in Figure 4.23(a); the unstable manifolds appear in magenta and the stable manifolds are plotted in blue. At the intersection, the unstable manifold crossing is propagated in reverse time until it reaches the 1:2 resonant orbit; the stable manifold crossing is propagated in forward time until it reaches the 2:3 resonant orbit. The two resulting manifold arcs are decomposed into smaller subarcs that seed a multiple shooting algorithm. In the corrections scheme, continuity in position and velocity at each intermediate patch point is enforced, producing a natural, maneuver-free path that departs the 1:2 resonant orbit and approaches the 2:3 resonance. The resulting heteroclinic trajectory appears plotted in Figure 4.24(a). Recall that a homoclinic connection is calculated from the intersection of the stable and unstable manifolds associated with the same periodic orbit. The homoclinic connection in Figure 4.24(b) asymptotically departs and approaches the 1:2 resonance in forward and backward time; similarly, the homoclinic connection in Figure 4.24(c) asymptotically departs and approaches the 2:3 resonance in forward and backward time. To aid in the visualization of the trajectory, the 1:2 and 2:3 resonant orbits appear plotted in magenta and blue, respectively.

Similar to periodic resonant chains as constructed in the Saturn-Titan system, it may be possible to numerically correct these type of natural trajectories to obtain periodic orbits that shadow the invariant manifolds associated with one or more resonant orbits of interest, thus, creating a cycle between resonances in the Earth-Moon system. Consistent with previous resonant orbits, a family of periodic resonant cycles can be generated, although the existence of such a family is dependent on the relationship between their associated invariant manifolds. For instance, both homoclinic trajectories plotted in Figures 4.24(b)-4.24(c) offer good candidates for periodic resonant chains. The first homoclinic connection departs and approaches the

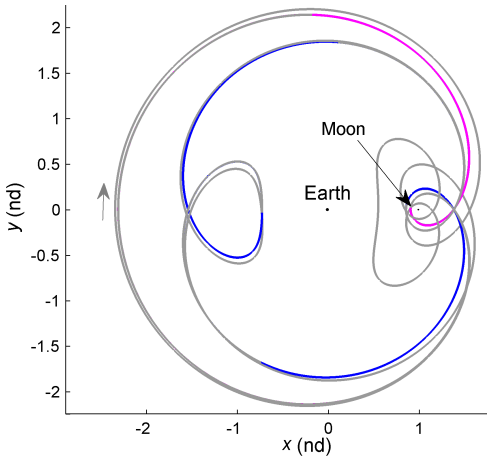

(a) Heteroclinic Connection

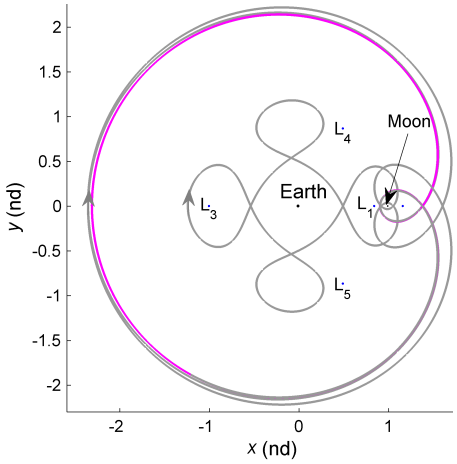

(b) Homoclinic Connection (1:2)

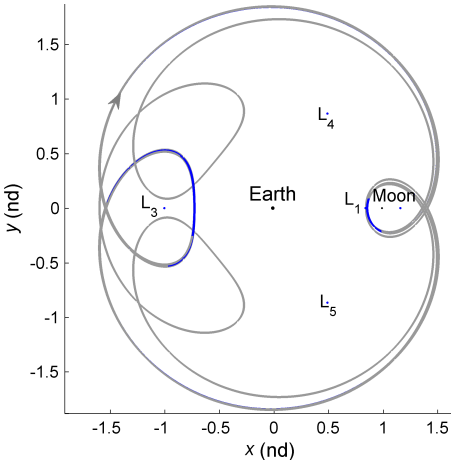

(c) Homoclinic Connection (2:3)

Figure 4.24. Two-Dimensional Heteroclinic and Homoclinic Connections Between 1:2 and 2:3 Resonant Orbits Plotted in the Rotating Frame (Moon Enlarged x2)

1:2 exterior resonant orbit but also transitions through the interior region shadowing a 5:4 interior resonant orbit. Note that to demonstrate the relationship that may exist between the 1:2 and 5:4 resonant orbits at this energy level, it is necessary to display the fixed points and invariant manifolds associated with the 5:4 resonant orbits on the Poincaré maps in Figure 4.23. Unlike the 1:2 resonant homoclinic connection, the homoclinic connection in Figure 4.24(c) does not transition through the interior region; the trajectory departs and approaches the 2:3 resonant orbit illustrated in Figure 4.22(b), shadowing a member in the family of exterior 3:4 resonant orbits plotted in Figure 3.17(l). These are only two illustrative examples, but other similar natural transitions can be calculated to demonstrate the close relationship between the natural dynamics associated with resonant orbits.

4.4.2 Three-Dimensional Natural Transfers: Resonant Homoclinic- and Heteroclinic-Type Connections

The relationship between unstable resonant orbits in the Earth-Moon system is not unique to the planar problem. Similar three-dimensional trajectories between resonant orbits that follow the natural dynamics of the system also exist. In this investigation, the analysis and construction of 3D natural transfer trajectories is completed with the aid of higher-dimensional maps. Recall that for the planar CR3BP in $\Re^4$, the surface of section, or hyperplane Σ, is typically specified by fixing one of the coordinates, frequently $y = 0$, producing a surface in $\Re^3$. The 3D surface is projected onto a plane by specification of another parameter. For example, to generate a two-dimensional Poincaré section in the CR3BP, a value for the Jacobi constant is specified and a grid of initial conditions for x and $\dot{x}$ are selected and integrated forward in time. The intersections of each trajectory with the surface of section create the Poincaré map. With C, x and $\dot{x}$ initially defined, as well as the hyperplane $y = 0$, the corresponding initial values for $\dot{y}$ can be calculated from the expression for the Jacobi constant. However, the spatial problem in $\Re^6$ presents some additional chal-

lenges. The surface of section, Σ, is specified in a similar way, that is, by fixing one of the coordinates, usually $y = 0$, and producing a surface in $\Re^5$. The dimension of the problem is further reduced by the specification of another parameter, such as Jacobi constant, C. In this analysis, to represent a trajectory on a higher-dimensional map (4D), three coordinates are employed, i.e., x and $\dot{x}$ in the plane and z along the vertical axis, and a non-physical quantity reflects the value of the third component of the velocity, i.e., $\dot{z}$. Then, the corresponding value for $\dot{y}$ is calculated from the expression for the Jacobi constant in equation (2.76). A number of researchers employ various approaches to represent higher-dimensional Poincaré maps [24, 83–88]; one option to represent the fourth dimension or component in a 3D figure is the use of an arrow of varying length [88]. In this investigation, a variation is employed where, at the manifold crossing only $(x, \dot{x}, z)$ in the 3D figure, a second coordinate system representing velocity space is introduced ($\dot{x}, \dot{y}, \dot{z}$ labeled V_x, V_y, V_z). Directional arrows are added in an attempt to qualitatively represent the direction of the velocity associated with the manifold at the plane crossing and are scaled according to the magnitude of the $\dot{z}$ component.

To illustrate some of the out-of-plane results, consider the unstable, 3D, 'northern' 1:2 resonant orbit at $C = 2.5945$ as illustrated in Figure 4.25. This orbit, in resonance with the Moon, is symmetric across the xz-plane, assuming that the initial state is located such that $y_0 = 0$, then $\dot{x}_0 = \dot{z}_0 = 0$. For visualization purposes, the projections of the 3D orbit onto the xy-plane and xz-plane appear in Figures 4.25(b)-4.25(c), respectively. Once an unstable resonant orbit is identified, the associated invariant manifolds are computed and displayed on a surface of section. The invariant manifolds computed in conjunction with the 1:2 resonant orbit in Figure 4.25 are displayed in Figure 4.26 and appear as a 3D-projection of a 4D surface of section. The stable and unstable manifold are plotted in blue and magenta, respectively. Two-dimensional views are represented in Figures 4.26(b)-4.26(c). The fixed points associated with the periodic orbit are displayed on the map as black dots. At the intersection between the stable and unstable manifold, as viewed on the 3D figure, two directional arrows reflect

the direction of the velocity and the magnitude of the $\dot{z}$ component corresponding to each crossing and thus, qualitatively represent the fourth dimension.

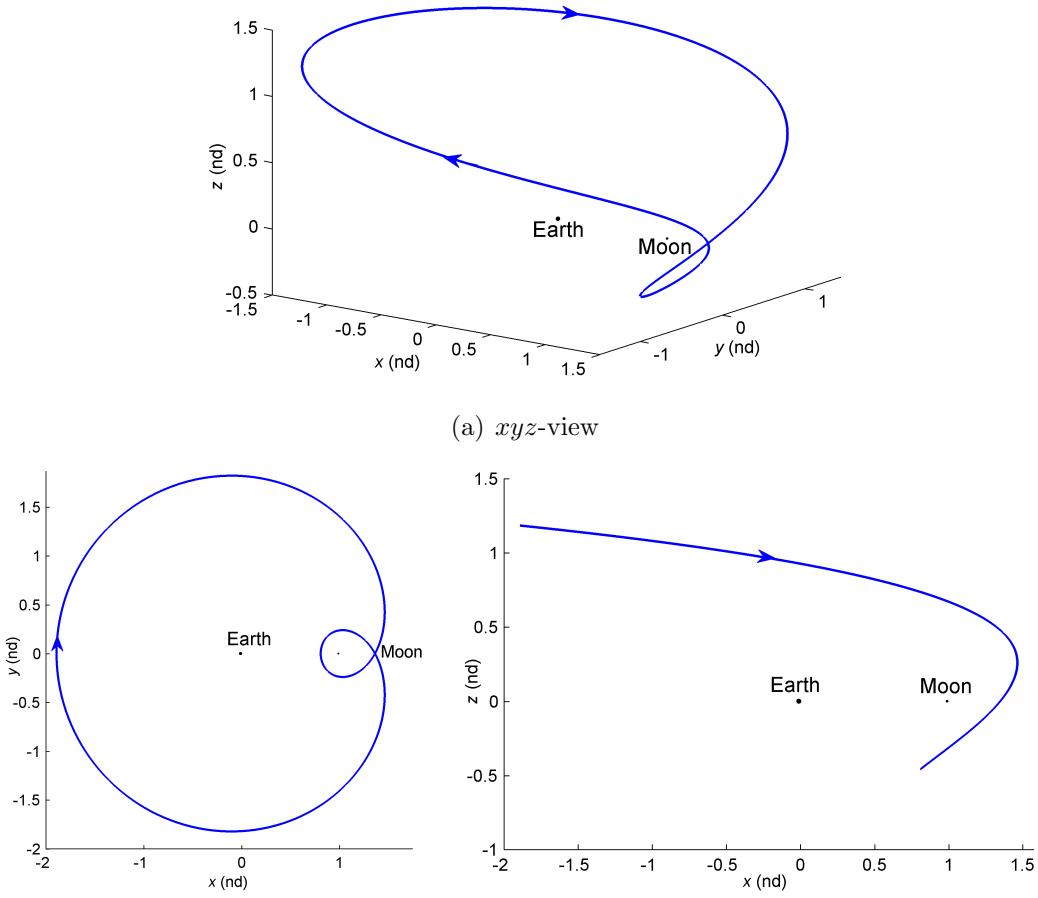

(a) xyz-view

(b) xy-view

(c) xz-view

Figure 4.25. Three-Dimensional 'Southern' 1:2 Resonant Orbit in the Earth-Moon System (Moon Enlarged x2 for Visualization)

The next step in the process of calculating natural transitions between resonant orbits employing manifold arcs is the identification of other resonant orbits in the vicinity of the intersections of the unstable and stable manifolds on the 4D map. Points on the map with $\dot{x} = \dot{z} = 0$ and near the intersection of the manifolds are sought as 3D resonant candidates. Using two-body approximations and a corrections algorithm, a new resonant orbit is generated. As an illustrative example, a 2:3

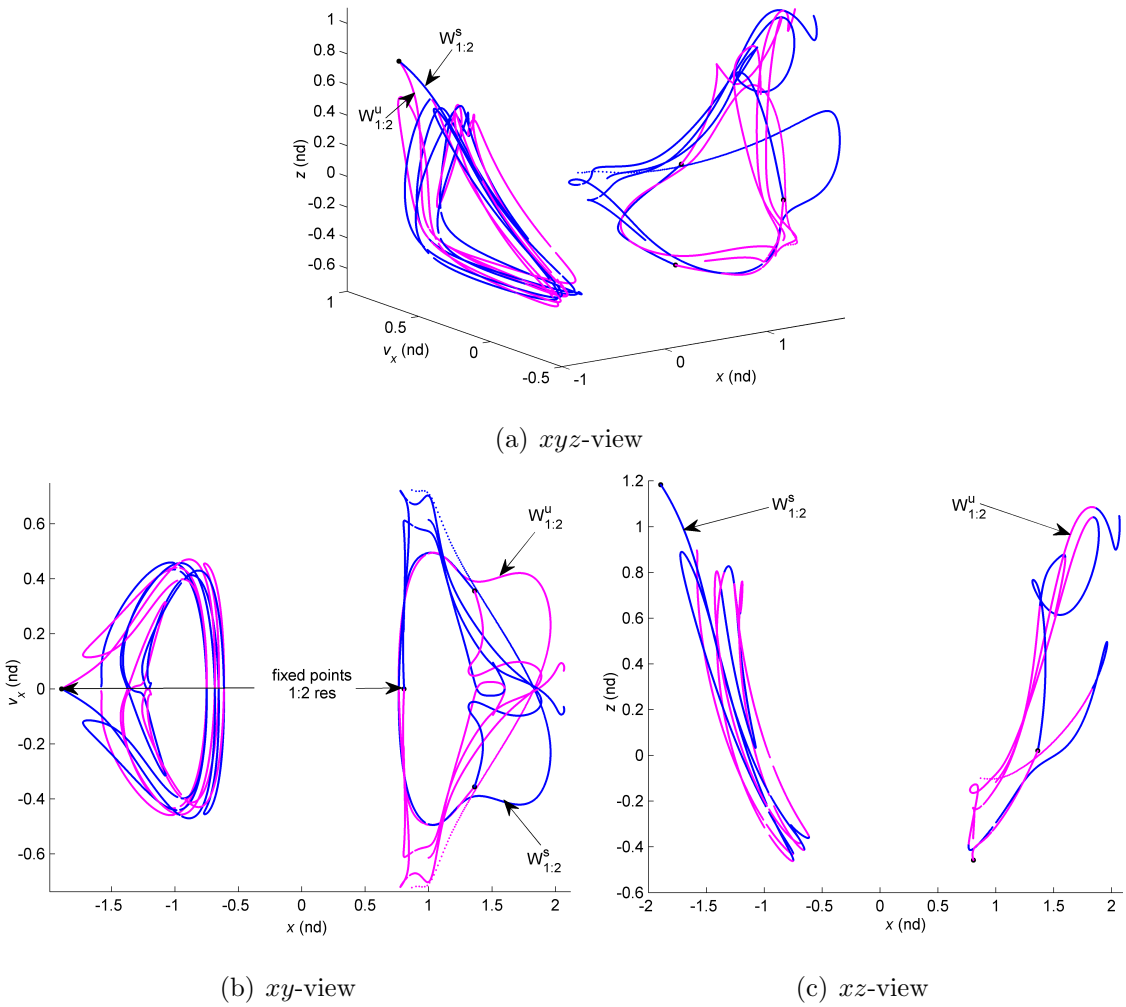

(a) xyz-view

(b) xy-view

(c) xz-view

Figure 4.26. Position-Velocity Representation of the Stable (Blue) and Unstable (Magenta) Manifolds Associated with the 1:2 Resonant Orbit in Figure 4.25

'northern' resonant trajectory is computed and represented in Figure 4.27. This new periodic orbit possesses the same value of Jacobi constant as the 1:2 resonant orbit in Figure 4.25, that is, $C = 2.5945$.

As illustrated in Figure 4.26, the invariant manifolds associated with 3D resonant orbits form well-defined, almost closed contours when represented in terms of position and velocity components, that is, x, $\dot{x}$ and z. From the representation of the invariant manifolds in Figure 4.26, it is possible to locate potential intersections between the

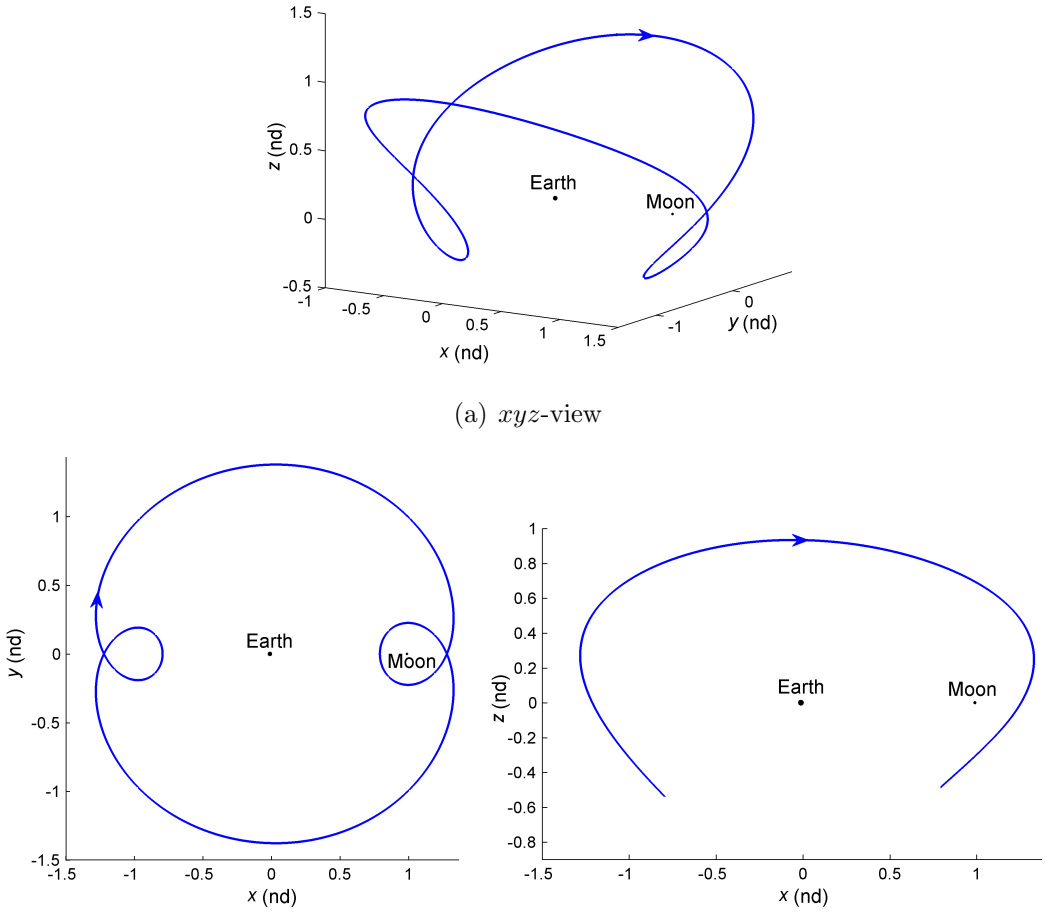

(a) xyz-view

(b) xy-view

(c) xz-view

Figure 4.27. Three-Dimensional 2:3 'Southern' Resonant Orbit in the Earth-Moon System (Moon Enlarged x2 for Better Visualization)

stable and unstable manifolds associated with one or more resonant orbits of interest to yield 'natural' connecting paths. Such an intersection in phase space is determined from an intersection on the 4D map where the values of x, $\dot{x}$ and z are the same and the corresponding directional arrows are parallel in orientation (direction) and possess the same length. Since all the manifold trajectories are computed at the same energy level, the corresponding value for $\dot{y}$ can be recovered from the expression for Jacobi constant. Lastly, the surface of section is defined at $y = 0$, so both trajectories share this value at the intersection. Because only a finite number of stable and un-

stable manifold trajectories are computed, it may not be possible to locate an 'exact' intersection on the 4D map. However, nearby intersections are clearly identifiable from Figure 4.26 and, with the aid of a corrections algorithm, it is possible to remove the small difference that may exist in the position and velocity states. Thus, once a potential connection is identified, the point at the intersection on the map associated with the stable manifold is propagated forward in time and the point at the intersection associated with the unstable manifold is propagated backward in time until each manifold trajectory reaches the associated resonant orbit. Then, each manifold arc is decomposed into smaller subarcs to reduce the sensitivities in the numerical corrections process. A multiple shooting algorithm is employed to reconnect the subarcs and remove the small discontinuity that exists, yielding a three-dimensional trajectory continuous in position and velocity. Continuity in position and velocity is enforced at each patch point, but other constraints are also specified to ensure that the resulting trajectory departs and approaches the resonant orbit(s) of interest. Each manifold trajectory is propagated forward (stable) or backward (unstable) in time until the trajectories wrap around the resonant orbit(s) for two revolutions. After propagation, the position of the end points on each manifold arc is fixed and the value of Jacobi constant is enforced to guarantee that the resulting transfer is at the same energy level as the two periodic orbits of interest. In this analysis, the resulting 3D path, continuous in position and velocity, is termed a 'homoclinic-type' trajectory if the connected manifolds are associated with *one* resonant orbit; it is labeled a 'heteroclinic-type' trajectory if the connected manifolds are associated with *two* resonant orbits.

As an illustrative example of such three-dimensional connections between resonant orbits in the Earth-Moon system, consider the unstable resonant orbits represented in Figures 4.25 and 4.27. The invariant manifolds associated with these resonant trajectories are employed as transfer mechanisms between the orbits. A homoclinic-type connection asymptotically departs and approaches the same resonant orbit when propagated forward and backward in time. As an illustrative example, consider a 3D

homoclinic-type trajectory associated with the 1:2 resonance in Figure 4.25. A 4D map representing the stable (blue) and unstable (magenta) manifolds associated with this 1:2 resonant orbit appears in Figures 4.28(a)-4.28(b). At the intersection of the manifolds in Figure 4.28(b), the magenta and blue arrows are associated with the unstable and stable manifolds, respectively. Recall that the direction of these arrows indicates the velocity direction at each crossing; the arrows are scaled consistent with the magnitude of the out-of-plane component of the velocity, i.e. $\dot{z}$, at the crossing of the hypersurface. A similar approach is employed to remove the discontinuity that exists in both position and velocity; the resulting out-of-plane trajectory is plotted in Figure 4.28(c). For visualization purposes, two-dimensional views of the 3D trajectory on the xy- and xz-plane are represented in Figures 4.28(d)-4.28(e).

Another type of natural connecting path that exploits the invariant manifolds associated with two different resonant orbits can also be computed at this particular value of Jacobi constant. That is, a heteroclinic-type connection is available from the intersection of the stable manifold associated with the 1:2 resonant orbit and the unstable manifold associated with the 2:3 resonant orbit. As an illustrative example, consider a 3D heteroclinic-type connection asymptotically departing the 1:2 resonance and asymptotically approaching the 2:3 resonant orbit. Note, however, that a heteroclinic-type trajectory exists from each orbit, that is, asymptotically departing the 1:2 resonance and approaching the 2:3 resonant and vice versa. A 4D map representing the unstable manifolds associated with the 1:2 resonant orbit (magenta) and the stable manifolds associated with the 2:3 resonant orbit (blue) is generated and represented in Figure 4.29(a). The invariant manifolds are propagated for 217 days. The map intersection that is employed to generate the stable and unstable manifold arcs is also highlighted in Figure 4.29(a). Recall that, at this intersection, the trajectories share very similar values of x, $\dot{x}$ and z and the associated directional arrows at the crossing are oriented along the same direction and possess approximately the same length, which indicate a potential match in the $\dot{z}$ component as well. The resulting three-dimensional natural trajectory that transitions between the two resonances

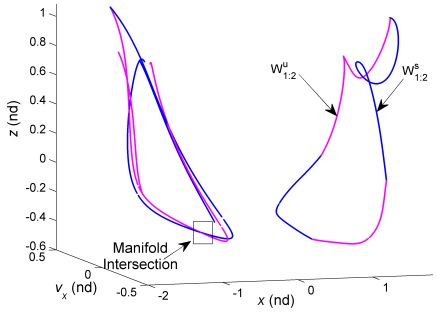

(a) Manifold Representation

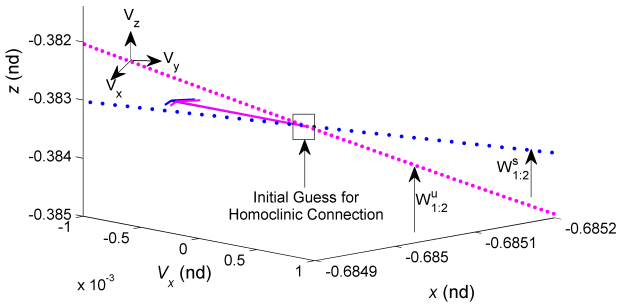

(b) Zoomed View of Initial Guess

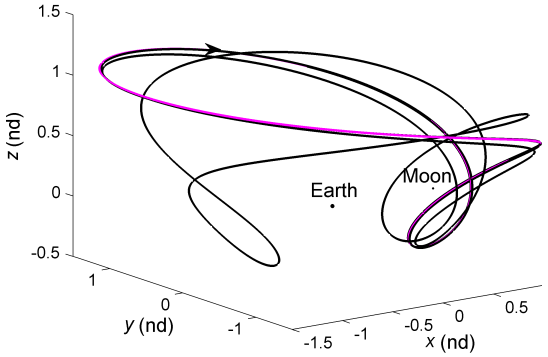

(c) xyz-view Homoclinic

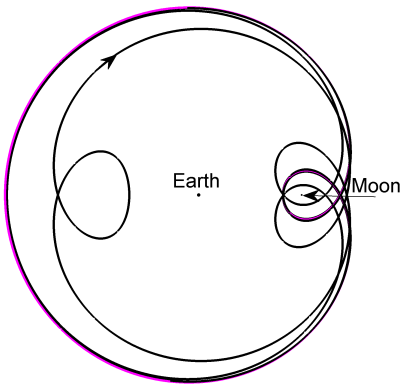

(d) xy-view Homoclinic

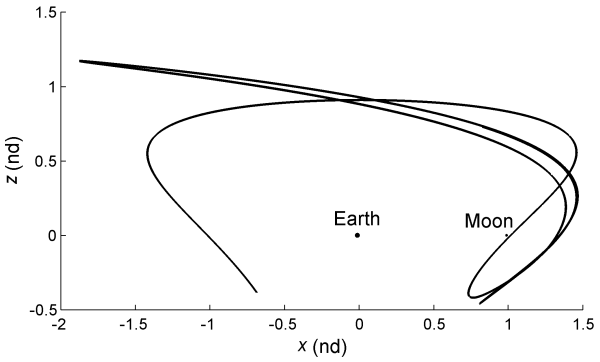

(e) xz-view Homoclinic

Figure 4.28. (a)-(b) Higher-Dimensional Surface of Section Illustrating Stable (Blue) and Unstable (Magenta) Invariant Manifolds and (c)-(e) Three-Dimensional Homoclinic-Type Transfer Trajectory Between a 1:2 Resonant Orbit in the Earth-Moon System

in the Earth-Moon system appears in Figure 4.29(b). Note that this trajectory is continuous in position and velocity. The corrections process is already incorporated

to remove the small discontinuity that exists between the states obtained from the intersection highlighted on the map in Figure4.29(a).

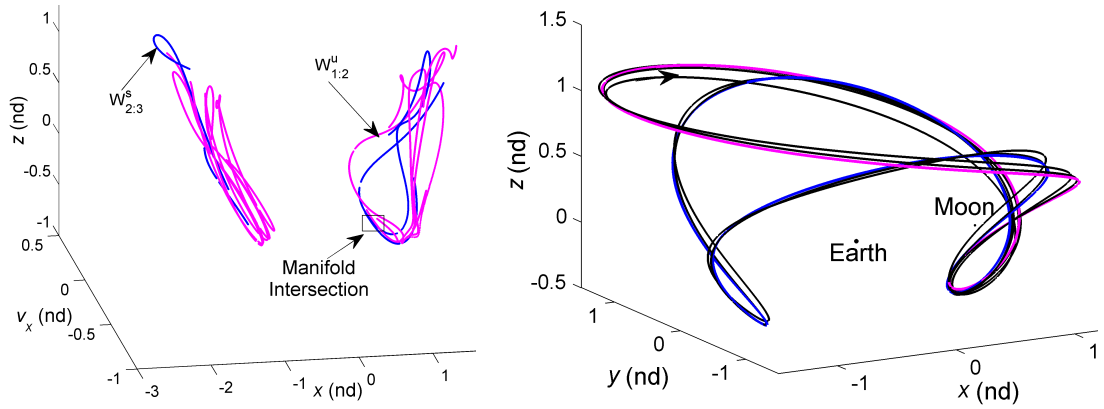

(a) Manifold Representation

(b) 3D Heteroclinic-Type Connection

Figure 4.29. Higher-Dimensional Surface of Section Illustrating Stable (Blue) and Unstable (Magenta) Invariant Manifolds in (a) and Three-Dimensional Heteroclinic-Type Transfer Trajectory Between a 1:2 and a 2:3 Resonant Orbit in (b)

The natural connecting paths in Figure 4.28 and Figure 4.29 are not unique to these particular resonances. In fact, similar trajectories are computed for other resonant orbits at this particular energy level. Note that the two 3D resonant orbits in Figures 4.28-4.29 are denoted 'northern' resonant orbits. The 'southern' counterparts also exist and are computed with the same numerical scheme. Similar natural transfer trajectories also exist between the southern periodic orbits.

4.4.3 Planar ΔV-Transfers: Trajectories from Low Earth Orbit to Selected Libration Point Orbits

A strategy in trajectory design that involves the exploitation of the invariant manifolds associated with resonant orbits is proposed. This concept is employed to generate orbits in multi-body systems as well transfer paths with specific itineraries to and from selected orbits. If a natural transfer is not available to link the initial

and final orbits of interest, the multiple shooting algorithm is modified to accept any number of intermediate maneuvers to accommodate any discontinuities that may exist in velocity, producing a single continuous trajectory in position that includes a desired number ΔVs at selected locations.

It is well-known that libration point orbits, such as 2D Lyapunov orbits or 3D halo orbits, and their associated natural dynamics, i.e., invariant manifolds, are fundamental structures in the mission design process. However, the dynamical environment in multi-body systems is not limited to libration point orbits. In this investigation, resonant orbits are incorporated into the design process to potentially enable the construction of more cost-efficient, or even novel, transfer scenarios. To explore such an option, it is necessary to, first, expand the orbit architecture in the Earth-Moon CR3BP by cataloging resonant orbits, and second, to assess the role of resonant orbits in the design of transfer trajectories. Chapter 2 includes a variety of planar and three-dimensional families of resonant orbits in the Earth-Moon system as well as in the ephemeris model. To assess the role of resonant orbits in trajectory design, and given the increased interest in employing Earth-Moon libration point orbits for a variety of purposes, transfer trajectories from low Earth orbit to a selection of libration point orbits near each of the five Earth-Moon equilibrium points are designed by leveraging conic arcs and invariant manifolds associated with resonant orbits as well as libration point orbits. Resonant manifolds in the Earth-Moon system, particularly those emanating from exterior resonant orbits, offer trajectories that tour the entire Earth-Moon space in reasonable time intervals. These trajectories also pass relatively close to the Earth, offering good candidates for direct transfers from LEO. Then, the arrival phase into various libration point orbits is facilitated by the use of the associated libration point orbit stable manifolds. Thus, the design technique that is employed to construct these efficient transfer trajectories exploits a variety of connecting arcs emerging from the manifolds associated with both resonant and libration point orbits. The CR3BP serves as a basis to quickly generate solutions that meet specific requirements. Candidate transfer trajectories are then transitioned to a

higher-fidelity model that includes solar gravitational effects to validate the solutions generated in the 3B model and to demonstrate the existence of resonant conditions in multi-body regimes. A preliminary transfer cost and time-of-flight analysis illustrates the benefits of incorporating intermediate resonant arcs into the design process.

In contrast to the invariant manifolds associated with Lyapunov or halo orbits, the trajectories along the invariant manifolds associated with resonant orbits are tangled and complicated to visualize. Thus, it is necessary to incorporate a technique that offers a different representation of these manifold trajectories. Recall that, in the search and computation of resonant transitions, a position-velocity (x-$\dot{x}$) map at $y = 0$ aids in visualization and offers clues concerning the relationships between resonant manifolds and other structures in the phase space. However, a single map representation of these trajectories may not offer sufficient insight to construct cost-efficient transfer trajectories between LEO and the libration point orbit of interest. Note that previous transfers, natural or with intermediate maneuvers, involved resonant orbits as the initial and final orbits. In the following scenarios, resonant orbits are exploited as transfer mechanisms only.

Three different mapping representations are employed in this analysis to identify the connecting arcs during the three phases that define a transfer between the initial LEO and the final libration point orbit. Consider a transfer from LEO to an Earth-Moon L_1 Lyapunov orbit. The various phases along a transfer path are identified in the diagram in Figure 4.30. The first phase links the LEO and the stable manifold arc associated with a resonant orbit. The second phase involves an arc that delivers the vehicle to the vicinity of the libration point orbit of interest, and the third (and final) phase along the transfer trajectory is focused on the LPO insertion. Note that Phase 1 may be omitted from the design process in cases where the stable manifold arc passes close to the vicinity of the Earth.

Three different mappings, each associated with a transfer phase, supply a representation in a suitable design space: (i) a map reflecting position only (x-y) defined from apse locations, (ii) a position-velocity representation (x-$\dot{x}$) of the invariant manifolds

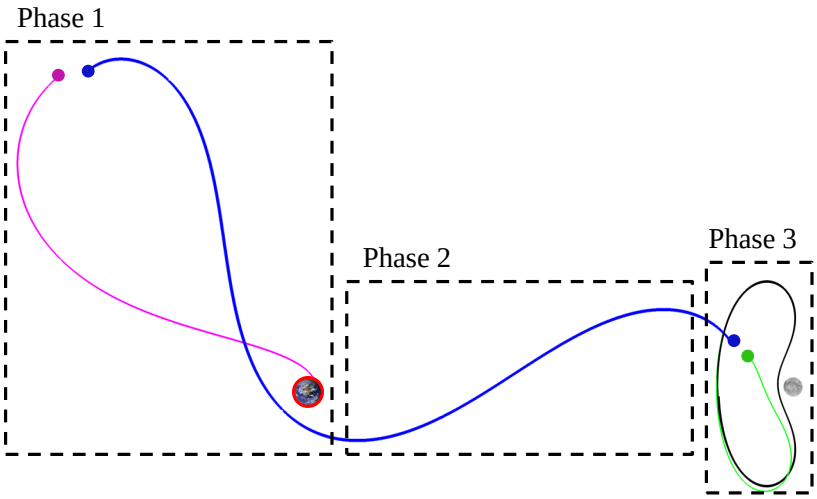

Figure 4.30. General Transfer Phases Diagram

on a surface of section defined at $y = 0$, and (iii) a position-velocity representation (y-$\dot{y}$) of the invariant manifolds on a surface of section defined at $x = K$, where K reflects a constant location along the x-axis, e.g., in the vicinity of the Moon, or $K = 1 - \mu$. Once potential resonance transitions corresponding to each phase are identified from the maps, a corrections scheme is employed to blend the LEO, the connecting arcs and the arrival libration point orbit into a continuous path. Although the resulting transfer path benefits from a reduced maneuver cost (ΔV) by shadowing the manifold trajectories, direct optimization techniques are sometimes employed *a posteriori* to further reduce the propellant requirements. For reference, the strategy proposed in this analysis to construct transfer trajectories from LEO to selected Earth-Moon libration point orbits is defined in section 4.2. The maps are constructed only once after the departure (LEO), arrival (LPO), and intermediate (resonant) orbits are selected and any associated manifolds are constructed. Thus, the transfer design process is straightforward and is easily automated to allow for the computationally efficient construction of transfers with different patterns and itineraries.

The effect of the Moon's gravity on periodic resonant orbits in the vicinity of the Earth can be significant, potentially delivering useful transfer scenarios. The large value of the mass parameter, μ, also influences the stability of the orbits in resonance with the Moon. Periodic resonant orbits in a family defined in terms of a p:q resonant ratio may be unstable in the Earth-Moon system but linearly stable in other systems. For instance, consider the family of 4:3 resonant orbits plotted in Figure 4.31. The effect of the Moon, through a higher mass ratio, on the periodic orbits compared to the effect of Titan on orbits with very similar characteristics is immediately obvious. All members in the 4:3 resonant family in the Earth-Moon system are unstable, with the largest unstable eigenvalue $|\lambda_u| = 2,513.2$. In contrast, most of the 4:3 resonant orbits in the Saturn-Titan family are linearly stable; only a few orbits possess an unstable eigenvalue of magnitude $|\lambda_u| = 1.4704$. The Moon also affects the period of these resonant orbits [89]. The large gravitational effect of the Moon on resonant conditions reveals potentially useful transfer scenarios. In fact, the Earth-Moon resonant orbits illustrated in Figure 4.31(a) offer a continuous "tour" of the system and, thus, these orbits are candidates for transfers to the vicinity of any of the five Earth-Moon libration points. The periodic orbit plotted in Figure 4.31(c) is selected from the 4:3 resonant family in the Earth-Moon system in Figure 4.31(a) to serve as a basis for the transfers that follow, but other members in the family can be employed, as well as other resonant orbits, to expand the design options.

As an application of resonant orbits in the design of transfer trajectories to other, perhaps non-resonant, orbits in the Earth-Moon system, consider planar transfers from LEO to the vicinity of *any* of the libration points, L_i. Given the increased interest in utilizing Earth-Moon LPOs for different purposes, a variety of planar libration point orbits are considered in this preliminary transfer analysis. Sample orbits in the families of L_1, L_2, and L_3 Lyapunov orbits as well as sample short period orbits at L_4 and L_5 are represented in Figure 4.32. Recall that sample libration point orbits in this transfer investigation are computed via a multiple shooting algorithm

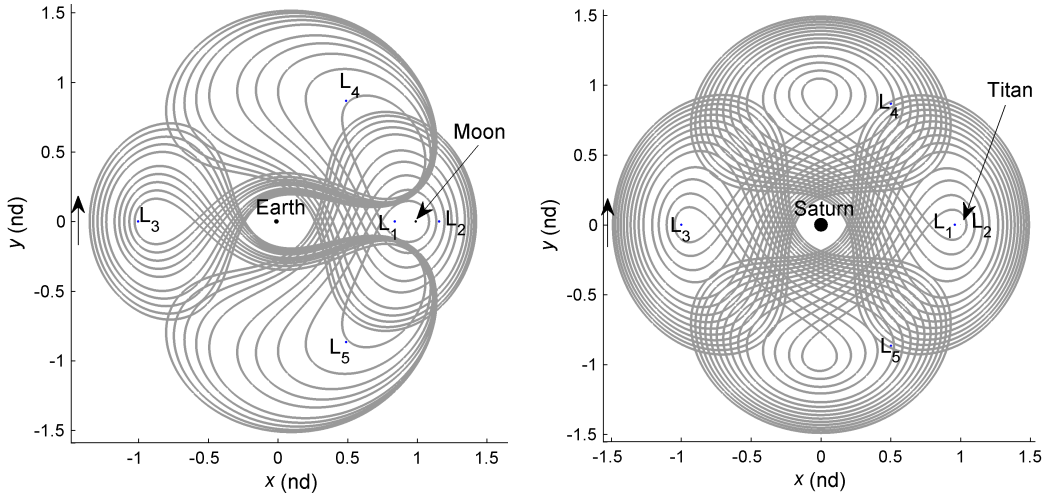

(a) Earth-Moon System

(b) Saturn-Titan System

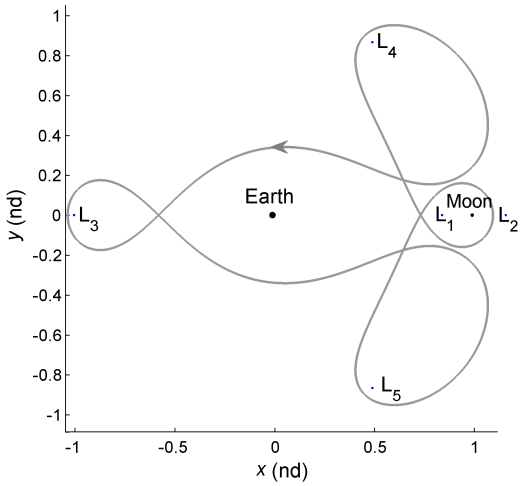

(c) Selected 4:3 Resonant Orbit

Figure 4.31. Representative Members in a Family of 4:3 Resonant Orbits in the Earth-Moon and Saturn-Titan Systems in (a) and (b) and Selected Earth-Moon Periodic Orbit for Transfers to Libration Point Orbits in (c)

that incorporates a pseudo-arclength continuation scheme: families are constructed via a step in a direction tangent to the family [50].

To construct the transfers, an initial 180-km altitude LEO and a final libration point orbit are incorporated into the design process, as well as various intermediate

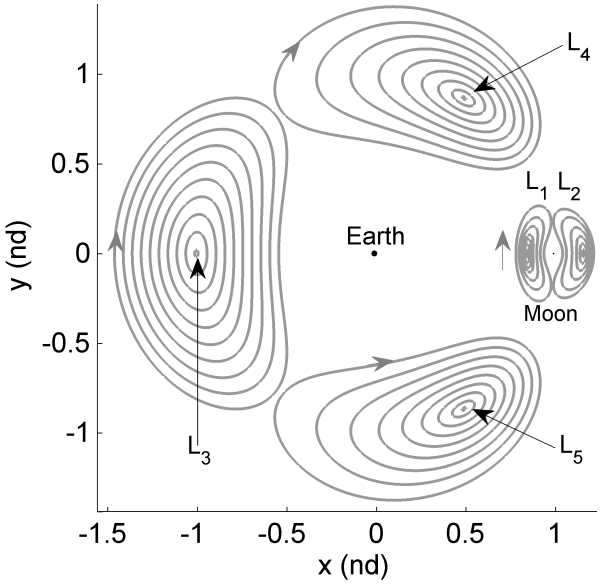

Figure 4.32. Representative Orbits in Families of 2D Earth-Moon Libration Point Orbits

segments. A total of two to three impulsive maneuvers are added along the transfer path, but the corrections algorithm can accept any number of ΔVs. Recall that, in this analysis, a combination of conic arcs and invariant manifolds associated with resonant orbits as well as libration point orbits serve as the initial guess for the connecting segments. The manifolds are displayed on a surface of section to aid in the visualization of the trajectories in phase space and in locating regions of potential intersection that may yield low-cost connections. A variety of mapping techniques are exploited to facilitate the design process and improve the connecting arcs that are selected as initial guesses for each transfer phase. The resulting Poincaré maps appear in Figure 4.33. The map in Figure 4.33(a) displays the apse locations of the stable manifolds associated with the resonant orbit (blue) as well as the conic segments (magenta) that serve as departure legs from LEO. For reference, representative Lyapunov orbits at L_1, L_2, and L_3, as well as short period orbits near L_4 and L_5 are also plotted on the map. An apse map is constructed by selecting $r\dot{r} = 0$, where r is defined as the radial distance between the spacecraft and the Earth, i.e,

$r = \sqrt{(x+\mu)^2 + y^2 + z^2}$, and $\dot{r}$ is the speed of the spacecraft relative to the rotating frame. Periapsis and apoapsis are identified by the sign of the radial acceleration, i.e., positive at periapsis and negative at apoapsis. Note that periapse maps have been widely employed by many researchers to classify trajectory behavior in multi-body environments [60, 87, 90] and to demonstrate their use in various mission design scenarios [60, 67, 91]. The maps in Figures 4.33(b)-4.33(c) offer a position-velocity representation of the conic arcs and the invariant manifold trajectories associated with the resonant orbit and the libration point orbits. The surfaces of section are located along the x-axis, i.e., $y = 0$, and at a given constant value in the vicinity of the Moon, that is, $x = 0.65$, respectively. The resonant manifold trajectories (blue) in Figure 4.33(b) are also plotted against a background map (gray) that highlights other dynamical structures at this particular energy level and, thus, aids in the identification of regions of periodic, quasi-periodic, and chaotic motion in the vicinity of the Earth and the Moon. Recall that each Poincaré map is employed to identify an initial guess for a connecting arc for each phase along the transfer, that is, the apse map in Figure 4.33(a) is used for Phase 1 connecting an Earth departure leg (conic arc) to a stable manifold associated with a resonant orbit. The x-$\dot{x}$ map illustrated in Figure 4.33(b) highlights options for the intermediate – and longest – transfer arc for Phase 2, linking the vicinity of the Earth to the vicinity of the LPO of interest. Note that the segment in Phase 2 may be constructed from one or more intermediate arcs. Lastly, a path for the final approach to the LPO is obtained from the y-$\dot{y}$ map represented in Figure 4.33(c), exploiting manifold arcs emerging from both resonant orbits and LPOs. Note that only manifold trajectories are employed in the final transfer phase. Conic arcs serve as connecting legs between LEO and the intermediate manifold trajectories.

A selection of transfer trajectories that leverage conics as well as manifold arcs emerging from resonant orbits and libration point orbits are illustrated in Figures 4.34-4.36. The initial guess employed to generate each of these trajectories is obtained from each of the maps illustrated in Figure 4.33. Note that the nature of the initial

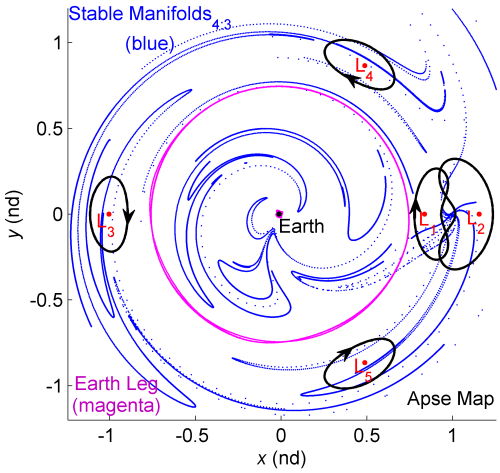

(a) Apse Map ($\bar{r} \cdot \dot{\bar{r}} = 0$) – Phase 1

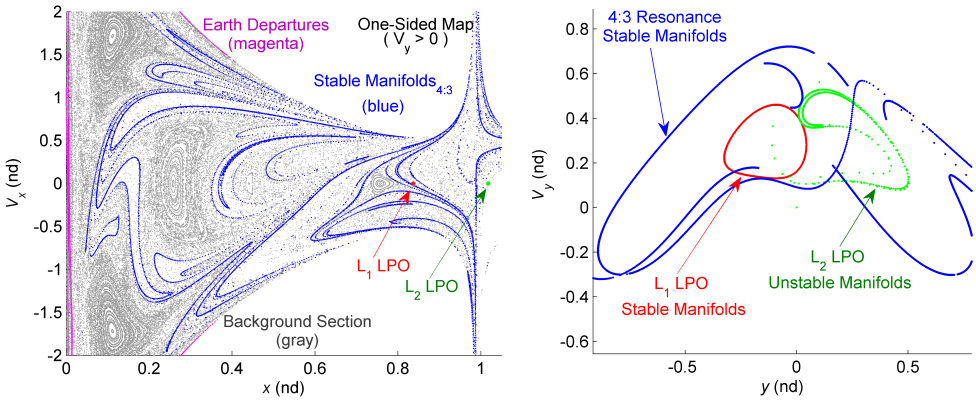

(b) x-$\dot{x}$ Map ($y = 0$) – Phase 2

(c) y-$\dot{y}$ Map ($x = 0.65$) – Phase 3

Figure 4.33. Poincaré Maps Illustrating the Relationship between the Conic Arcs and Invariant Manifolds Associated with Resonant Orbits and Libration Point Orbits for Each Transfer Phase Defined in Figure 4.30

guess is not maintained throughout the corrections process; for example, the conic arc that serves as the initial guess to join LEO and the first manifold arc is no longer a conic arc after the multiple shooting scheme blends the arcs together into a single continuous transfer path. Yet, for reference, the color coding and labeling on the following plots represents the nature of the initial guess. That is, the conic arc, or Earth departure leg, is represented in magenta, the stable manifold arc associated

with the resonant orbit appears in blue, and the stable manifolds associated with the L_1 and L_2 LPOs are plotted in green. The arrival LPO is represented in black and the locations of the impulsive maneuvers that are required to construct a continuous transfer path from LEO to the selected Earth-Moon LPO are highlighted in each plot. In all the sample transfers, the initial maneuver that is required to tangentially depart the 180-km LEO, i.e., ΔV_1, ranges in value between 3.10 km/s and 3.14 km/s. Note, however, that any initial altitude and inclination values can be easily incorporated into the transfer analysis, although the initial cost of departure is influenced by the initial departure orbit. The cost associated with the remaining maneuvers, i.e., ΔV_2 and ΔV_3, as well as the time-of-flight, are detailed in Table 4.2 for each transfer. Note that the cost and time-of-flight associated with the L_1, L_2 and L_3 transfers is not optimized, although these transfers certainly benefit from a reduced ΔV-cost and TOF.

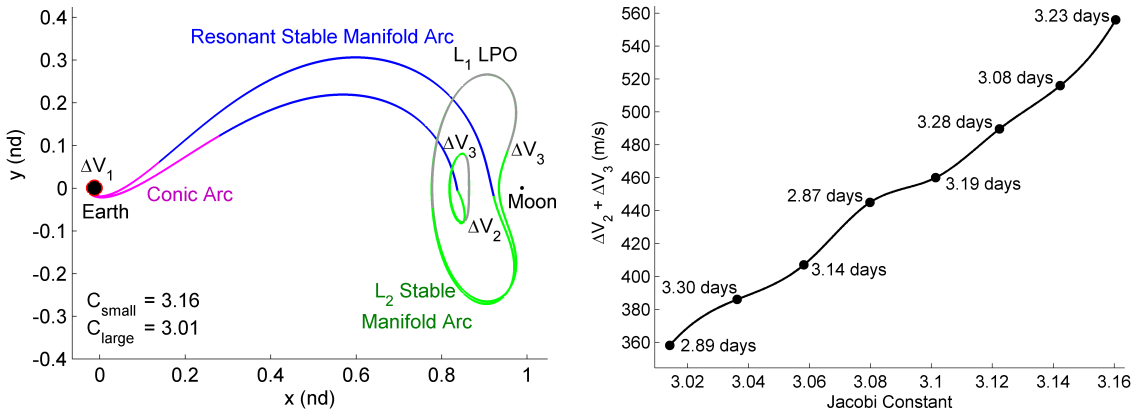

(a) Sample LEO-L_1 Transfers

(b) Cost and TOF Analysis

Figure 4.34. Sample Transfers to Selected Earth-Moon L_1 Lyapunov Orbits via Conic, Resonant and LPO Manifold Arcs in (a) and Maneuver Cost and Time-of-Flight as a Function of Jacobi Constant Associated with a Family of Transfers in (b)

Incorporating resonant manifold arcs into the transfer design process may supply alternative transfer scenarios or even reduce the cost associated with transfer trajectories to LPOs. However, an isolated transfer trajectory may not provide insight into

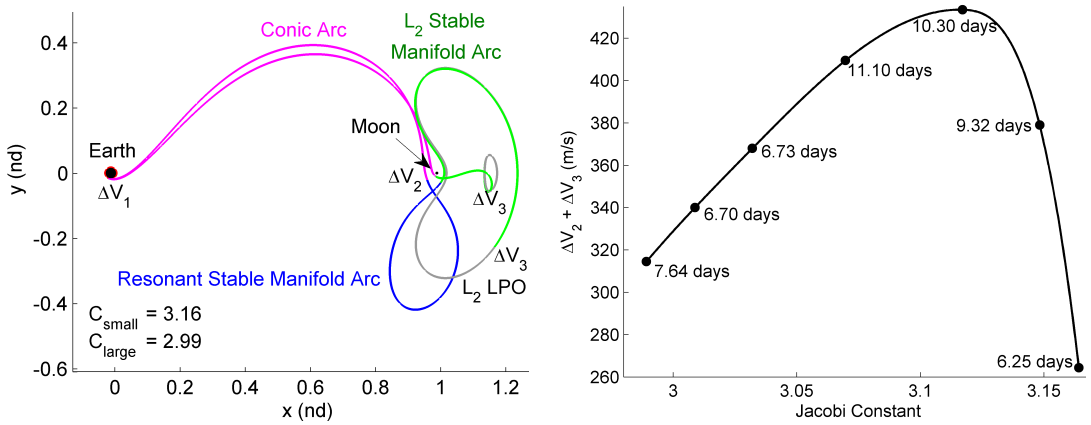

(a) Sample LEO-L_2 Transfers

(b) Cost and TOF Analysis

Figure 4.35. Sample Transfers to Selected Earth-Moon L_2 Lyapunov Orbits via Conic, Resonant and LPO Manifold Arcs in (a) and Maneuver Cost and Time-of-Flight as a Function of Jacobi Constant Associated with a Family of Transfers in (b)

the transfer options. To gain a better understanding of the effect of blending a combination of conic, resonant and LPO manifold segments, transfer trajectories to a range of L_1 and L_2 Lyapunov orbits at different energy levels are considered. The associated intermediate cost of the transfer to each arrival orbit is evaluated as a function of Jacobi constant and appears in Figures 4.34(b)-4.35(b). For reference, the associated time-of-flight is also labeled for each transfer trajectory. Transfers to the vicinity of L_1 generally possess characteristics as expected: the maneuver cost increases as the value of Jacobi constant decreases, that is, it is more efficient to insert into larger y-amplitude Lyapunov orbits. Generally, the time-of-flight follows a similar pattern, that is, the transfer duration decreases as the value of Jacobi constant increases; in other words, it is faster to insert into larger y-amplitude Laypunov orbits at L_1. For transfers to the vicinity of L_2, the behavior is slightly different. It appears to be equally efficient to insert into both higher- and lower-energy Lyapunov orbits at L_2 in a global sense. As expected, it is more affordable to access higher-energy orbits at L_2. However, it is possible to insert into the lower-energy orbits by exploiting the gravitational effect of the Moon, that is, by introducing the intermediate maneuver,

ΔV_2, in the vicinity of the Moon. The cost of inserting into the lowest-energy orbit in this preliminary transfer analysis is low and the time-of-flight is short, suggesting that more efficient options may be available even at lower energies. Recall that these transfer trajectories to the vicinity of L_1 and L_2 are sub-optimal trajectories and, thus, more cost effective options may be available.

A number of transfer trajectories from LEO to libration point orbits in the vicinity of L_3, L_4, and L_5 are generated using the same design approach. A sample of three trajectories appear in Figure 4.36, although other examples are available [92, 93]. In contrast to the periodic libration point orbits considered at L_2, most of the libration point orbits near L_3, L_4, and L_5 are linearly stable, that is, there is no natural flow to and from the orbit that can be exploited to access these orbits. Therefore, by choice, only a combination of conic segments and manifold arcs associated with resonant orbits are employed as an initial guess to construct the transfer trajectories in Figure 4.36. Note, however, that despite the orbits being linearly stable, the maneuver cost to access L_3, L_4, and L_5 is generally lower than to insert into L_1 and L_2 Lyapunov orbits, but the time-of-flight is inevitably longer.

Table 4.2 Maneuver Cost and Time-of-Flight Associated with Transfers in Figures 4.34-4.36

Transfer	ΔV_1 (km/s)	ΔV_2 (m/s)	ΔV_3 (m/s)	ΔV_T (km/s)	TOF (Days)
LEO - $L_{1(C=3.16)}$	3.12	555.00	0.80	3.67	3.23
LEO - $L_{1(C=3.01)}$	3.13	358.00	0.80	3.46	2.89
LEO - $L_{2(C=3.16)}$	3.13	264.40	0.75	3.39	6.25
LEO - $L_{2(C=2.99)}$	3.12	314.15	1.00	3.43	7.64
LEO - L_3	3.10	166.96	33.03	3.30	31.74
LEO - L_5	3.11	272.17	288.22	3.67	27.68
L_5 - L_4	0.08	72.96	–	0.15	26.67

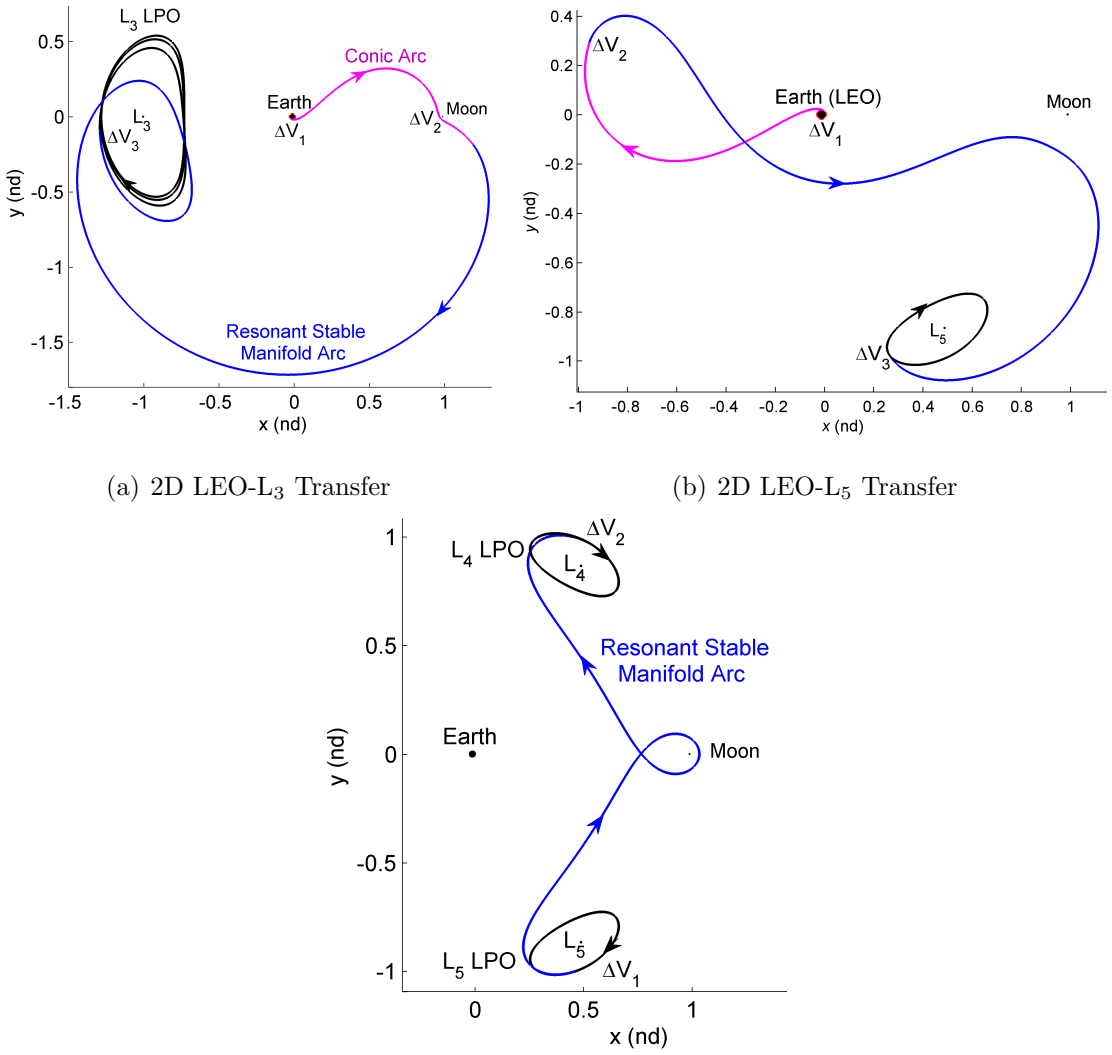

(a) 2D LEO-L_3 Transfer

(b) 2D LEO-L_5 Transfer

(c) 2D L_5-L_4 Transfer

Figure 4.36. Transfers to Selected Earth-Moon L_3, L_4, and L_5 Libration Point Orbits via Conic and Resonant Manifold Arcs

The transfer scenarios from LEO to selected libration point orbits at L_3, L_4, and L_5 that are detailed in this section highlight the role of resonant orbits and potential benefits of their incorporation into the trajectory design process. Obtaining an initial guess when the departure and arrival orbits do not possess invariant manifolds, e.g., for the initial LEO departure orbit and the final LPOs at at L_3, L_4, and L_5, is very nontrivial and perhaps the most challenging step in the process. In this type of

design scenario, unstable resonant orbits, such as the family of 4:3 resonant orbits in Figure 4.31, may be invaluable in producing a suitable initial guess for the desired transfer trajectory.

Locally Optimal Transfer from LEO to an L_5 Short Period Orbit

Any transfer trajectory from Earth to the vicinity of the libration points, constructed by linking stable and unstable manifold segments associated with resonant or libration point orbits, is a sub-optimal trajectory although it benefits from a reduced cost. However, it is possible to locally optimize these transfer trajectories. As an illustrative example, the transfer trajectory to the vicinity of L_5 from an initial 180-km LEO as represented in Figure 4.36(b) is considered for optimization. The transfer illustrated in Figure 4.36(b) is employed as an initial guess to construct a more direct transfer to the vicinity of L_5 that exploits a relatively close pass by the Moon. The objective is to minimize the cost of transfer from LEO to the selected short period orbit at L_5 as well as to reduce the time-of-flight along the stable manifold arc as much as possible. To do so, the location of the second maneuver (ΔV_2) is shifted from the first to the second apoapse location along the stable manifold trajectory. In the optimization process, a single, locally optimal transfer trajectory is identified by 1) specifying the desired departure and arrival orbits and 2) modifying the initial state of the spacecraft along each of the intermediate connecting arcs as well as the time-of-flight associated with each segment. Note that this optimization technique is similar to the one employed in the calculation of locally optimal transfer trajectories to Hyperion's orbit in the Saturn-Titan system. Recall that the initial and final position states along the transfer trajectory are not fixed but are constrained to the departure and arrival orbits, which is achieved by varying the integration times along the periodic orbits and by formulating the initial and final position states as equality constraints. The decision variables include the initial position and initial velocity associated with the transfer arcs and the integration times, that is,

$\bar{X} = [\bar{x}_{0C} \;\; \bar{x}_{0R} \;\; \mathrm{TOF_{LEO}} \;\; \mathrm{TOF_C} \;\; \mathrm{TOF_R} \;\; \mathrm{TOF_{L5}}]^{\mathrm{T}}$, where sub-vectors in $\bar{X}$, $\bar{x}_{0C}$ and $\bar{x}_{0R}$, represent the 6D initial states (position and velocity relative to the rotating frame and expressed in rotating coordinates) associated with the conic ($\bar{x}_{0C}$) and resonant arcs ($\bar{x}_{0R}$), respectively. Recall that, because of the linear stability, manifolds associated with the selected libration point orbits are not available and, thus, only resonant manifold arcs are considered. The first ($\mathrm{TOF_{LEO}}$) and fourth ($\mathrm{TOF_{L5}}$) integration times specify the departure and arrival locations along the LEO and along the short period orbit at L_5, respectively. The intermediate integration times, i.e., $\mathrm{TOF_C}$ and $\mathrm{TOF_R}$, correspond to the times of flight along the conic arc and the resonant manifold arc that link the initial and final orbits. The objective function evaluation returns the minimum magnitude of the sum of the initial, intermediate, and final maneuvers that are required to depart the 180-km LEO orbit and to insert into the selected L_5 short period orbit, that is, $J(\bar{X}) = \Delta V_1 + \Delta V_2 + \Delta V_3$. MATLAB's `fmincon` function is the optimization routine also employed in this analysis. In this optimization process, numerical gradients are used and all constraints are met within the specified non-default tolerances (`TolX` = `TolCon` = `TolFun` = 1×10^{-12}). An `exitflag` value of 1 is achieved, which indicates that first optimality conditions are satisfied. The resulting locally optimal transfer trajectory is plotted in Figure 4.37(b) and the magnitude of the sum of the minimum initial, intermediate, and final maneuvers along with the associated time-of-flight are detailed in Table 4.3. The total transfer cost and the TOF are reduced by approximately 270 m/s and 4 days, respectively.

Table 4.3 Maneuver Cost and Time-of-Flight Associated with Transfers in Figure 4.37

Transfer	ΔV_1 (km/s)	ΔV_2 (m/s)	ΔV_3 (m/s)	ΔV_T (km/s)	TOF (Days)
LEO - L_5	3.11	272.17	288.22	3.67	27.68
LEO - $L_{5(\mathrm{opt})}$	3.10	261.84	39.24	3.40	23.78

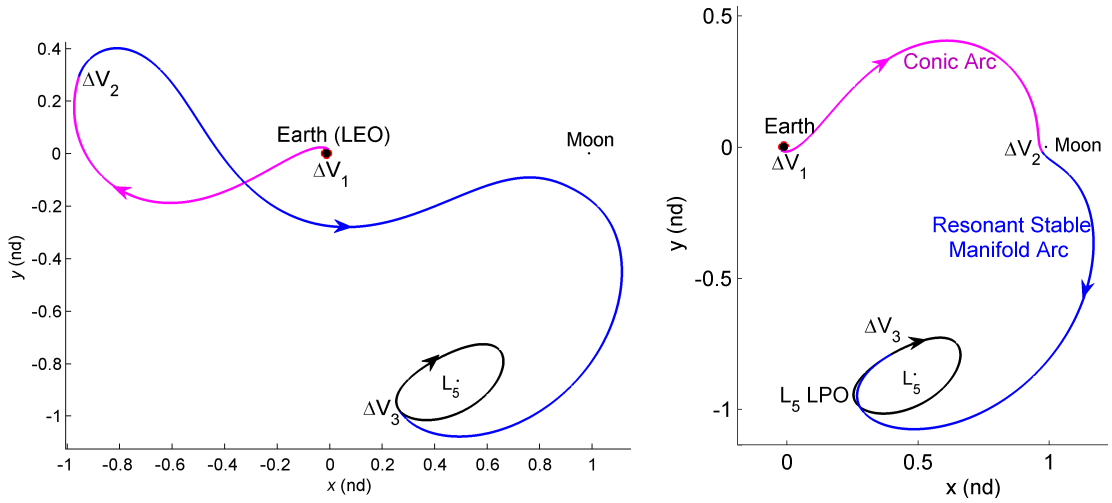

(a) Sub-Optimal Transfer

(b) Locally Optimal Transfer

Figure 4.37. Sub-Optimal and Locally Optimal Transfers to Selected L_5 Short Period Orbit via Conic and Resonant Manifold Arcs

The optimization process is illustrated via this particular example in the Earth-Moon system, but all other transfers offer good candidates for further cost reduction as well. An alternative approach to reduce the propellant consumption is the incorporation of a maximum-ΔV_T constraint to the corrections algorithm, that is, to limit the magnitude of the total maneuver cost by specifying an upper bound: $\Delta V_T \leq \Delta V_{max}$. The resulting transfers are sub-optimal solutions, yet possess improved propellant cost efficiency.

4.4.4 Three-Dimensional ΔV-Transfers: Trajectories from Low Earth Orbit to Selected Libration Point Orbits

The transfer design technique is not limited to the planar problem. Natural transfers between 3D resonant orbits as well 3D transfers from Earth orbit to out-of-plane resonant orbits exist and are computed with the aid of higher-dimensional Poincaré maps in Section 4.4.1. Similarly, it is possible to generate 3D transfer trajectories to the vicinity of any libration point orbit by exploiting 3D resonant and LPO mani-

fold arcs via a modified corrections scheme. As an example, consider an out-of-plane transfer from LEO to a 3D axial orbit near L_4. In contrast to similar periodic orbits at L_1 and L_2, the selected orbit at L_4 is linearly stable, and thus, manifold trajectories to access the orbit are not available. Consequently, a maneuver is required to insert into the L_4 axial orbit. To construct the out-of-plane transfer, two intermediate periodic orbits are considered: a member from the family of 3:2 axial resonant orbits plotted in Figure 3.19(g) and a sample axial orbit at L_2. Both intermediate orbits are represented in Figures 4.38(b)-4.38(c). For reference, the conic arc (magenta) and the selected intermediate orbits (blue) appear in Figure 4.38(a). The low Earth orbit at departure is represented in red and the associated planar Lyapunov orbits at L_2 and 3:2 resonant family are plotted in gray.

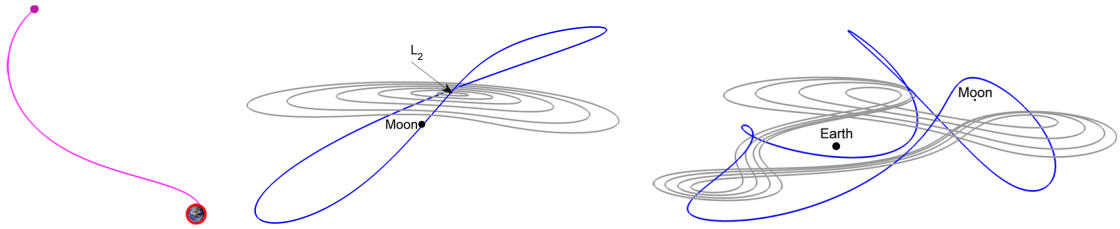

(a) Conic Arc (b) Axial Orbit at L_2 (c) 3:2 Axial Resonant Orbit

Figure 4.38. Conic Arc and Intermediate Periodic Orbits Employed in the Construction of a 3D Transfer Trajectory from 180-km Low Earth Orbit to an Axial Orbit Near L_4 in the Earth-Moon System

A stable manifold trajectory associated with the axial orbit at L_2 offers a transition arc from LEO to the vicinity of the Moon and an unstable manifold trajectory associated with the 3:2 axial resonant orbit supplies the path to the vinicity of L_4. Note that the use of a conic arc to connect the initial Earth orbit to the stable manifold is not necessary as the manifold trajectories associated with the axial orbit at L_2 already pass close to the Earth. The initial and final orbits along with the intermediate arcs are blended using a corrections scheme and the resulting transfer trajectory appears in Figure 4.39. For reference, the stable and unstable manifolds employed in the initial guess are highlighted in green and red, respectively. A total of three

impulsive maneuvers are incorporated throughout the transfer path; however, the cost associated with linking the two intermediate manifold arcs is reduced to zero. For completeness, the location of the maneuver is labeled in Figure 4.39. The largest plane change occurs in the vicinity of the Moon to significantly reduce the cost of insertion into the axial orbit at L_4 by leveraging the gravitational effect of the Moon. The associated cost of transfer and time-of-flight are detailed in Table 4.4.

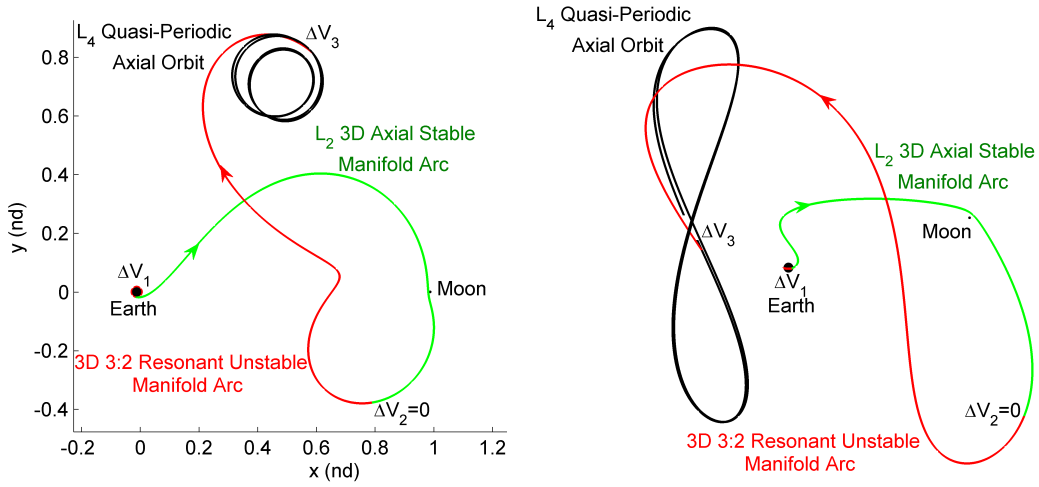

(a) xy-View (b) xyz-View

Figure 4.39. Transfer Trajectory to Selected 3D Axial Orbit in the Vicinity of L_4 via Resonant and LPO Manifold Arcs

The long-term stability associated with the selected axial orbit at L_4 is demonstrated by further propagating the end state of the transfer trajectory for 120 years. The resulting bounded motion is illustrated in Figure 4.40. Consequently, little station-keeping is required to maintain the vehicle on the orbit over the long term. Other advantages associated with the selected orbit are full coverage of both the Earth and the Moon and uninterrupted communication capabilities with the Earth and Moon as well. Therefore, given the small insertion maneuver and short time-of-flight, this transfer trajectory could be applicable in various design scenarios.

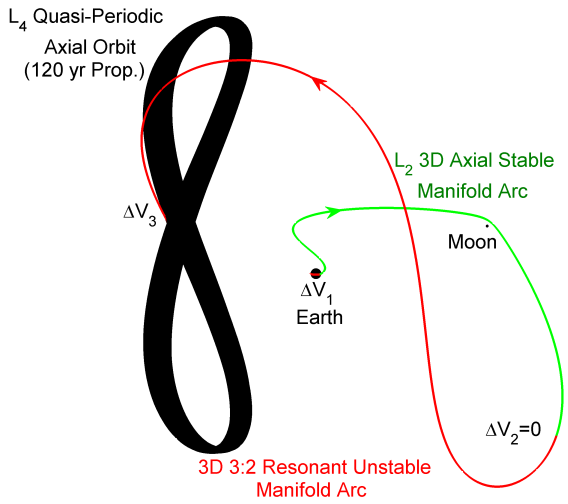

Figure 4.40. Long Term Propagation of End State Along Transfer Trajectory to Selected 3D Axial Orbit in the Vicinity of L_4

Table 4.4 Maneuver Cost and Time-of-Flight Associated with Transfers in Figure 4.37(b) and Figure 4.37(b)

Transfer	ΔV_1 (km/s)	ΔV_2 (m/s)	ΔV_3 (m/s)	ΔV_T (km/s)	TOF (Days)
LEO - L_4 Axial	3.10	170.00	0.00	3.27	22.54

4.4.5 Higher-Fidelity Transfers from LEO to the Vicinity of L_5

The versatility and potential usefulness of this design process is illustrated through various trajectory design scenarios but, ultimately, the solutions obtained in the CR3BP must be transitioned to higher-fidelity models for validation. To illustrate the impact of additional gravitational forces on the solutions initially generated in a 3B model, the locally optimal transfer trajectory from LEO to the vicinity of L_5 in Figure 4.37(b) is generated in an ephemeris model including solar gravity effects. Recall that periodic orbits in the CR3BP exist as quasi-periodic trajectories in the ephemeris model. Therefore, the design constraint that enforces the end state along the transfer path to occur along the specified periodic arrival orbit is no longer applicable in the ephemeris model. Alternatively, arrival at a quasi-periodic orbit is enforced. The

resulting path in the ephemeris model appears in purple in Figure 4.41(b); the relationship between the CR3BP and the ephemeris transfer trajectory is apparent and the associated total maneuver cost is similar, as detailed in Table 4.5. However, the cost associated with the trajectory in the ephemeris model is dependent on the epoch, that is, departure during certain months of the selected year (2020) are more cost effective than others. To address this dependency, a preliminary cost analysis appears in Figure 4.41(c), illustrating the transfer cost as a function of the initial epoch. For reference, the transfer cost associated with the CR3BP transfer is also labeled on the plot. In general, and for the year selected, launching during the summer months is less cost effective than during the winter months. All the relevant bodies move in orbits that are oriented differently with respect to each other throughout the year so such cost variations are not surprising. Note that the ephemeris trajectories are not optimal and, thus, more efficient solutions may be available.

Table 4.5 Maneuver Cost and Time-of-Flight Associated with Transfers in Figure 4.37(b) and Figure 4.41(b)

Transfer	ΔV_1 (km/s)	ΔV_2 (m/s)	ΔV_3 (m/s)	ΔV_T (km/s)	TOF (Days)
LEO - $L_{5(\mathrm{CR3BP})}$	3.10	261.84	39.24	3.40	23.78
LEO - $L_{5(\mathrm{eph})}$	3.10	226.56	33.43	3.36	23.78

The cost and time-of-flight associated with the selected transfer trajectories, 2D and 3D, from LEO to various libration point orbits in the Earth-Moon system are very reasonable and comparable to Earth-Moon transfer trajectories available in the literature [43, 94, 95], including transfers to L_1 and L_2 halo orbits [42, 96, 97] that exclusively exploit invariant manifolds associated with LPOs. The addition of resonant orbits to the transfer design process may offer more insight into the design space and potentially deliver more efficient transfer trajectories. Note also that departure and arrival along the periodic orbit is enforced in all of the CR3BP transfers. However, the transfer cost can be significantly reduced – in some cases by over 100 m/s –

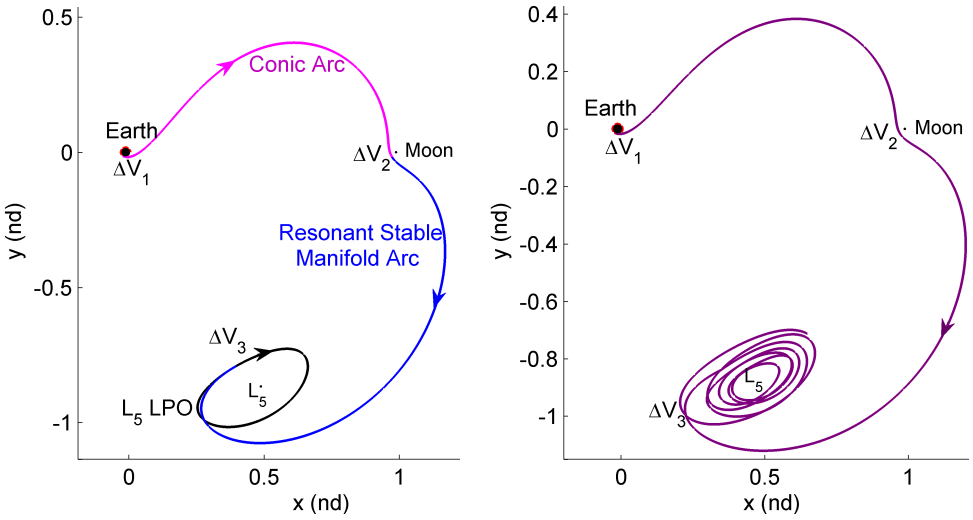

(a) LEO-L_5 CR3BP Transfer

(b) LEO-L_5 Ephemeris Transfer

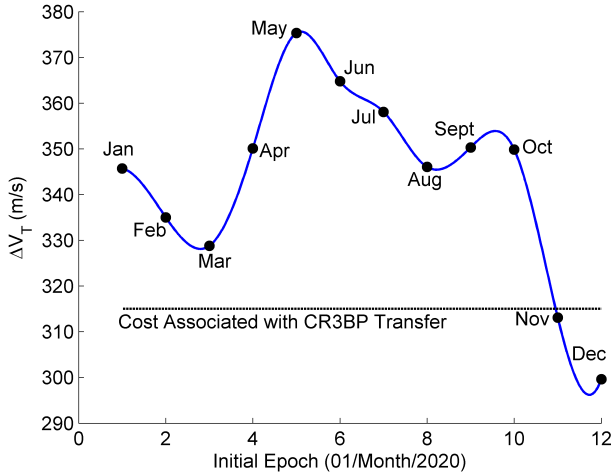

(c) Preliminary Cost Analysis

Figure 4.41. Comparison of Transfers to a Short Period Orbit at L_5 in the CR3BP and in Ephemeris Model in (a) and (b); Cost Chart Illustrating the ΔV-Cost As a Function of the Initial Launch Epoch Associated with a Family of Transfer Trajectories in the in the Ephemeris Model in (b)

if this design constraint is relaxed, i.e., if the arrival orbit is allowed to be slightly quasi-periodic. Nevertheless, the objective is not to produce minimum-ΔV or TOF transfer trajectories but (i) to supply quick and efficient maps for the generation of

candidate transfers, and (ii) to demonstrate the applicability of resonant orbits as transfer mechanisms between non-resonant orbits in the Earth-Moon system.

4.4.6 Libration Point Orbit Tours in the Earth-Moon System

The role of resonant orbits in the design process for transfer trajectories in multi-body environments is assessed in this investigation through various applications. To demonstrate the versatility of unstable resonant orbits and their associated invariant manifolds, a variety of transfers from LEO to the vicinity of each individual Earth-Moon libration point is detailed. However, with the aid of the automated design process, the transfer arcs employed in the design of these transfer trajectories are combined to design a tour of selected periodic orbits near each of the five libration points. A return segment to Earth is added that originates from the last libration point orbit in the tour. Virtually, with the aid of intermediate unstable resonant orbits and stable and unstable manifold arcs, any combination and itinerary is possible. As an illustrative example, consider the LPO tour plotted in Figure 4.42. A spacecraft placed on such trajectory departs a 180-km low Earth orbit on a conic arc to the vicinity of L_1, where it orbits a Lyapunov orbit for several revolutions. A transition into an L_2 Lyapunov orbit is enabled through exploitation of the associated stable and unstable manifold trajectories. After spending several days in the vicinity of the Moon, the spacecraft transfers to the vicinity of L_5 via an unstable manifold arc associated with a 4:3 resonant orbit; from the short period orbit at L_5, it transitions to a mirror short period orbit at L_4, subsequently ending in the vicinity of L_3. At the end of the tour, a maneuver along the L_3 Lyapunov orbit enables a safe return to low Earth orbit. Alternatively, small station-keeping maneuvers can be designed to maintain the vehicle near L_3 for long periods of time. A total of six intermediate maneuvers are required to transition between these equilibrium point regions, i.e., $\Delta V_{2:7} = [374.12 \quad 58.11 \quad 49.21 \quad 80.44 \quad 79.41 \quad 29.59]$ m/s and the total time-of-flight between each libration point orbit is 165 days. That is, the time spent orbiting

the actual libration point orbits is not accounted for in this total time-of-flight. In addition to $\Delta V_{2:7}$, an expectedly large initial maneuver is required to depart LEO, i.e., $\Delta V_1 = 3.13$ km/s, and a departure maneuver from the L_3 Lyapunov orbit allows a return to LEO, i.e., $\Delta V_8 = 634.17$ m/s.

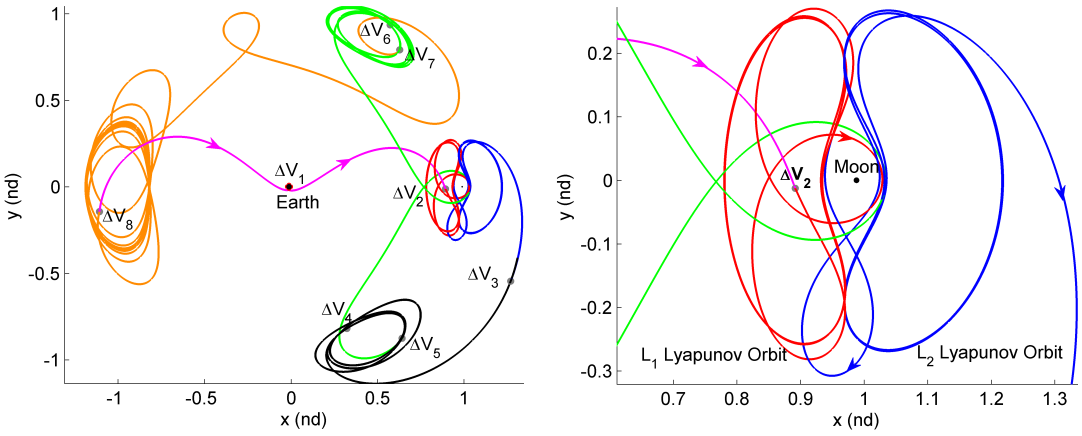

(a) Libration Point Orbit Tour

(b) Zoomed-View of L_1 and L_2 Region

Figure 4.42. Tour of Five Libration Point Orbits in the Earth-Moon System with 180-km LEO Departure and Arrival

The tour of the Earth-Moon libration point orbits represented in Figure 4.42 benefits from a reduced ΔV-cost by exploiting invariant manifolds as transfer mechanisms. Yet, the associated cost and TOF can be further minimized by applying local optimization techniques. Additionally, alternative itineraries may offer better ΔV-TOF trade offs.

4.4.7 Earth-Moon Periodic Cyclers

The need to develop an infrastructure near the Moon to support telecommunications, navigation and, potentially a human outpost requires the computation of trajectories that periodically transition between the Earth and the Moon. Cycler orbits, in general, have been investigated in the past by several researchers in the Sun-Earth-Mars system for human mission applications [66, 98–101] as well in vari-

ous planet-moon systems [102–104]. More recently, cyclers have been proposed for the support of lunar exploration and utilization missions in the Earth-Moon system [105, 106]. Criteria for assessing the utility of a cycler includes maximum and minimum distance relative to both the Earth and the Moon, period, stability properties, and lunar coverage (cislunar or circumlunar passage) [105]. In this investigation, families of resonant orbits that periodically travel to the vicinity of the Earth and the Moon and meet these criteria are proposed as potentially useful Earth-Moon cyclers. The objective in this analysis is to complement previous investigations in cycler orbit theory by offering sample resonant cycler trajectories that benefit from short repeat periods and frequent launch opportunities.

Families of resonant trajectories that encircle both the Earth and the Moon are sought as Earth-Moon cyclers. Only resonant trajectories that meet several design criteria are considered as viable Earth-Moon cyclers. Note that this design criteria is consistent with the criteria specified by other researchers [105, 106].

- *Close approach to the Earth*: Cyclers with small perigee radius are preferable to reduce the cost of inserting a spacecraft into the cycler orbit. It is assumed that the vehicle is initially orbiting the Earth in a circular orbit of radius $r_E + r_{min} < r < r_E + r_{max}$, where r_E is the radius of the Earth, $r_{min} = 180$ km, and $r_{max} = 35,786$ km, which is equivalent to a geostationary orbit. Consequently, only interior resonant orbits are considered and the size of trajectories is bounded by the desired maximum and minimum distances relative to the Earth. Recall that an interior resonant orbit is defined in terms of the resonant ratio, p:q, such that $p¿q$.

- *Close approach to the Moon*: Similarly, the cycler insertion cost, measured in terms of the propellant that is required to transfer mass to and from the cycler orbit, is reduced if the periodic trajectory passes near the surface of the Moon or in the vicinity of selected libration point orbits. It is also assumed that the cargo is delivered to either the surface of the Moon or inserted into a small –

measured in terms of y- and z-amplitudes – L_1 or L_2 libration point orbit. For communications purposes, both circumlunar and cislunar cyclers are considered.

- *Period*: Shorter travel times between the Earth and the Moon are essential in the transportation of humans to a lunar outpost and preferable in the transportation of cargo so, to accommodate both types of missions, the time-of-flight between Earth and Moon along the cycler trajectory is limited to 7 days.

- *Stability*: In general, the cost associated with maintaining a spacecraft on the cycler is reduced if the trajectory is stable, that is, the less sensitive the cycler is to perturbations, the smaller the station-keeping costs. Therefore, only resonant cyclers that are stable or possess small unstable modes are considered in this investigation.

Based on these requirements, which are consistent with the criteria for cyclers established by Mondelo and Villac [105, 106], two families of resonant cycler orbits are selected. As illustrated in Figure 4.43, these trajectories periodically cycle between the vicinity of the Earth and the Moon. For reference, sample members in the family of L_1 and L_2 Lyapunov orbits are also represented. Color represents the different energy levels associated with each trajectory. The family of 2:1 resonant cyclers illustrated in Figure 4.43(a) offers a circumlunar passage and, thus, a suitable connection to libration point orbits at L_2. The family of 3:1 resonant cyclers plotted in Figure 4.43(b) is better suited for cislunar passage – between the Earth and the Moon – and connection to libration point orbits at L_1. Recall that the trajectories in Figure 4.43(a) complete two revolutions around the Earth in approximately the same time it takes the Moon to complete one revolution. Similarly, a 3:1 resonant cycler completes three revolutions around the Earth in approximately the time the Moon completes one revolution. The time-of-flight along the 2:1 cyclers from the vicinity of the Earth to the vicinity of the Moon ranges from 4.91 days for a cycler with $C = 2.66$ to 6.39 days for a cycler with $C = 1.98$. Similarly, the arc from the Earth to the Moon along the 3:1 cycler orbits ranges from 4.90 days for a cycler with $C = 2.54$ to 5.04

days for a cycler with $C = 3.13$. To better illustrate some of the characteristics of these trajectories, an energy-stability plot representing the associated values of Jacobi constant, stability indices, and initial states appears in Figure 4.44. Recall that the stability properties associated with each member in a family of periodic orbits is represented on the $\nu - C$ plot in terms of in-plane and out-of-plane stability indices. The length of the arrow reflects ν_{2D} qualitatively; likewise, color offers a sense for ν_{3D} values. The associated values of Jacobi constant are represented on the y-axis and the x-component of the initial state, x_0, is represented along the x-axis. The cyclers in Figure 4.43 are planar and, thus, the initial state has the form $[x_0 \;\; 0 \;\; 0 \;\; 0 \;\; \dot{y}_0 \;\; 0]^T$. Therefore, the initial state corresponding to each cycler in the family is completely available from the graph in Figure 4.44, as $\dot{y}_0$ value can be calculated from the x_0 and C values and the expression for Jacobi constant. For reference, the Jacobi constant value corresponding to L_1 in the Earth-Moon system is indicated on the $\nu - C$ plot by a dotted black line.

The $\nu - C$ plot in Figure 4.44 provides relevant information on the orbital characteristics but also offers valuable insight in terms of transfer opportunities. Recall that a free-transfer between two periodic orbits may exist if both orbits are unstable and possess the same value of Jacobi constant. As illustrated in Figure 4.44, a cost-free transfer between a 2:1 and a 3:1 cycler is available at energy levels such that $2.66 < C < 2.54$ approximately. For example, if the frequency of encounters must be altered due to time-of-flight constraints, selecting two unstable cyclers at the same energy level is desirable to minimize the propellant consumption that is required during the transfer phase. Likewise, a natural connection between a 3:1 cycler and a Lyapunov orbit at L_2 exists and could be used in end-phase scenarios to deliver cargo to the selected libration point orbit at no cost.

The design space is large and many considerations must be incorporated in the design of an orbital infrastructure to service the Moon and nearby libration point orbits. Multiple applications also exist for different cycler orbits, e.g., Earth-Moon communications vs. periodic cargo transport to the Moon. However, certain families

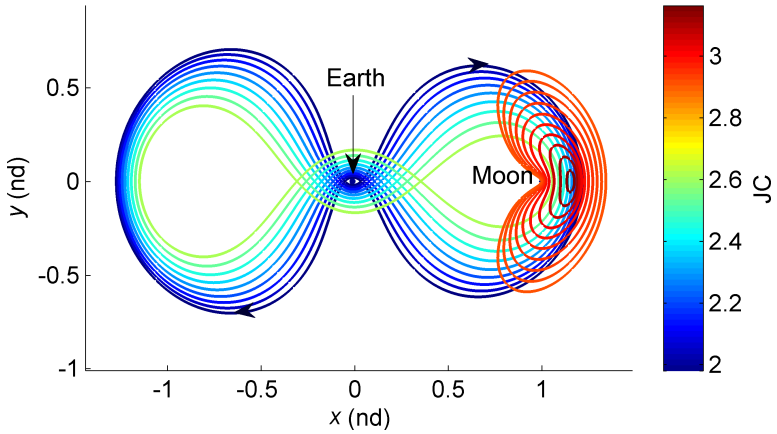

(a) 2:1 Resonant Cyclers and Sample L_2 Lyapunov Orbits

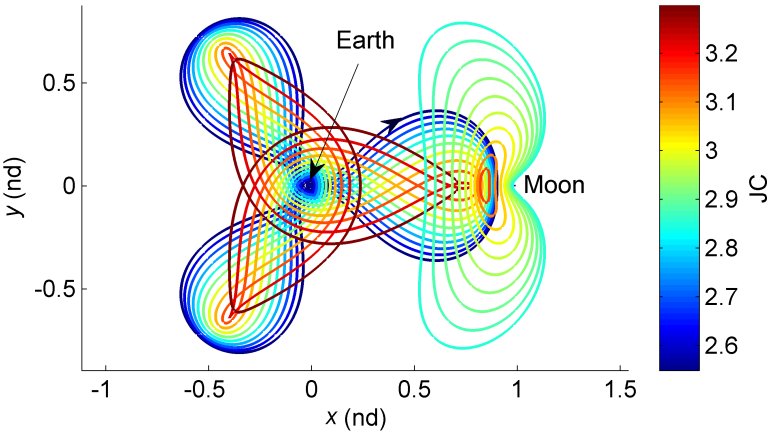

(b) 3:1 Resonant Cyclers and Sample L_1 Lyapunov Orbits

Figure 4.43. Sample Earth-Moon Resonant Cyclers

of resonant orbits offer many advantages over other classes of orbits for this particular application and, thus, further analysis is guaranteed.

4.5 System Translation

Transfer trajectories with predetermined itineraries are efficiently generated exploiting various dynamical structures and Poincaré mapping techniques. However, orbital characteristics vary from system to system and a number of computations are required before the desired transfer trajectory is produced. The capability of selecting

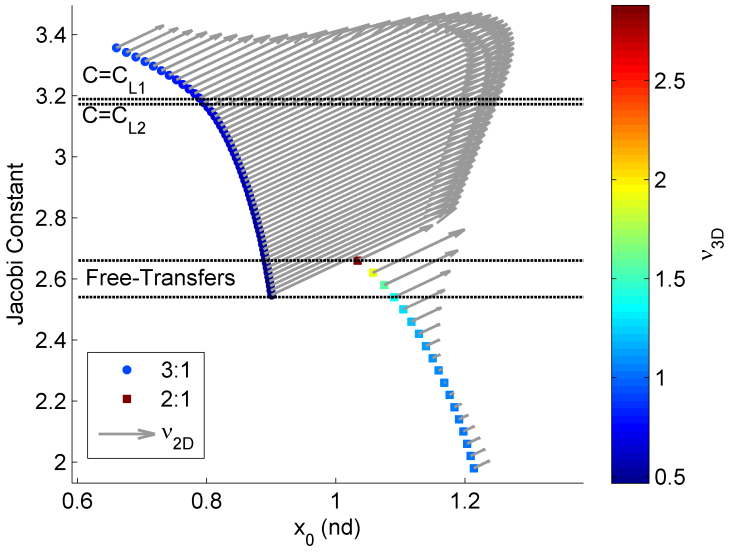

Figure 4.44. Stability-Energy Plot for Families of Periodic, Resonant Earth-Moon Cycler Trajectories in Figure 4.43

a trajectory in the Earth-Moon system and directly translating it to a different three-body system without the necessity of generating periodic orbits, invariant manifolds, and Poincaré maps in the new system is highly valuable. Thus, a system translation technique is detailed in this section to generate sample periodic orbits and transfer trajectories in the Saturn-Titan and Saturn-Enceledus systems directly from solutions previously computed in the Earth-Moon system.

4.5.1 Periodic Orbits

Different strategies are available to translate a point solution from one 3B system to another, but perhaps the simplest approach is the use of a multiple shooting algorithm wrapped in a single-parameter continuation scheme, where the mass parameter, μ, is progressively varied until the desired value is achieved. This corrections scheme is implemented in a particularly straightforward manner when the point solution to be translated from one 3B system to another is a periodic orbit. Two illustrative examples follow: a sample 3D 3:1 axial resonant orbit from the family represented

in Figure 3.19(f) and a sample low prograde orbit from the family represented in Figure 3.7(c).

Axial Resonant Orbits: Earth-Moon to Saturn-Titan System

The periodic, resonant orbit in the Earth-Moon system selected from the family plotted in Figure 3.19(f) serves as the initial guess that seeds the differential corrections algorithm. The mass parameter associated with the converged solution, i.e., μ_{EM}, is then varied. Employing the successful orbit with the perturbed parameter as a new guess, the differential corrections algorithm produces a second converged solution, that is, a new periodic, resonant orbit in a system with a different mass parameter. This process is continued until the desired value of the mass parameter (μ_{ST}) is achieved and a converged solution in the Saturn-Titan system is produced. The resulting resonant orbit in the Saturn-Titan system is illustrated in Figure 4.45. For reference, the original axial resonant orbit in the Earth-Moon system is also plotted in blue. Note, however, that the primaries depicted in Figure 4.45 are Saturn and Titan and the nondimensional units are scaled differently in each system ($l^*_{EM} = 384,400$ km and $l^*_{ST} = 1,221,830$ km). Consequently, the size of the orbits differ but the general characteristics are preserved. The similarities between the two orbits are apparent but the computation process is remarkably faster for the orbit in the Saturn-Titan system given that no *a priori* knowledge of the design space is necessary to generate the orbit.

To demonstrate the validity of the translated solution, the axial resonant orbit in the Saturn-Titan system that is computed using the system translation technique is integrated in a higher-fidelity model that includes solar perturbations. The initial epoch is randomly selected to be June 1, 2020 and a total of 10 revolutions are stacked to create the ephemeris orbit represented in Figure 4.5.1. As illustrated in Figure 4.5.1, the similarities between the 3B periodic orbit and the ephemeris quasi-periodic orbit are apparent, as expected.

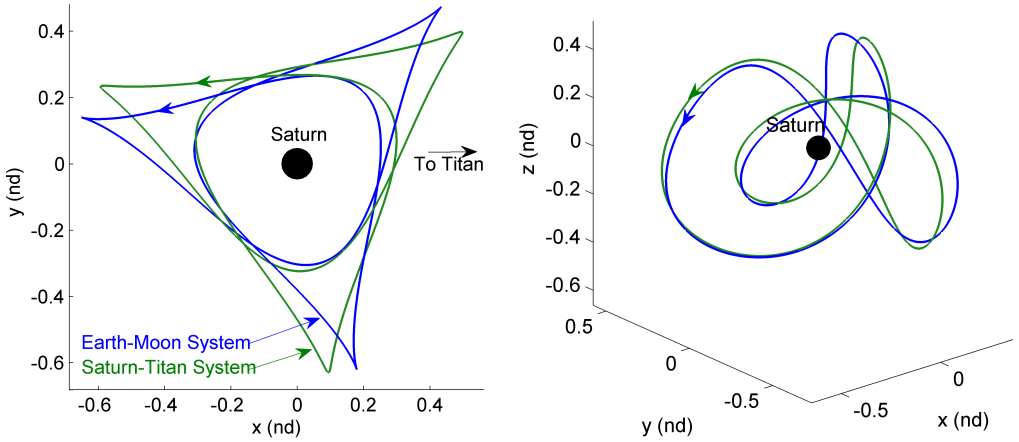

(a) (b)

Figure 4.45. 3:1 Axial Resonant Orbit in Earth-Moon System (Blue) and Saturn-Titan System (Green) Computed via System Translation Technique

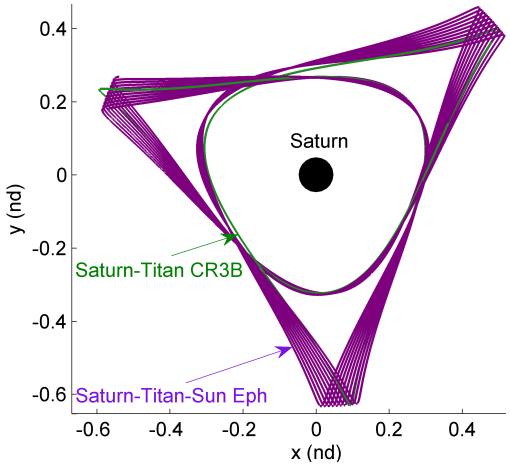

Figure 4.46. Validation of 3:1 Axial Resonant Orbit in the Ephemeris Model

Low Prograde Orbits: Earth-Moon to Sun-Saturn System

The system translation technique is successfully applied to the transition of a 3D axial resonant orbit in the Earth-Moon system to the Saturn-Titan system. The implementation of the algorithm is straightforward and the similarities between the two orbits are apparent. However, such similarities are expected to exist since the

selected resonant orbit is not in close proximity to any of the two primaries, that is, Saturn or Titan. To better illustrate the capability of the proposed method, a more dynamically challenging environment is sought via the transition of a low prograde orbit in the Earth-Moon system to the Sun-Saturn system.

As an illustrative example, consider a member of the family of low prograde orbits in the Earth-Moon system represented in Figure 3.7(c). The selected orbit as plotted in Figure 4.47(a) seeds the continuation scheme in which the mass parameter is varied until the desired value is attained, i.e., $\mu_{Sun-Sat} = 2.8577 \times 10^{-4}$. Note that the initial guess that is required to generate distant periodic orbits is obtained from the Hill's framework [107], and, therefore, computation of low prograde orbits in the CR3BP is non-trivial. The system translation process offers an efficient alternate method of quickly generating these orbits in *any* given three-body system. Given this periodic orbit, a family of orbits could now be straightforwardly constructed in the Sun-Saturn system if desired.

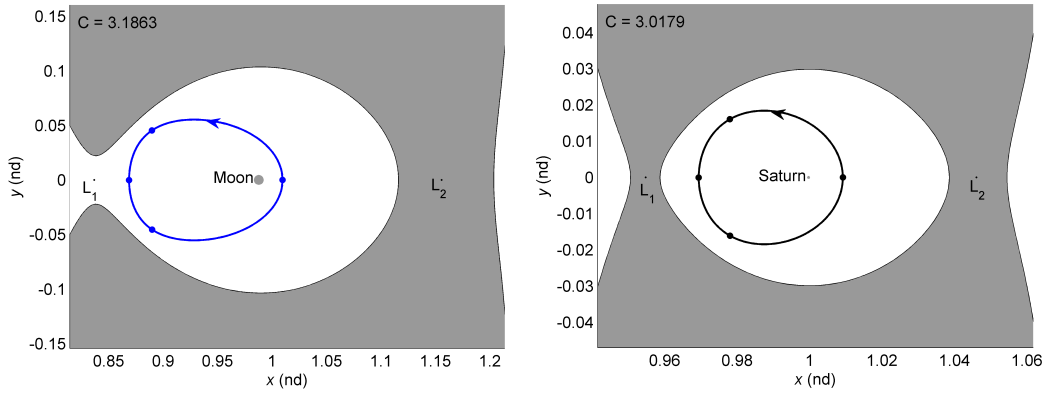

(a) Earth-Moon System

(b) Sun-Saturn System

Figure 4.47. Low Prograde Orbit in the Earth-Moon System in (a) and in the Sun-Saturn System in (b) Computed via the System Translation Technique (Saturn Enlarged ×10 for Visualization)

An interesting feature arises after evaluating the two orbits plotted in Figure 4.47. In the Earth-Moon system, the family of low prograde orbits only exists for $C > C_{L2}$, that is, for values of Jacobi constant such that the L_2 gateway is closed. However,

the family of low prograde orbits in the Sun-Saturn system exist for a larger range of Jacobi constant values. The range of instability across the orbits in the Sun-Saturn system is also greater. The characteristics of these two families are better visualized if represented on an energy-stability plot. Recall that $\nu - C$ plots, introduced in Section 3.1.2, include information on the initial state, energy level, and stability indices for each member in a family that is constructed. The quantities employed to represent each orbit on the map are the x-component of the initial state, x_0, along the x-axis and the associated energy level, C, along the y-axis. Color is then used to represent the in-plane stability index values, ν_{2D}, and the length of an arrow indicates the out-of-plane stability index values, ν_{3D}. Recall that the absence of an arrow indicates that the orbit is stable; conversely, a longer arrow represents a more unstable orbit. Figure 4.48(a) illustrates the stability and energy properties associated with members in the family of low prograde orbits in the Earth-Moon system; similarly, Figure 4.48(b) illustrates properties associated with members in the family of low prograde orbits in the Sun-Saturn system calculated via the system translation technique.

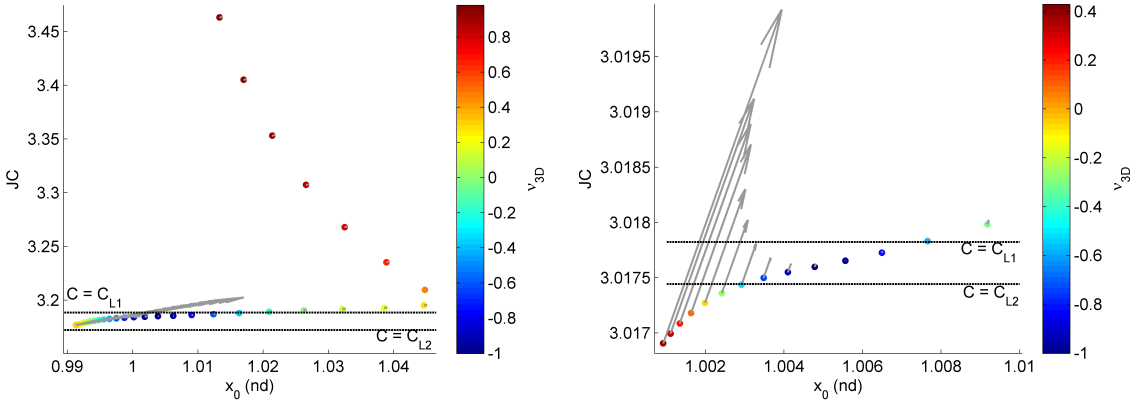

(a) Earth-Moon System

(b) Sun-Saturn System

Figure 4.48. Stability-Energy Plots Associated with a Family of Low Prograde Orbit in the Earth-Moon System in (a) and in the Sun-Saturn System in (b)

The system translation technique allows for the efficient computation of low prograde orbits in the Sun-Saturn system without any *a priori* knowledge on the system and the stability-energy plots offer insightful information regarding the comparison of the two families considered in each three-body system.

4.5.2 Transfer Trajectories

The translation of periodic orbits from system to system is straightforward; however, transfer trajectories are intrinsically more complex due to the proximity to the primaries and the additional design constraints. Yet, with the appropriate modifications, the three-body system translation technique based on a mass parameter continuation scheme can also be applied for the direct transition of Earth-Moon transfer trajectories to the Saturn-Titan and Saturn-Enceladus systems.

Design of a 3D Transfer to an Axial Orbit at L_4: Earth-Moon to Saturn-Titan System

The translation of transfer trajectories to different three-body systems does inevitably offer challenges; for example, the proximity of the trajectory to the Earth at departure and the low perilune altitude may result in convergence difficulties when the mass parameter is varied. To avoid convergence issues, additional constraints are enforced along the transfer path. Before initializing the mass parameter continuation scheme, the size of the departure orbit is increased to accommodate the size difference between the two larger primaries in each system, that is, Earth and Saturn. A single-parameter continuation scheme is implemented to shift the initial 180-km LEO to a Saturn-centered circular orbit with altitude $h = 0.2$ nondimensional units, equivalent to 244,366 km. For reference, the E Ring, Saturn's second outermost ring, is located 166,000 km from the surface [75], originating near the orbit of Mimas and terminating near the orbit of Rhea. To avoid impact with the smaller primary, a minimum closest approach distance constraint is also implemented. Once the additional constraints

are enforced, the mass parameter continuation process is initialized. To illustrate the system translation process, consider the transfer trajectory to the quasi-periodic axial orbit at L_4 represented in Figures 4.39(a)-4.39(b). The 3B system translation technique is applied to the original transfer in the Earth-Moon system and the resulting trajectory in the Saturn-Titan system is plotted in Figure 4.49. The intermediate arcs differ slightly, but the axial orbit at L_4 preserves its general characteristics. To add further flexibility to the algorithm, the inclination of the departure orbit is allowed to vary, that is, the position of the first patch point is constrained to be on a sphere of radius $r = 0.2$ nondimensional units. For illustration purposes, the departure sphere is illustrated as a gray sphere centered at Saturn.

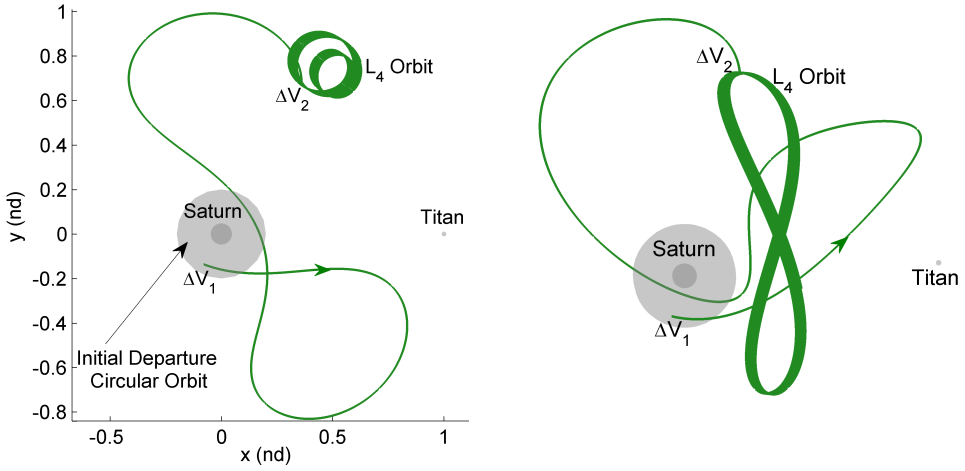

(a) *xy*-View (b) *xyz*-View

Figure 4.49. Transfer to a Quasi-Periodic Axial Orbit at L_4 in the Saturn-Titan System After Translation from a Similar Transfer Trajectory in the Earth-Moon System

The main advantage offered by the system translation technique is that no *a priori* knowledge concerning the design space is required to construct a transfer in a different 3B system, resulting in a fast and efficient method of generating preliminary trajectories. Initially, a continuous path is sought when translating a solution from the Earth-Moon system to the Saturn-Titan system. However, additional design

constraints can be incorporated to produce a transfer path with a specific pattern. For example, if desired, a flyby altitude at Titan can be specified and the propellant consumption and time-of-flight can be constrained after a continuous path is produced.

Design of a Transfer to a Distant Retrograde Orbit: Earth-Moon to Saturn-Enceladus System

Saturn's tiny icy moon Enceladus is a popular solar system destination for future robotic missions, but the insignificant size of Enceladus and its close proximity to Saturn combine to render a challenge in the design of transfer trajectories in such a multi-body environment. Nevertheless, the mass parameter continuation scheme is employed to translate point solutions directly from the Earth-Moon to the Saturn-Enceladus system. For reference, the mass parameter in the Saturn-Enceladus three-body system is five orders of magnitude smaller than the mass parameter in the Earth-Moon system, that is, $\mu_{S-Enc} = 1.9 \times 10^{-7}$. The almost negligible gravitational effect of Enceladus on the spacecraft path not only complicates the design process but reduces the availability of natural trajectories. Most resonant orbits in the Saturn-Enceladus system are linearly stable, but even for the few unstable orbits, the manifold trajectories are bounded in the exterior region near the zero velocity curves. Thus, there is limited availability of manifold trajectories that travel to the vicinity of Saturn. Hence, a preliminary transfer from a Saturn-centered circular orbit to a libration point orbit via a manifold-based approach is a particular challenge. However, the mass parameter continuation scheme offers an alternative transfer construction process initiated from a previously known trajectory with specific characteristics in the Earth-Moon system.

The versatility of the system translation technique is demonstrated in this section through a design example involving a transfer from a P_1-centered circular orbit to a stable distant retrograde orbit. Distant retrograde orbits (DROs) generally exhibit

long-term stability and are of particular interest for a variety of missions. Hénon, who initially examined distant retrograde orbits, labeled them the 'f family' [107]. Although most members in a family of distant retrograde orbits are linearly stable, there is a small range of unstable DROs that pass near the larger primary, including some orbits that actually impact the surface. The stability and the period associated with planar DROs are evaluated as a function of y-amplitude in Figure 4.50(a) and Figure 4.50(b); for reference, unstable DROs appear in red and stable orbits are plotted in black. As illustrated in Figure 4.50(b), smaller y-amplitude DROs possess shorter periods (11 hrs) but the integration time along each orbit progressively increases until it reaches a plateau at $P = P_{Moon}$, i.e., approximately 27 days. Thus, part of the planar family is in a 1:1 resonance with the Moon. Additionally, the change in stability across the family indicates the presence of a bifurcation, from which a family of 3D DROs is generated. Representative members in the 3D family appear in Figure 4.51. Note that out-of-plane DROs are also in a 1:1 resonance with the Moon.

Distant retrograde orbits have been investigated by numerous authors in different planar three-body systems. For instance, Lam and Whiffen explore the application of DROs around Europa [108]. Parker and Lo examine a family of DROs in the Earth-Moon system and their application in mission design [41] and Demeyer and Gurfil develop transfer trajectories from Earth to distant retrograde orbits in the Sun-Earth planar CR3BP [109]. To expand upon this application, a transfer from a 180-km low Earth orbit to a 3D DRO in a 1:1 resonance with the Moon is first constructed. The usefulness of the proposed system translation technique is demonstrated by translating the Earth-Moon transfer path directly to the Saturn-Enceladus system. The 3D DRO in a 1:1 resonance with the Moon, plotted in red in Figure 4.51, is selected as the arrival periodic orbit. A conic arc and a stable manifold trajectory associated with the 4:3 resonant orbit plotted in Figure 4.31(c) are combined to construct a transfer arc from a 180-km LEO to the selected DRO. A multiple shooting algorithm with a number of design constraints is employed to initially generate the transfer trajectory

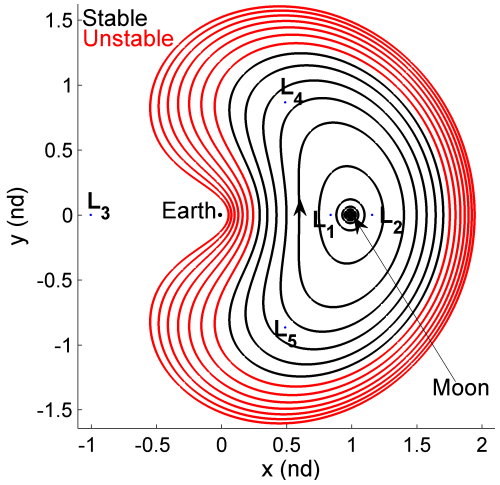

(a) Stable vs. Unstable DROs

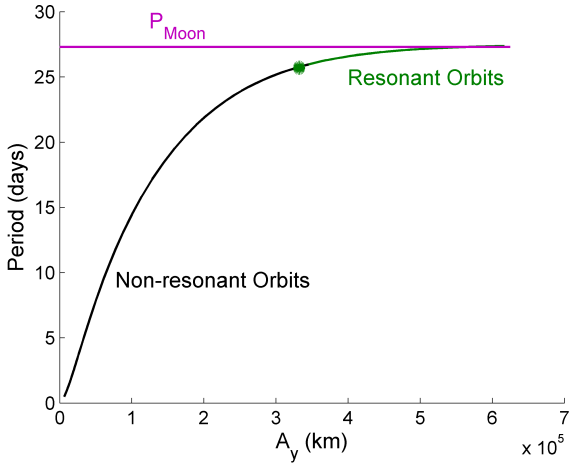

(b) Period vs. y-Amplitude

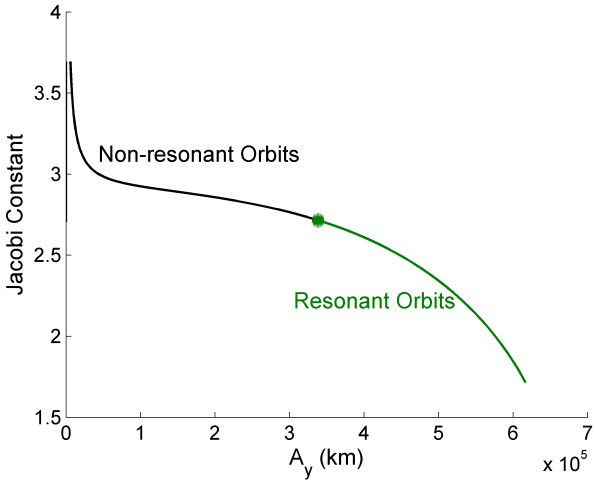

(c) Energy vs. y-Amplitude

Figure 4.50. Stability, Energy, and Period Analysis of Planar Distant Retrograde Orbits in the Earth-Moon System

in the Earth-Moon system, plotted in Figure 4.52(a). Note that no specific arrival location along the path is required, but the end state along the transfer path is constrained to be along the DRO. The resulting trajectory in the Earth-Moon system then seeds the mass parameter continuation scheme to generate a transfer trajectory with similar characteristics in the Saturn-Enceladus system. To simplify the algorithm and reduce the computational time, the constraint to arrive along the periodic

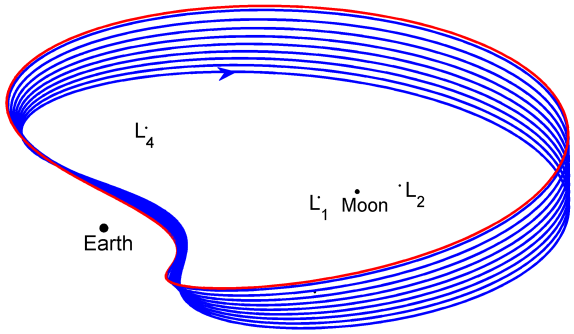

Figure 4.51. Three-Dimensional Distant Retrograde Orbits in a 1:1 Resonance with the Moon

orbit is removed and an alternative arrival at a 5-revolution quasi-periodic DRO is enforced. Otherwise, a new periodic distant retrograde orbit must be computed for each of the selected μ values throughout the mass parameter continuation process. The initial inclined departure orbit, plotted as a gray sphere in Figure 4.52(b), is also modified to be defined with an altitude of $h = 0.28$ nondimensional units, equivalent to 66,625 km.

In this scenario, the objective of the system translation process is not the immediate design of an optimal transfer from a primary-centered circular orbit to a 3D distant retrograde orbit in either three-body system, but it is worth highlighting the maneuver cost and TOF associated with each transfer trajectory. In the Earth-Moon system, $\Delta V_2 = 228.00$ m/s and TOF $= 14.30$ days; in the Saturn-Enceladus system, the size of the maneuver is larger, i.e., $\Delta V_2 = 374.70$ m/s, but the time-of-flight is much shorter, i.e., TOF $= 0.930$ days. Note that optimization techniques can be applied *a posteriori* to further reduce the propellant requirements, time-of-flight, or enforce other physical constraints along the transfer path.

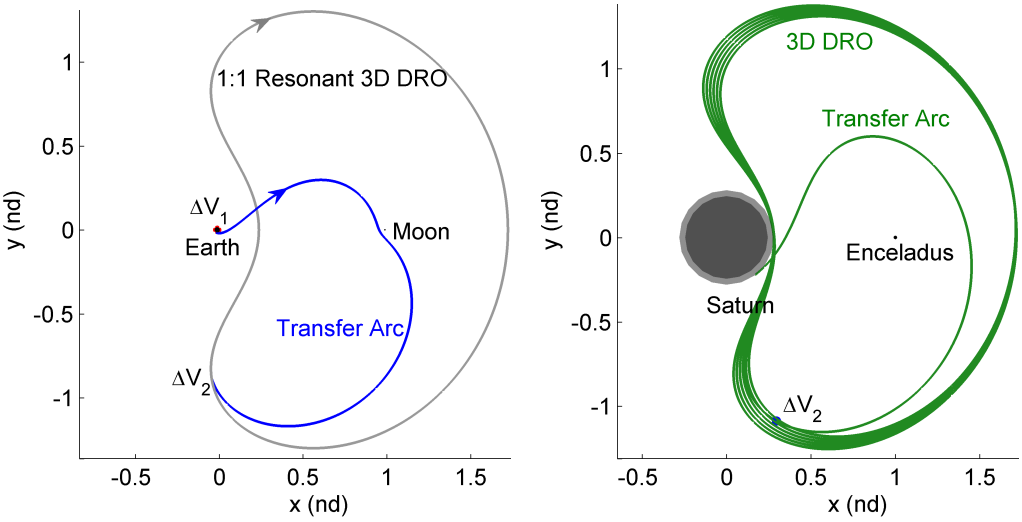

(a) Earth-Moon Transfer

(b) Saturn-Enceladus Transfer

Figure 4.52. xy-View of a 3D Transfer to an Earth-Moon Distant Retrograde Orbit in (a) and xy-View of a 3D Transfer to a Quasi-Periodic Distant Retrograde Orbit in the Saturn-Enceladus System in (b)

5. CONCLUDING REMARKS

An investigation of the dynamical environment correlated with planar and three-dimensional resonant orbits in multi-body environments is presented and their role in the design of transfer trajectories is assessed. Thus far, resonant orbits have been widely employed in mission design for flybys and, more recently, as trajectories that support long-term stability of Earth-orbiting spacecraft. In this analysis, the exploitation of resonant orbits as transfer mechanisms is evaluated through various trajectory design applications in multi-body environments. The goals of this investigation are twofold: (1) to expand the orbit architecture in multi-body regimes by cataloging families of resonant orbits and (2) to assess the role of these resonant families in the design of cost-efficient, even novel, transfer trajectories.

5.1 Orbital Architecture in the Restricted Three-Body Problem

The computation of multi-body transfer trajectories in this analysis begins with the search, identification, and computation of resonant orbits. The concept of resonance is typically defined within the context of the two-body problem. Thus, the computation of resonant orbits in multi-body regimes requires the use of corrections algorithms and, in regimes where the gravitational effect of the smaller primary is rather large, different strategies must be applied in the computation of resonant orbits. The steps required in the process are defined as follows: (i) definition and computation of any planar p:q resonant orbits in a two-body (2B) model, (ii) transition of the 2B model solution to a 3B model trajectory via a corrections process and a continuation scheme, and (iii) analysis of the stability characteristics to identify the availability of three-dimensional p:q resonant orbits of similar characteristics. To illustrate this process, a selection of interior and exterior planar and three-dimensional families of

stable and unstable resonant orbits are computed in the Earth-Moon system and the associated orbital characteristics are evaluated with the aid of stability-energy plots. A comprehensive study of periodic orbits in this regime, including planar and three-dimensional libration point orbits as well as distant prograde and retrograde periodic orbits, is provided and it is demonstrated that families of resonant orbits are a valuable addition to an existing map of the orbit architecture in the CR3BP. Virtually any p:q ratio exists and the corresponding resonant orbit can be computed within the context of the CR3BP, facilitating the construction of periodic orbits with different characteristics, i.e., interior versus exterior, short versus long periods, and stable versus unstable. Unlike Lyapunov or halo orbits, resonant orbits are not associated with a libration point orbit or a particular region in space, that is, certain resonant orbits extend far beyond the vicinity of the primaries while others pass very closely between both primaries, delivering a variety of potentially useful trajectory design scenarios.

5.2 Transfer Design Capability

The availability of reduced-cost transfer trajectories is enabled through the exploitation of invariant manifolds and Poincaré mapping techniques. Once the periodic orbits of interest are identified and computed in the CR3BP, it is necessary to assess their stability to determine whether natural flow exists to and from the orbits. In this analysis, the computation of low-cost transfer trajectories is enabled primarily by the exploitation of the stable and unstable manifold trajectories associated with resonant orbits. Due to the complexity of the manifold structure emanating from resonant orbits, Poincaré mapping techniques are employed as an alternative visualization method. Poincaré maps offer reduction of dimension, conceptual clarity, and global dynamics. A variety of mapping representations are employed in the display of the manifold trajectories associated with resonant orbits; the flow in the vicinity of periodic orbits is then also revealed. These sections are also particularly effective

in identifying two- and three-dimensional *unstable* resonant orbits and displaying the associated manifold structures. From the maps, appropriate intermediate segments are identified and employed as initial guesses for the construction of transfer trajectories with a wide variety of desired itineraries. A robust and versatile corrections process yields a transfer path that meets the specified design constraints. The result is a continuous trajectory that may be natural (cost-free) or include maneuvers if a natural option is not available.

5.3 Applications of Resonant Orbits to Trajectory Design

The role of resonant orbits in the design of transfer trajectories in multi-body environments is assessed in this investigation through a variety of trajectory design applications. For each application, the versatility and usefulness of the proposed transfer design capability is illustrated through different design scenarios of current interest in preliminary mission design concepts, such as the accessibility of the L_4 and L_5 Lagrange points from low Earth orbit or the approachability of the orbit of Hyperion, a natural satellite of Saturn in resonance with Titan, from an initial orbit around Saturn.

The Saturn-Titan regime is explored by searching for trajectories that naturally transition between interior and exterior resonant orbits as well as between libration point orbits. A family of homoclinic cycles is generated and its existence is demonstrated through a set of Poincaré maps. The problem of accessing Hyperion from both interior and exterior orbits that are resonant with Titan is also examined. Two sample transfer trajectories that exploit invariant manifolds associated with resonant orbits are computed and the associated cost of insertion into Hyperion's orbit is detailed. In addition, a local constrained optimization algorithm is employed to optimize the initial maneuver required to target Hyperion's orbit from one of these initial orbits, and the result demonstrates the close relationship between the local optimal and the manifold trajectory.

In the Earth-Moon system, homoclinic and heteroclinic connections that transition between the interior and exterior regions are calculated with the aid of Poincaré maps. The gravitational influence of the Moon on resonant orbits reveals a number of 2D and 3D resonant families that can exploited in several transfer design scenarios. The transfer design capability is successfully applied in the Earth-Moon system to generate (i) planar and three-dimensional transfer trajectories from LEO to the vicinity of all five Earth-Moon libration points, (ii) periodic Earth-Moon cyclers, and (iii) tours of the regions near all five libration points. Due to the nature of these transfer trajectories, it is necessary to add multiple maneuvers along the transfer path. However, direct optimization techniques are incorporated into the design process to reduce the maneuver cost and time-of-flight associated with selected transfer trajectories. It is, perhaps, this type of application, where unstable resonant orbits in the Earth-Moon are exploited to supply a suitable initial guess for transfer trajectories to and from stable periodic orbits, that clearly highlights the benefits of incorporating resonant arcs into the design process.

Trajectories with predetermined itineraries are efficiently generated exploiting dynamical structures and Poincaré mapping techniques through the transfer design capability. Nevertheless, orbital characteristics vary from system to system and a number of computations are required before the desired transfer trajectory is produced. The capability of selecting a trajectory in the Earth-Moon system and directly translating it to a different three-body system without the necessity of generating periodic orbits, invariant manifolds, and Poincaré maps in the new three-body system is highly valuable. In this investigation, a system translation technique is developed to generate sample periodic orbits and transfers in the Sun-Saturn, Saturn-Titan, and Saturn-Enceledus systems directly from solutions initially generated in the Earth-Moon system by incorporating a mass parameter continuation scheme into the design process.

5.4 Higher-Fidelity Model Analysis

Although the majority of this analysis is developed within the framework of the restricted three-body problem, selected periodic orbits and transfer solutions are transitioned to a higher-fidelity model for validation. The full dynamical model developed in this investigation includes perturbations from additional gravitational bodies and planetary ephemerides. For the subset of trajectories that are explored here, it is verified that the trajectory characteristics are preserved, including resonance conditions, when additional gravitational perturbations are incorporated into the model. The similarities between the trajectories in both models are apparent and a preliminary cost and time-of-flight analysis shows the close comparison between the estimated cost and TOF for associated with the CR3BP and ephemeris solutions.

5.5 Recommendations for Future Work

Exploration and exploitation of Poincaré sections and dynamical systems theory for application to trajectory design in astrodynamics has emerged only recently, but offers great insight. There are many directions for future work concerning the application of resonant orbits to trajectory design. Possible directions for future efforts include:

- *Resonant Families.* The dynamics related to the planar and three-dimensional families of resonant orbits in the restricted problem have been extensively analyzed in this investigation, but their relationship to other periodic orbits that are known to exist in three-body systems remains unexplored. Resonant orbits, along with libration point orbits and distant orbits, offer a good foundation for the construction of an architecture for mission planning options within the context of the CR3BP. However, mapping these families more completely and understanding the dynamical relationships between them may offer significant advantages for design. The stability-energy plots offer an alternative composite view of large sets of families of periodic orbits and may reveal potential rela-

tionship between members if developed in more detail and new solutions may be uncovered.

- *Maneuver Strategies and Poincaré Mapping Techniques.* The proposed transfer design capability benefits from flexibility and automation by incorporating features such as the multi-burn design constraint, which allows the placement of any number of ΔVs along the transfer path. However, the patch points that include intermediate maneuvers are determined by the user input. The analysis of maneuver placement strategies that supply a more suitable location for the intermediate burns is worth pursuing. For instance, local Lyapunov exponents could be used to determine locations where a maneuver would be most effective and potentially reveal regions where navigation would be more difficult.

  Poincaré maps are computationally expensive; however, it is demonstrated that their computation is necessary in the display and analysis of the invariant manifolds associated with resonant orbits. If the end goal is the implementation the design process to quickly produce preliminary feasible trajectories that meet desired constraints or potentially as part of an automated, onboard corrections scheme, a more computationally efficient visualization method may be considered. As an alternative, a large map can be decomposed into smaller sections depending on the region of space being explored, speeding up the computation time. Investigation of alternative quantities used to represent the sections is also recommended. Cartesian coordinates are almost exclusively employed in this analysis to represent returns to the map. However, other representations, such as Delauney variables, may offer valuable insight. Ultimately, the goal of incorporating Poincaré maps into the design process is to supply better initial guesses and, thus, further improvement of planar and higher-dimensional mapping techniques is warranted.

- *Analysis in a Full Ephemeris Model.* The ephemeris model developed in this investigation includes n-body dynamics and planetary ephemeries. More specif-

ically, the solutions initially generated in the Earth-Moon CR3BP are transitioned to a higher-fidelity model that includes the gravitational effects of the Earth, Moon, and Sun, as well as lunar eccentricities. However, additional non-gravitational perturbations such as solar radiation pressure effects are not currently incorporated into the model. As illustrated, the gravitational influence of the Earth, Moon, and Sun can significantly impact a trajectory and the associated cost of a transfer and even time-of-flight, especially near the two primaries. Therefore, by exploiting these simultaneous effects, the design efforts can not only benefit from better predictions and more accurate modeling of the trajectory but the number of trajectory design options available may also increase, including the availability of more cost effective solutions.

Historically, resonant orbits have been a valuable source for mission designers, particularly in the design of flyby trajectories involving multiple planets and moons. More recently, the applicability of orbital resonance to trajectory design has increased through the long-term stability support of artificial satellites in Earth orbits. The exploitation of resonant orbits as cost efficient transfer mechanisms between non-resonant orbits in multi-body environments unveils yet another source of possibilities.

LIST OF REFERENCES

LIST OF REFERENCES

[1] J. A. Sims. Jupiter Icy Moons Orbiter Mission Design Overview. In *16th AAS/AIAA Space Flight Mechanics Conference*, Tampa, Florida, January 22-26 2006. Paper AAS-06-185.

[2] National Aeronautics and Space Administration. Planetary Science Decadal Survey: Jupiter Europa Orbiter Component of EJSM, March 2010.

[3] D. J. McComas. Interstellar Boundary Explorer. http://www.ibex.swri.edu, February 2013.

[4] J. D. Harrington. NASA Selects Explorer Investigations for Formulation, National Aeronautics and Space Administration News Release 13-088, April 2013.

[5] H. Poincaré. *Science and Hypothesis*. Walters Scott Publishing, London, 1905.

[6] I. Peterson. *Newton's Clock: Chaos in the Solar System*. W. H. Freeman and Company, New York, 1993.

[7] G. D. Birkhoff. *Dynamical Systems*, volume 9 of *American Mathematical Society Colloquium Publications*. American Mathematical Society, Providence, Rhode Island, 1927.

[8] V. I. Arnold. Proof of a Theorem by A. N. Kolmogorov on the Invariance of Quasi-Periodic Motions Under Small Perturbations of the Hamiltonian. *Uspekhi Matematicheskikh Nauk*, 18(5):13–40, 1963.

[9] A. N. Kolmogorov. On the Conservation of Conditionally Periodic Motions for a Small Change in Hamilton's Function. *Doklady Akademii Nauk SSSR*, 98:525–530, 1954. English Translation in *LNP* 93:51-56, 1979.

[10] J. Moser. On Invariant Curves of Area-Preserving Mappings of an Annulus. *Nachr. Akad. Wiss. Gttingen Math.-Phys. Kl. II*, 1:1–20, 1962.

[11] K. C. Howell. Families of Orbits in the Vicinity of the Collinear Libration Points. *Journal of the Astronautical Sciences*, 49(1):107–125, January-March 2001.

[12] R. W. Farquhar and A. A. Kamel. Quasi-periodic Orbits About the Translunar Libration Point. *Celestial Mechanics*, 7:458–473, 1973.

[13] K. C. Howell. Three-dimensional, Periodic, 'Halo' Orbits. *Celestial Mechanics*, 32(1):53–71, January 1984.

[14] R. W. Farquhar. The Flight of ISEE-3/ICE: Origins, Mission History, and a Legacy. *Journal of the Astronautical Sciences*, 49(1):23–73, January-March 2001.

[15] V. Domingo, B. Fleck, and A. I. Poland. The SOHO Mission: An Overview. *Solar Physics*, 162:1–37, 1995.

[16] P. Sharer and T. Harrington. Trajectory Optimization for the ACE Halo Orbit Mission. In *AAS/AIAA Astrodynamics Specialist Conference*, San Diego, California, 29-31 July 1996. Paper AAS 93-3601.

[17] C. L. Bennett, M. Bay, M. Halpern, G. Hinshaw, C. Jackson, N. Jarosik, A. Kogut, M. Limon, S. S. Meyer, L. Page, D. N. Spergel, G. S. Tucker, D. T. Wilkinson, E. Wollack, and E. L. Wright. The Microwave Anisotropy Probe Mission. *Astrophysical Journal*, 583:1–23, January 2003.

[18] C. Conley. Low Energy Transit Orbits in the Restricted Three-Body Problem. *SIAM Journal of Applied Mathematics*, 16:732–746, 1968.

[19] G. Gómez, J. Llibre, R. Martínez, and C. Simó. *Dynamics and Misison Design Near Libration Points Vol. I Fundamentals: The Case of Collinear Libration Points, Volume 2 of World Scientific Monograph Series in Mathematics*. World Scientific, New Jersey, 2001.

[20] K. C. Howell, B. T. Barden, and M. W. Lo. Application of Dynamical Systems Theory to Trajectory Design for a Libration Point Mission. *The Journal of Astronautical Sciences*, 45(2):161–178, April-June 1997.

[21] K. C. Howell, B. T. Barden, and R. S. Wilson. Trajectory Design Using a Dynamical Systems Approach with Application to GENESIS. In *AAS/AIAA Astrodynamics Specialist Conference*, August 4-7 1997. Paper AAS 97-709.

[22] M. Lo and S. Ross. Low Energy Interplanetary Transfers Using Invariant Manifolds of L1, L2, and Halo Orbits. In *AAS/AIAA Space Flight Mechanics Meeting*, Monterey, California, February 9-11 1998.

[23] M. W. Lo. The Interplanetary Superhighway and the Origins Program. In *IEEE Space 2002 Conference*, Big Sky, Montana, March 2002.

[24] G. Gómez, W. S. Koon, M. W. Lo, J. E. Marsden, J. Masdemont, and S. D. Ross. Connecting Orbits and Invariant Manifolds in the Spatial Three-Body Problem. *Institute of Physics Publishing, Nonlinearity*, 17:1571–1606, May 2004.

[25] M. Lo and S. D. Ross. Application of Dynamical Systems Theory to a Very Low Energy Transfer. In *AAS/AIAA Space Flight Mechanics Conference*, Maui, Hawaii, February 8-12 2004.

[26] M. A. Minovitch. A Method for Determining Interplanetary Free-Fall Reconnaissance Trajectories. Technical Memorandum 312-130, Jet Propulsion Laboratory, August 1961.

[27] M. A. Minovitch. The Determination and Characteristics of Ballistic Interplanetary Trajectories under the Influence of Multiple Planetary Attractions. Technical Report 32-464, Jet Propulsion Laboratory, October 1963.

[28] J. R. Johannesen and L. A. D'Amario. Europa Orbiter Mission Trajectory Design. In *AAS/AIAA Astrodynamics Specialist Conference*, Girdwood, Alaska, August 16-19 1999. Paper AAS 99-360.

[29] R. Malhotra. Nonlinear Resonances in the Solar System. *Physica D: Nonlinear Phenomena*, 77(1-3):289–304, October 1994.

[30] E. Belbruno and B. Marsden. Resonance Hopping in Comets. *Astronomical Journal*, 113(4):1433–1444, 1997.

[31] W. S. Koon, M. W. Lo, J. E. Marsden, and S. D. Ross. Heteroclinic Connections Between Periodic Orbits and Resonance Transitions in Celestial Mechanics. *Chaos*, 10(2):427–469, June 2000.

[32] W. S. Koon, M. W. Lo, J. E. Marsden, and S. D. Ross. Resonance and Capture of Jupiter Comets. *Celestial Mechanics and Dynamical Astronomy*, 81(1-2):27–38, 2001.

[33] K. C. Howell, B. Marchand, and M. W. Lo. Temporary Satellite Capture of Short-Period Jupiter Family Comets from the Perspective of Dynamical Systems. *The Journal of the Astronautical Sciences*, 49(4):539–557, October-December 2001.

[34] M. W. Lo, R. L. Anderson, G. Whiffen, and L. Romans. The Role of Invariant Manifolds in Low Thrust Trajectory Design (Part I). In *AAS/AIAA Spaceflight Dynamics Conference*, Maui, Hawaii, February 2004. Paper AAS 04-288.

[35] R. L. Anderson and M. W. Lo. The Role of Invariant Manifolds in Low Thrust Trajectory Design (Part II). In *AAS/AIAA Spaceflight Dynamics Conference*, Providence, Rhode Island, August 2004. Paper AAS 06-190.

[36] M. W. Lo, R. L. Anderson, T. Lam, and G. Whiffen. The Role of Invariant Manifolds in Low Thrust Trajectory Design (Part III). In *AAS/AIAA Spaceflight Dynamics Conference*, Tampa, Florida, January 2006. Paper AAS 06-190.

[37] A. F. Heaton, N. J. Strange, J. M. Longuski, and E. P. Bonfiglio. Automated Design of the Europa Orbiter Tour. *Journal of Spacecraft and Rockets*, 39(1), January-February 2002.

[38] R. L. Anderson and M. W. Lo. Flyby Design Using Heteroclinic and Homoclinic Connections of Unstable Resonant Orbits. In *21st AAS/AIAA Space Flight Mechanics Meeting*, New Orleans, Louisiana, February 13-17 2011. Paper AAS-11-125.

[39] M. Vaquero. Poincaré Sections and Resonant Orbits in the Restricted Three-Body Problem. M.S. Thesis, School of Aeronautics and Astronautics, Purdue University, West Lafayette, Indiana, 2010.

[40] M. Vaquero and K. C. Howell. Poincaré Maps and Resonant Orbits in the Circular Restricted Three-Body Problem. In *AAS/AIAA Astrodynamics Specialist Conference*, Girdwood, Alaska, July 31 - August 4 2011. Paper AAS-11-428.

[41] J. S. Parker and M. W. Lo. Unstable Resonant Orbits near Earth and Their Applications in Planetary Missions. In *AIAA/AAS Astrodynamics Specialist Conference*, Providence, Rhode Island, August 2004. AIAA 2004-22819.

[42] J. S. Parker and G. H. Born. Direct Lunar Halo Orbit Transfers. In *17th AAS/AIAA Space Flight Mechanics Meeting*, Sedona, Arizona, January 28 - February 1 2007. Paper AAS-07-229.

[43] E. Perozzi and A. Di Salvo. Novel Spaceways for Reaching the Moon: An Assessment for Exploration. *Celestial Mechanics and Dynamical Astronomy*, 102(1-3):207–218, 2008.

[44] J. S. Parker and M. W. Lo. Shoot the Moon 3D. In *AAS/AIAA Astrodynamics Specialist Conference*, Lake Tahoe, California, August 7-11 2005. Paper AAS-05-383.

[45] M. Standish. JPL Planetary and Lunar Ephemerides. Technical Report, Jet Propulsion Laboratory, JPL IOM 312.F-98-048, Pasadena, California, August 1998.

[46] V. Szebehely. *Theory of Orbits: The Restricted Problem of Three Bodies*. Academic Press, Inc., New York, New York, 1967.

[47] T. A. Pavlak. Mission Design Applications in the Earth-Moon System: Transfer Trajectories and Stationkeeping. M.S. Thesis, School of Aeronautics and Astronautics, Purdue University, West Lafayette, Indiana, 2010.

[48] D. J. Grebow. Trajectory Design in the Earth-Moon System and Lunar South Pole Coverage. Ph.D. Dissertation, School of Aeronautics and Astronautics, Purdue University, West Lafayette, Indiana, 2010.

[49] H. Poincaré. *Les Méthodes Nouvelles de la Mécanique Celeste*, volume II. Gauthier-Villars, Paris, 1893.

[50] E. J. Doedel et al. Elemental Periodic Orbits Associated with the Libration Points in the Circular Restricted 3-Body Problem. *International Journal of Bifurcation and Chaos*, 17(8):2625–2677, January 2007.

[51] Z. P. Olikara. Computation of Quasi-Periodic Tori in the Circular Restricted Three-Body Problem. M.S. Thesis, School of Aeronautics and Astronautics, Purdue University, West Lafayette, Indiana, 2010.

[52] V. A. Yakubovich and V. M. Starzhinskii. *Differential Equations with Periodic Coefficients*. John Wiley and Sons, New York, 1975.

[53] B. T. Barden. Using Stable Manifolds to Generate Transfers in the Circular Restricted Problem of Three Bodies. M.S. Thesis, School of Aeronautics and Astronautics, Purdue University, West Lafayette, Indiana, 1994.

[54] N. Bosanac. Exploring the Influence of a Three-Body Interaction Added to the Gravitational Potential Function In The Circular Restricted Three-Body Problem: A Numerical Frequency Analysis. M.S. Thesis, School of Aeronautics and Astronautics, Purdue University, West Lafayette, Indiana, 2012.

[55] D. J. Grebow. Generating Periodic Orbits in the Circular Restricted Three-Body Problem with Applications to Lunar South Pole Coverage. M.S. Thesis, School of Aeronautics and Astronautics, Purdue University, West Lafayette, Indiana, 2006.

[56] T. S. Parker and L. O. Chua. *Numerical Algorithms for Chaotic Systems*. Springer-Verlag, New York, 1989.

[57] J. Guckenheimer and P. Holmes. *Nonlinear Oscillations, Dynamical Systems, and Bifurcations of Vector Fields*. Springer-Verlag, New York, 1983.

[58] L. Perko. *Differential Equations and Dynamical Systems*. Springer-Verlag, New York, 1991.

[59] K. C. Howell, M. Beckman, C. Patterson, and D. Folta. Representation of Invariant Manifolds for Applications in Three-Body Systems. *The Journal of the Astronautical Sciences*, 54(1)(1), January-March 2006.

[60] K. C. Howell, D. C. Davis, and A. F. Haapala. Application of Periapse Maps for the Design of Trajectories Near the Smaller Primary in Multi-Body Regimes. *Mathematical Problems in Engineering*, 2012, 2012. Article ID 351759, 22 pages, 2012. doi:10.1155/2012/351759.

[61] M. Hénon. Numerical Exploration of the Restricted Three-Body Problem. *International Astronomical Union. Simposium no. 25*, page 157, 1966. Academic Press, London.

[62] V. V. Markellos and A. E. Roy. Hill Stability of Satellite Orbits. *Celestial Mechanics*, 23:269–275, March 1981.

[63] R. L. Anderson. Low Thrust Trajectory Design for Resonant Flybys and Captures Using Invariant Manifolds. Ph.D. Dissertation, School of Aeronautics and Astronautics, University of Colorado, Boulder, Colorado, 2005.

[64] L. R. Irrgang. Investigation of Transfer Trajectories To and From the Equilateral Libration Points L_4 and L_5 in the Earth-Moon System. M.S. Thesis, School of Aeronautics and Astronautics, Purdue University, West Lafayette, Indiana, 2008.

[65] R. Seydel. *Practical Bifurcation and Stability Analysis: From Equilibrium to Chaos*. Springer-Verlag, New York, 1994.

[66] R. A. Broucke. *Periodic Orbits in the Restricted Three-Body Problem with. Earth-Moon Masses*. Jet Propulsion Lab, Technical Report 32-1168, Pasadena, California, 1968.

[67] D. C. Davis and K. C. Howell. Characterization of Trajectories Near the Smaller Primary in the Restricted Problem for Applications. *Journal of Guidance, Control, and Dynamics*, 35(1):116–128, January-February 2012.

[68] M. W. Lo and J. S. Parker. Chaining Simple Periodic Three-Body Orbits. In *AIAA/AAS Astrodynamics Specialist Conference*, Lake Tahoe, California, August 7-11 2005. Paper AAS-05-380.

[69] J. S. Parker, K. E. Davis, and G. H. Born. Chaining Periodic Three-Body Orbits in the Earth-Moon System. volume 67, pages 623–638, 2010.

[70] D. Folta, T. Pavlak, A. Haapala, K. Howell, and M. Woodard. Earth-Moon Libration Point Orbit Stationkeeping: Theory, Modeling, and Operations. *Acta Astronautica*, February 2013. Available at: http://dx.doi.org/10.1016/j.actaastro.2013.01.022.

[71] R. W. Farquhar. The Control and Use of Libration-Point Satellites. Ph.D. Dissertation, Stanford University, Stanford, California, 1968.

[72] B. Marchand. Temporary Satellite Capture of Short-Period Jupiter Family Comets from the Perspective of Dynamical Systems. M.S. Thesis, School of Aeronautics and Astronautics, Purdue University, West Lafayette, Indiana, 2000.

[73] D. J. Grebow, M. T. Ozimek, K. C. Howell, and D. C. Folta. Multi-Body Orbit Architectures for Lunar South Pole Coverage. *Journal of Spacecraft and Rockets*, 45(2):344–358, 2008.

[74] D. Landau, J. Dankanich, N. Strange, J. Bellerose, P. Llanos, and M. Tantardini. Trajectories to Nab a NEA (Near-Earth Asteroid). In *23rd AAS/AIAA Space Flight Mechanics Meeting*, Kauai, Hawaii, February 10-14 2013. Paper AAS-13-409.

[75] C. D. Murray and S. F. Dermott. *Solar System Dynamics*. Cambridge University Press, Cambridge, Cambridge, United Kingdom, 1999.

[76] J. Carrico et al. Lunar-Resonant Trajectory Design for the Interstellar Boundary Explorer (IBEX) Extended Mission. In *AAS/AIAA Astrodynamics Specialist Conference*, Girdwood, Alaska, July 31 - August 4 2011. Paper AAS-11-454.

[77] D. J. McComas et al. A New Class of Long-Term Stable Lunar Resonance Orbits: Space Weather Applications and the Interstellar Boundary Explorer. *Space Weather*, 9:9, November 2011.

[78] M. Vaquero and K. C. Howell. Transfer Design Exploiting Resonant Orbits and Manifolds in the Saturn-Titan System. *Journal of Spacecraft and Rockets*, February 2013. DOI: 10.2514/1.A32412.

[79] S. D. Ross, W. S. Koon, M. W. Lo, and J. E. Marsden. Design of a Multi-Moon Orbiter. In *13th AAS/AIAA Space Flight Mechanics Meeting*, Ponce, Puerto Rico, February 9-13 2003. Paper AAS-03-143.

[80] R. Bevilacqua, O. Menchi, A. Milani, A. M. Nobili, and P. Farinella. Resonances and Close Approaches. I. The Titan-Hyperion Case. *Earth, Moon, and Planets*, 22(2):142–152, April 1980.

[81] Jet Propulsion Laboratory. Horizons (Version 3.36). http://ssd.jpl.nasa.gov/?horizons, October 2010.

[82] G. N. Vanderplaats. *Multidiscipline Design Optimization*. VR&D, 2007.

[83] G. Gómez, M. Marcote, and J. M. Mondelo. The Invariant Manifold Structure of the Spatial Hills Problem. *Dynamical Systems: An International Journal*, 20(1):115–147, March 2005.

[84] A. Jorba and J. Masdemont. Dynamics in the Center Manifold of the Collinear Points of the Restricted Three Body Problem. *Physica D: Nonlinear Phenomena*, 132(1-2):189–213, 1999.

[85] M. O. Ward. A Taxonomy of Glyph Placement Strategies for Multidimensional Data Visualization. *Information Visuallization*, 1:194–210, December 2002.

[86] R. Pickett and G. Gristein. Iconographic Displays for Visualizing Multidimensional Data. *Proceedings of the 1988 IEEE International Conference on Systems, Man, and Cybernetics*, 1:514–519, August 1988.

[87] M. E. Paskowitz and D. J. Scheeres. Robust Capture and Transfer Trajectories for Planetary Satellite Orbiters. *Journal of Guidance, Control, and Dynamics*, 29(2):342–353, March-April 2006.

[88] A. F. Haapala and K. C. Howell. Representations of Higher-Dimensional Poincaré Maps with Applications to Spacecraft Trajectory Design. In *63rd International Astronautical Congress*, Naples, Italy, October 1-5 2012. Paper IAC-12.C1.7.2.

[89] M. Vaquero and K. C. Howell. Design of Transfer Trajectories Between Resonant Orbits in the Earth-Moon Restricted Problem. *Acta Astronautica*, May 2013. Available at: http://dx.doi.org/10.1016/j.actaastro.2013.05.006.

[90] B. F. Villac and D. J. Scheeres. Escaping Trajectories in the Hill Three-Body Pproblem and Applications. *Journal of Guidance, Control, and Dynamics*, 26(2):224–232, March-April 2003.

[91] D. C. Davis and K. C. Howell. Trajectory Evolution in the Multi-Body Problem with Applications in the Saturnian System. *Acta Astronautica*, 69:1038–1049, 2011.

[92] M. Vaquero and K. C. Howell. Leveraging Resonant Orbit Manifolds To Design Transfers Between Libration Point Orbits in Multi-Body Regime. In *23rd AAS/AIAA Spaceflight Mechanics Meeting*, Kauai, Hawaii, February 10-14 2013. Paper AAS-13-334.

[93] M. Vaquero and K. C. Howell. Design of Transfer Trajectories Between Resonant Orbits in the Restricted Problem with Application to the Earth-Moon System. In *1st IAA Conference on Dynamics and Control of Space Systems*, Porto, Portugal, March 19-21 2012. Paper IAA-AAS-DyCoSS1-05-09.

[94] K. E. Davis, G. H. Born, M. Deilami, A. Larsen, and E. A. Butcher. Transfers to Earth-Moon L_3 Halo Orbits. In *AIAA/AAS Astrodynamics Specialist Conference*, Minneapolis, Minnesota, August 13-16 2012. Paper AIAA 2012-4593.

[95] A. Larsen et al. Optimal Transfers with Guidance to the Earth-Moon L_1 and L_3 Libration Points using Invariant Manifolds: A Preliminary Study. In *AIAA/AAS Astrodynamics Specialist Conference*, Minneapolis, Minnesota, August 13-16 2012. Paper AIAA 2012-4667.

[96] R. L. Anderson and J. S. Parker. Comparison of Low-Energy Lunar Transfer Trajectories to Invariant Manifolds. In *AAS/AIAA Astrodynamics Specialist Conference*, Girdwood, Alaska, July 31 - August 4 2011. Paper AAS-11-423.

[97] F. J. T. Salazar, C. F. de Melo, E. E. N. Macau, and O. C. Winter. Three-Body Problem, Its Lagrangian Points and How to Exploit Them Using an Alternative Transfer to L_4 and L_5. *Celestial Mechanics and Dynamical Astronomy*, 114(1-2):201–213, October 2012.

[98] D. V. Byrnes, J. M. Longuski, and Buzz Aldrin. Cycler Orbit Between Earth and Mars. *Journal of Spacecraft and Rockets*, 30(3):334–336, 1993.

[99] T. T. McConaghy, C. H. Yam, D. F. Landau, and J. M. Longuski. Two-Synodic-Period Earth-Mars Cyclers with Intermediate Earth Encounter. In *AIAA/AAS Astrodynamics Specialist Conference*, Big Sky, Montana, August 3-7 2003. Paper AAS-03-509.

[100] T. T. McConaghy, R. P., Russell, J. M. Longuski. Towards a Standard Nomenclature for Earth-Mars Cycler Trajectories. *Journal of Spacecraft and Rockets*, 42(4):694–698, 2005.

[101] R. P., Russell and C. A. Ocampo. Systematic Method for Constructing Earth-Mars Cyclers Using Free-Return Trajectories. *Journal of Guidance, Control, and Dynamics*, 27(3):321–335, 2004.

[102] R. P., Russell and C. A. Ocampo. Global Search for Idealized Free-Return Earth-Mars Cyclers. *Journal of Guidance, Control, and Dynamics*, 28(2):194–208, 2005.

[103] R. P., Russell and C. A. Ocampo. Optimization of a Broad Class of Ephemeris Model EarthMars Cyclers. *Journal of Guidance, Control, and Dynamics*, 29(2):354–367, 2006.

[104] R. P. Russell and N. J. Strange. Planetary Moon Cycler Trajectories. In *17th AAS/AIAA Space Flight Mechanics Meeting*, Sedona, Arizona, January 28 - February 1 2007. Paper AAS-07-118.

[105] J. Casoliva, J. M. Mondelo, B. F. Villac, K. D. Mease, E. Barrabes, and M. Ollé. Families of Cycler Trajectories in the Earth-Moon System. In *AIAA/AAS Astrodynamics Specialist Conference and Exhibit*, Honolulu, Hawaii, August 18-21 2008. Paper AIAA-2008-6434.

[106] J. Casoliva, J. M. Mondelo, B. F. Villac, K. D. Mease, E. Barrabes, and M. Ollé. Families of Cycler Trajectories in the Earth-Moon System. volume 33, pages 1623–1640, 2010.

[107] M. Hénon. Numerical Exploration of the Restricted Problem. V. Hill's Case: Periodic Orbits and Their Stability. *Astronomy and Astrophysics*, 1:223–238, February 1969.

[108] T. Lam and G. J. Whiffen. Exploration of Distant Retrograde Orbits Around Europa. In *15th AAS/AIAA Spaceflight Mechanics Meeting*, Copper Mountain, Colorado, January 23-27 2005. Paper AAS-05-110.

[109] J. Demeyer and P. Gurfil. Transfer to Distant Retrograde Orbits Using Manifold Theory. *Journal of Guidance, Control and Dynamics*, 30:1261–1267, September-October 2007.

VITA

VITA

Mar Vaquero received a Bachelor of Science Degree in Aerospace Engineering with a minor in Mathematics in 2006, and a Bachelor of Science Degree in Physics in 2007 from Parks College, Saint Louis University. She completed her Master's Degree at Purdue University in May 2010. Her master's thesis focused on the application of Poincaré sections and manifold theory to search for natural transfers between resonant orbits in multi-body environments. In August 2010, Mar continued to pursue a Ph.D. Degree in Astrodynamics and Space Applications in the School of Aeronautics and Astronautics at Purdue University. Her doctoral research focused on resonant orbits in the solar system and their application to mission design. Throughout her graduate education, she was an instructor of Spanish at the School of Languages and Cultures at Purdue University, an instructor of Flight Science at the Johns Hopkins University Center for Talented Youth, and a participant in the International Space University Space Studies Program at NASA Ames Research Center in Moffett Field, California. She plans to join the Jet Propulsion Laboratory in August 2013 as a Mission Design Engineer in the Mission Design and Navigation Section.